Charges and Charged Defects in Pb-based Ferro- and Antiferroelectric Ceramics

Zur Erlangung des akademischen Grades Doktor-Ingenieur (Dr.-Ing.)
Genehmigte Dissertation von Binxiang Huang aus Shanghai, China
Tag der Einreichung: 05.06.2023, Tag der Prüfung: 28.07.2023

1. Gutachten: Prof. Dr. Andreas Klein
2. Gutachten: Prof. Dr. Tadej Rojac
Darmstadt, Technische Universität Darmstadt

TECHNISCHE UNIVERSITÄT DARMSTADT

Materials and Earth Sciences Department

Electronic Structure of Materials

Charges and Charged Defects in Pb-based Ferro- and Antiferroelectric Ceramics

Accepted doctoral thesis by Binxiang Huang

1. Review: Prof. Dr. Andreas Klein
2. Review: Prof. Dr. Tadej Rojac

Date of submission: 05.06.2023
Date of thesis defense: 28.07.2023

Darmstadt, Technische Universität Darmstadt

Erklärungen laut Promotionsordnung

§8 Abs. 1 lit. c PromO

Ich versichere hiermit, dass die elektronische Version meiner Dissertation mit der schriftlichen Version übereinstimmt.

§8 Abs. 1 lit. d PromO

Ich versichere hiermit, dass zu einem vorherigen Zeitpunkt noch keine Promotion versucht wurde. In diesem Fall sind nähere Angaben über Zeitpunkt, Hochschule, Dissertationsthema und Ergebnis dieses Versuchs mitzuteilen.

§9 Abs. 1 PromO

Ich versichere hiermit, dass die vorliegende Dissertation selbstständig und nur unter Verwendung der angegebenen Quellen verfasst wurde.

§9 Abs. 2 PromO

Die Arbeit hat bisher noch nicht zu Prüfungszwecken gedient.

Darmstadt, 05.06.2023

Binxiang Huang

Abstract

Ferroelectric (FE) and antiferroelectric (AFE) ceramics are widely used in capacitors for various purposes because of their specific dielectric properties and outstanding insulating nature. Several types of charges and charged point defects are considered to exist in these materials, participating in the mechanisms of charge compensation from different perspectives, such as the compensation within the bulk material which determines the electrical conductivity, the compensation at the domain walls which rationalizes the domain structures, and the compensation at the electrode/dielectric interfaces which screens the depolarization fields and thereby stabilizes the switched FE states. Therefore, identifying these charge carriers and understanding their compensation behavior are fundamental to the design and optimization of these FE and AFE materials.

In this work, three composition series based on the well-known Pb-based perovskite AFE system $(Pb,La)(Zr,Sn,Ti)O_3$ (PLZST) were studied by dc conductivity measurement and X-ray photoelectron spectroscopy (XPS). By combining these two characterization techniques, fundamental correlations in terms of the electronic structures could be explored between the charge compensations and the dielectric properties. These ceramic samples were prepared with traditional solid-state reaction method. Prior to the conductivity and XPS studies, several basic characterizations were performed first, including hysteresis loops, dielectric permittivities, crystalline structures by X-ray diffraction, and microstructures by scanning electron microscopy, in order to get the basic information of the sintered ceramics.

High resistivity is a necessary condition for the FE and AFE materials, and it can be described principally by the charge compensation and transport within the bulk. In order to get an overview of the conduction behavior of these samples, dc conductivities were measured under different thermal and electrical conditions. Variations in the conductivity, which are very likely caused by the migration and redistribution of oxygen and/or lead vacancies, have been observed. The comparisons among different compositions reveal that donor- or “net-donor” doping can effectively reduce the conductivity of these Pb-based ceramics. The Arrhenius relations of the donor-doped samples are nearly parallel at 300°C–400°C, indicating very similar transport mechanisms. Besides, a higher conductivity has been noticed in a field-induced FE state compared to that in its AFE state before the AFE-to-FE phase transition. This implies an additional conducting contribution in a FE phase, probably related to the existence of charged domain walls.

As it has been realized in the conductivity studies that the low conductivities of these Pb-based dielectrics cannot be well explained without taking the traps for electrons and holes into account, a novel in situ XPS method has been developed to explore such traps within the band gap of a dielectric. Making use of the migration of oxygen species, the sandwich capacitor structure can be operated as a solid electrochemical cell, where the dielectric acts as the electrolyte. Electrochemical reduction and oxidation, which can be characterized by XPS, are expected to take place at the cathodic and anodic interfaces, respectively. By this means, the reduction and oxidation potentials, which indicate the existence of trap levels, are used to identify the upper and lower limits of the Fermi energy of the dielectric, respectively. In this work, an

electron trap $Pb^{2+/0}$ has been detected in some of the studied materials, different from the electron trap $Ti^{4+/3+}$ and the hole trap $Pb^{2+/3+}$ that are widely accepted in the literature on $Pb(Zr,Ti)O_3$. Moreover, the observation of the reduced Pb exhibits a composition dependence, implying that the preferred site for such reduction might be related to the states at the bottom of the conduction band.

Regarding the charge compensation at the electrode/dielectric interfaces, selected FE and AFE compositions have been studied by another in situ XPS approach, where sufficiently high electric fields can be applied to the sandwich capacitor structure in order to change the polarization state within the bulk ceramic and XPS is measured meanwhile through a thin top electrode. According to the electrode screening theory, an extra electric potential drop occurs at the electrode interface when the bound charges and the free compensating charges are spatially separated by a screening length. This extra potential drop can be characterized by a binding energy shift of the dielectric elements in the XPS spectrum. By detecting such emission shifts, the magnitude of FE polarization, the extent of dipole alignment, and the depth of the charge compensation can be analyzed. In this part, electrode-material-dependent asymmetric screening behavior has been observed for the FE samples. Moreover, no binding energy shift has been seen at the electrode/AFE interface even when the applied field already exceeds the AFE-to-FE transition point. This implies a fundamental discrepancy between the electrode/FE and the electrode/AFE interfaces in terms of the depth where the bound charges of a FE state are compensated. Based on these observations, several screening models that involve charge injection through the electrode interfaces have been suggested, in which the previously mentioned trap levels of electrons and/or holes may play certain roles.

The novelty of this work is reflected in both technology and research. New technical strategies of XPS have been developed for extracting useful information from insulating bulk materials, which is usually thought to be difficult because of the charging problem. More importantly, this work can highlight the roles of different charges existing in the dielectric materials and provide some fundamental understanding of the dielectric properties from the viewpoint of electronic structures.

Zusammenfassung

Ferroelektrische (FE) und antiferroelektrische (AFE) Keramiken sind wegen ihrer spezifischen dielektrischen und herausragenden isolierenden Eigenschaften in Kondensator-artigen Strukturen für verschiedene Anwendungsbereiche weit verbreitet. Unterschiedliche Ladungen und geladene Defekte tragen in diesen Materialien in verschiedener Weise zur Ladungskompensation bei: Die Kompensation im Inneren der Materialien bestimmt deren elektrische Eigenschaften, die Kompensation geladener Domänenwände beeinflusst die Domänenstruktur und damit die dielektrischen Eigenschaften, während Ladungen an der Elektrodengrenzfläche die Polarisation abschirmen und damit zu deren Stabilisierung beitragen. Ein grundlegendes Verständnis der beitragenden Ladungen und deren Einfluss auf das Kompensationsverhalten ist daher von großer Bedeutung, um die Eigenschaften ferroelektrischer und antiferroelektrischer Materialien gezielter einstellen zu können.

In dieser Arbeit wurde der Einfluss der Zusammensetzung gut bekannter Pb-basierter (anti)ferroelektrischer Perowskite mit der allgemeinen Zusammensetzung (Pb,La)(Zr,Sn,Ti)O_3 (PLZST) mittels elektrischer Leitfähigkeitsmessungen und Röntgen-Photoelektronenspektroskopie (XPS) untersucht. Durch Kombination der Ergebnisse der beiden Messverfahren wurden grundlegende Zusammenhänge zwischen den Ladungskompensationsmechanismen und den (di)elektrischen Eigenschaften und deren Bezug zur elektronischen Struktur der Materialien untersucht. Hierzu wurden Volumenkeramiken mit systematischer Variation der Zusammensetzung über die konventionelle Festkörpersynthese hergestellt. Neben der elektrischen und XPS Charakterisierung wurden ebenfalls die grundlegenden Eigenschaften der Materialien wie die Hystereschleifen, die dielektrische Permittivität sowie deren Kristall- und Mikrostruktur erfasst.

Ein hoher elektrischer Widerstand ist Voraussetzung für die Anwendung ferroelektrischer und antiferroelektrischer Materialien. Um einen Überblick über das elektrische Verhalten in Abhängigkeit der Zusammensetzung der Proben zu bekommen wurden elektrische Gleichstrommessungen bei unterschiedlichen Temperaturen und elektrischen Feldern durchgeführt. Die beobachteten Änderungen der elektrischen Leitfähigkeit sind vermutlich auf die Migration und Umordnung von Sauerstoff- und/oder Blei-Leerstellen zurückzuführen. Der Vergleich unterschiedlicher Proben bestätigt, dass die elektrische Leitfähigkeit durch Donator-Dotierung deutlich erniedrigt wird. Die Donator-dotierten Proben zeigen ein nahezu paralleles Arrhenius-Verhalten im Bereich 300°C–400°C, was auf einen ähnlichen Ladungstransportmechanismus hinweist. Bei niedrigeren Temperaturen konnte eine erhöhte Leitfähigkeit im feldinduzierten ferroelektrischen Bereich von AFE Materialien gegenüber dem AFE Grundzustand nachgewiesen werden. Die erhöhte Leitfähigkeit im ferroelektrischen Zustand weist auf einen zusätzlichen Leitfähigkeitspfad hin, der möglicherweise durch geladene Domänenwände gegeben ist.

Die elektrische Leitfähigkeit donator-dotierter Materialien kann nicht durch freie Ladungsträger beschrieben werden. Vielmehr müssen lokalisierte Ladungsträger betrachtet werden. Um die energetische Lage dieser Ladungsträger innerhalb der Bandlücke der Materialien zu identifizieren, wurde eine neue Methode zu deren Charakterisierung mit in-situ XPS entwickelt. Die Methode nutzt die Migration

der Sauerstoffleerstellen in einer Kondensatorstruktur bei angelegtem elektrischem Feld, in der der Kondensator bei höheren Temperaturen als elektrochemische Zelle funktioniert. Das Dielektrikum wirkt dabei als Elektrolyt für Sauerstoffionen. Eine elektrochemische Reduktion bzw. Oxidation wird dabei an der Kathoden- bzw. der Anodengrenzfläche erwartet. Bei hinreichend geringer Dicke der Elektrode, kann die Reduktion bzw. Oxidation direkt mit der XPS beobachtet werden. Mit derartigen Messungen kann die durch die elektrochemische Reduktion oder Oxidation begrenzte Lage des Fermi-Niveaus in der Bandlücke quantifiziert werden. In dieser Arbeit konnte erstmals eine Reduktion des Bleis, $Pb^{2+/0}$, in einigen der untersuchten Materialien identifiziert werden. Die Reduktion des Blei ergänzt die in der Literatur zu $Pb(Zr,Ti)O_3$ weithin akzeptierte Reduktion des Ti, $Ti^{4+/3+}$, und Oxidation des Bleis, $Pb^{2+/3+}$. Die Ergebnisse legen nahe, dass die Reduktion des Pb bzw. Ti in erster Linie durch die Zusammensetzung der Probe und damit durch die elektronischen Zustände am Leitungsbandminimum bestimmt werden.

Hinsichtlich der Ladungsträgerkompensation an der Elektrodengrenzfläche wurden unterschiedliche FE und AFE Materialien mittels einer weiteren in-situ XPS Methode untersucht. Dabei werden ebenfalls dünne Elektroden verwendet, um die Lage des Fermi-Niveaus an der Grenzfläche, d.h. die Schottky Barrierenhöhe, in Abhängigkeit des Polarisationszustands zu quantifizieren. Der Polarisationszustand kann durch Anlegen ausreichend hoher elektrischer Felder bei nicht zu hohen Temperaturen in der XPS direkt verändert werden. Die Änderung der Barrierenhöhe hängt von der Position der Abschirmladungen ab, die zu einem Sprung im elektrostatischen Potential führt. In dieser Arbeit wurde in Abhängigkeit des Elektrodenmaterials ein unterschiedlich asymmetrisches Abschirmverhalten bei ferroelektrischen Proben beobachtet. Vor allem aber konnten keine Änderungen der Barrierenhöhe bei antiferroelektrischen Materialien bei feldinduziertem Wechsel vom AFE in den FE Zustand beobachtet werden. Dabei spielte es keine Rolle ob die AFE Hysterese durch die Zusammensetzung oder die Messtemperatur induziert wurden. Dies weist auf einen fundamentalen Unterschied in der Position der Abschirmladungen zwischen FE und AFE Materialien hin. Ausgehend von diesen Beobachtungen wurden unterschiedliche Szenarien vorgeschlagen, die eine unterschiedliche Injektion von Ladungsträgern für das unterschiedliche Abschirmverhalten verantwortlich machen. Die bereits erwähnten Energieniveaus der lokalisierten Ladungsträger sollten dabei eine wichtige Rolle spielen.

Die in der Arbeit beschriebenen Fortschritte sind sowohl technischer als auch wissenschaftlicher Natur. Neue experimentelle Ansätze ermöglichen die Untersuchungen der elektronischen Struktur höchstisolierender Materialien mittels XPS, die normalerweise wegen Aufladungen nicht zugänglich sind. Vor allem aber lieferten die Untersuchungen wichtige neue Erkenntnisse zum Einfluss unterschiedlicher Ladungen in dielektrischen Materialien und dem Einfluss der elektronischen Struktur auf die dielektrischen Eigenschaften.

Contents

List of Figures

List of Tables

1. Introduction

Electrical energy conversion and storage have become vital topics in both research and industry in the context of humans' growing requirement for sustainable development. The technological progress of energy storage in recent decades enables the electricity generated by different approaches to be used more flexibly. In general, batteries and capacitors are two groups of common devices for electrical energy storage. The batteries, due to their relatively stable and continuous conversion between chemical and electrical energies, are extensively utilized as power sources for long-term applications [1]. By contrast, the capacitors directly store charges and generate much higher electrical power output than batteries in the course of discharging, so that they can play a complementary but indispensable role in energy storage where pulsed power output is needed, for example, in electric vehicles, renewable energies, medical apparatus, and mining industries [2–6].

The basic structure of most capacitors is an insulating layer sandwiched by two conductive electrodes. This layer is usually called dielectric. One of the core concepts of dielectrics is electric polarization, which describes the collective effect of all dipoles within a dielectric [7]. As the charging and discharging performance of capacitors is predominantly determined by the behaviors of dipoles, exploring and optimizing the polarization features of dielectrics are then thought as one of the main objectives for both researchers and manufacturers. According to the relation between induced polarization and applied electric field, dielectric materials can be categorized into linear and nonlinear dielectrics. The latter include ferroelectric (FE), antiferroelectric (AFE), and relaxor-ferroelectric materials [5]. In this work, we discuss mainly on AFE ceramics and their FE counterparts.

FEs have spontaneous polarizations resulting from their non-centrosymmetric lattice structures, whose directions can be switched when an external electric field is applied. From the viewpoint of microstructures, each grain of a FE ceramic is made up of one or more domains. All spontaneous polarizations inside each domain are pointing to the same direction, but several domains within each grain can have different orientations depending on the actual crystalline structure [8]. Unlike FEs, the AFEs have antiparallelly aligned dipole arrays within an initial AFE domain, which leads to a zero net spontaneous polarization macroscopically [9]. More importantly, an AFE will undergo a phase transition and become FE state if a sufficiently high electric field is applied [10]. This AFE-to-FE phase transition is generally regarded as reversible, i.e., the material will return to an AFE state once the electric field is removed. In practice, it is this particular phase transition that contributes to AFEs' impressive polarization versus electric field relation and therefore makes them a group of promising candidate dielectrics for energy storage capacitors.

In order to optimize the performance of capacitors, several technical criteria should usually be taken into account: capacitance, dielectric loss, resistance, operating temperature range, breakdown strength, electrical and mechanical fatigue, and so on [5, 6]. From a physical perspective, most of the above-mentioned properties in dielectrics can be regarded as the effects of several types of charges. The first type is bound charges, which are the equivalent positive or negative charges lying at two ends of the

physical model of dipole arrays. They are virtually attached to the lattice, and their quantities and relative positions in a dielectric describe the status of dipoles. Thus they are always underlined in most discussions on dielectric properties. Besides the bound charges, there is another concept called free charges. According to Griffiths' classic textbook of electrodynamics, the free charges can be defined as all other types that are not a result of polarization [7]. During the deduction of some important relations in a dielectric, for example the one between induced polarization and applied electric field, the free charges in the dielectric layer are usually neglected on purpose, which acts as a helpful approximation for insulators. However, the classification of charges does not seem to be an easy binary opposition. It has indeed more complexity for real dielectrics.

In general, the free charges include at least two groups: electronic charges (electrons and holes) and ionic defects that carry charges (lattice vacancies, interstitial or substitutional ions, and so on). The electronic charges can appear not only within the dielectric material but also on the conductive electrodes or the surfaces outside of the dielectric. They possess different behaviors and states: they may flow through the whole dielectric layer via band conduction; they may be localized by trapping at somewhere, either being permanently static or hopping to the neighboring sites; or they may inject through the electrode interfaces [11, 12]. As for the ionic defects, they could migrate within the dielectric; they could participate in the exchange of substances at surfaces or interfaces; or they could even act as the trap centers for the electronic charges [13, 14]. Besides, all these electronic and ionic charges should be involved in certain compensation mechanisms, so that the charge neutrality of the material can be satisfied in an equilibrium state. Furthermore, these free charges could modify the distribution of bound charges once they are staying at the positions related to the dipole configuration [15, 16]. In brief, the behaviors of charges are playing non-negligible roles in the properties of dielectric capacitors, and they are worth a deep and systematic investigation.

Regarding the AFE ceramics used as energy storage capacitors, there are several issues of interest to us:

(1) Charges can influence the configuration and stability of FE domains by compensating the exaggeratively high depolarization fields. Theories of charged domain walls [17–19] and dielectric screening [20–22] have given insight into the charge compensation modes in between FE domains and at electrode/FE interfaces, respectively. More complicated scenes would be expected in AFEs due to their special domain structures, which are still unclear.
(2) AFE capacitors have to release the stored energy via the backward FE-to-AFE phase transition, i.e., the field-induced FE state is not stable, which implies actually a very intrinsic difference between a field-induced FE phase out of AFE and an originally stable and switchable FE phase. The existence and roles of certain charges might offer a new strategy to understand FE and AFE in a different way.
(3) As the AFE-to-FE phase transition needs to be completed during the operation of AFE capacitors in order to obtain the maximum stored electrical energy, AFE materials are required to survive in much higher operating electric fields than what normal FE devices should withstand. Thus charge transport is undesired for AFE capacitors, i.e., the AFE materials must be even less conductive than FEs. From a microscopic point of view, most of the probable free charges within the dielectric, which could respond to the bound ones and play roles in stabilizing FE or AFE domains and promoting AFE-to-FE phase transitions, are expected to be localized and not totally "free", forming or existing with certain types of charged defects.

The motivation of this work is to search evidences for the existence of free or localized charges in the FE and AFE materials, in terms of their types, origins, amounts, positions, and impacts on properties.

The well-developed Pb-containing perovskite system $(Pb,La)(Zr,Sn,Ti)O_3$ (PLZST) [23] was selected as the main materials for the study. Figure 1.1 gives an overview of the charge-related physical problems included in this work. In the capacitors made of FE and AFE ceramics, there are at least four positions where the charges may play important roles, indicated schematically by dashed circles in Figure 1.1(a, b):

(1) Homogeneous bulk material (red circles). Without thinking of any interfacial effect, this is one of the most intrinsic-level features of the materials. The stoichiometry and defect chemistry should be discussed, which constitute the basis of the electrical conduction mechanisms.

(2) Domain walls of FEs or domain boundaries of AFEs (blue circles). They are the most obvious structural features of FE and AFE materials, which can be usually characterized by optical and electron microscopes. What is concerned here is the possible origin of extra free or "partially free" compensating charges when the bound charges are not fully counterbalanced at their boundaries. If such interfaces are charged, they may also contribute to the electrical conduction.

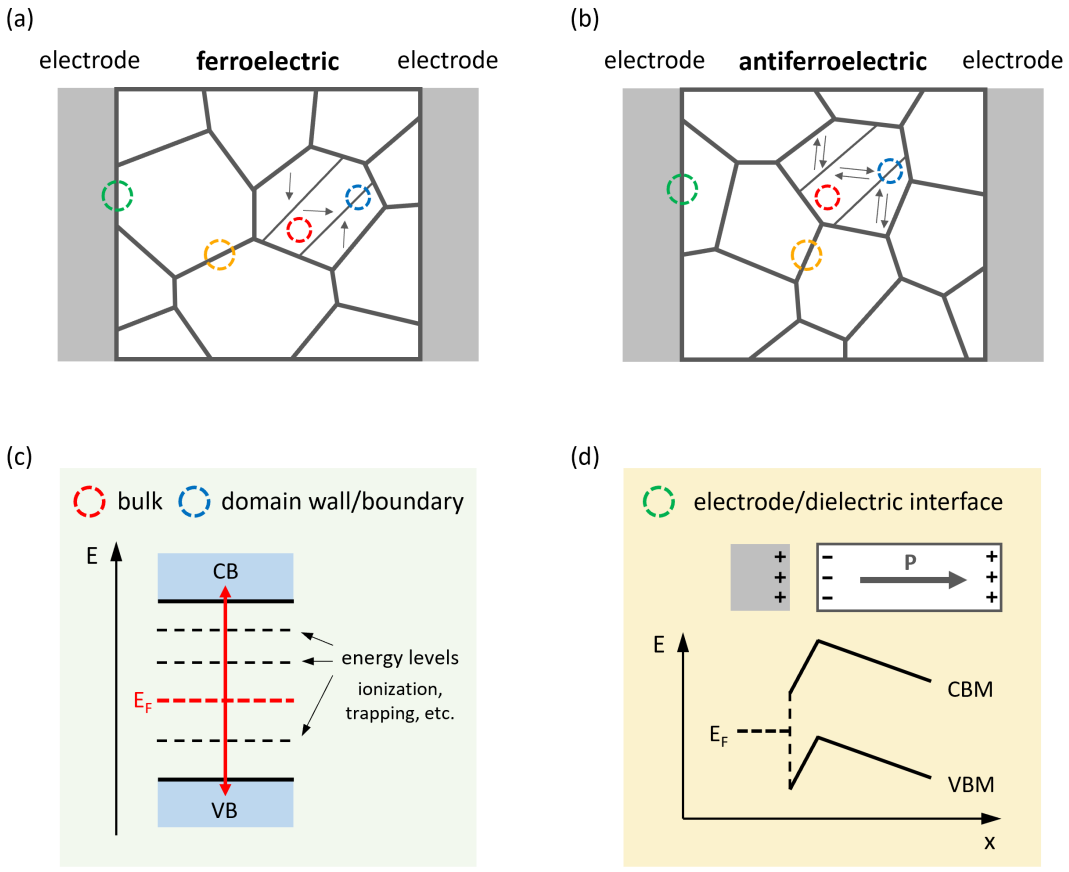

Figure 1.1.: Overview of charge-related physical problems in the capacitors based on polycrystalline ferroelectric and antiferroelectric materials. (a) Model of ferroelectric-based capacitor; (b) model of antiferroelectric-based capacitor; (c) schematic energy band structure within the dielectric layer; (d) energy band model at the interface between the electrode and the dielectric layer with ferroelectric polarization. (CB: conduction band; VB: valence band; E_F: Fermi level; CBM: conduction band minimum; VBM: valence band maximum.)

(3) Grain boundaries (yellow circles). Various effects can happen at the grain boundaries for polycrystalline materials, for example the segregation of dopant ions or point defects, which would modify the local band structures and thereby influence the charge transport within the bulk materials.
(4) Electrode/dielectric interfaces (green circles). Both bound charges from the dielectric layers and free charges from the electrodes are involved in these narrow regions. Their relations and interactions could strongly influence the dielectric and charge transport properties. It should be noted that the behaviors at the electrode/dielectric interfaces might be correlated to some of the previously mentioned points.

Figure 1.1(c) shows the schematic energy band diagram that can be used to describe the possible types, origins, and amounts of charge carriers in the homogeneous bulk materials. Several energy levels are placed within the band gap schematically. They could be related to the ionization of dopant ions, trapping and de-trapping of charge carriers, etc., which may further cause the so-called Fermi level pinning if one attempts to modify the Fermi level over the range of band gap (see the red arrows) through doping or redox processes. With the understanding of such band diagram, the conduction mechanisms contributed by the bulk materials can be interpreted. Also, the origins of the charges needed for compensating the charged domain walls/boundaries could be explained based on the same model. Figure 1.1(d) sketches the energy band structure at an electrode/dielectric interface which shows an extra electrical potential offset caused by the spatial separation of bound and free charges. Such charge configuration strongly depends on the actual status of the polarization within the dielectric layer, namely the magnitude and orientation of the dipoles under the condition of external electric field. The band structure models shown in Figure 1.1(c, d) are the bases of the experiments and understanding in this work. More details about the fundamental theories will be given in Chapter 2.

The experimental studies in this work are divided into four parts. Firstly, several necessary kinds of basic characterizations were carried out on the as-sintered ceramic samples in Chapter 4, where comprehensive comparisons about the dielectric properties and structural information of all synthesized ceramics will be given. Secondly, a series of dc electrical conductivity measurements were performed in Chapter 5 so as to obtain basic information for understanding the conduction behavior of these PLZST-related ceramics based on the band structure model in Figure 1.1(c). Subsequently, two in situ X-ray photoelectron spectroscopy (XPS) methods were realized. Several compositions were selected for the following parts. In Chapter 6, a new strategy has been established to engineer the Fermi level at the electrode/dielectric interface in order to explore the trap levels and the Fermi level limits of the dielectrics by XPS. It should be noted that this method can also be used to extract information on bulk properties of dielectric materials although the experiment itself was interface-based. The critical transition levels obtained through this method can be treated also according to the model shown in Figure 1.1(c), which could probably provide an interpretation of the high resistivity of the Pb-based AFE ceramic materials. After that, the second type of in situ XPS experiments were carried out in Chapter 7 to study the evolution of domain configuration at the electrode interfaces during the domain switching in FE samples and during the AFE-to-FE phase transitions in AFE samples. This method was based on the model illustrated in Figure 1.1(d). A clear difference between the FE and AFE cases has been observed and some speculations will be attached.

After the four chapters of experimental results, a short discussion based on all the charge-related observations throughout this work has been made in Chapter 8. Lastly, Chapter 9 gives the conclusion and outlook.

2. Fundamental Theories

This chapter will introduce backgrounds, concepts and theories on six aspects that are related to the following experimental studies. First of all, basic and general concepts of electrostatics for dielectric materials will be introduced in Section 2.1. Then the dielectric properties of AFE materials will be given with details in Section 2.2 through comparison with FEs. Section 2.3 will subsequently focus on the $PbZrO_3$-based material families, which are the main materials used for the experimental studies in this work. After that, short reviews on three charge-relevant topics, mostly for FE materials, will be provided separately. Sections 2.4 and 2.5 will refer to the charges only existing within the dielectrics, while Section 2.6 will deal with the case in which the charges from the electrodes participate as well. Specifically, Section 2.4 will concern the homogeneous bulk materials without taking any interfacial effect into account. Charge compensation mechanisms related to extrinsic dopants and electron/hole traps will be involved. Section 2.5 will first introduce the charged domain walls in FEs and the corresponding model for charge compensation and then give a review on the domain structures in AFE materials where uncompensated boundaries may also exist. Section 2.6 will provide the basics and physical model for the screening effect at the electrode/dielectric interfaces in a FE-based capacitor.

2.1. Electrostatic basics of dielectrics

Before introducing FE and AFE materials, it is necessary to review some classical electrostatic concepts of dielectrics and capacitors. Then the relation between polarization and electric field will be briefly described by using the typical model of parallel-plate capacitors. Unless otherwise noted, the current section is based on the books by Moulson & Herbert [13], Griffiths [7], Kao [12], and Lines & Glass [8].

2.1.1. Electric dipole and polarization

Unlike conductors that have substantial free charges supporting long-distance charge transport through the bulk materials, dielectrics are commonly regarded as insulators. In an ideal insulator, the charges can move only within a limited region around each atom or molecule. When a dielectric is placed in an electric field that is assumed to be not too strong, the Coulomb forces generated by the external field tend to pull the positive and negative charges apart. This induces slight offsets of these charges away from their initial equilibrium positions. The relative displacements of charges with opposite signs form electric dipoles, and such effect is called electric polarization. In real dielectrics, there are numerous dipoles that can respond to the electric field, and their collective effect determines the macroscopic properties. From a microscopic point of view, there are several mechanisms of polarization describing the above-mentioned charge displacements on different scales. Every dielectric should contain at least one of the following types of polarization process under an electric field:

(1) Atomic polarization: due to the distortion and slight offset of electron clouds away from the nucleus in an atom, existing in all materials;
(2) Ionic polarization: resulting from the relative displacement of cations and anions in ionic crystals;
(3) Dipolar polarization: aligning the permanent dipole moments along the direction of external field in dipolar substances (e.g. water);
(4) Space charge polarization: formed by the accumulating charges near the grain or phase boundaries because they block the long-distance transport of charges.

Each electric dipole holds a moment $\vec{p}$, whose magnitude and direction can be calculated based on the actual charge distribution in space. However, the calculation always shows complexity. For some practical issues, therefore, the dipole can be simplified into a physical model with equal and opposite charges $\pm q$ separated by a distance of d:

$$\vec{p} = q\vec{d}, \tag{2.1}$$

where the direction of $\vec{d}$ is from $-q$ to $+q$. In addition, the sum of dipole moments per unit volume is termed the polarization $\vec{P}$ to express the collective or average effects of dipoles in materials:

$$\vec{P} = \frac{\sum \vec{p}}{V}. \tag{2.2}$$

2.1.2. Bound charges, free charges, and the relation between polarization and electric field

Besides the polarization induced by an external electric field, another non-negligible fact is that the polarization will lead to some extra electric fields, which superimpose and tend to reduce the external one. It is this resultant total field that is actually controlled via the external circuit when discussing the polarization versus field relation for capacitors. In order to determine the electric field induced by polarization, the concept of bound charges came into being.

In general, dealing with charge distributions could provide more convenience than other methods when using Gauss's law in dielectrics and related structures to obtain the potential or electric field. The bound charges of a polarized object are therefore defined as the accumulating charges with a certain distribution that can produce the same electric field as what is made by the polarization. They are called "bound" because they are immobile to some extent. In other words, they should be attached to their atoms, ions, or molecules, and they contribute nothing to charge transport through the matter. Figure 2.1 gives two physical models, by which equivalent bound charges can be located in polarized objects.

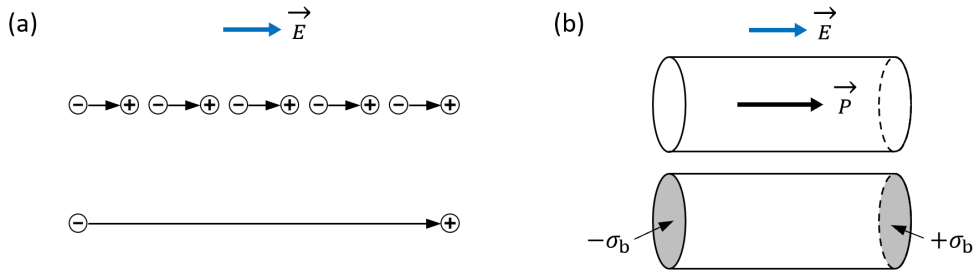

Figure 2.1.: Physical models to determine bound charges for (a) a 1-dimensional dipole string and (b) a polarized infinitesimal cylinder parallel to $\vec{P}$.

In Figure 2.1(a), a 1-dimensional string of identical dipoles is replaced by a longer one. The leftmost negative charge and the rightmost positive one are the bound charges, while the rest are thought to be canceled by their adjacent dipoles. The model in Figure 2.1(b) is more practically useful, where an infinitesimal cylinder has been uniformly polarized along its length. In this geometry, the electric field induced by polarization $\vec{P}$ can be equated with the one generated by the bound charges only on the left- and right sides of the cylinder (in gray) with surface charge density of $\mp\sigma_{\mathrm{b}}$, respectively. Here $\vec{P}$ and σ_{b} have very straightforward quantitative relation:

$$P = \sigma_{\mathrm{b}}. \tag{2.3}$$

It should be noted that this simplified geometry is only valid when the polarization inside the bulk is uniform and when the surfaces with bound charges are perpendicular to the direction of $\vec{P}$. In a more general scene of a dielectric with inhomogeneous polarization distribution and oblique cut surfaces, the equivalent bound charges consist of an extra component inside the bulk with a volume density of

$$\rho_{\mathrm{b}} = -\nabla \cdot \vec{P}, \tag{2.4}$$

and the surface one with a density of

$$\sigma_{\mathrm{b}} = \vec{P} \cdot \vec{\hat{n}}, \tag{2.5}$$

in which $\vec{\hat{n}}$ is the unit normal vector of the surface where bound charges are placed. Considering that this work only involves the model of parallel-plate capacitors, which fits the situation illustrated in Figure 2.1(b) quite well, it is sufficient to use Equation 2.3 hereinafter unless otherwise stated.

In contrast to the bound charges, all the other ones that do not result from the polarization can be categorized as free charges. In the case of a parallel-plate capacitor using an ideal insulator where only the polarization effect is involved and the other contributions such as long-distance charge transport can be ignored, the free charges would mostly mean the ones that can be placed on and removed from the conductive electrodes through externally connected electrical circuit. With the strategy of transforming polarization-related problems always into analyzing charge distributions in dielectric materials, the relation between applied electric field and induced polarization can be easily derived.

Figure 2.2 shows how the electric fields are developed in a parallel-plate capacitor by filling the space between two electrodes with a vacuum or with a solid dielectric. In both cases, the parallel plates (in gray) that represent conductive electrodes are separated by a distance of d. When the same external voltage U is applied to these two capacitors, the induced electric fields between plates are also identical, both labeled as $\vec{E}$. In Figure 2.2(a), the space is filled with vacuum and the electrodes have total surface charge density $\pm\sigma_{\mathrm{t0}}$, which are all regarded as free charges. According to Gauss's law, the electric field inside the gap is

$$E = \frac{\sigma_{\mathrm{t0}}}{\varepsilon_0}, \tag{2.6}$$

where ε_0 is called the dielectric constant or permittivity of vacuum, which is equal to 8.854×10^{-12} F·m^{-1}. In Figure 2.2(b), where a solid piece of dielectric placed between the two plates has been polarized, the total electric field inside the dielectric layer $\vec{E}$ can be described by taking both free and bound charges into account:

$$E = \frac{\sigma_{\mathrm{t}} - \sigma_{\mathrm{b}}}{\varepsilon_0}, \tag{2.7}$$

where σ_{t} and σ_{b} are the absolute values of the total free charge density carried by each electrode and the bound charge density induced by the polarization $\vec{P}$, respectively. This expression means that part of the free charges on the electrode (marked in red) have to compensate the bound charges on the

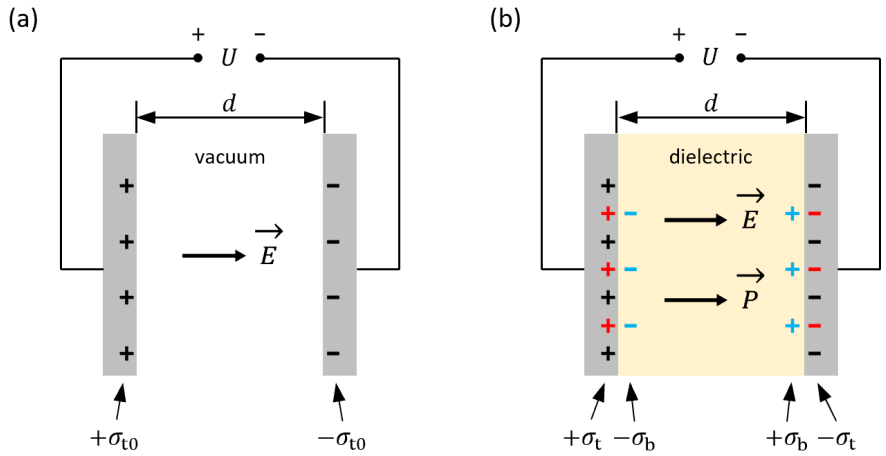

Figure 2.2.: Parallel-plate capacitor models using (a) vacuum and (b) a solid dielectric layer between two electrodes.

dielectric side of the electrode interface (marked in blue). It is the net charge density at two electrode interfaces (marked in black) that maintains the externally applied electric field exactly in the same way as what the free charges $\pm\sigma_{t0}$ are doing in Figure 2.2(a).

Instead of using "nothing" (a vacuum) as separation, the model in Figure 2.2(b) with a solid dielectric layer gives the elementary structure of a more general dielectric capacitor. In order to obtain the relation between electric field and polarization, Equation 2.7 can be written as

$$\sigma_t = \varepsilon_0 E + \sigma_b. \tag{2.8}$$

Since $\sigma_b = P$ (Equation 2.3) is valid for the geometry in Figure 2.2(b), we have

$$\sigma_t = \varepsilon_0 E + P. \tag{2.9}$$

In electrostatics, electric displacement $\vec{D}$ is introduced to help the description of electric fields in the presence of dielectric substance, and its magnitude is equal to the total free charge density σ_t. Consequently, Equation 2.9 can be modified to the following relation of vectors:

$$\vec{D} = \varepsilon_0 \vec{E} + \vec{P}. \tag{2.10}$$

2.1.3. Linear dielectrics

When a dielectric has the induced polarization that is proportional to the electric field, it is called linear dielectric. The relation can be written as

$$\vec{P} = \varepsilon_0 \chi_e \vec{E}, \tag{2.11}$$

where χ_e is called the electric susceptibility, which is a dimensionless second-rank tensor. It can be simplified as a scalar here, as $\vec{P}$ and $\vec{E}$ are always parallel in this work. By substituting Equation 2.11 into Equation 2.10, we obtain

$$\vec{D} = \varepsilon_0 \vec{E} + \vec{P} = \varepsilon_0 \vec{E} + \varepsilon_0 \chi_e \vec{E} = \varepsilon_0 (1 + \chi_e) \vec{E}, \tag{2.12}$$

which reveals the linear relation between $\vec{D}$ and $\vec{E}$. Here the factor before $\vec{E}$ is defined as the permittivity of the dielectric:

$$\varepsilon = \varepsilon_0(1 + \chi_\mathrm{e}). \tag{2.13}$$

Furthermore, the ratio between ε and ε_0 is defined as the relative permittivity of the dielectric (or relative dielectric constant):

$$\varepsilon_\mathrm{r} = \frac{\varepsilon}{\varepsilon_0} = 1 + \chi_\mathrm{e}, \tag{2.14}$$

so that Equation 2.12 now becomes

$$\vec{D} = \varepsilon\vec{E} = \varepsilon_0\varepsilon_\mathrm{r}\vec{E}. \tag{2.15}$$

With the aforementioned relations, the capacitance of a parallel-plate capacitor using a dielectric separation (as shown in Figure 2.2(b)) can be calculated as:

$$C = \frac{Q_\mathrm{t}}{U} = \frac{\sigma_\mathrm{t}A}{Ed} = \frac{DA}{Ed} = \varepsilon\frac{A}{d} = \varepsilon_0\varepsilon_\mathrm{r}\frac{A}{d}, \tag{2.16}$$

in which Q_t is the total charge on each electrode and A is the area of each plate. Similarly, the capacitance of a vacuum-separated model (in Figure 2.2(a)) is

$$C_0 = \varepsilon_0\frac{A}{d}. \tag{2.17}$$

The comparison between Equations 2.16 and 2.17 shows obviously that a capacitor using a dielectric material with relative permittivity of ε_r can increase the capacitance by a factor of ε_r or $1 + \chi_\mathrm{e}$ relative to the case with a vacuum filling.

2.1.4. Nonlinear dielectrics and dielectrics in alternating electric field

It should be noted and emphasized that Equation 2.11 can only describe the case under a not too high electric field. Every dielectric may still possess nonlinearity at extreme conditions of field even though they are categorized as linear ones. Besides, the existence of spontaneous polarization in some dielectric materials can cause nonlinearity as well, for example in FEs. This will be introduced in more detail in Section 2.2. For nonlinear dielectrics, the electric susceptibility χ_e in Equation 2.11 is no longer a constant but a function of $\vec{E}$. In other words, $\vec{P}$ can be written as the Taylor expansion in powers of $\vec{E}$ and then the right side of Equation 2.11 is just the first nonzero term of the expansion. Moreover, the calculation of capacitance should follow the differential form:

$$C = \frac{\mathrm{d}Q}{\mathrm{d}U}. \tag{2.18}$$

In addition to the nonlinearity of dielectric materials, there is another consideration for capacitors, which is about their behavior in alternating current (ac) applications. Unlike the electrostatic case reviewed in the previous paragraphs, power dissipation must be taken into account when a “lossy” dielectric is placed in an alternating electric field. Here the word “lossy” depicts the dielectric capacitor with a conductive component apart from the expected capacitive one, which is actually a common and inevitable situation for many dielectric materials. Normally, complex quantities are used in the context of ac fields to describe the current and voltage in terms of frequency and time. For real dielectric materials, the complex relative permittivity ε_r^* can be expressed as:

$$\varepsilon_\mathrm{r}^* = \varepsilon_\mathrm{r}' - \mathrm{i}\varepsilon_\mathrm{r}'', \tag{2.19}$$

where ε_r' and ε_r'' denote its real and imaginary parts, respectively. Besides, dielectric loss tangent $\tan\delta$ is more frequently utilized to describe the "lossy" property of dielectrics, which can be obtained by

$$\tan\delta = \frac{\varepsilon_r''}{\varepsilon_r'}. \tag{2.20}$$

2.2. Antiferroelectricity

FE and AFE are two inseparable concepts because they can be converted into each other through compositional modifications or various external conditions. Such mutual relations are well described by abundant phase diagrams in many material systems, and they are the foundation of most applications for AFE materials. Hence, this section will start with a short review of FE materials, and then introduce the general background and knowledge of AFEs needed for this work.

2.2.1. Brief review of ferroelectric materials

There are several important subgroups of dielectric materials: ferroelectrics $\subset$ pyroelectrics $\subset$ piezoelectrics $\subset$ dielectrics ($\subset$ denotes their inclusion relations). The classification is based mostly on their crystalline structures, which can further bring about their properties related to the change of polarization under different external conditions, such as electric field, temperature, stress, etc. Out of the 32 crystallographic point groups, 21 have no center of symmetry. Except for the point group 432, all of the remaining 20 exhibit piezoelectricity, i.e., the materials can get polarized and induce bound charges when external stresses are loaded. Also, the piezoelectrics will experience mechanical deformation under electric fields, which is termed the inverse piezoelectric effect. In addition to the non-centrosymmetry, there is another crucial concept called spontaneous polarization, namely the polarization already existing in the dielectrics due to certain polar crystalline structures in the absence of external mechanical or electric field. Among the 20 piezoelectric point groups, 10 have such spontaneous polarization and are known as pyroelectrics. The amount and distribution of their bound charges can vary during a change of temperature. Table 2.1 lists all point groups that give rise to piezoelectricity, sorted by whether they have spontaneous polar structures [24]. Out of these 10 pyroelectric symmetries, ferroelectrics are defined as the ones whose spontaneous polarization can be reversed when electric fields are applied. Unlike piezoelectrics and pyroelectrics, the confirmation of FEs needs not only structure information but also experimental proof (hysteresis loop). Therefore, the point groups of FE are not specifically marked in Table 2.1.

FE materials have already a history of more than 100 years [25]. The first report on FE was made by Valasek in 1921 [26]. In that paper the author was able to measure the charges on the electrodes of a Rochelle salt ($KNaC_4H_4O_6{\cdot}4H_2O$) capacitor when applying an electric field. The signal of charges, which represented the dielectric displacement, or approximately the polarization, showed a hysteresis relative to the electric field that was changing stepwise. Since then, the hysteresis loop of polarization versus electric field (P–E loop) became the principal characteristic or criterion to identify FE materials. However, the FE concept did not attract much attention until the perovskite barium titanate ($BaTiO_3$ or BTO) emerged in the 1940s [27]. On the one hand, BTO is an invaluable capacitor material due to its very high permittivity [28]. On the other hand, it is also a chemically simple and stable compound that provides great convenience for scientific research purposes. A series of characterizations on BTO

Table 2.1.: Crystallographic classification of all piezoelectric point groups according to crystal system and structural polarity. All pyroelectrics are the piezoelectrics that possess spontaneous polarization [24].

Crystal system	Piezoelectric point group	
	Non-polar	Polar (pyroelectric)
Cubic	$\bar{4}3m$, 23	
Hexagonal	622, $\bar{6}m2$, $\bar{6}$	$6mm$, 6
Tetragonal	422, $\bar{4}2m$, $\bar{4}$	$4mm$, 4
Rhombohedral	32	$3m$, 3
Orthorhombic	222	$mm2$
Monoclinic		2, m
Triclinic		1

ceramics and single crystals were finished within just a few years, including their crystalline structures, domain patterns, dielectric behaviors, and piezoelectric properties [29–35]. Soon after the breakthrough of BTO, another classic perovskite oxide, lead zirconate titanate ($Pb(Zr,Ti)O_3$ or PZT), was discovered to possess FE features. PZT is a solid solution of lead zirconate ($PbZrO_3$ or PZ) and lead titanate ($PbTiO_3$ or PT). Although the former is AFE and the latter FE, most of their solid solutions have FE structures [36, 37]. One of the shining points of this material system is the so-called morphotropic phase boundary (MPB), which is the phase boundary between the two FE regions (rhombohedral and tetragonal) [38, 39]. As excellent electromechanical properties were found in compositions near this special boundary, the MPB was then regarded as the base of many PZT materials for piezoelectric applications [40, 41]. After some chemical modifications and processing improvements, mature PZT piezoelectric ceramics started becoming promising commercial products by the end of the 1950s [42]. Up to the present, BTO, PZT, and their derivatives are still the most representative and indispensable FE material systems. Their extensive applications include generally the following aspects: (1) stress sensors, sonars, actuators, ultrasonic transducers, etc. (piezoelectricity) [24]; (2) ferroelectric random access memories (ferroelectricity) [43]; (3) ceramic capacitors (high dielectric constant) [28]; (4) pyroelectric infrared sensors (pyroelectricity) [44].

In this work, only perovskite-type FE and AFE ceramics are involved. Thus some relevant descriptions on this structure should be given here. The perovskite oxides are an important group of materials with the general formula of ABO_3, in which cation A is normally monovalent, divalent, or trivalent and cation B is correspondingly pentavalent, tetravalent, or trivalent. Figure 2.3(a) is the schematic diagram of a perovskite unit cell (using cubic symmetry as example). A-site cations (relatively larger ones, drawn in green) occupy the cube corners (actually one A cation in each unit cell), while one B cation (relatively smaller one, in blue) stays at the body center surrounded by 6 face-center oxygen ions, which compose a so-called oxygen octahedron. Figure 2.3(b) gives another common way to treat perovskites. The whole lattice structure can be regarded as a 3-dimensional network of corner-linked "BO_6" oxygen octahedra (in gray), every 8 of which can form a relatively large space for one A cation (in green). The description with oxygen octahedra is usually more worthwhile than just looking at the primitive cell because the tilting, distortion, and rotation of such oxygen octahedra are the most important structural

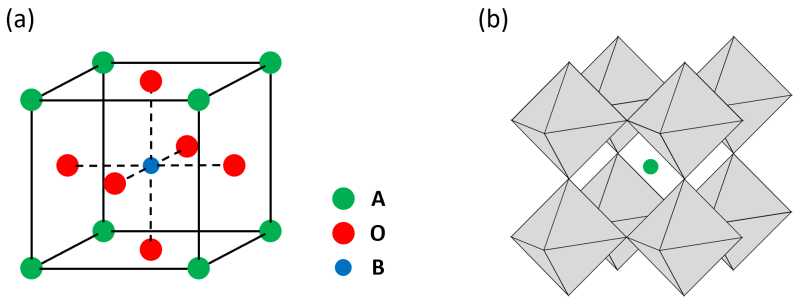

Figure 2.3.: Schematic structure of perovskite oxide ABO_3. (a) A perovskite unit cell; (b) the network of corner-linked oxygen octahedra.

characteristics of perovskites when they are not ideally cubic [8, 45]. In most cases, the perovskites are not perfectly cubic, basically depending on the combination of A- and B-site cations with different ionic radii. The tolerance factor t is therefore utilized to predict the perovskite structures [46]:

$$t = \frac{R_A + R_O}{\sqrt{2}(R_B + R_O)}, \tag{2.21}$$

where R_A, R_B, and R_O are the ionic radii of A, B, and oxygen ions, respectively. In general, cubic perovskite oxides should have the t value very close to 1 because of approximately ideal packing in the space. When t is greater than 1, namely using a too large A cation or a too small B cation, the structure will have the tendency to be tetragonal ($c > a$) and manifest FE feature [47]. An example for this case is BTO, which has $t = 1.06$ corresponding to a tetragonal FE phase at room temperature. Here the effective ionic radii reported by Shannon are used for calculating t values [48]. Briefly, the concept of the tolerance factor is frequently used for rough predictions of the crystalline structures during the synthesis work of perovskites, especially when chemical substitutions are needed to optimize the properties of materials. More relevant information about PZ-based FEs and AFEs will be provided in Section 2.3.2.

2.2.2. Dielectric properties of antiferroelectrics compared to ferroelectrics

In this part, the main dielectric properties of AFEs will be introduced together with the related or corresponding features in FEs, including hysteresis loops (field-dependent polarization and strain), energy storage performance of capacitors, field- and temperature-dependent dielectric permittivities. Unless otherwise noted, the current section is based on the review papers by Hao [2] and Liu *et al.* [3].

Hysteresis loops of polarization and strain versus electric field

Three types of polarization vs. electric field relations are illustrated in Figure 2.4, corresponding to the cases for a linear dielectric, a FE, and an AFE. The polarization is acquired when a bipolar triangular or sinusoidal waveform of voltage is applied to a parallel-plate capacitor. The red and black solid arrows indicate the course of increasing and decreasing voltage, respectively. In linear dielectrics, P is proportional to E (Equation 2.11) when E is not too high, so Figure 2.4(a) just shows a straight line toward both polarities. FEs and AFEs are nonlinear dielectrics, and both of them possess the so-called P–E hysteresis loops due to the response of their spontaneous polarization to the electric

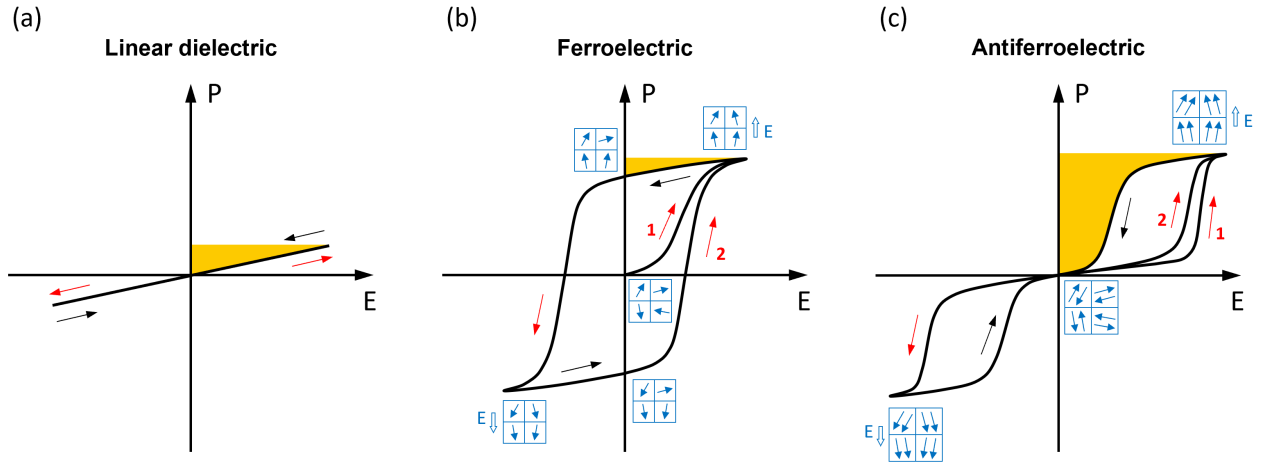

Figure 2.4.: Relations of polarization vs. electric field for (a) linear dielectric, (b) ferroelectric, and (c) antiferroelectric materials.

field. In order to minimize the electrostatic energy resulting from spontaneous polarization, a bulk FE material normally tends to break up itself into small domains, in each of which all dipoles point to the same direction. A ceramic comprises plenty of grains, and each grain usually consists of domains with different orientations. The response of FEs to electric fields basically means domain switching (re-orientation), which further includes domain nucleation and growth processes. AFEs also contain many domains in every grain. However, their domains have entirely different internal alignment of dipoles from the ones of FEs. For depicting the property–structure relation of AFE materials here, we firstly take the most simplified model by Kittel [9], in which the AFE is defined as one crystallographic state with antiparallelly aligned arrays of dipoles giving rise to a zero net spontaneous polarization of the dielectric. In Figure 2.4(b, c), the blue frames and the arrows inside denote schematic domain boundaries and dipole orientations, respectively. Several stages along the P–E loops are illustrated for FE in Figure 2.4(b) and for AFE in Figure 2.4(c). Unlike FE, the AFE case has an initial status where each domain manifests the antiparallel dipoles.

A typical P–E loop for FEs is shown in Figure 2.4(b), and both the first and second cycles are involved (see the two red arrows labeled with “1” and “2”) when the material is originally unpoled. Following the 1st cycle, a FE should have randomly oriented domains as an initial state. Once the positive electric field increases to a sufficiently high level, all domains have the tendency to switch to the directions of external field and a considerable nonlinear increase of the macroscopic polarization can be obtained until a saturation. Here the switched domains can only reach some directions as parallel to the field as possible because the attainable polar axes of dipoles are limited by the real crystallographic orientations. If the electric field is now removed, the polarization will only drop to a limited extent along the black arrow in Quadrant I, instead of returning to zero. This is because most switched domains will keep their orientations and only a minority of them will switch back. The intersection of the loop and the P-axis is termed remanent polarization. When the field is increased again but towards the negative polarity, all domains will start to switch and establish a new saturation state as parallel to the reversed field as possible, along the red arrow in Quadrant III. During this process, the loop has an intersection with the E-axis, which is called coercive field. Afterwards, the polarization will repeat the aforementioned course

when the negative electric field is reversed again into the positive side. By following the black arrow in Quadrant III and then the red arrow labeled with “2”, the FE hysteresis loop is closed. A complete FE loop should be ideally symmetric and display the remanent polarization and the coercive field on both polarities.

In contrast to FEs, AFEs are characterized by double hysteresis loop as shown in Figure 2.4(c), where the remanent polarization on both sides vanishes. At the beginning of each cycle, the polarization goes up slowly following an approximately linear slope with applied electric field. Once the field exceeds a critical level, the AFE-to-FE forward phase transition takes place and the material undergoes a rapid nonlinear increase of polarization (see the red arrow labeled with “2” in Quadrant I). Similar to the previous FE loop, the AFE loop also shows a saturation at a sufficiently high field, where all FE domains that are transformed from the original AFE ones (now in parallel arrays) should have the tendency to be aligned as much as possible toward the direction of the external field. Different from the FE case, however, the polarization drops to a low value when the decreasing external field reaches another critical level that is normally lower than the previous one of the forward transition, following the black arrow in Quadrant I. After the field is completely removed, the material is considered to recover the original AFE phase, giving rise to ideally a zero remanent polarization. Instead of the coercive fields in FEs, the switching fields, or more accurately the AFE-to-FE and FE-to-AFE transition fields, are used to describe the critical electric fields where the forward and backward phase transitions occur, respectively. As for the negative polarity, the same process is expected but with every physical quantity reversed, as shown in Quadrant III. An ideal P–E loop of an AFE material should be symmetric as well. Moreover, if the material is originally unpoled, the AFE-to-FE transition field is usually a little larger in the first half cycle (see the red arrow labeled with “1” in Quadrant I) than that in the following cycles [23].

Another information that can be extracted from the P–E loops is the energy storage performance, which has practical significance for capacitor materials [49, 50]. Only considering the course of Quadrant I in each P–E loop in Figure 2.4, the stored electrical energy density of a dielectric capacitor during charging can be written as:

$$J_{\mathrm{st}} = \int_0^{P_{\mathrm{max}}} E \mathrm{d}P, \tag{2.22}$$

where P_{max} is the polarization at the maximum applied field. As the capacitor is subsequently discharged, the released or recoverable energy density can be expressed by:

$$J_{\mathrm{re}} = -\int_{P_{\mathrm{max}}}^{P_{\mathrm{r}}} E \mathrm{d}P, \tag{2.23}$$

where P_{r} is the remanent polarization at zero field. The values of J_{re} are displayed as yellow shaded areas in all cases in Figure 2.4. Generally, the recoverable energy density of FE materials is lower than that of AFEs due to their higher remanent polarization. Linear dielectrics normally have much lower polarization than FEs and AFEs, so the resulting recoverable energy is also not sufficient for the application of energy storage capacitors. Among the three types of dielectric in Figure 2.4, AFE possesses the best energy storage performance if the energy loss ($J_{\mathrm{st}} - J_{\mathrm{re}}$) can be reduced to an acceptably small magnitude.

Besides the P–E loops, hysteresis behaviors of strain can also be observed in both FEs and AFEs when the bipolar triangular waveforms of electric field are applied. The evolution of strain in FEs is ascribed to the re-orientation of FE domains under the applied field, whereas the strain variation of AFEs is essentially due to the different volumes of the perovskite unit cell of the AFE and FE states. Therefore, the strain-field (S–E) loops of FEs and AFEs have intrinsically different mechanisms that should be

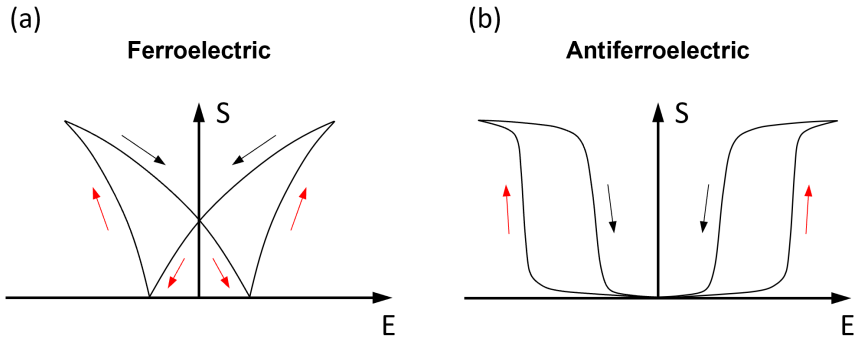

Figure 2.5.: Relations of strain vs. electric field for (a) ferroelectric and (b) antiferroelectric materials.

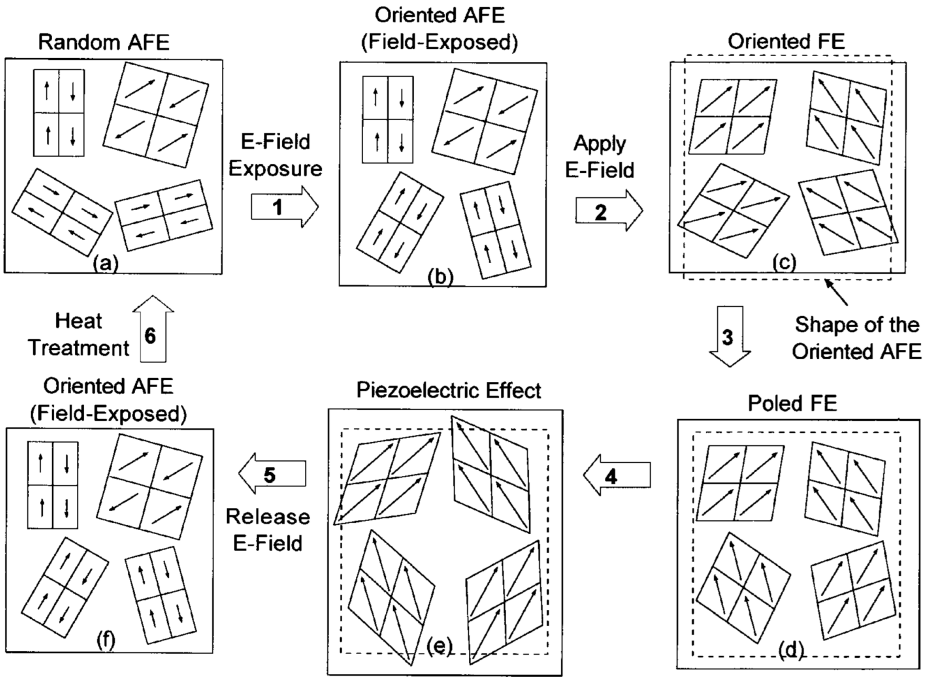

Figure 2.6.: Schematic sequence of the field-induced phase transitions in antiferroelectric materials. Both the AFE-to-FE forward and the FE-to-AFE backward transitions are included. Reprinted from Ref. [51] with the permission of AIP Publishing. Copyright (1997) American Institute of Physics.

clearly distinguished. Typical S–E loops of FEs and AFEs are illustrated in Figure 2.5, where red and black arrows denote the course of increasing and decreasing electric field in both polarities, respectively.

It must be noted here that the evolution of domain configurations (the blue frames and the arrows inside) in Figure 2.4(b, c) is only schematic. The relative orientations, the real boundaries, and the growth and decline of specific domains have more complexity and are temporarily not taken into consideration. In order to figure out such details, it is necessary to utilize diffraction methods or high-resolution electron microscopy on specific materials. By combining structural analysis and dielectric measurements, Park *et al.* provided a representative example for studying domain evolution in AFEs [51]. A comparison of

the X-ray diffraction (XRD) data before and after the electric-field exposure indicated the establishment of a preferentially oriented AFE domain configuration after poling. Together with the clear decoupling effect between polarization and longitudinal strain discovered in the hysteresis measurements, the authors proposed a stepwise procedure for AFE-to-FE and FE-to-AFE transitions, as shown in Figure 2.6. When the applied electric field is increasing, in addition to the field-induced structural phase transition (AFE-to-FE), several other steps should be taken into account, including the re-orientation of AFE domains (from a random AFE to an oriented AFE, see step 1), the re-orientation of FE domains (see step 3), and the stage dominated by piezoelectric effect (see step 4). Because the material has experienced the previous steps, the AFE state after releasing of the field is thought to be different from the very original AFE one in terms of its re-oriented domain configurations. Similar structural study has also been carried out recently in synchrotron with more details [52].

Dielectric permittivity

The dielectric permittivity is calculated from capacitance. For non-linear dielectrics such as FEs and AFEs, it is usually expressed in three different forms in terms of the electric field and temperature dependences. This part principally refers to the paper of Jaffe [49] unless otherwise noted.

The first form is the differential dielectric permittivity (also referred to as "large-field permittivity"), which is proportional to the slope of the P–E loop. The capacitance can be written as:

$$C = \frac{\mathrm{d}Q}{\mathrm{d}U} = \frac{A \cdot \mathrm{d}P}{d \cdot \mathrm{d}E}, \tag{2.24}$$

where A is the electrode area and d is the sample thickness. Then the relative dielectric permittivity can be derived through:

$$\varepsilon_\mathrm{r} = \frac{d \cdot C}{A \cdot \varepsilon_0} = \frac{1}{\varepsilon_0}\frac{\mathrm{d}P}{\mathrm{d}E}. \tag{2.25}$$

Figure 2.7(a, b) gives the schematic curves of the differential dielectric permittivities of a FE and an AFE, respectively. For each polarity, the red arrows indicate the increasing fields, and the black ones show the decreasing fields. It is very easy to link the presence of peaks with the positions where the P–E loop exhibits its largest slopes. Two peaks can be found in the FE, and four peaks in the AFE. One should be careful when looking at the magnitudes of these peaks. As they are nothing more than a simple calculation about $\mathrm{d}P/\mathrm{d}E$, the accuracy of their magnitudes would strongly depend on the density of data points and the noise of the P–E curves.

The second form is the small-field incremental dielectric permittivity. It can be measured with a small ac signal superposed on a direct current (dc) bias which is varying slowly. The dc bias is used to switch the FE domains or to trigger the AFE-to-FE and FE-to-AFE phase transitions, and the small ac field can simultaneously measure the capacitance at different states of the sample. A schematic shape of such a permittivity curve of an AFE sample is given in Figure 2.7(d). When the applied field is rising from zero to the AFE-to-FE transition field, the small-signal method can usually obtain a less obvious increase of permittivity than that measured with the differential form. Afterwards, the AFE sample is transformed into a FE state and its permittivity starts to drop quickly with the further increase of the field. When the field is removed, the permittivity will return to the original level but undergo a hysteresis. Within one complete cycle, four peaks would be still possible to identify but they heights are expected to be less remarkable than the case shown in Figure 2.7(b). Similar difference can be found in FE samples measured with the incremental method, where the magnitude of the permittivity at high electric field should be notably lower than that measured at small field as well (see Figure 2.7(c)).

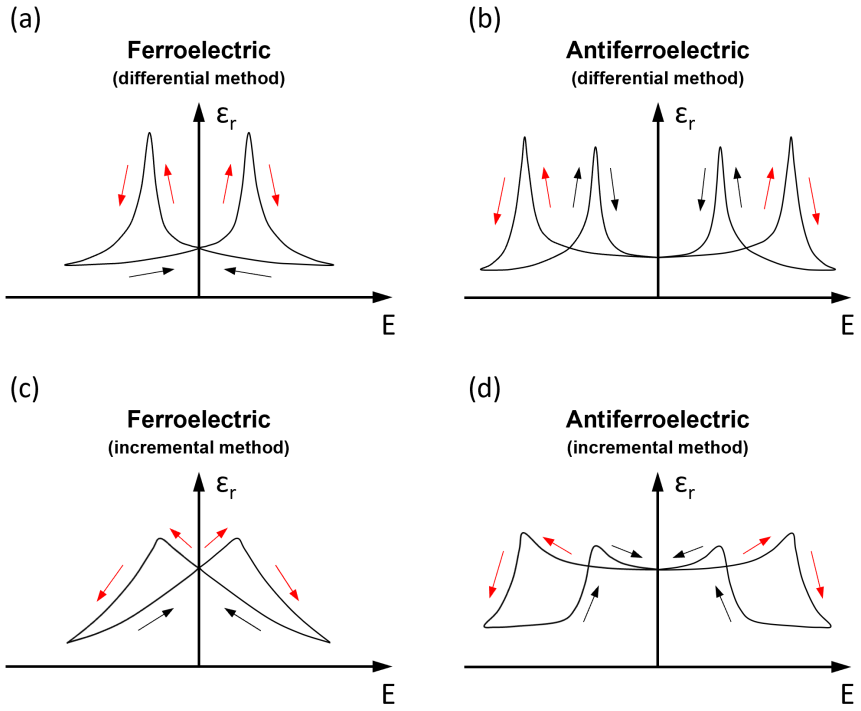

Figure 2.7.: Relations of relative dielectric permittivity vs. electric field for (a, c) ferroelectric and (b, d) antiferroelectric materials [49]. Two forms of dielectric permittivities are given here: (a, b) with the differential method; (c, d) with the small-field incremental method.

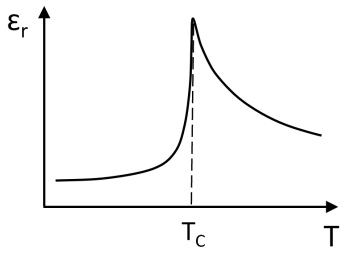

Figure 2.8.: Relation of relative dielectric permittivity vs. temperature for ferroelectric or antiferroelectric materials.

Besides the previous two field-dependent plots, there is the third form that displays the temperature-dependence, where the dielectric permittivity and loss are measured still under low ac field but plotted versus temperature. The application of the slowly varying dc bias is optional. Using this method, specific transition temperatures among different phases can be identified where the permittivity shows maxima. For both FEs and AFEs, the transition to the high-temperature paraelectric cubic phase, which is called the Curie point or Curie temperature (T_C), normally attracts more attention because it gives the upper limit of operating temperature of such functional materials. In general, FEs and AFEs have similar shapes of the permittivity vs. temperature curves in the vicinity of T_C [9, 10, 53, 54], as schematically shown in Figure 2.8. With the increase of temperature, the dielectric permittivity increases first and approaches a maximum at T_C, and then starts to drop. The curve on the higher-temperature side of T_C

should conform to the Curie-Weiss law [13, 53, 54]:

$$\varepsilon_{\mathrm{r}} = 1 + \frac{C_0}{T - T_0} \approx \frac{C_0}{T - T_0} \tag{2.26}$$

where T_0 is a characteristic temperature close to (but not equal to) T_{C} and C_0 is a constant. Both T_0 and C_0 depend on the material.

2.3. $PbZrO_3$-based material systems

The AFE ceramic materials that are currently being reported in the literature are classified into Pb-containing and Pb-free ones. It is well known that the Pb-containing materials can cause environmental problems because of the evaporation of Pb at high temperatures during synthesis. Although the tendency is to stepwise adopt the Pb-free systems in both researches and industries, the Pb-containing ones are still worth more fundamental studies, which could persistently provide advices for the development of the Pb-free replacements. From here on, we will only focus on the $PbZrO_3$-based perovskite ceramics in the rest of this work.

2.3.1. Prototypical antiferroelectric $PbZrO_3$

The history of AFE materials can date back to the early 1950s. The theoretical definition and prediction of antiferroelectricity were firstly proposed by Kittel in 1951 [9]. Almost at the same time, the prototype compound PZ was identified as AFE. In 1950, Roberts reported PZ as a FE candidate that has the similar temperature-dependent dielectric constant compared to the one of BTO [53]. After more detailed dielectric studies, Sawaguchi *et al.* noticed in 1951 that there may be no spontaneous polarization below T_{C} of PZ, which implies the existence of a new type of dielectrics, the so-called antiferroelectrics [54]. Soon afterwards, two milestone papers were published. In the first paper, Shirane, Sawaguchi, and Takagi succeeded in observing anomalous double hysteresis loops on PZ ceramic only in a very narrow temperature range just below its T_{C}, which are impressively different from those of typical FEs and are regarded as the principal characteristic of AFEs [10]. They also provided a tentative interpretation of such double hysteresis loops of PZ in terms of the competition among free energies of its three phases (FE, AFE, and paraelectric) under different external conditions of temperature and electric field [10]. The second milestone paper was published by Sawaguchi, Maniwa, and Hoshino still in 1951, where they managed to use a small untwinned crystal and determine the structure of PZ at room temperature as an orthorhombic supercell containing 8 perovskite unit cells [55], which gives a more intricate picture than the previous understanding of Megaw that PZ should have a tetragonal symmetry with $a = 4.150$ Å and $c/a = 0.988$ [56]. Figure 2.9 is the schematic superstructure of PZ proposed by Sawaguchi *et al.* [55], which shows the projection of the lattice along the direction of $\vec{c}_{\mathrm{t}}$ (or $\vec{c}_{\mathrm{o}}$ because $\vec{c}_{\mathrm{o}} \parallel \vec{c}_{\mathrm{t}}$). Here the subscripts "t" and "o" denote tetragonal and orthorhombic, respectively. The red rectangle and vectors $\vec{a}_{\mathrm{o}}$, $\vec{b}_{\mathrm{o}}$ represent the orthorhombic supercell on the base of an undistorted tetragonal perovskite lattice (see dash lines with vectors $\vec{a}_{\mathrm{t}}$, $\vec{b}_{\mathrm{t}}$, and its unit cell in green), and their lattice parameters have the relations of $a_{\mathrm{o}} = \sqrt{2} \times a_{\mathrm{t}}$, $b_{\mathrm{o}} = 2\sqrt{2} \times a_{\mathrm{t}}$, and $c_{\mathrm{o}} = 2 \times c_{\mathrm{t}}$. The short black arrows pointing to the hollow circles represent the off-center displacements of Pb^{2+} ions along the direction of $\vec{a}_{\mathrm{o}}$, which form an ↑↑↓↓ configuration within each orthorhombic unit cell. Similar to Kittel's model (↑↓ configuration) [9], this antiparallel dipole arrangement induces a zero net spontaneous polarization and is thought to cause the antiferroelectricity of PZ.

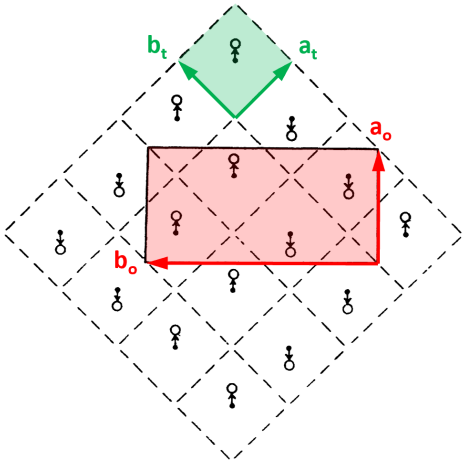

Figure 2.9.: The antiferroelectric structure of $PbZrO_3$ suggested by Sawaguchi *et al.* in 1951. Only the projection of the lattice along $\vec{c}_t$ (or $\vec{c}_o$) is shown here. Modified from Ref. [55] with the permission from the American Physical Society. Copyright (1951) American Physical Society.

Although AFE materials based on PZ have experienced tremendous development since the early 1950s, the prototypical material PZ still left some problems unsettled for decades, one of which is about the assignment of its space group, especially for the room temperature phase. In addition to the displacements of Pb^{2+} ions within the ab plane according to Figure 2.9, Sawaguchi *et al.* also suggested two possible orthorhombic space groups for PZ depending on the existence of an extra polar component along $\vec{c}_o$ direction: $Pbam$ and $Pba2$ [55]. The space group $Pbam$ is centrosymmetric without considering c-direction shift (belonging to point group mmm, not involved in Table 2.1), while $Pba2$ is non-centrosymmetric (belonging to point group $mm2$, listed in Table 2.1), which should produce a piezoelectric or even a FE effect along the c-axis due to the additional ionic displacement. There are basically two routes for making an exact choice between $Pbam$ and $Pba2$. The researchers could either indirectly look for the evidence of piezo-, pyro-, and ferroelectricity along the c-axis [57–60], or directly do atomic structure refinement on X-ray or neutron diffraction patterns to define the shift of Pb, Zr, and O atoms along different directions or planes [61–63]. Interestingly, these routes showed conflicting results. In brief, there has been no uniform answer to the question which space group should be correct for PZ. The exact space group assignment of this material depends on many factors, such as the quality of single-domain crystals, intricate structural distortions, and pseudo-symmetries [64]. Nevertheless, the centrosymmetric $Pbam$ at room temperature is more frequently adopted for PZ-related studies in recent years [3, 65–68].

Besides the atomic structure at room temperature, the phase transitions near PZ's T_C have also become an emphasis when exploring the nature of this model AFE material. Using the soft-mode theory that had been well developed for FE materials [69–72], the characteristic crystalline structures of AFEs can also be converted into a series of lattice vibration modes (phonons). The so-called softening means that the frequency of phonon drops towards zero when approaching the structural transition temperature. In FEs, the transitions are generally accompanied by softening behaviors happening at the Brillouin zone center, while AFE transitions correspond to softening at Brillouin zone edges [70, 73]. As for PZ, two primary modes are commonly utilized to describe its structure. The antiparallel displacements of Pb^{2+} ions on the ab plane can be principally expressed as a Σ mode with wave vector of $(2\pi/a)(1/4, 1/4, 0)$ (a denotes the cubic lattice parameter), and the tilting and rotation of oxygen octahedra can be regarded as an R

mode with wave vector of $(2\pi/a)(1/2, 1/2, 1/2)$ [73–75]. By transforming the structure information into vibration modes, one can comprehensively depict the process of phase transitions near the transition temperature, combined with the experimental methods such as neutron scattering, Raman- and infrared spectroscopy [72, 76, 77]. Also some additional mode behaviors like coupling and damping can provide more possibilities for structure analysis [8, 76]. One detailed example for PZ is the *ab initio* study of Íñiguez *et al.*, in which a cooperative trilinear coupling among different modes is considered to facilitate the process of PZ to select the $Pbam$ over several competing structural variants [78].

Despite the uncertainty and complexity when identifying its structure and phase transition process, PZ is widely thought as a model AFE material. Since the discovery of its AFE characteristics in the 1950s, a great number of relevant materials have been synthesized based on this prototype composition. The fundamental studies on the prototype itself are still shedding light on the strategies how to design and optimize the FE and AFE materials.

2.3.2. Chemical modifications based on $PbZrO_3$

From the viewpoint of application, the largest problem of the prototype PZ is its operating temperature. It is widely acknowledged that the P–E loop of PZ with an obvious field-induced AFE-to-FE phase transition could be observed only within a very narrow temperature range below T_C ($\sim 233°C$) [10]. People believe that the reason for this phenomenon is the excessively high switching field of PZ compared to the breakdown strength of ceramics in such a relatively low and practically useful temperature range. Following the linear extrapolation made by Sawaguchi & Kittaka, the switching field of PZ at room temperature could roughly be estimated as up to 35 kV/mm [79], which is indeed quite challenging for ceramics. In order to make use of the whole process of the hysteresis feature of AFEs for energy storage, one should either improve the material's breakdown strength or reduce the AFE-to-FE transition field. The former is principally a technical problem for synthesis, which will not be deeply involved in this work. As for the latter, it can be realized by chemical modifications. Here some of the typical material systems based on the prototype PZ will be simply introduced.

$(Pb,Ba)ZrO_3$ and $(Pb,Sr)ZrO_3$

The first group of important compositions are $(Pb,Ba)ZrO_3$ (PBZ) and $(Pb,Sr)ZrO_3$ (PSZ) [80]. Figure 2.10(a) is the composition–temperature phase diagram of these two solid solution systems, where pure PZ is located in the middle representing the end-member composition shared by both sides [81]. It is obvious that the effect of adding either $BaZrO_3$ or $SrZrO_3$ is to open a new intermediate phase region in between the previous high-temperature paraelectric phase and low-temperature AFE phase of PZ. The intermediate phase due to $SrZrO_3$ is identified as another AFE phase, whereas the one induced by additional $BaZrO_3$ is a rhombohedral FE phase. In other words, Sr^{2+} substitution on the A-site tends to stabilize the AFE structure, and Ba^{2+} is doing the other way around.

$Pb(Zr,Ti)O_3$

The next famous solid solution system is $Pb(Zr,Ti)O_3$ (PZT), in which the B-site Zr^{4+} of PZ is partially replaced by Ti^{4+}. In 1952, Shirane *et al.* determined the phase diagram of these solid solutions over the whole range of concentration [36–38]. Later in 1953, Sawaguchi made some complements to this phase diagram especially with more details in two narrow regions: the one adjacent to the pure PZ and the one near the MPB [39]. The PZT phase diagram shown in Figure 2.10(b) is redrawn after

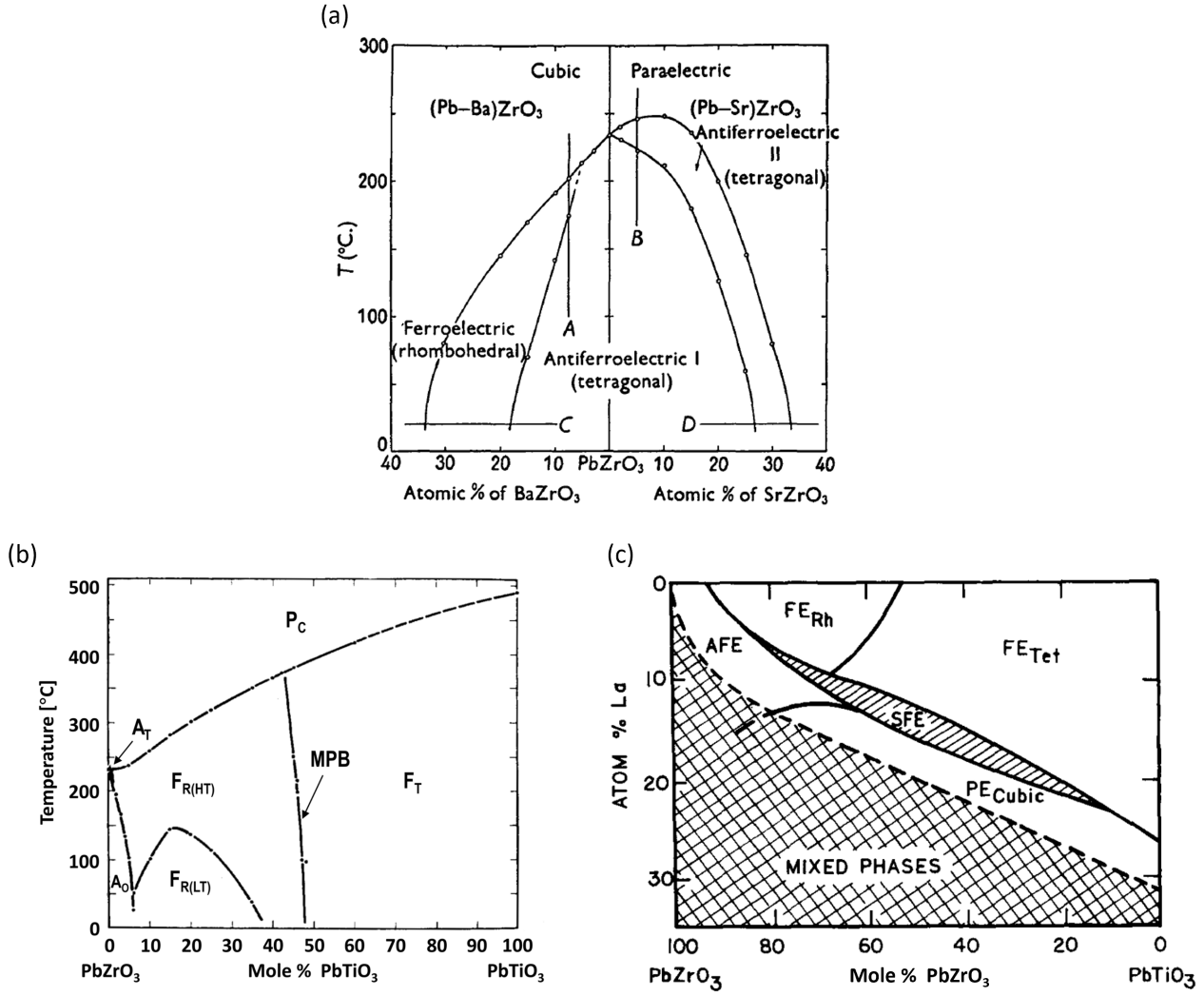

Figure 2.10.: Phase diagrams of several $PbZrO_3$-based material systems. (a) $(Pb,Ba)ZrO_3$ and $(Pb,Sr)ZrO_3$, reprinted with permission from Ref. [81]. Copyright (1954) The International Union of Crystallography. (b) $Pb(Zr,Ti)O_3$, adapted with permission from Ref. [23]. Copyright (1966) IEEE. (c) $(Pb,La)(Zr,Ti)O_3$, adapted from Ref. [82] with the permission of Taylor & Francis Group. Copyright (1987) Gordon and Breach Science Publishers S.A.

the version in Ref. [23]. It can be seen that the neighboring concentration of pure PZ can still remain the orthorhombic AFE structure at room temperature until the PT content exceeds a critical point of ca. 7%. At higher temperatures, the Ti^{4+} substitution plays the similar role compared to the case of $(Pb,Ba)ZrO_3$, namely opening a rhombohedral FE region between the high-temperature paraelectric phase and the low-temperature AFE phase. Another crucial constituent part of this phase diagram is the MPB. As shown in Figure 2.10(b), the MPB concentration is expressed by the nearly vertical line between the tetragonal FE phase (F_T) and the high-temperature rhombohedral FE phase ($F_{R(HT)}$). Based on the MPB composition, the ceramic samples can achieve remarkable piezoelectric properties and possess excellent practical value [40–42]. Furthermore, it is noticeable that most ratios of PZ to PT exhibit FE structures rather than the original AFE as pure PZ. Therefore, this classic solid solution

system has actually attracted more attention to the researches and applications related to ferroelectricity and piezoelectricity.

(Pb,La)(Zr,Ti)O_3

Besides the isovalent substitutions, it is also frequent to replace the A- or B-site cations in perovskites with aliovalent ions. The trivalent rare-earth element lanthanum is one of the most widely used A-site substitutions for PZT system. Figure 2.10(c) is the room-temperature phase diagram of (Pb,La)(Zr,Ti)O_3 (PLZT) with La substitution up to about 35 at.%. It was originally established by Haertling & Land in 1971 [83], and the figure reprinted here is the modified version belonging to the review paper by Haertling in 1987 [82]. Here a slight increase of La concentration can result in a noticeable change of proportion among AFE, rhombohedral FE (FE_{Rh}), and tetragonal FE (FE_{Tet}) phases. More explicitly, the La additive undermines the stability of the FE_{Rh} state that specifically exists on the PZ-rich side. When the La content continues growing, eventually, all ratios of PZ to PT will come to either a cubic state (PE_{Cubic}) or a region with mixed phases. In addition, there is a slim-loop ferroelectric region (SFE) appearing basically along the boundary between the two FE and PE_{Cubic} regions, which is famous for its relaxor features [84–87]. As an outstanding material system for electrooptic devices, PLZT can be operated principally in three modes: memory, linear, and quadratic, corresponding to its three main phase areas: FE_{Rh}, FE_{Tet}, and SFE, respectively [88].

Pb(Nb,Zr,Sn,Ti)O_3 and (Pb,La)(Zr,Sn,Ti)O_3

Despite that the fantastic functional material systems like PZT and PLZT were created during the studies on compositional modifications of PZ, the problem of such solid solutions for real applications that use AFE characteristics did not get solved for some time, i.e., the double hysteresis loops were still difficult to be obtained in a reasonably wide and useful temperature range by Ba- or Ti-modifications on PZ [39, 80]. The situation has changed as Jaffe found that substituting Sn^{4+} for the B-site $(Zr,Ti)^{4+}$ can effectively lower the free energy difference between the FE and AFE states of a composition over a wide temperature range below its T_C, which makes the electric-field induced AFE-to-FE phase transition easier to happen [49]. Based on this discovery, the two most studied PZ-based AFE material systems, Pb(Nb,Zr,Sn,Ti)O_3 (PNZST) and (Pb,La)(Zr,Sn,Ti)O_3 (PLZST), were discovered [23, 89, 90]. The Zr-rich parts of their room-temperature phase diagrams are displayed in Figure 2.11 [23]. Although these two cases result from substitutions on different cation sites of perovskites (Nb^{5+} on the B-site but La^{3+} on the A-site), they exhibit basically similar distribution of phase areas in the ternary diagrams. Relatively low Ti content gives rise to AFE structures, while growing Ti transforms the solid solutions into different FE phases. The orthorhombic AFE (A_O), tetragonal AFE (A_T), low-temperature rhombohedral FE ($F_{R(LT)}$), high-temperature rhombohedral FE ($F_{R(HT)}$), and tetragonal FE (F_T) in both cases can generally find their corresponding states in the PZT phase diagrams in Figure 2.10(b). It is noticeable that the AFE regions are considerably broadened in these two systems and therefore flexible compositional design becomes possible. In early studies the compositions near the phase boundary between A_T and $F_{R(LT)}$ attracted more attention because the switching fields for AFE-to-FE transitions are relatively low so that the materials can display opened P–E loops easily without breakdown and can be used for transducers [23]. In recent years, owing to the improved techniques for sintering ceramics, there have been more attempts on the compositions close to the bottom of these two phase diagrams (low-Ti regions) [91–93], where the combination of a very high AFE-to-FE transition field and a satisfactory induced polarization makes such compositions promising candidates for energy storage capacitors.

Another noteworthy point regarding the PNZST and PLZST systems is the existence of metastable regions

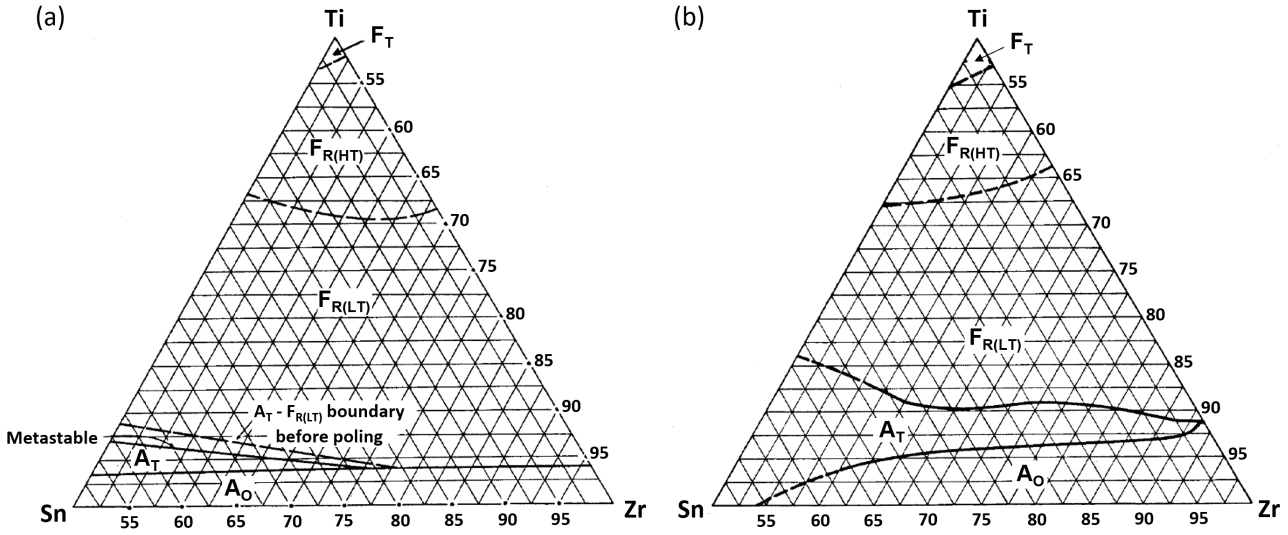

Figure 2.11.: Phase diagrams for (a) $Pb_{0.99}[Nb_{0.02}(Zr,Sn,Ti)_{0.98}]O_3$ and (b) $(Pb_{0.97}La_{0.02})(Zr,Sn,Ti)O_3$ at room temperature. Adapted from Ref. [23] with permission of IEEE. Copyright (1966) IEEE.

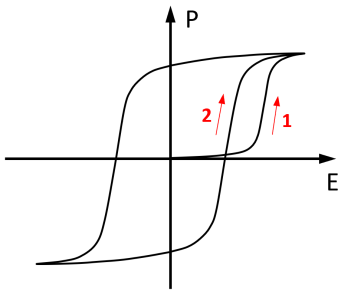

Figure 2.12.: Schematic polarization vs. electric field hysteresis loop for the compositions in the metastable region between the A_T and $F_{R(LT)}$ phases in PNZST and PLZST systems.

between the A_T and $F_{R(LT)}$ phases [23]. Such a narrow region is depicted in the PNZST phase diagram in Figure 2.11(a). The characteristic of the compositions within this region is that the field-induced FE phase (from AFE) stays in a metastable FE state when the field is removed, instead of returning to the AFE state. Figure 2.12 is the sketch of the P–E loop of such samples, where the first cycle possesses an AFE-like behavior in Quadrant I with a transition field higher than the coercive field of the stable FE loop measured from the second cycle on. It should be noted that the hysteresis behavior for this metastable region has different mechanism from the "pure" FE case described in Figure 2.4(b). Besides, the PLZST system also has this metastable region, which does not show up in the well-known diagram in Figure 2.11(b), because Berlincourt only plotted the phase boundaries based on unpoled samples for PLZST in his work [23]. As can be found in the literature, the metastable compositions have caught a lot of attention [94–96]. On the one hand, their metastable states are very sensitive to external conditions (e.g. temperature and electric field), which provides many opportunities for comprehensive investigations on the AFE-to-FE phase transition. On the other hand, their irreversible AFE-to-FE transitions may help to

understand the reversible AFE-to-FE transitions in more extensive AFE materials with practical value.

Based on the PLZST system, some other compositional modifications including (Pb,Ba,La)(Zr,Sn,Ti)O_3 and (Pb,Sr,La)(Zr,Sn,Ti)O_3 were produced for further optimizing the dielectric properties of the AFEs [97, 98]. Table 2.2 summarizes some common or important PZ-based material systems related to AFE. Their types of chemical modification are classified according to the cation sites and the valence states of substitutions.

Table 2.2.: List of important antiferroelectric-relevant $PbZrO_3$-based material systems.

Material	A-site		B-site		Reference
	isoval.	alioval.	isoval.	alioval.	
$PbZrO_3$ (PZ)					[10, 54, 55, 68, 74, 78, 79, 99]
(Pb,Ba)ZrO_3 (PBZ)	Ba^{2+}				[53, 80, 81, 100]
(Pb,Sr)ZrO_3 (PSZ)	Sr^{2+}				[80, 81]
(Pb,La)ZrO_3 (PLZ)		La^{3+}			[60, 101]
Pb(Zr,Ti)O_3 (PZT)			Ti^{4+}		[36–41]
(Pb,La)(Zr,Ti)O_3 (PLZT)		La^{3+}	Ti^{4+}		[82–88, 102–105]
(Pb,La)(Zr,Sn,Ti)O_3 (PLZST)		La^{3+}	Ti^{4+}, Sn^{4+}		[23, 51, 106–112]
Pb(Nb,Zr,Sn,Ti)O_3 (PNZST)			Ti^{4+}, Sn^{4+}	Nb^{5+}	[23, 52, 89, 90, 113–116]
(Pb,La)(Nb,Zr,Sn,Ti)O_3		La^{3+}	Ti^{4+}, Sn^{4+}	Nb^{5+}	[117]
(Pb,Ba,La)(Zr,Sn,Ti)O_3	Ba^{2+}	La^{3+}	Ti^{4+}, Sn^{4+}		[97, 98, 118]
(Pb,Sr,La)(Zr,Sn,Ti)O_3	Sr^{2+}	La^{3+}	Ti^{4+}, Sn^{4+}		[97, 98, 119]

As there are so many possibilities to modify the material properties chemically, conclusive strategies are always required for interpreting the roles of different elements and for predicting new materials. Regarding the AFE-related families, optimizing the AFE properties usually refers to the broadening or stabilizing of phase regions and the tailoring of the free energy difference between the original AFE phase and the field-induced FE phase. In the literature, one of the most common tools is the tolerance factor (see Section 2.2.1), with which the favored crystal structures can be predicted in perovskites. Table 2.3 lists the effective ionic radii of all host and substitution ions from Table 2.2 used for calculating the tolerance factors [48]. As for the A-site, Ba^{2+} has a larger radius than Pb^{2+}, whereas Sr^{2+} and La^{3+} have smaller ones. According to Equation 2.21, adding larger Ba^{2+} increases the tolerance factor, which is widely thought to stabilize the FE ordering by affecting the oxygen network [66, 97, 98]. This idea is also used to explain the emergence and expansion of an intermediate FE phase between the high-temperature paraelectric phase and the low-temperature AFE phase in PBZ system [80, 100], as indicated in the phase diagram of Figure 2.10(a). Relatively smaller A-site substitutions such as Sr^{2+} and La^{3+}, which lower the tolerance factor, by contrast, can destabilize the FE phase or stabilize the AFE phase [60, 66, 80, 96–98, 119, 120]. Therefore, the intermediate phase in PSZ is a tetragonal AFE one, opposite to the case in PBZ [80]. As shown in Figure 2.11(b), the two broad AFE phase regions in the PLZST system can be attributed to the AFE-stabilizing effect due to the smaller size of La^{3+} ions as well. Analogous to the A-site, sometimes the effect of the B-site substitutions can also be described with the tolerance factor. For example, Ti^{4+}, which is smaller than Zr^{4+}, is considered to suppress the

Table 2.3.: Effective ionic radii of the host and substitution ions in the relevant $PbZrO_3$-based material families [48]. All values are given according to the coordination numbers (CNs) of different sites in the perovskite oxide.

	A-site (CN=12)				B-site (CN=6)				O (CN=6)
	Pb^{2+}	Ba^{2+}	Sr^{2+}	La^{3+}	Zr^{4+}	Ti^{4+}	Sn^{4+}	Nb^{5+}	O^{2-}
Ionic radius (Å)	1.49	1.61	1.44	1.36	0.72	0.605	0.69	0.64	1.40

AFE and expand the FE phase in the PZT phase diagram (see Figure 2.10(b)). In the PNZST system, the B-site Nb^{5+} ion, which is smaller than Zr^{4+} and is expected to increase the tolerance factor and stabilize the FE state, however, plays the similar role compared to that of the A-site La^{3+} substitution in the PLZST. Such a contradiction implies that there must be other factors which determine the preferable crystal structures of these materials.

One of the possible mechanisms in addition to the tolerance factor is the valence states of the substitution ions. In the case of aliovalent substitutions, for example the La^{3+} and Nb^{5+} in Table 2.2, the compounds cannot maintain the electrical neutrality unless the introduction and compensation of charges are taken into consideration. In contrast to the aliovalent substitutions, the isovalent ones, which have the same valence states as the host ions, are normally expected to do nothing on the charge-related issues. More details about the aliovalent substitutions, which are termed dopants in semiconductor physics, will be given in Section 2.4.

2.4. Charges and charged point defects in $PbZrO_3$-based homogeneous bulk materials

In order to utilize the AFE materials for energy storage, one should obtain sufficiently opened double hysteresis loops. One of the prerequisites for realizing this is that the materials should be good insulators and be able to survive under fairly high applied electric fields. Hence the investigation on the conduction mechanisms of AFEs becomes necessary. This part will principally focus on the conduction within homogeneous bulk materials in terms of defect chemistry. Some interface-relevant considerations, such as the grain boundaries in polycrystalline ceramics and the domain walls/boundaries in FEs/AFEs, will be outlined later. All introduction will be mainly based on the PZT system and on the La modification that is used for PLZST AFEs.

2.4.1. Charge compensations in undoped and La-doped $Pb(Zr,Ti)O_3$

In general, the studies on electrical conduction mechanisms involve the determination of the types, positions or distributions, amounts, and behaviors of the charge carriers. These can be described with defect chemistry, which usually deals with the point defects.

Undoped Pb(Zr,Ti)O_3

For the undoped PZT, the following point defects should be taken into account: electrons and holes (e', $h^{\cdot}$), A-site lead vacancies (V''_{Pb}), and oxygen vacancies ($V^{\cdot\cdot}_{O}$). Here Kröger–Vink notation is used [13]. Besides e and h, the main symbol can also be an element or V (vacancy). The subscript means the lattice site where the specific defect is located (e or h has no lattice site). The superscript denotes the effective electrical charge carried by a defect. "$\cdot$", "$\prime$", and "$\times$" stand for one single positive electronic charge ($+e$), one single negative electronic charge ($-e$), and neutral state, respectively. Normally in PZT, each lead vacancy carries $-2e$ (V''_{Pb}) but each oxygen vacancy $+2e$ ($V^{\cdot\cdot}_{O}$). B-site cation vacancies and interstitial ions are usually considered to be unlikely in the PZT system [45, 121, 122].

Compared to BTO, which has a relatively well defined defect chemistry [123–125], the determination of the actual defect concentrations in PZT has more complexities, mainly due to the high volatility of PbO during high-temperature synthesis. The PbO volatility can be expressed as:

$$O^{\times}_{O} + Pb^{\times}_{Pb} \rightleftharpoons V''_{Pb} + V^{\cdot\cdot}_{O} + PbO \uparrow . \tag{2.27}$$

According to this formula, it seems that the ratio between the generated V''_{Pb} and $V^{\cdot\cdot}_{O}$ should be $1:1$. However, this is not the complete picture. During the sintering of PZT ceramics, the $V^{\cdot\cdot}_{O}$ also needs to establish an equilibrium with the ambient oxygen atmosphere. Hence, two more reactions should be considered as well [126, 127]:

$$O^{\times}_{O} \rightleftharpoons \frac{1}{2}O_2 \uparrow + V^{\cdot\cdot}_{O} + 2e'; \tag{2.28}$$

$$Pb^{\times}_{Pb} \rightleftharpoons Pb \uparrow + V''_{Pb} + 2h^{\cdot}. \tag{2.29}$$

It can be noticed that the defect equilibrium is actually controlled by the balance between the vapor partial pressures p_{Pb} and p_{O_2} (or between p_{PbO} and p_{O_2} in certain contexts). It is widely accepted in the literature that the PZT possesses more V''_{Pb} than $V^{\cdot\cdot}_{O}$ [45, 128, 129]. Therefore, Equation 2.29 dominates the defect chemistry and the holes ($h^{\cdot}$) that compensate the excess V''_{Pb} bring about a p-type conduction in the PZT. In practice, the high-temperature sintering of PZT ceramics is usually carried out with excess PbO or within Pb-rich atmosphere in order to counterbalance the deficiency of Pb content. However, such strategy would further increase the uncertainty for determining the real defect equilibrium.

Effect of La doping

Besides the nominally undoped one, great attention has been attracted by the chemically modified PZT, especially the ones using aliovalent ions (dopants) that can considerably optimize the dielectric properties. In terms of the valence of dopant relative to that of the host ion which is replaced, doped PZT can be classified into hard and soft ones [126, 130]. Doping with lower valent ions (acceptors) gives rise to the so-called hard PZT, e.g. the case with Fe^{3+} substitution on the B-site. The soft PZT, by contrast, refers to the case doped with higher valent ions (donors), e.g. with La^{3+} on the A-site or Nb^{5+} on the B-site. In the hard PZT, less sharp P–E loops can be obtained, i.e. they are relatively difficult to be polarized. This is because the lower valence of the acceptor is mainly compensated by generating $V^{\cdot\cdot}_{O}$. High concentration of $V^{\cdot\cdot}_{O}$ would result in domain wall pinning when the FE is switching under electric field. Compared to the hard PZTs, the soft ones are easier to be polarized and their P–E loops normally show lower coercive fields and more square shapes. In this case, the donor doping is mostly compensated by immobile V''_{Pb}, and meanwhile the amount of $V^{\cdot\cdot}_{O}$ can be significantly suppressed [14, 126].

The electrical conductivity/resistivity of PZT ceramics with various dopants have been extensively studied [128, 129, 131, 132]. La, as one of the most common and crucial donor-type substitutions for PZ-based materials (see Table 2.2), is expected to contribute e′ which can counteract the p-type conduction of PZT. Although it has been experimentally proved that adding La can reduce the conductivity of PZT [129, 131], the material seemed to reach a low level of conductivity and not to transform further into n-type conduction when more and more donors are added [45]. This behavior is different from the situation of donor-doped BTO [125]. It is widely believed that the conduction feature in La-doped PZT should be ascribed again to the high PbO volatility during sintering [14, 45]. Taking the La additive (La_2O_3) into account, the high-temperature reaction can be written as [13, 45]:

$$La_2O_3 + 3Pb_{Pb}^{\times} \longrightarrow 2La_{Pb}^{\cdot} + V_{Pb}'' + 3PbO \uparrow, \tag{2.30}$$

which indicates that the donor-doping in PZT tends to be compensated ionically by generating more V_{Pb}'' with the help of evaporation of PbO. As V_{Pb}'' can still be an acceptor center, the whole material could thereby maintain a balance between n- and p-conduction and manifest an intrinsically low conductivity. Additionally, the molecular formula $(Pb_{0.97}La_{0.02})(Zr,Sn,Ti)O_3$ for PLZST, appearing in the caption of Figure 2.11(b), exactly expresses the consequence of the reaction with an A-site cation compensation in Equation 2.30.

Oxygen vacancies and resistance degradation

Great effort has been made to figure out the concentration, distribution, and motion of the $V_O^{\cdot\cdot}$ in the researches of perovskite oxides. The existence of $V_O^{\cdot\cdot}$ is usually attributed to the acceptors, which can be introduced into the materials not only via the intentional doping but also due to the naturally-occurring impurities of raw materials [133]. Since a large concentration of $V_O^{\cdot\cdot}$ may lead to some undesirable effects on FE materials, it is sometimes necessary to suppress or even eliminate them. One of the common strategies is the donor-doping. In BTO and $SrTiO_3$ (STO), generally, the donor-doping is thought to almost totally suppress the concentration of $V_O^{\cdot\cdot}$ [125, 134]. However, the suppression seems to be not so effective in the case of donor-doped PZT. Due to the PbO evaporation during high-temperature sintering, it is unavoidable that there is a certain amount of $V_O^{\cdot\cdot}$ remaining [127, 135–138]. Also, both $[V_O^{\cdot\cdot}]$ and $[V_{Pb}'']$ ([ ] denotes the concentration of the defect) would still be difficult to clearly determine in such donor-doped PZT.

One of the consequences of the existence of numerous $V_O^{\cdot\cdot}$ in dielectric materials is the so-called resistance degradation. It is characterized by a decrease of resistance or an increase of leakage current (of a capacitor) under dc voltage stress at elevated temperature. This issue has been comprehensively investigated in BTO and STO [134, 139–141]. The increase of leakage current is attributed to an ionic de-mixing process, which refers to the spatial redistribution of the mobile $V_O^{\cdot\cdot}$ along the direction of electric field within the dielectric layer. The positively charged $V_O^{\cdot\cdot}$ migrate towards the cathode, while O^{2-} move to the anode correspondingly. In a single crystal, where the obstructing effect of grain boundaries on the migration of $V_O^{\cdot\cdot}$ is excluded, there will be an $V_O^{\cdot\cdot}$-rich (e′-rich) and an $V_O^{\cdot\cdot}$-depleted ($h^{\cdot}$-rich) layer emerging in the vicinities of the cathodic and the anodic interfaces, respectively. As a result, the total conductivity between the two electrodes increases. For polycrystalline ceramics, similar phenomena can be observed but the influences from the grain boundaries must be taken into account. In the PZT system, resistance degradation due to the ionic migration of $V_O^{\cdot\cdot}$ has also been reported [137, 142, 143].

2.4.2. Trapped electrons and holes

Trapping and valence changes on dopant and host ions

The concept of trapped electrons and holes has to be included in the defect chemistry studies on dielectric materials. Although the conduction mechanisms could be qualitatively described with the defect models containing the aliovalent substitutions (doping centers) and the consequent compensating charge carriers (ionic: e.g. cation and anion vacancies; electronic: e', $h^{\cdot}$), there are sometimes difficulties to correlate charge equilibria, charge transport and their doping-dependences without obvious contradiction. One of the reasons for such difficulties is the highly insulating characteristic of these commonly used material families. A defect model would fail, for example, when the experimentally obtained conductivity is several orders of magnitude lower than that estimated from the possible electron or hole concentration and the corresponding mobility values belonging to free electronic charge carriers. One detailed quantitative analysis was given by Slouka *et al.* with respect to such concerns in acceptor- and donor-doped PZT ceramics [14].

One of the solutions for the aforementioned problem is to consider the electrons or holes to be trapped or localized. In general, there are many candidates for the traps within the materials, including the lattice vacancies, the donor- or acceptor ions, the host ions, etc. As for the latter two, trapping or de-trapping of electronic charges involves a change of the valence state of the relevant ion. For example, in the theory of the resistance degradation in Fe-doped STO, the crystals experience a so-called electrocoloration process [144]. The variation of color in the bulk material along the direction of electric field is caused by the valence change of the Fe ions which substitute for the B-site Ti ions according to the following reaction:

$$Fe'_{Ti} + h^{\cdot} \rightleftharpoons Fe^{\times}_{Ti}. \tag{2.31}$$

In this equation, Fe'_{Ti} refers to Fe^{3+} and $Fe^{\times}_{Ti}$ is the oxidized Fe^{4+}. Here Fe^{3+} is regarded as a hole trap. Apart from the impurity ions, the host ions can trap electrons and holes as well. In PZT, the most frequently reported hole trap is the Pb^{2+} ion [14, 143, 145–148], where either one hole or two holes could be trapped:

$$Pb^{\times}_{Pb} + h^{\cdot} \rightleftharpoons Pb^{\cdot}_{Pb}; \tag{2.32}$$

$$Pb^{\times}_{Pb} + 2h^{\cdot} \rightleftharpoons Pb^{\cdot\cdot}_{Pb}. \tag{2.33}$$

$Pb^{\cdot}_{Pb}$ and $Pb^{\cdot\cdot}_{Pb}$ are also called Pb^{3+} and Pb^{4+} in the literature, respectively. By using electron paramagnetic resonance (EPR), the Pb^{3+} trap state was observed in PZT and identified to be a shallow state very close to the valence band maximum [145, 146]. Also, the possible roles of Pb^{4+} in the charge compensation for the acceptor dopants have been discussed in Ref. [14]. Concerning the trap for electrons, Ti^{4+} is a major candidate in PZT systems [145, 146, 148], and it can form Ti^{3+} according to

$$Ti^{\times}_{Ti} + e' \rightleftharpoons Ti'_{Ti}. \tag{2.34}$$

Such Ti^{3+} has been experimentally observed via EPR only in the PZT compositions close to the MPB [145, 146], which is obviously different from the case of Pb^{3+}. Recently, the Ti-site used as an electron trap has also been confirmed in pure PT by *ab initio* calculations [149].

It can be noticed that the concept of electron/hole traps gives rise to more flexibility and completeness of consideration for defect chemistry studies. On the one hand, the trapping and de-trapping of electrons and holes may help us to establish self-consistent correlation about conduction mechanisms among electrical conductivities, activation energies, defect concentrations and mobilities, etc., even in the

comparatively insulating materials. On the other hand, some extra charges might be needed for interpreting the functionalities of FE-relevant materials within their operating temperature ranges (e.g. $< 200°C$). However, the charge equilibrium derived from the ionic compensations actually cannot describe a true picture in such conditions because the diffusion of ionic species has been already frozen at several hundred degrees above the room temperature during the cooling-down process after sintering. In this case, those electron/hole traps could be regarded as reasonable sources for the needed charges, and their contributions to the charge equilibrium should be therefore taken into account.

Fermi level confinement related to the trapping of electrons and holes

From the viewpoint of semiconductor physics, the electrical conducting/insulating characteristics of dielectrics such as BTO, STO, and PZT can be explained by the concept of Fermi level confinement. These materials normally have band gaps of 3–4 eV [151, 152]. One important precondition for them to be sufficiently insulating is that their Fermi level (E_F) should be situated far from the valence band maximum (VBM) and the conduction band minimum (CBM), namely $\geqslant 1$ eV [150, 153]. Figure 2.13(a) gives a collection of Fermi level positions relative to the band edges ($E_F - E_{VB}$) of (Ba,Sr)TiO_3 (BST) and PZT [150]. All data points were measured by XPS on thin film samples and the bands from both sides were aligned according to the offset value of 1.1 eV, which was determined by XPS as well. By changing the substrates and deposition parameters for these films, the Fermi level positions are found to vary within a range, which does not spread over the whole band gap for both cases. The difference is that such a Fermi level range in BST is located at the upper half of the gap approaching its CBM but the range in PZT sits only in the middle of the gap. By this means, one may speculate about the existence of an upper and a lower limit of accessible positions of Fermi level within the gap for each given material. As for PZT, both the upper and lower Fermi level limits remain a distance of about 1 eV to their corresponding band edges, which ensures an effective suppression on any conduction mechanisms

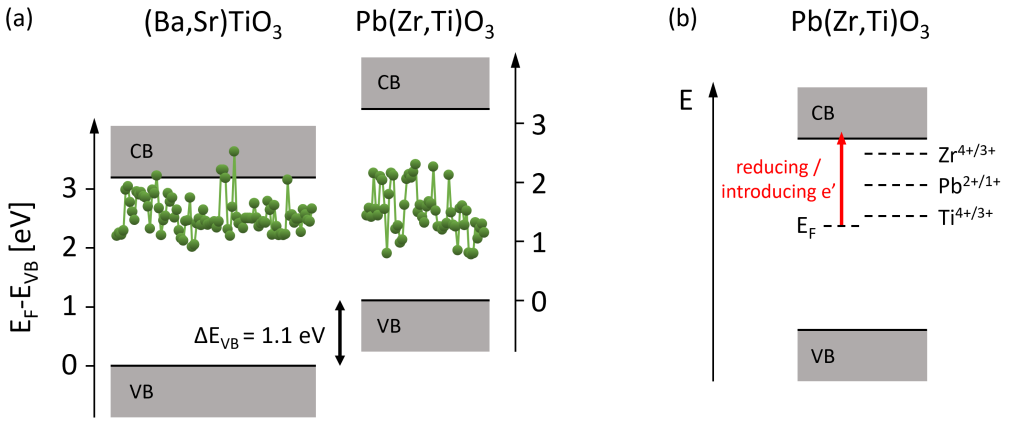

Figure 2.13.: Fermi level confinement in Pb(Zr,Ti)O_3 system. (a) Fermi level positions at the surfaces of a collection of (Ba,Sr)TiO_3 and Pb(Zr,Ti)O_3 thin films measured by X-ray photoelectron spectroscopy. Different substrates and deposition conditions were used and each green dot represents one sample. Redrawn with permission from Ref. [150]. Copyright (2011) American Physical Society. (b) Schematic band diagram of Pb(Zr,Ti)O_3 demonstrating the relation between the energy levels for electron trap candidates and the variation of Fermi level during a reducing process.

involving the two energy bands. In contrast to PZT, the fairly high relative Fermi level range in BST, which even overlaps slightly with its conduction band, indicates that the material would be able to show n-type conductivity much easier than PZT through doping or being equilibrated in reducing atmosphere. This is also consistent with the knowledge about the defect chemistry of BTO [125].

Several mechanisms may contribute to the limitation of varying Fermi level within the band gap, including the way through a dopant state and the way through a trap state (on the host ions). Concerning the PZT system doped with La, the latter seems to be more likely. Figure 2.13(b) shows a simplified band diagram for PZT, where three possible electron trap levels, $Ti^{4+/3+}$, $Pb^{2+/1+}$, and $Zr^{4+/3+}$, are schematically placed in the upper half of the band gap. Since Ti 3d state is lower than Pb 6p in pure PT but Zr 4d is higher than Pb 6p in pure PZ [146, 152], the three relevant states constituting the conduction band of PZT solid solution should have the order: Ti 3d $\rightarrow$ Pb 6p $\rightarrow$ Zr 4d (from low to high). Correspondingly, the three trap levels sitting within the band gap are expected to follow such sequence, as labeled in Figure 2.13(b). Once the material is placed in a reducing atmosphere for a new charge equilibrium (or some extra electrons are introduced into the material by other means, e.g. by doping or interface tuning), its Fermi level E_F should shift upward (see the red arrow). When E_F reaches a trap level (e.g. the lowest one $Ti^{4+/3+}$) and tries to surmount it, a valence change would take place on the Ti ions ($Ti^{4+} \rightarrow Ti^{3+}$), continuously consuming the inserted electrons and pinning the variation of E_F. This pinning effect results in the above-mentioned Fermi level confinement. It should be noted that other transitions may happen first in an actual material (on different host ions or with different valence changes from what is labeled in the schematic diagram). Analogously, the lower limit of Fermi level variation could also be observed when the material is oxidized.

2.5. Charge compensation related to ferro- and antiferroelectric domains

Regarding microstructures, one of the largest features of FE materials is the FE domain. Suppose there is a piece of single-domain FE crystal with homogeneous spontaneous polarization inside, the polarization-induced bound charges can bring about a huge electrostatic field. If this field is not compensated, it will depolarize the material. In order to stabilize the FE polarization, in general, the crystal need some extra charges to compensate such depolarizing fields or it breaks itself into smaller domains, which will reduce the strong electrostatic effect [8]. The extra charges in the former case can be contributed either by the flow of free charge in the bulk (for sufficiently conducting materials) or by the free charges in the surrounding medium (air, electrodes, etc., especially for insulators). The charge compensation taking place at the electrode/FE interfaces will be introduced later in Section 2.6. In this part, we will first deal with the situation where the too-high depolarizing field is compensated by the formation of multiple domain structures.

2.5.1. Charged domain walls in ferroelectrics

The interfaces between neighboring domains within the same grain (domain walls) are used to describe the microstructures of FEs, in terms of their spatial orientations, amounts (or densities), motions, interactions with other defects, etc. As already mentioned in Section 2.2.2, the orientations of the domains which belong to the same grain should follow the crystalline orientation, rather than being random. Adjacent domains and the corresponding domain wall in between will form certain geometrical relationships so that the system could lower its energy electrostatically and mechanically. It is thus easy

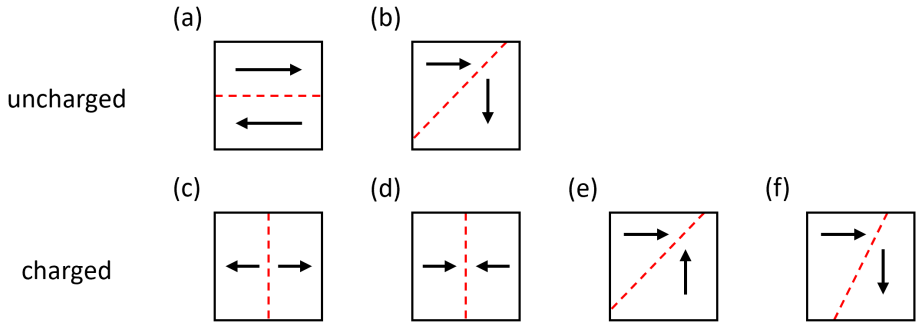

Figure 2.14.: Typical examples for (a, b) uncharged and (c–f) charged domain walls.

to understand that different crystal symmetries can lead to various domain structures in real materials. Taking the typical FE system PZT as an example, the Ti-rich tetragonal compositions are dominated by 90° and 180° domain walls, while 71° and 109° domain walls have been observed on the Zr-rich rhombohedral side [154–157]. Here the domain wall configurations are named after the angle between the orientations of two neighboring domains. Figure 2.14 gives the schematic for several types of domain wall structures (2-dimensional-simplified), where types (a, c, d) are 180° domain walls and types (b, e, f) are 90° ones. It can be seen that the domain wall (red dashed line) in type (a) is parallel to the directions of both domains which are antiparallelly arranged. Differently, the 180° domain walls in types (c, d) are perpendicular to the two domain orientations, which leave the bound charges from both sides uncompensated. These two cases are known as tail-to-tail and head-to-head domain walls, respectively [17]. It is similar in the cases of 90° domains that the domain wall can form different angles relative to both domains, for example 45° in types (b, e), and some other non-45° angle as schematically drawn in type (f). Based on such angular relations between the polarization vectors and the domain wall, here emerges a concept called charged domain wall. It is defined as the wall that carries non-zero net bound charges since the positive and negative contributions of bound charge densities from both sides cannot cancel out completely on the wall. In Figure 2.14, types (c–f) are charged domain walls. Type (a) has no bound charge on the wall at all, and type (b) manifests a fully compensating configuration. As a result, they are both regarded as uncharged domain walls.

The charged domain walls have been observed and studied in different FE materials, including BTO [158, 159], PT [160, 161], PZT [162–164], $BiFeO_3$ [165, 166], $(K,Na)NbO_3$ [167], etc. Transmission electron microscopy (TEM) is one of the most crucial tools to characterize the existence and structures of the charged domain walls. In the early years, TEM principally provided the possibility to observe the shape of domain walls. Combined with the information like lattice orientation extracted from electron diffraction patterns, one can determine whether these walls are electrically compensated or not [154, 162]. Recently, with the development of high-resolution TEMs, researchers have obtained the opportunities to identify more detailed and visualized atomic displacements in the region around the domain walls or even the configuration inside the walls [165, 166, 168]. Other techniques, for example piezo-force microscopy (PFM), conductive atomic force microscopy (c-AFM), and polarization microscopy, have been utilized to explore the charged domain walls on different scales. All these methods were very well summarized in the review article of Bednyakov *et al.* [19].

The importance of the charged domain walls is the screening (or compensation) of their bound charges with free charges. Firstly, it is widely accepted that the non-zero net bound charges on the walls must be compensated by some other charge carriers as completely as possible [17, 19]. Otherwise, the

strong depolarizing field arising from the bound charges (more descriptions will be given in Section 2.6) would destabilize the polarization of FEs. Secondly, one question must be answered: what is the source of the needed free charges for the compensation? Bednyakov *et al.* listed several possible mechanisms, including carriers excited over band gap (electron-hole), carriers generated by external photons, electronic carriers mixed with mobile ionized impurities, charges from external injection, and so on [159]. Nevertheless, as for the common FE materials like BTO and PZT, which are normally regarded as good insulators (used in capacitors), complete charge compensation seems to be not realistic [17, 18, 169]. Sluka *et al.* have proposed a model to describe the screening behavior at the charged domain wall [18]. As shown in Figure 2.15, they took a head-to-head 90° wall (left) and a tail-to-tail 90° wall (right) in a BTO crystal as example. Some free negative and positive charges are placed on the two walls, respectively. It is assumed that such charge compensation is still not sufficient, so that an electric potential difference occurs between these two walls, which can bend the conduction and valence bands. Under such condition, the CBM could become low enough to touch the Fermi level locally at the head-to-head wall, whereas the VBM could be high enough to touch the Fermi level at the tail-to-tail wall. In this case, the relative Fermi level positions within the band gap at both walls are expected to allow "more sufficient" concentrations of electrons and holes for a "more perfect" screening. In other words, this model is actually searching a balanced charge distribution in order to solve the problem that

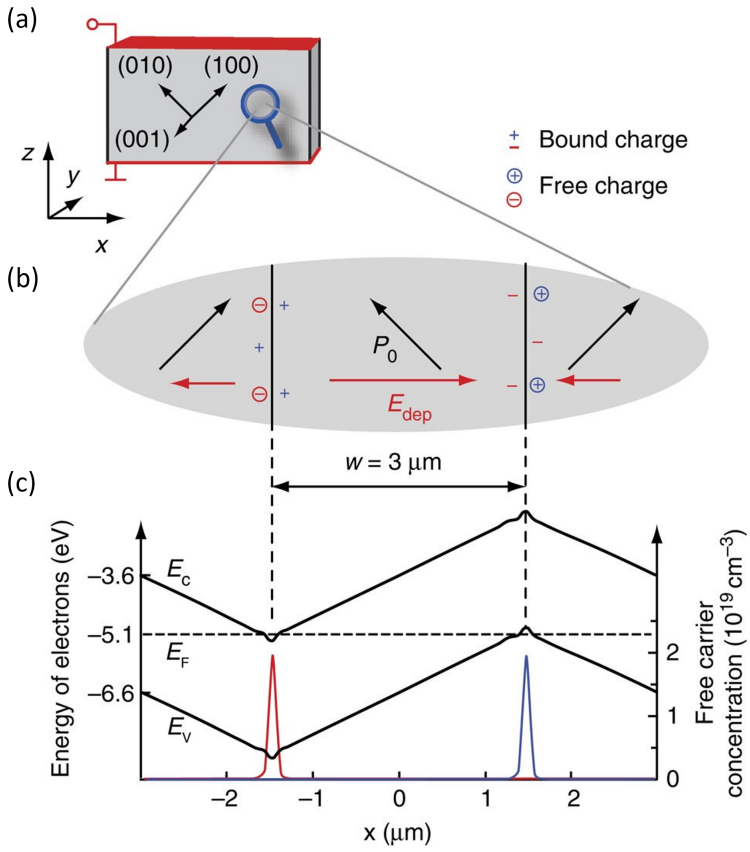

Figure 2.15.: Band bending model for $BaTiO_3$ at a pair of charged domain walls where the band bending causes that the conduction band and the valence band touch the Fermi level locally in the region of the walls. Reprinted under CC BY-NC-SA 3.0 license from Ref. [18]. Copyright (2012) Macmillan Publishers Limited.

insulating FEs cannot provide enough free charges to screen the potentially existing charged domain walls. Moreover, a higher electrical conductivity on the charged domain walls contributed by the free screening charges could bring about conducting paths for a short-circuit between two electrodes. Sluka *et al.* also included the simulated distributions of free carrier concentration at the junctions where the charged domain walls meet the electrodes. It was found that the high charge concentrations at all junctions show the normal level as the bulk and the questioned conducting paths are not connected to the electrodes. This phenomenon was attributed to the fact that the electric potentials on the electrodes are fixed and the band bending effect is therefore suppressed in the vicinity of the electrodes [18].

2.5.2. Domain structures in antiferroelectrics

Similar to FE materials, AFEs are also composed of numerous domains. In a FE domain, all dipoles are arranged toward the same direction. By contrast, the antiparallelly aligned dipoles lead to zero net polarization within each AFE domain, and therefore the electrostatic effect of the polarization-induced bound charges is usually neglected (or difficult to discuss). Instead, the mechanical factor (e.g. the strain) receives more attention when the formation of AFE domain structures is discussed [170]. Additionally, there are at least three types of interfaces related to the AFE domains: (i) the border between every two neighboring narrow "FE-like" regions with opposite polarization directions, which is sometimes also regarded as a kind of 180° FE domain wall [171]; (ii) the interface between two AFE domains; (iii) the interface between an AFE and a FE domain if they coexist in the material. For accurate expression, the latter two are always termed domain boundaries rather than domain walls.

Based on the features of structural phase transitions in AFE materials, experimental observations of their domain structures have principally been carried out under different conditions, such as at room temperature and at original state [107, 108, 112], at varying temperatures [172–174], and under external electric fields [113, 171, 175, 176]. The comparisons among samples with diverse compositional modifications are always involved as well [112, 115, 174]. As for Pb-containing AFEs, 60°, 90°, and 180° domain boundaries were identified in the prototype PZ [99, 177]. Within individual domains, the typical ↑↑↓↓ dipole arrangement was observed [115], which fits the crystalline structure model proposed in the early years [55]. Compared with the pure PZ, the chemically modified AFEs, such as PLZST and PNZST, manifest obviously different domain characters. Figure 2.16 gives schematic domain structure models and representative TEM images for PZ and PNZST (reprinted after Ref. [113]). In Figure 2.16(a), the stripes of the pure PZ possess a commensurate modulation of dipoles with a periodicity of 4. By contrast, the stripes of the modified PZ in Figure 2.16(b) are composed of a series of commensurate modulations whose periodicities are 7 or 8. As a result, the whole domain structure can be regarded as a so-called incommensurate modulation and its periodicity takes the average value of those of all constituent stripes, i.e. some non-integer between 7 and 8 in this example [108, 113]. Moreover, unequal modulation periodicities on the two sides of a domain boundary would break the charge neutrality on such interface. This effect can be eliminated by forming local atomic steps, as depicted in Figure 2.16(c). Figure 2.16(d) shows a real TEM image at such a domain boundary in PNZST. Besides the incommensurate modulations, another domain character in PLZST and PNZST is the "checkerboard" and "zebra-like" domain patterns (within grains) in TEM images, which are also related to the distinct orientations of modulated domains [107]. Figure 2.16(e) provides an example of the checkerboard domain pattern in PNZST.

As mentioned at the beginning of this section, it is widely believed that the electrostatic effect in AFEs stemming from the bound charges is not as important as in FEs. This is because the alternating positive

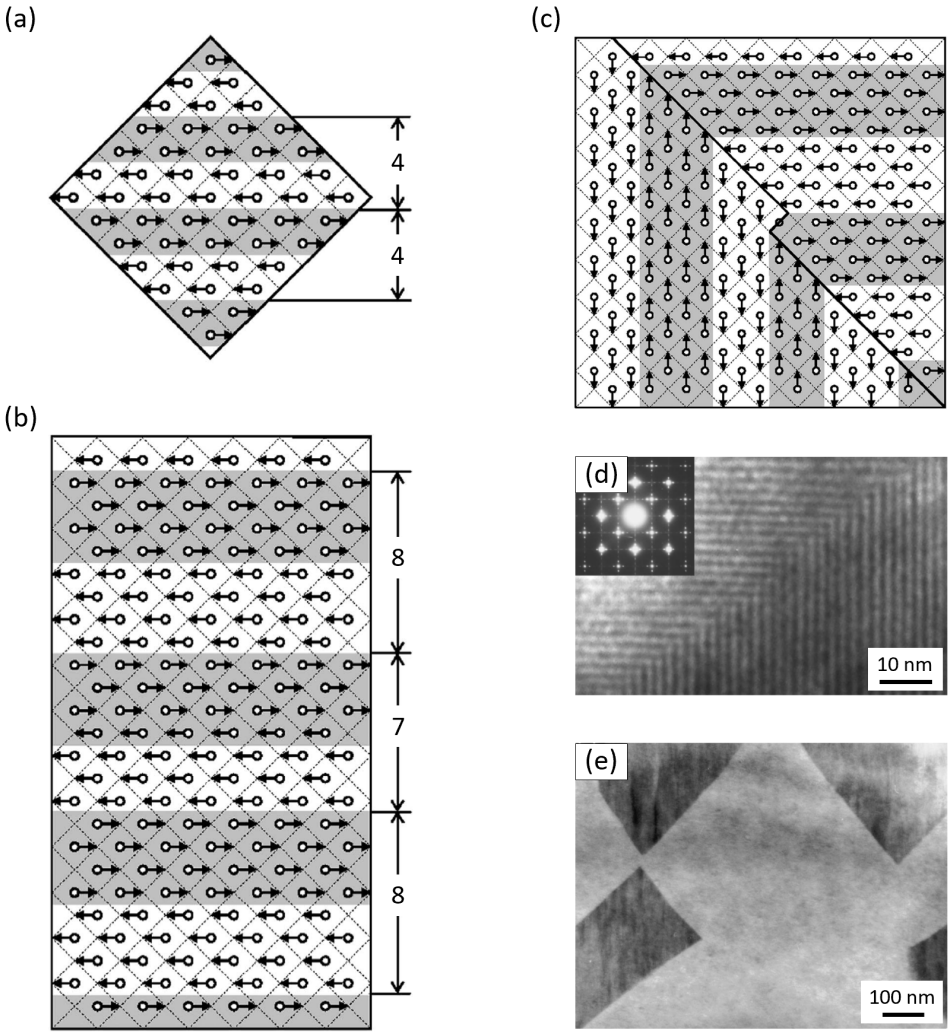

Figure 2.16.: Representative models and TEM images of antiferroelectric domain structures. (a) Model for $PbZrO_3$; (b) Model for a modified antiferroelectric composition based on $PbZrO_3$; (c) Schematic configuration of a 90° domain boundary in a modified $PbZrO_3$ with incommensurate modulations; (d) TEM image for the incommensurate modulation across the 90° domain wall in a PNZST sample; (e) TEM image for the checkerboard pattern of antiferroelectric 90° domains in PNZST. Reprinted with permission from Ref. [113]. Copyright (2005) The American Physical Society.

and negative bound charges densely distributed on the domain boundaries are expected to sufficiently counterbalance each other according to the classic understanding on AFE materials. However, the nature of AFEs shows more complexity in terms of the alignment of numerous constituent dipoles and their actual compensating or screening status. Thanks to the development of high-resolution TEM techniques, nowadays researchers can extract the relative displacements of atoms/ions in the TEM images and obtain an approximate mapping of electric dipole vectors within a certain region [179]. Following this strategy, visualized dipole configurations inside the domain or at the domain walls/boundaries become available. Figure 2.17 gives one example of such studies on AFE materials (reprinted after Ref.

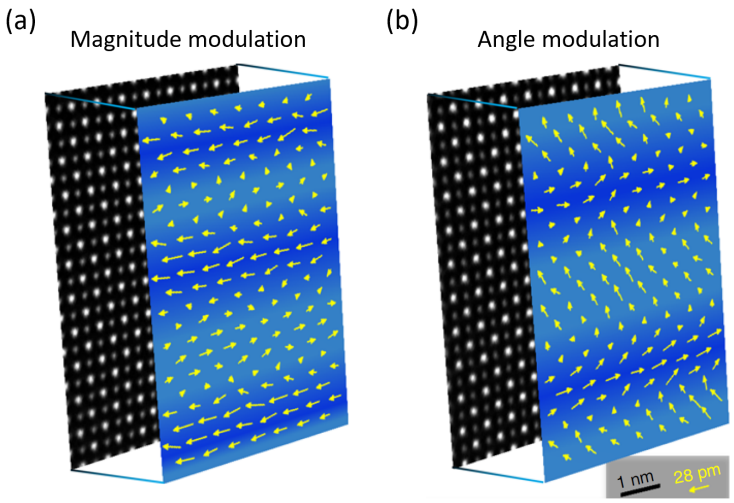

Figure 2.17.: Polarization mappings extracted from the relative cation displacements in TEM images of $Pb_{0.97}La_{0.02}(Zr_{0.50}Sn_{0.375}Ti_{0.125})O_3$ ceramic with (a) magnitude modulation and (b) angle modulation on the dipole arrangement. Reprinted under CC BY 4.0 license from Ref. [112]. Copyright (2020) The Author(s) of Ref. [112].

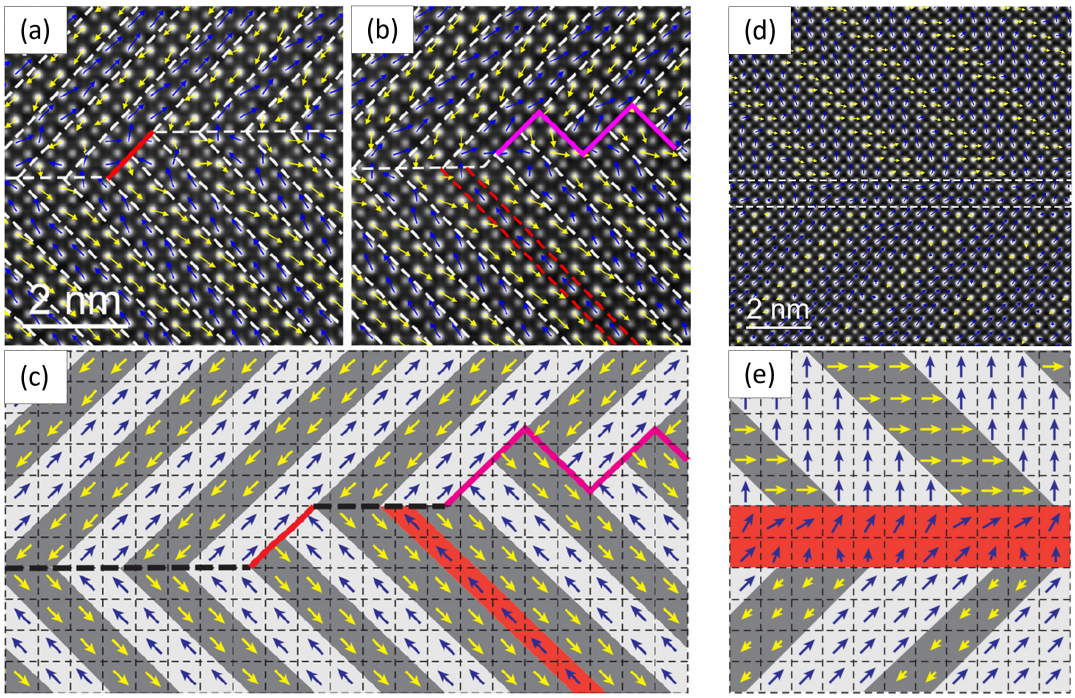

Figure 2.18.: Polarization mappings in the vicinity of 90° domain boundaries extracted from TEM images of (a, b) $PbZrO_3$ and (d) $Pb_{0.99}Nb_{0.02}[(Zr_{0.57}Sn_{0.43})_{0.95}Ti_{0.05}]_{0.98}O_3$ ceramics. (c) and (e) are the schematic mappings of domain configurations, based on the images in (a, b) and (d), respectively. Reprinted from Ref. [178] with the permission of AIP Publishing. Copyright (2019) The Author(s) of Ref. [178].

[112]). Two regions belonging to the same composition of a PLZST ceramic were observed by TEM and their polarization mappings extracted from cation displacements were compared [112]. As can be seen, the problem here is that the alignment of dipoles is not always rigorously parallel or antiparallel. Either the magnitudes or the orientations of these polarization vectors can non-negligibly deviate, corresponding to the magnitude modulation mode in Figure 2.17(a) and the angle modulation mode in Figure 2.17(b), respectively. It was also discovered in Ref. [112] that these two modes can coexist and interchange freely in the PLZST samples but the magnitude modulation mode shows dominance. Such phenomenon with a partial dipole compensation is always referred to as ferrielectricity in the literature [112, 180, 181]. Here comes a question now: Can the charges carried by the dipoles from the two sides of the AFE-domain-related interfaces be completely compensated? Here the interfaces refer to at least two types. One is the border between every two adjacent stripes within an AFE domain (e.g. somewhere between the dark- and light-blue stripes in Figure 2.17), and the other is the domain boundary. The results extracted from the TEM figures manifest complicated scenes that still cannot provide a clear answer to the question above. Similar observations with uncompensated polarizations were also reported within the domains of PNZST ceramics [115] and AFE $PbHfO_3$ ceramic [182], and on the domain boundaries of PZ and PNZST ceramics [178]. Figure 2.18 selects some TEM images and corresponding models for the dipole configurations at the domain boundaries in PZ and PNZST from Ref. [178]. Relatively less regular dipole arrangement can be found in the vicinity of 90° domain boundaries in the TEM pictures of both cases, indicating the existence of local electrostatic impacts due to imperfect charge compensation. The interesting scenes with planar defects and mismatched stripes located at the domain boundaries are also included, as shown in Figure 2.18(c, e), respectively [178].

From a technical point of view, TEM is one of the very few tools that can approach atomic scale for the visualized studies on domain structures. However, it should be noticed that the contrast in TEM is contributed by many columns of atoms aligning parallel to the direction of the incident electron beam, rather than single atoms within a plane. Any out-of-plane information is inaccessible and small in-plane offsets of the atoms that compose each column can cause certain ineluctable deviation during displacement determination. Nevertheless, TEM is the only technique to resolve local atomic displacements, which could indicate the presence of charges at domain walls/boundaries in the FEs/AFEs.

2.6. Charge compensation at electrode/ferroelectric interfaces

This section will introduce the charge compensation taking place at the electrode/FE interfaces of a FE-based capacitor, where the free charges from the electrodes also participate. This is always referred to as the so-called screening effect, which is the basis of the second in situ XPS method in this work (Section 3.4.6 and Chapter 7). In the following content, we will first provide some basic electrostatic considerations about the screening for a FE-based capacitor. After that, the way how the electrostatic conditions can modify the band offsets and the Schottky barrier heights at the electrode interfaces will be described.

2.6.1. Electrostatics of ferroelectric-based capacitors

The screening effect in dielectric capacitors refers to the compensation of bound charges by a distribution of free charges on the electrode. Such compensation reduces the depolarizing field that results from the polarization-induced bound charges [20]. The screening issue, which is actually a size effect, shows

specific importance during the miniaturization of FE-based capacitors [183]. High-permittivity gate dielectrics and non-volatile random access memories are two examples of the many applications of these capacitors based on FE thin films [184].

In the applications that take advantage of the high permittivity of FEs, one of the main concerns is the presence of "dead layers" [185], which is thought to be an interfacial layer between the dielectric and the electrode possessing a relatively low permittivity. According to the classical "series capacitor model" [185–187], the total capacitance C_{total} of the whole structure is

$$\frac{1}{C_{\text{total}}} = \frac{1}{C_{\text{i}}} + \frac{1}{C_0} + \frac{1}{C_{\text{i}}}, \tag{2.35}$$

where C_{i} is the interfacial capacitance (counted twice because there are two electrode interfaces within each capacitor) and C_0 is the capacitance of the rest of the dielectric layer with a normal permittivity. It is easy to see that the existence of the dead layers can lower the overall capacitance and this effect would become more noticeable when a much thinner dielectric layer is required. As for the application of FE-based non-volatile memories where the FE polarization and switching are needed, similarly, thickness dependence of the FE features also becomes an unavoidable question to answer. The critical thickness of the ultrathin film to keep the stability of ferroelectricity has been widely studied [188]. Among the many aspects that have been discussed in the literature for interpreting the dead layer and the critical thickness phenomena, the depolarizing field was very frequently involved, which principally depicts the profiles of electric potential along the thickness direction of the capacitors under different external electrical conditions. Here we also treat the interfacial models following this electrostatic point of view.

The terms of screening, depolarizing field, and dead layer are closely correlated. The core concept is the spatial separation of the bound charges and their corresponding screening or compensating charges in the region around the electrode interface [20, 22]. Simplified parallel-plate capacitor models concerning charge distribution are illustrated in Figure 2.19. Here it is assumed that both FE capacitors have been polarized before and are shorted at present. The direction of the remanent polarization is defined as positive direction of the systems. The charges labeled in blue are bound charges ($\pm\sigma_{\text{b}}$) and we call the red ones screening charges ($\pm\sigma_{\text{s}}$). For simplification, all these charges are temporarily assumed to be distributed in planes with infinitely small thickness. In the capacitor on the left-hand side, there is no spatial separation of the bound and the screening charges at each electrode interface. It should be noted that this is just an ideal physical model where both kinds of charges are placed intentionally at the same position exactly on each electrode/FE interface. This case is called perfect screening, with a separation distance (screening length) of zero. Under the condition of short-circuit, the electric potential on the two electrodes must be the same. If $\sigma_{\text{s}} = \sigma_{\text{b}}$, the electric fields generated by the bound and the screening charges will cancel out everywhere along the x-axis. Therefore, zero total field (see the E–x plot) and a flat potential profile (see the V–x plot) are expected within the whole capacitor structure. In contrast to the perfect screening case, the bound and the screening charges around each electrode interface are separated by a non-zero screening length λ in the model on the right-hand side. This separation forms two dipoles in the space near both electrode/FE interfaces. Because the dipoles have the same sign, the potential drops generated by them also have the same direction, i.e. both decreasing along the x-axis in the example demonstrated here. Since this capacitor is also under the short-circuit condition, i.e. the electric potentials in the bulk of both electrodes (not the very narrow interfacial parts within the range of λ) are fixed at the same level, there must be an increase of potential (negative field) inside the central FE layer in order to satisfy electrostatic relations. This non-zero electric field pointing to the opposite direction of the polarization is known as the depolarizing field, which can affect the stability of the as-polarized FE layer. Such case with a screening length λ and an induced depolarizing

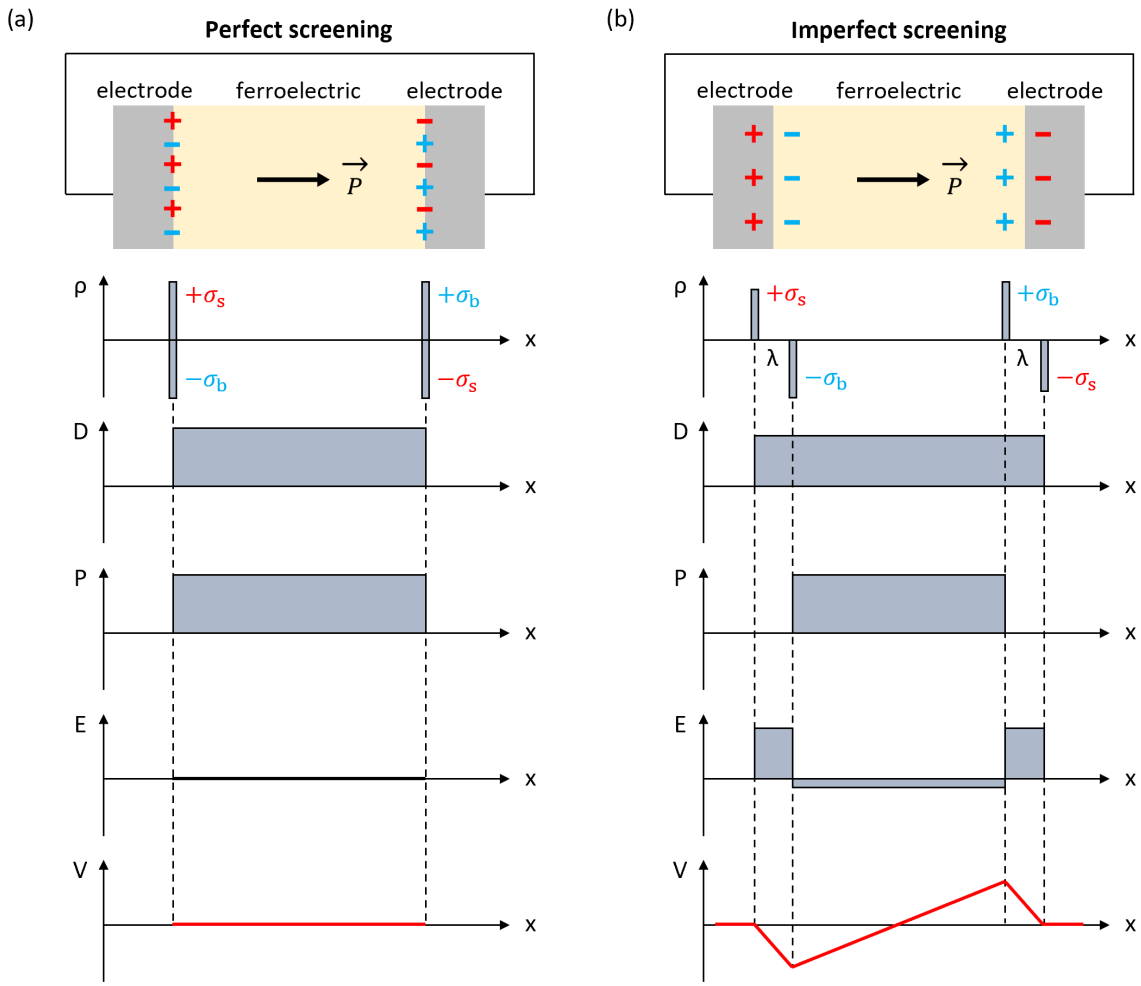

Figure 2.19.: Models of ferroelectric capacitors with (a) perfect screening and (b) imperfect screening under short-circuit condition. For both models, the profiles of charge ρ, displacement D, polarization P, total electric field E, and electric potential V along the thickness direction are given correspondingly.

field is then called imperfect screening. It can be noticed that the imperfect screening model shown in Figure 2.19 need slightly fewer screening charges than the bound charges defined by the polarization. This is actually the result solved from electrostatic relations under the short-circuit condition.

In literature there are at least two common types of electrical boundary conditions for treating the electrostatics in a capacitor: (i) closed-circuit boundary condition with a fixed applied voltage (or a fixed applied electric field); (ii) open-circuit boundary condition with a fixed amount of free or screening charges on the electrodes [189]. In this work, we only adopt the former one that shows more practicality for real devices and setups. Figure 2.19 compares the perfect and imperfect screening cases only under short-circuit condition. More behaviors under different operating conditions, for example throughout the hysteresis loop of a FE capacitor, are necessary to know. Figure 2.20 depicts such complete courses by comparing perfect and imperfect screening again. Five steps are included here, marked by the red dots on the P–E loops (following the yellow arrows). The $P_{\max}$ only means the polarization obtained at the maximum applied field $E_{\max}$, rather than an ideally saturated polarization. The most important

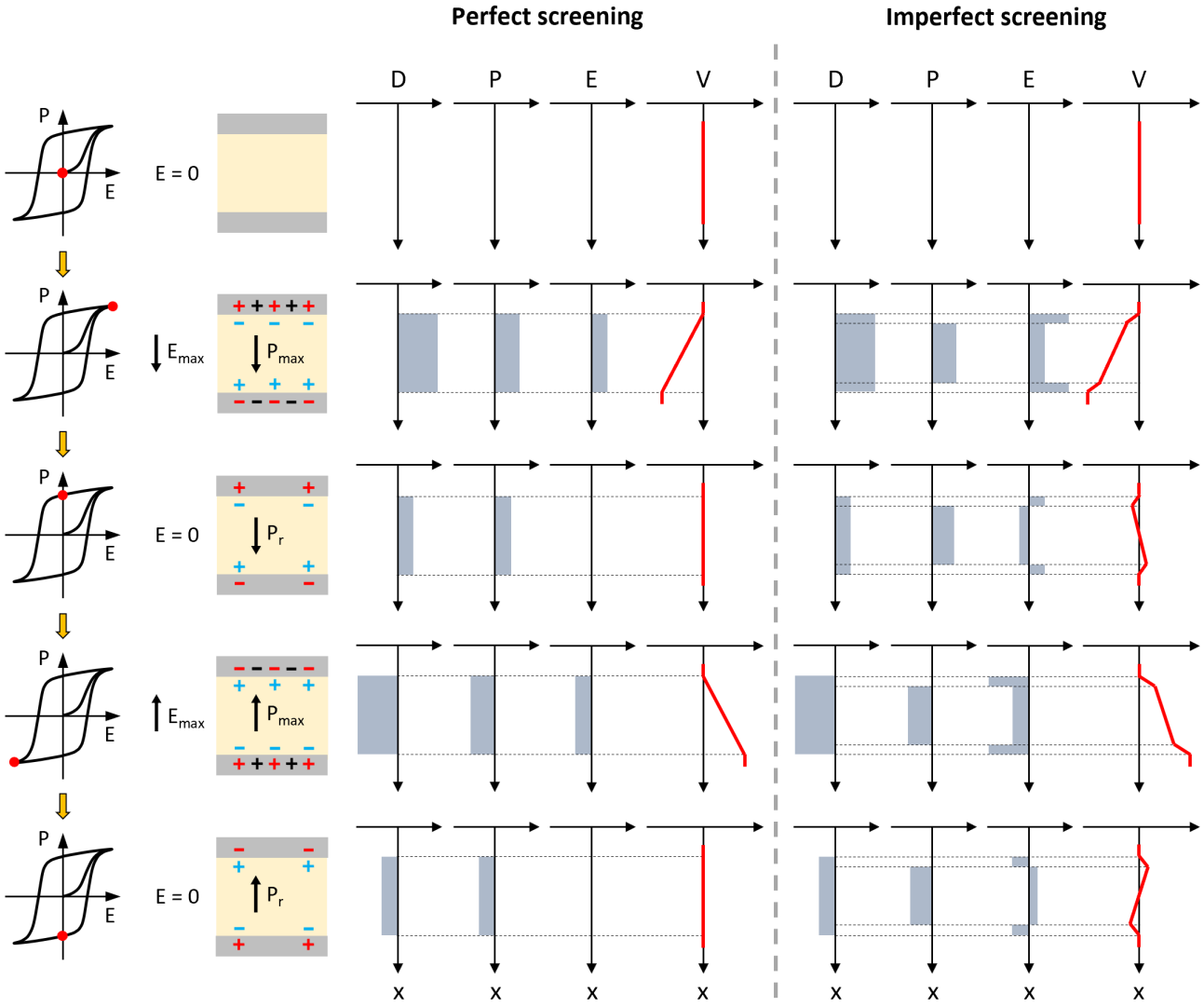

Figure 2.20.: The comparison between perfect and imperfect screening in ferroelectric capacitors in the course of measuring hysteresis loop. The profiles of displacement *D*, polarization *P*, total electric field *E*, and electric potential *V* along the thickness direction are illustrated for both cases.

information here is the evolution of deduced profiles of electric potentials (see the V–x plots). Taking the imperfect screening effect into account, the whole potential profile shows in total five distinguishable segments instead of three in the perfect screening case [20, 190, 191]. When the capacitor is working at $P_{\max}$, different from the short-circuit status, the electric field within the central FE layer keeps the same sign as that of the two interfacial layers, consistent with the direction of externally applied electric field.

One important issue that has been laid aside during describing the models in Figures 2.19 and 2.20 is the screening length, or more accurately, the real configurations and reasons of the charge separation at

the electrode/FE interfaces. Regarding this topic, abundant experimental and theoretical researches have been done. Based on where the charge separation is located, the common hypotheses in the literature can be divided into two main groups:

(1) The finite screening in the electrodes. In this theory, the screening charges on the electrode have a more realistic spatial distribution over a distance from the interface, rather than being concentrated within an ideal zero-thickness plane. Such phenomenon is thought to exist in both metallic [20, 183, 186] and semiconducting electrodes [21, 192, 193]. For metallic electrodes, the screening length is usually treated by Thomas-Fermi method [186, 194, 195]. By contrast, semiconducting electrodes have larger screening lengths because of their lower carrier concentrations, which can make the induced dead layer or depolarization field more noticeable. Important properties of FE thin films, including the magnitude of polarization, coercive field, the temperature and even the order of phase transition, can be affected by the depolarization fields when semiconducting electrodes are used [193]. Following the preceding understanding, modifications of thin film FE properties by intentionally controlling the amount of available screening charges on the electrodes have been reported to be feasible as well [21, 196].

(2) The non-uniformity of polarization within the FE layer, especially with a non-abrupt drop of polarization from the FE thin film to the electrode. In other words, the spatial distribution of bound charges actually results in the screening length on the FE side [22, 190, 197]. The core strategy to elucidate the polarization profiles adjacent to the electrode/FE interface is to introduce a surface term of free energy in addition to the normal bulk term [190, 198, 199]. Moreover, as for the compensation between the bound and the screening charges under such condition, two mechanisms of so-called "in situ screening" are necessary to be considered [22]: the free charges from the electrode penetrate into the FE layer (charge injection) [200, 201], or alternatively the bound charges penetrate into the electrode (ionic displacements in oxide electrodes) [22].

Besides the aforementioned two categories, there are many other mechanisms. For example, the screening at electrode interfaces can be very intrinsically related to the soft-mode hardening within perovskite oxides [185] and the stiffness of chemical bonds locally between FE and electrode layer [202]. From a more realistic point of view, one should keep in mind that the low-permittivity interfacial layers could also stem from the quality of film growth in terms of defects, strains, or grain boundaries [203, 204]. Additionally, these mechanisms are very likely to coexist to a certain extent in real materials, forming different types of equivalent capacitance, and it would be therefore difficult to distinguish. Despite the complexities in the screening effects, here we mainly focus on the charge separation itself for the moment (using the so-called effective screening length λ_{eff} to include all possible effects [202, 205]), and adopt the most simplified electrostatic model to describe the basics directly related to our experimental work.

2.6.2. Band offsets at the electrode/ferroelectric interfaces

In semiconductor physics, the concept of Schottky barriers is used to describe the features of the interface between a metal and a semiconductor, in terms of the charge transport or capacitive behavior [11]. The Schottky barrier height (SBH) is one of the most important parameters at such interfaces, which can be defined based on either electrons ($q\phi_n$) or holes ($q\phi_p$). Here q is the absolute value of the unit electronic charge (following the tradition in semiconductor physics, equivalent to e). The capacitor, which consists of a dielectric layer sandwiched by two electrodes, possesses two such interfaces whose SBHs (both $q\phi_n$ and $q\phi_p$) should have positive values in order to avoid the Ohmic contacts that can

attenuate the dielectric performance [191]. In the following part, the specific features of a Schottky barrier at an electrode/FE interface is introduced, according to the papers of Stengel *et al.* [191] and Hong *et al.* [206] unless otherwise noted.

Suppose there is a metallic electrode with Fermi level E_{F} and a FE with the energies of conduction band minimum E_{CB} and valence band maximum E_{VB}. All of these three are called the band-structure terms. Here the position of E_{F} is determined based on a reference level within the electrode layer $\langle V_{\mathrm{H}}^{\mathrm{electrode}} \rangle$, which can be regarded as an averaged electrostatic potential in the bulk of the electrode (far away from the interface). Similarly, the values of E_{CB} and E_{VB} are relative to their own reference $\langle V_{\mathrm{H}}^{\mathrm{ferroelectric}} \rangle$ in the FE bulk. When an electric contact is established between two sides, the two reference levels should be lined up. In the case of the electrode/FE interface, the lineup is modified by the extra potential drop caused by the imperfect screening. The difference between the reference levels is defined as the electrostatic lineup term and is used to describe the dipole at the interface:

$$q \cdot \Delta\langle V \rangle = q \cdot (\langle V_{\mathrm{H}}^{\mathrm{ferroelectric}} \rangle - \langle V_{\mathrm{H}}^{\mathrm{electrode}} \rangle). \tag{2.36}$$

Then the SBHs can be expressed by involving both the band-structure terms and the lineup term:

$$q\phi_n = E_{\mathrm{CB}} - E_{\mathrm{F}} + q \cdot \Delta\langle V \rangle, \tag{2.37}$$

$$q\phi_p = E_{\mathrm{F}} - E_{\mathrm{VB}} - q \cdot \Delta\langle V \rangle. \tag{2.38}$$

Rigorously, both the band-structure terms of FE (E_{CB} and E_{VB}) and the lineup term ($q \cdot \Delta\langle V \rangle$) are dependent on the existence of polarization in the FE layer, so Equations 2.37 and 2.38 can be written as the functions of electric displacement D (only the normal component to the interface is used here for simplification):

$$q\phi_n(D) = E_{\mathrm{CB}}(D) - E_{\mathrm{F}} + q \cdot \Delta\langle V \rangle(D), \tag{2.39}$$

$$q\phi_p(D) = E_{\mathrm{F}} - E_{\mathrm{VB}}(D) - q \cdot \Delta\langle V \rangle(D). \tag{2.40}$$

The dependence of polarization on the band-structure terms has been interpreted through the hybridization theory within the perovskites [191, 207]. However, this is not directly related to this work. Here only the term $\Delta\langle V \rangle(D)$ is being considered, and it can be expressed by the profile of electric potential in the simplified screening model as shown in Figures 2.19 and 2.20. The electric field within the region of the effective screening length λ_{eff} is a constant in this case, which is equal to D/ε_0. Subsequently, one can write the linear relation:

$$\Delta\langle V \rangle(D) = \Delta\langle V \rangle(0) + \lambda_{\mathrm{eff}} \frac{D}{\varepsilon_0}. \tag{2.41}$$

By comparing the states of this FE capacitor being forward and backward polarized (with D and $-D$, respectively), the variation of the SBHs is

$$q \cdot \Delta\phi = q \cdot |\Delta\phi_n| = q \cdot |\Delta\phi_p| = q \cdot (\Delta\langle V \rangle(D) - \Delta\langle V \rangle(-D)) = 2q\lambda_{\mathrm{eff}} \frac{D}{\varepsilon_0}, \tag{2.42}$$

which is valid for both cases of $q\phi_n$ and $q\phi_p$.

Figure 2.21 sketches the variation of the electrostatic potential at the same electrode interface when the polarization is being reversed in a FE-based capacitor by applying external electric field. The potential of the electrode is always fixed by the external circuit, while the potential profile in both the interfacial screening layer and the FE bulk is varying when the capacitor is polarized at four states as shown.

In the ideal situation, the lines of $-P_{\mathrm{max}}$ and $-P_{\mathrm{r}}$ should be the mirror images of those belonging to P_{max} and P_{r}, respectively. As marked in the figure, the effective screening length λ_{eff} can result in an increase of electrostatic potential by $\lambda_{\mathrm{eff}}\frac{D}{\varepsilon_0}$ in a linear simplification when there exists a remanent polarization pointing to the left-hand direction under the short-circuit condition (thin blue lines). It is then easy to understand that the sum of upward and downward variations of the electric potential due to polarization reversal is just double of $\lambda_{\mathrm{eff}}\frac{D}{\varepsilon_0}$. Moreover, the variations corresponding to $\pm P_{\mathrm{max}}$ (thick lines) are expected to be somehow larger than those of $\pm P_{\mathrm{r}}$ because the former ones involve the contribution from the external bias. Lastly, these variations in electrostatic potential can be added to the band-structure terms and modify the SBHs at such an electrode/FE interface according to Equations 2.39 and 2.40.

It should be noted that the model in this section was established based on the scene of a single domain with homogeneous polarization inside. However, it can be still considered to be valid for the electrode interfaces with polycrystalline FEs, where the band offsets at the interface mostly depend on the distribution of the free charges from the electrode and the bound ones belonging to the domains which are directly in contact with the electrode. Such model is the basis of the second in situ XPS method, which will be described in Section 3.4.6 with more experimental details.

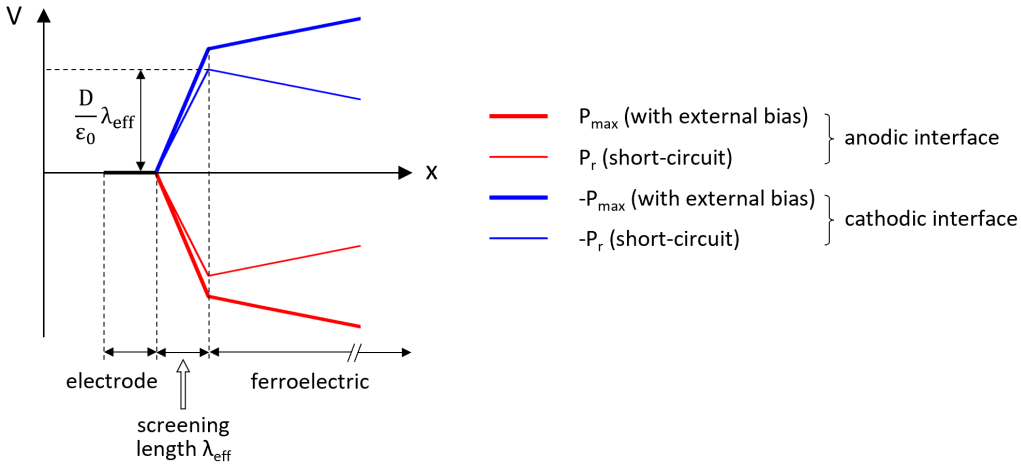

Figure 2.21.: Electrostatic potential profiles around one of the electrode interfaces of a ferroelectric capacitor with imperfect screening. The comparison involves four states of this electrode interface expressed by the polarization: P_{max}, P_{r}, $-P_{\mathrm{max}}$, and $-P_{\mathrm{r}}$. The positive direction follows $+x$. The effective screening length and the corresponding variation in the electrostatic potential due to the imperfect screening are marked.

3. Methodology and Experimental Procedures

The objective of this work is to investigate the possible conduction mechanisms and the relevant roles and behaviors of charges in the $PbZrO_3$-based AFE materials, which are very good insulators. First of all, three series of PLZST-related ceramic samples were synthesized by the conventional solid-state reaction method (Section 3.1). After the synthesis of the ceramic pellets, several basic characterizations were performed (Section 3.2). With the preliminary knowledge of all compositions, various types of temperature- and field-dependent dc conductivity studies were carried out, from which the degree of the conduction/insulation of such materials and the effects of chemical modifications were characterized (Section 3.3). Subsequently, two in situ XPS methods were applied (Section 3.4). Although XPS is usually regarded as a surface-sensitive technique, it was used in this work to explore the trap states and Fermi level limitations, which are expected to occur also in bulk materials (Section 3.4.5), and to characterize the screening behaviors at the electrode/dielectric interfaces (Section 3.4.6).

3.1. Synthesis of ceramic samples

3.1.1. Composition selection

Three series of compositions were selected for different purposes, shown in Figure 3.1 and Table 3.1. In the room-temperature phase diagram of $(Pb_{0.97}La_{0.02})(Zr,Sn,Ti)O_3$ [23], the effects of Ti/Sn ratio on dielectric properties have usually been investigated along a compositional line with a fixed Zr concentration across the A_T–$F_{R(LT)}$ phase boundary [94, 95, 208, 209]. In this work, $(Pb_{0.97}La_{0.02})(Zr_{0.75}Sn_{0.25-x}Ti_x)O_3$ (x=0, 0.04, 0.08, 0.09, 0.10, and 0.11) were selected as a principal group of compositions (C-series), marked with red dots in Figure 3.1(a). The four relatively Ti-rich compositions (C08–C11) are designed to exhibit the transition near the phase boundary between A_T and $F_{R(LT)}$, and the other two Ti-poor compositions (C00 and C04) should belong to the A_O phase region according to the phase diagram. Besides, there are two series of variants: the X-series (X01–X03) with a changing La content based on the composition of C09, and the A-series (A01–A02) with an increasing Fe doping concentration based on the Ti-free composition C00. The X-series are utilized to study the role of La on the PLZST system. For the A-series compositions, Fe^{3+} is expected to substitute for *B*-site ions and work as accepter [14]. Thus the A-series are nominally co-doped, which are designed to manifest a competition between donor La^{3+} and acceptor Fe^{3+}. The relations of all three series are shown in Figure 3.1(b) and the chemical formulas of all synthesized compositions are listed in Table 3.1 together with a simple description of their usage in the following chapters. For convenience, some abbreviations will be used to describe the types of the materials, which are also listed in Table 3.1. All these ceramic samples were prepared by the author of this work in the labs of Prof. Tongqing Yang at Tongji University, Shanghai, China.

In addition to the three PLZST-related series, some other ceramics were also used in this work for

comparisons, including $Pb(Zr_{0.53}Ti_{0.47})O_3$ (PZT53/47) and $Pb(Mg_{1/3}Nb_{2/3})O_3$ (PMN) ceramic pellets (both provided by Prof. Dr. Tadej Rojac of Jožef Stefan Institute, Ljubljana, Slovenia), and the commercial soft PZT ceramic $Pb_{0.99}(Zr_{0.45}Ti_{0.47}(Ni_{0.33}Sb_{0.67})_{0.08})O_3$ (PIC 151, PI Ceramic, Lederhose, Germany).

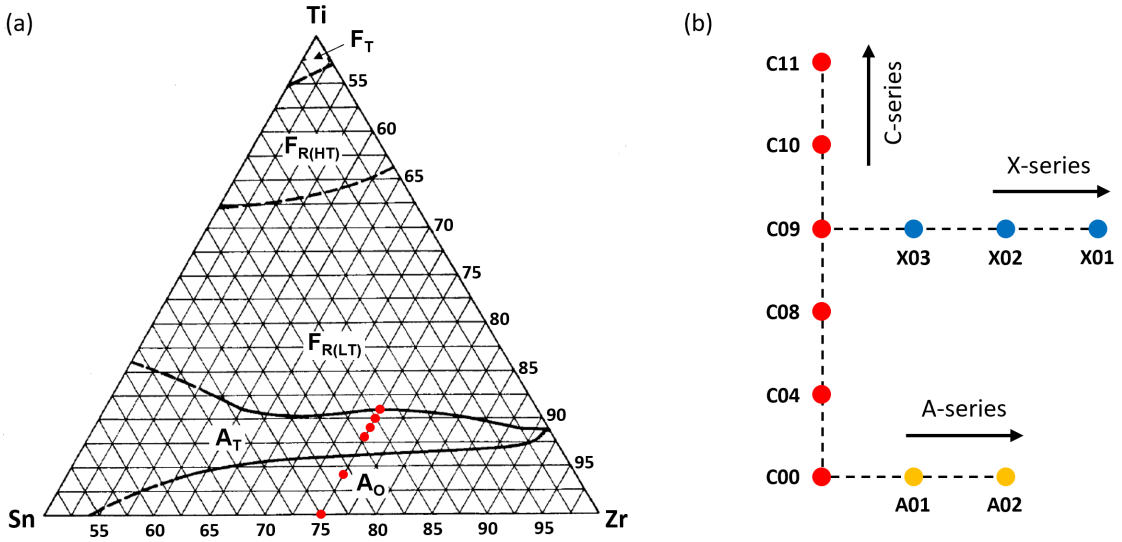

Figure 3.1.: Selected compositions to be synthesized in this work. (a) The positions of C-series in the ternary phase diagram of $(Pb_{0.97}La_{0.02})(Zr,Sn,Ti)O_3$ at 25°C. The phase diagram is used with permission from Ref. [23]. Copyright (1966) IEEE. (b) The relations among C-, X-, and A-series. Compositions C09 and C00 are located at the intersections of C-series with X- and A-series, respectively.

Table 3.1.: Ceramic compositions synthesized for this work and their usage in the following chapters. "XPS (electrochem.)" and "XPS (FE)" refer to the XPS methods with electrochemical oxidation/reduction (Chapter 6) and with ferroelectric polarization (Chapter 7), respectively.

#	Composition	Type (abbr.)	Usage in this work
C00	$(Pb_{0.97}La_{0.02})(Zr_{0.75}Sn_{0.25})O_3$	PLZS	conductivity
C04	$(Pb_{0.97}La_{0.02})(Zr_{0.75}Sn_{0.21}Ti_{0.04})O_3$	PLZST	reference
C08	$(Pb_{0.97}La_{0.02})(Zr_{0.75}Sn_{0.17}Ti_{0.08})O_3$	PLZST	reference
C09	$(Pb_{0.97}La_{0.02})(Zr_{0.75}Sn_{0.16}Ti_{0.09})O_3$	PLZST	conductivity, XPS (electrochem.), XPS (FE)
C10	$(Pb_{0.97}La_{0.02})(Zr_{0.75}Sn_{0.15}Ti_{0.10})O_3$	PLZST	conductivity, XPS (FE)
C11	$(Pb_{0.97}La_{0.02})(Zr_{0.75}Sn_{0.14}Ti_{0.11})O_3$	PLZST	conductivity, XPS (FE)
X01	$Pb(Zr_{0.75}Sn_{0.16}Ti_{0.09})O_3$	PZST	conductivity, XPS (electrochem.)
X02	$(Pb_{0.985}La_{0.01})(Zr_{0.75}Sn_{0.16}Ti_{0.09})O_3$	PLZST	conductivity
X03	$(Pb_{0.9775}La_{0.015})(Zr_{0.75}Sn_{0.16}Ti_{0.09})O_3$	PLZST	conductivity
A01	$(Pb_{0.97}La_{0.02})((Zr_{0.75}Sn_{0.25})_{0.99}Fe_{0.01})O_{2.995}$	PLZSF	conductivity
A02	$(Pb_{0.97}La_{0.02})((Zr_{0.75}Sn_{0.25})_{0.98}Fe_{0.02})O_{2.99}$	PLZSF	conductivity, XPS (electrochem.)

3.1.2. Solid-state reaction method for synthesis

The traditional solid-state reaction method was utilized to sinter all ceramic samples listed in Table 3.1. All compositions of C-, X-, and A-series were prepared with the same procedure in order to have more straightforward comparisons of their properties. The raw oxide powders of PbO ($\geqslant$ 99.0%), La_2O_3 ($\geqslant$ 99.99%), ZrO_2 ($\geqslant$ 99.0%), SnO_2 ($\geqslant$ 99.5%), TiO_2 ($\geqslant$ 98.0%), Fe_2O_3 ($\geqslant$ 99.0%) (Sinopharm Chemical Reagent Co., Ltd., China) were used. First, the powders were weighed stoichiometrically according to the chemical formulas in Table 3.1. 2% excess of PbO was added to all compositions to compensate for the volatilization of Pb during high-temperature processing. After weighing, the powders were mixed by ball-milling in deionized water with agate balls for 24 hours. Then the powders were dried at 80°C and calcined in alumina crucibles at 900°C for 2 hours. The calcined powders were once again ball-milled with agate balls for 18 hours, but using ethanol as milling medium. After drying at 80°C, the powders were manually granulated with 8 wt.% polyvinyl alcohol (PVA) binder and then pressed into pellets by uniaxial mold, which gave the pellets initial diameters of 10 mm. Subsequently, the pellets were directly placed on alumina plates and annealed at 600°C for 3 hours with a relatively slow heating-up rate to get rid of the PVA binder inside the pellets. After that the final sintering was carried out at 1250°C for 3 hours, during which the pellets were placed in a Pb-rich zirconia powder bed (also covered on the top for sealing). The zirconia powder used here was previously calcined at 1550°C so that it should be sufficiently nonreactive. More details of the procedures and corresponding instruments are given in Figure 3.2 and Table 3.2, respectively.

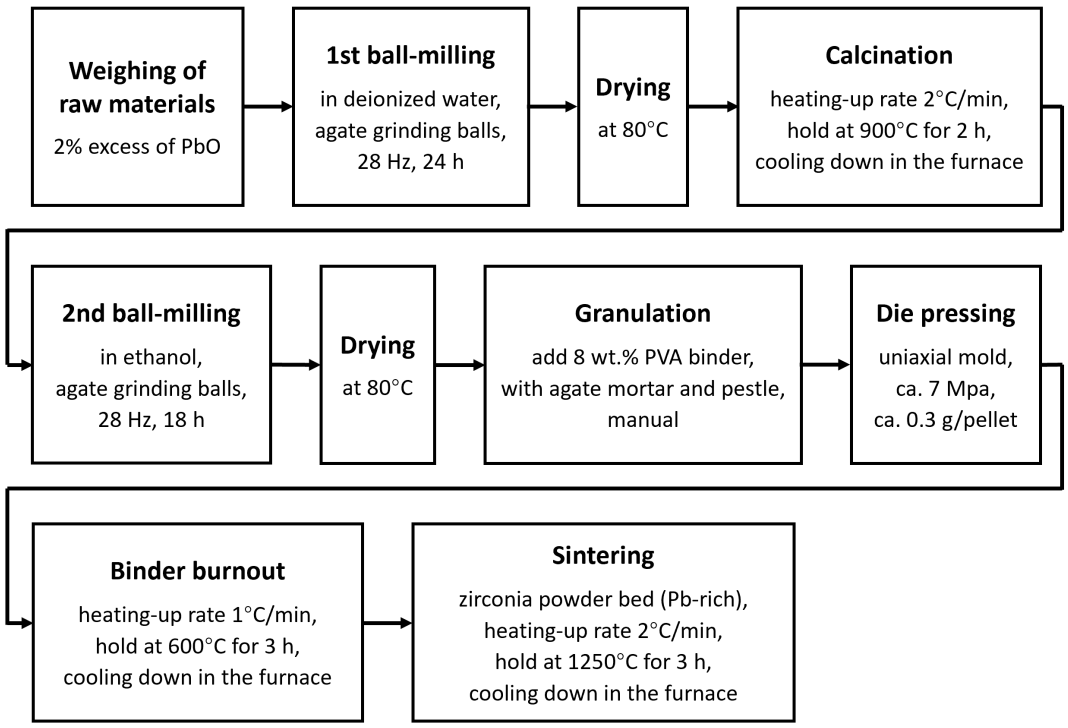

Figure 3.2.: Flow chart of the synthesis of C-, X-, and A-series ceramics by solid-state reaction method.

Table 3.2.: Instrument list for ceramic synthesis by solid-state reaction method.

Step	Model of device	Manufacturer
Weighing	AL204 analytical balance	Mettler-Toledo International Inc., USA
Ball-milling	Planetary ball mill QM-BP	Nanjing Nanda Instrument Co., Ltd., China
Die pressing	Electric tablet press DY-30	Tianjin Keqi High & New Technology Corp., China
Calcination	Box furnace KSL1100x	Hefei Kejing Materials Technology Co., Ltd., China
Binder burnout	Box furnace KSL1100x	Hefei Kejing Materials Technology Co., Ltd., China
Sintering	Box furnace TW-series	Shanghai Zufa Industry Co., Ltd., China

3.2. Basic characterizations of ceramic samples

3.2.1. Hysteresis behaviors

A Sawyer-Tower circuit was utilized to measure the P–E hysteresis loops, schematically illustrated in Figure 3.3. The as-sintered ceramic pellets were normally ground to suitable thicknesses and then sputtered with Pt electrodes (ca. 50 nm thick, Quorum Q300T D, Quorum Technologies Ltd., UK) on both sides to form capacitor structures. For each measurement, the sample (with capacitance C_{sample}) was connected to a reference capacitor (with capacitance C_{ref}) in series. It is known that two capacitors connected in series should have the same charges when an external voltage is applied. This relation can be written as

$$Q_{\text{sample}} = Q_{\text{ref}} \tag{3.1}$$

or

$$C_{\text{sample}} V_{\text{sample}} = C_{\text{ref}} V_{\text{ref}}, \tag{3.2}$$

where V_{sample} and V_{ref} are the voltages on the sample and on the reference capacitor, respectively. If an appropriate capacitance of the reference is chosen to fulfill $C_{\text{sample}} \ll C_{\text{ref}}$, one will have $V_{\text{sample}} \gg V_{\text{ref}}$. It means that most of the voltage from the source will be applied to the sample so that the electric

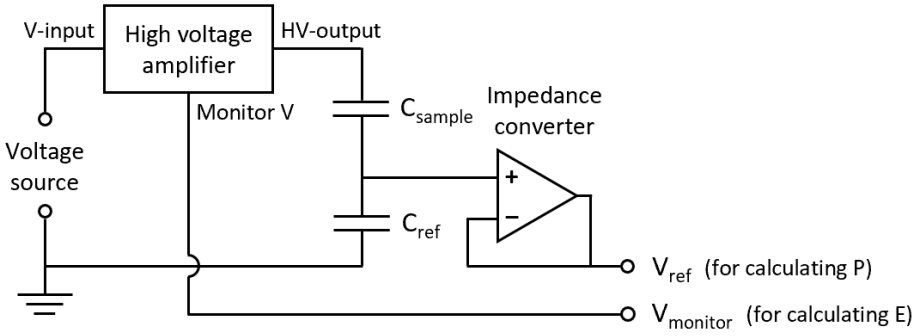

Figure 3.3.: Schematic diagram of the Sawyer-Tower circuit used for measuring the hysteresis loops of polarization vs. electric field.

field on the sample can be approximately calculated using the applied voltage divided by the sample thickness. Besides, the charge of the sample Q_{sample} can be obtained once V_{ref} is known:

$$Q_{\text{sample}} = Q_{\text{ref}} = C_{\text{ref}} V_{\text{ref}}. \tag{3.3}$$

Afterwards, the polarization of the sample can be calculated by Q_{sample} divided by the electrode area.

A multifunction I/O device (USB-6211, National Instruments, USA) was used as the voltage source in Figure 3.3. The generated triangular waveforms were firstly amplified through a high voltage amplifier (Trek 20/20C or 1HVA24-BP1-F, Advanced Energy Industries, Inc., USA, depending on the usage scenario) and subsequently applied to the two capacitors. The signal V_{monitor} was output by the amplifier and the product of V_{monitor} and the gain reflected the real-time applied high voltage. The potential V_{ref} was measured after an impedance converter. Both V_{monitor} and V_{ref} were acquired by the I/O device USB-6211 and further used for calculating the applied field and the induced polarization. The signal generation and acquisition on the I/O device USB-6211 were controlled through a LabVIEW program (National Instruments, USA).

In this work, there are three main usage scenarios of the P–E loop measurement, which correspond to different geometry types used for pellet and electrode preparation, as listed in Table 3.3. These scenarios are:

(1) Measuring the P–E and S–E loops at room temperature on the compositions with relatively low AFE-to-FE transition fields. The purpose is to comprehensively learn the hysteresis behaviors of the important compositions that are close to the AFE–FE phase boundaries. S–E loops (longitudinal strain) were measured together with the P–E loops through a fiberoptic displacement sensor (Model D63, PHILTEC, Inc., USA) in a specific sample holder using silicone oil as insulating medium. The frequency-dependent loops were also studied on several compositions that behave between AFE and FE. In order to make the loop measurements as accurate as possible, fully-covered electrodes are normally recommended [210] (see Table 3.3). The amplifier Trek 20/20C (Advanced Energy Industries, Inc., USA) was used in this scenario.

(2) Measuring the P–E loops at room temperature on the compositions with very high AFE-to-FE transition fields that could exceed 20 kV/mm. It is known by experience that thinner samples are beneficial to successful P–E loop measurements where sufficiently opened double loops can be seen. Hence the sample thicknesses should be strongly reduced by grinding. Meanwhile, the final thicknesses should still be able to maintain the intactness of fragile ceramics. Suitable thicknesses were then decided to be around 0.08–0.10 mm. Another difference on the sample geometry was that the electrodes were not fully covering the surfaces (see Table 3.3). Smaller top electrodes were adopted to avoid the breakdown through the edges of sample in the silicone oil. It was acceptable here to use not-fully-covered electrodes because the purpose of this scenario was just to ascertain whether these compositions could exhibit AFE feature or not. In this scenario, moreover, the way of mounting samples on the holder that was compatible for strain measurement became impracticable. Therefore, another holder that could contact samples with less pressure was used and the S–E loops were skipped for these compositions. The amplifier model Trek 20/20C (Advanced Energy Industries, Inc., USA) was used in this scenario.

(3) Measuring the P–E loops at varying temperatures on the compositions close to the AFE–FE phase boundaries. Most of these samples are expected to exhibit temperature-induced phase transitions. The P–E loop measurements were carried out basically in two ovens, one easy for heating and the other compatible for cooling with liquid N_2. Thus the geometry type should be able to make reliable electrical contacts inside the ovens (see Table 3.3). As for the amplifier, either model Trek

20/20C or 1HVA24-BP1-F (Advanced Energy Industries, Inc., USA) was used for applying high voltages depending on the needed electric fields.

Table 3.3.: Geometry types for the ceramic pellets and electrodes depending on different usage scenarios of *P–E* loop measurement.

Scenario	Composition	Thickness	Electrode geometry
(1)	C04, C08–C11, X01–X03	0.22–0.26 mm	rectangular, each edge 2.2–2.5 mm, fully covered
(2)	C00, A01, A02	0.08–0.10 mm	round, ⌀1.5 mm, not fully covered
(3)	C09–C11, X01–X03	0.12–0.15 mm	round, ⌀2.5 mm, not fully covered

Additionally, all samples were annealed at 350°C in air after mechanical grinding with sandpapers in order to remove residual stress as much as possible. Also, each sample was annealed again at a temperature higher than its T_C before a new round of P–E loop measurements to get rid of all remanent polarization induced previously. Relevant results can be found in Section 4.1.

3.2.2. Dielectric permittivity

The complex dielectric permittivity was measured with LCR meter 4284A (Hewlett Packard, USA) under small ac signals. The acquired capacitance value was used to calculate the real part of the complex relative permittivity ε_r', and the dielectric loss tangent $\tan\delta = \varepsilon_r''/\varepsilon_r'$ was directly output. In the rest of this work, the relative permittivities appearing in all relevant plots will specifically refer to ε_r' for convenience.

Two types of dielectric permittivity measurements using small ac signals were involved in this work (see the description in Section 2.2.2):

(1) Dielectric permittivity versus temperature. Considering the accuracy of temperature controlling, only the process during heating-up was adopted. A sequence of frequencies of the ac signal (stepwise increasing from 100 Hz to 1 MHz) were applied to every sample cyclically throughout the heating-up process (2°C/min). The root-mean-square (RMS) value of the ac signal was set to be 1.0 V. The samples always had a sandwich structure with a thickness of ca. 0.2–0.35 mm and Pt electrodes sputtered on both sides. Every sample was annealed before the measurement at sufficiently high temperature to ensure its unpoled state.

(2) Dielectric permittivity versus electric field at varying temperature. This part was carried out by Dr. Lovro Fulanović. Besides the LCR meter, the high voltage amplifier Trek PZD2000A (Advanced Energy Industries, Inc., USA) was utilized to produce the dc field. The LCR meter and the high voltage source were connected through a blocking circuit that was composed of two 1 μF capacitors and a 100 kΩ resistor for necessary protection. The ac signal for measuring the permittivity had an RMS of 1.0 V and a fixed frequency of 100 kHz. The high voltage amplifier generated triangular waveforms in the similar way to that for P–E loop measurements, but only a relatively low frequency of 5 mHz was applied here. As the high voltage signal was varying sufficiently slowly, it was still regarded as a dc bias. Due to the compatibility issue of the sample geometry, all samples for this measurement were prepared according to scenario (3) in Section 3.2.1. For each

sample, the curves of permittivity vs. electric field were always acquired at its "developed" states at several different temperature steps. Therefore, the pre-annealing to recover the unpoled state was not necessary in this part.

Relevant results can be found in Section 4.2.

3.2.3. Crystalline structures

The crystalline structures of the synthesized ceramics were studied by X-ray diffraction (XRD). All XRD patterns were measured on the clean surfaces of ceramic pellets at room temperature by the diffractometer D8 ADVANCE (Bruker, USA) with Cu-K_α radiation (wavelength for $K_{\alpha1}$: 1.5406 Å, $K_{\alpha2}$: 1.5444 Å) and with a step size of 0.02°. The measurements were performed by Mr. Jean-Christophe Jaud.

The purpose of this part is to obtain basic information of the crystalline structures and the sintering quality of different compositions. For every pellet, the side where XRD was measured had been ground with sandpaper in order to remove the as-sintered surface. This is because such surfaces that had unavoidable contacts with surroundings (for instance the gas or the packing powder in the crucible) during the high-temperature sintering are usually thought to be different from the bulks in terms of the stoichiometry, microstructures, etc. Thus, the materials under a sufficient depth should be exposed so that reliable bulk information could be characterized. Before the XRD measurement, all samples were annealed at 350°C for 1 hour to get rid of the stress introduced by mechanical grinding. Relevant results can be found in Section 4.3.

3.2.4. Microstructures

The microstructures of the bulk ceramics were characterized by field-emission scanning electron microscope (SEM). Model JEOL 7600F (JEOL, Ltd., Japan) was used and all measurements were carried out by Dr. Lovro Fulanović. The author also gratefully acknowledges the technical advice from Dr. Hui Ding. The main purpose of this characterization is to examine the quality of the synthesized ceramic samples principally with respect to the distribution of grain size and the existence of secondary phase.

Two types of SEM images were obtained:

(1) Images on the as-sintered ceramic surfaces. Although such surfaces usually cannot provide a valid representation of the microstructures inside the bulk ceramics, their morphology was still worth an observation. After basic cleaning, the as-sintered ceramic pellets were directly coated with approximately 10 nm of carbon using Emitech K950X (Quorum Technologies Ltd., UK). The SEM micrographs were taken in the lower secondary electron image (LEI) mode.

(2) Images of the samples after grinding and polishing. The pellet surfaces were firstly ground with sandpaper (#1200, #2400, #4000) and then polished with polishing discs and diamond paste (6, 3, 1, 0.25 μm). After necessary cleaning and annealing at 350°C for 1 hour to reduce the residual stress, some attempts were made to thermally etch the polished surfaces on several samples. The thermal etching is normally considered to be an effective means to expose the morphology of grain boundaries. However, the quality of the thermal etching was not ideal in this work. Some information can be found in Appendix A.3. For most of the samples, the polished surfaces were

coated with carbon directly and the thermal etching was skipped. Subsequently, the SEM images were taken in one of the modes with back scattered electron (COMPO), which were sufficiently good for detecting the contrast of different grains. Lastly, the image processing program ImageJ [211] was utilized to recognize the grains and calculate the average grain sizes (using more than 200 grains for each composition). Relevant results can be found in Section 4.4.

3.3. Electrical conductivity

In order to find out the conduction mechanisms and related charges within the FE and AFE ceramics, which are usually very good insulators, one should know the magnitude of the electrical conductivity first. In general, the conductivity can be measured with ac or dc method depending on materials, but this work will focus on the dc conductivity.

3.3.1. Sample preparation and setup for measurement

All electrical conductivity measurements in this work utilized the two-point method, in which a dc voltage U was applied to the ceramic sample with a sandwich capacitor structure and meanwhile the current flowing through the sample I (also called the leakage current of the capacitor) was measured. Using the electrode area A and the thickness d, the conductivity of the sample σ can be calculated according to

$$\sigma = \frac{I \cdot d}{U \cdot A}. \tag{3.4}$$

Here it should be noted that the two-point method is not the best option for the samples with extremely low conductivity/high resistivity. The very low current flowing through the sample may be overridden by other unwished currents, for example the leakage through the insulation of the test circuit or the surface current mainly due to the high humidity in the environment. In order to reduce such effects, guarding is sometimes needed [212]. However, no guard ring was added onto the sample surfaces in this work and only two electrodes (top and bottom) were used to form a typical sandwich structure for capacitors. The main reasons for such simplification were the small dimension of the ceramic pellets and the compatibility of the sample geometry with other measurements.

The ceramic pellets were ground by sandpaper first to get suitable thicknesses (0.13–0.15 mm), and then cut into small pieces. After annealing at 350°C for 1 hour to reduce the residual stress induced by the grinding, Pt electrodes were sputtered on both sides of each pellet (Quorum Q300T D, Quorum Technologies Ltd., UK). For most samples, the Pt electrodes were round and had a diameter of 2.5 mm. Both the top and the bottom electrodes did not fully cover the surfaces, always remaining a distance of ca. 0.5 mm to the edges of each pellet. Several samples were prepared with another geometry where larger ceramic pellets and correspondingly larger electrodes (round, ⌀6.5 mm) were applied in order to acquire higher current signals. Such individual cases will be specifically noted in Chapter 5 with relevant results.

Figure 3.4 gives the schematic diagram of the circuit and equipment used for the dc conductivity measurements. The picoammeter Keithley 6487 (with a built-in ±500 V dc voltage source, Tektronix, Inc., USA) was utilized throughout this work to apply dc voltages and read the currents flowing through the samples. The samples were mounted in a home-made tube furnace and connected with the voltage

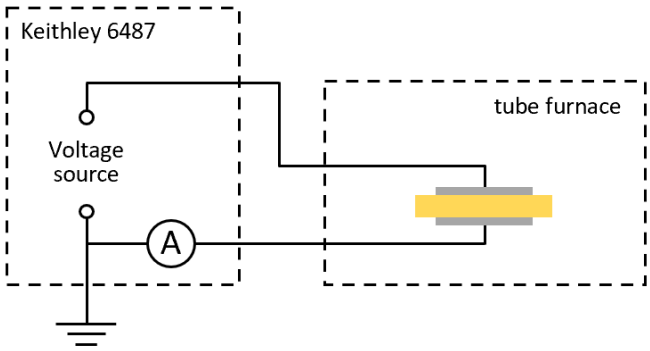

Figure 3.4.: Schematic diagram of the circuit and equipment used for dc conductivity measurements.

source and the ammeter in series. The circuit was able to reliably acquire currents in the range of 10^{-12} A, which helped the measurements for very low conductivity. Here the author gratefully acknowledges the technical support from Mr. Michael Weber. Moreover, the temperature of the sample was measured by a K-type thermocouple installed inside the furnace very close to the sample, and the data were collected via the thermocouple input module NI USB-TC01 (National Instruments, USA). The operation of the tube furnace was controlled by a Eurotherm temperature/process controller Model 2416 (Schneider Electric, France). The electrical measurements were realized by a LabVIEW program (National Instruments, USA). All conductivity experiments were classified into static and dynamic ones depending on the controlling of their temperatures. The following two parts will introduce these two strategies respectively.

3.3.2. Electric-field- and temperature-dependent dc conductivity by static method

Owing to the complicated electrical conduction mechanisms of common functional ceramics, the actual current–voltage characteristic (or I-V relationship) may not be in accordance with Ohm's law. Hence, it is necessary to study the electric-field-dependence of the conductivity on these materials. Figure 3.5 sketches the conditions of such experiments, where the applied voltage (electric field) changed step by step but the temperature remained the same during this process. Because of the charging and discharging behaviors of capacitive devices, the duration of each step of applying voltage would affect the

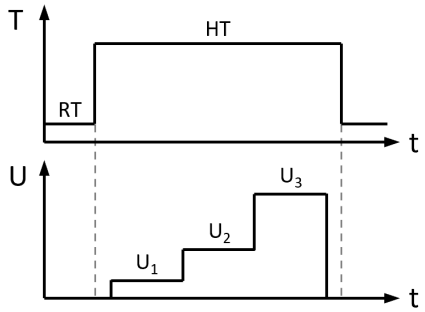

Figure 3.5.: Schematic for the conditions of the static conductivity measurements at a fixed temperature and with several voltage steps. (RT: room temperature; HT: high temperature.)

determination of the conductivity concerning the degree of saturation of the leakage current. Detailed descriptions and comparisons will be given in Section 5.1 with real data. The process shown in Figure 3.5 only includes one step of temperature. In order to obtain the temperature dependence of conductivity, the same voltage conditions should be applied again on the sample at different temperatures. All these tests where each voltage step takes place at a fixed temperature are called static measurements in this work.

3.3.3. Electrical conductivity by dynamic method and determination of activation energy

Another measuring strategy was to control the increase and decrease of the temperature but keep the applied voltage constant. This is called dc dynamic method in this work. Figure 3.6(a) shows the conditions schematically. The temperature increased at a constant rate to a certain high temperature and then dropped back to room temperature at the same rate. During such a thermal cycling process, a fixed dc voltage was applied all the time and the current through the sample was recorded. It should be noted that the last stage of the cooling-down (when approaching the room temperature) was usually not well-controlled due to the feature of the ovens and the actual temperature always showed a delay compared to the programmed value.

In semiconductors or insulators, generally, the conductivity increases with the increase of temperature. Such temperature dependence can usually be written in the form of an Arrhenius behavior [13]:

$$\sigma = \sigma_0 \exp\left(-\frac{E_\mathrm{a}}{kT}\right), \tag{3.5}$$

where E_a is an activation energy, k the Boltzmann constant, and σ_0 a constant value depending on the specific material. If one plots $\ln\sigma$ vs. $1/T$ (T stands for the thermodynamic temperature in Kelvin), the relation expressed by Equation 3.5 becomes a straight line and its slope is equal to $-E_\mathrm{a}/k$. Such diagram is termed Arrhenius plot, as shown in Figure 3.6(b).

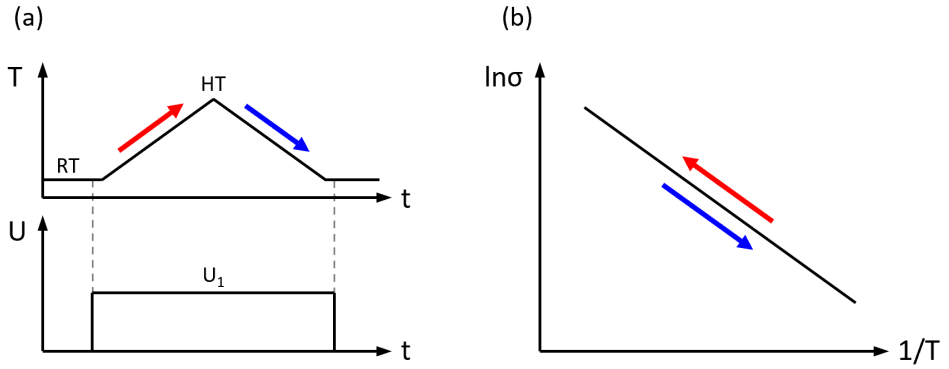

Figure 3.6.: (a) Schematic for the conditions of the dynamic conductivity measurements with a dc bias and under a temperature cycling. (b) Sketch for an Arrhenius plot of electrical conductivity for a material having an ideally single activation energy over the whole temperature range. The red and blue arrows indicate the heating-up and cooling-down processes, respectively. (RT: room temperature; HT: high temperature.)

From a practical point of view, the Arrhenius plot for the electrical conductivity of a real ceramic is very likely not an ideal straight line. Instead, it may manifest several segments with different slopes indicating non-unique conduction mechanisms within different temperature ranges. In addition, the heating-up and the cooling-down processes in the Arrhenius plot may show deviations, which are worth investigations as well.

It should be noted that a series of discrete conductivity values determined by the previously mentioned static method can also be used to depict the Arrhenius relationship. These two methods may lead to different results to some extent. Relevant comparisons will be given in Section 5.2.2. Moreover, in the actual experiments, there were different variations in the measuring conditions, such as changing the applied electric field or the profile of temperature (the rates of heating-up and cooling-down, extra temperature-dwelling steps). Figures 3.5 and 3.6 only illustrate the elemental processes. The actual conditions will be described in more detail when relevant data are displayed in Chapter 5.

3.4. X-ray photoelectron spectroscopy

3.4.1. Basics of X-ray photoelectron spectroscopy

X-ray photoelectron spectroscopy (XPS) is a powerful surface-sensitive characterization technique that utilizes the external photoelectric effect. It has been extensively used to identify the chemical compositions of materials and the valence states of relevant elements. From the viewpoint of semiconductors, XPS also provides the possibility to characterize the local electrostatic potentials formed at the surfaces and interfaces of the devices. Here basic knowledge of XPS, which is directly related to the current work, will be introduced first. Unless otherwise stated, this part will be based on the book by Hüfner [213], the short review chapter by Klein *et al.* [214], and the handbook by Moulder *et al.* [215].

The so-called external photoelectric effect refers to the process where the illumination of the sample by photons leads to an emission of electrons (termed photoelectrons). The condition for such effect is that the incident photon energy should be greater than the binding energy of the electron so that the emitted photoelectrons can escape from the sample surface by using the remaining energy (in the form of kinetic energy). In the operation of XPS measurement, specifically, the photoelectric effect can be described by the following formula:

$$E_{\text{kin}} = h\nu - E_{\text{B}} - \phi_{\text{sp}}, \tag{3.6}$$

where $h\nu$ is the incident photon energy of X-ray, E_{kin} the kinetic energy of the photoelectrons, E_{B} the binding energy, and ϕ_{sp} the work function of the spectrometer. As there are numerous energy states existing within the material that can emit photoelectrons, the analyzer will detect electrons with a series of E_{kin}. After transforming E_{kin} into E_{B} based on Equation 3.6, the XPS spectrum, which plots the numbers of photoelectrons versus the binding energy, can be obtained. In addition, the last term ϕ_{sp} in Equation 3.6 is related to the instrument and can be adjusted by defining the binding energy at the Fermi edge of the clean surface of a metal as 0 eV. By this means, all conductive samples that have good electrical contact with the spectrometer possess the same reference level (Fermi level located at 0 eV). In other words, all the measured binding energies are relative to the Fermi level and can be therefore compared directly.

By analyzing the XPS spectra, a lot of information about the chemical states and electronic structures of

the samples can be extracted. The most important components in an XPS spectrum are the photoemission lines of the core-level states. They stem from deep electron orbitals that do not participate in chemical bonding, and have a very wide distribution in an XPS spectrum. Each element possesses a characteristic distribution of such emission lines, so XPS can be used to determine the chemical compositions of compounds. One of the most obvious features of the core-level emission lines is the splitting of p-, d-, and f-emissions in doublets, which is caused by the interaction of the spin and orbital angular momentum when a photoelectron has been emitted and an unpaired electron still remains in that core level. By contrast, s-orbital emissions have no spin-orbit splitting. Another important feature of the core levels is the so-called chemical shift, which refers to the shift in binding energies when the elements under detection changes its oxidation states (the density of the valence electrons). Usually, a higher positive oxidation state can result in a higher binding energy. In this work, the characterization by XPS will focus on the measurement of binding energies of core-level emissions and the determination of valence states based on the chemical shifts.

Besides the core-level emissions, the XPS spectra also provide other information including the emission of the valence band region, Auger lines, shake-up lines, etc. Considering that they are not directly relevant in this work, details will not be given here.

3.4.2. Challenges of the study on insulating ceramics by XPS

In general, there are at least two aspects of technical limitations in the XPS study on insulating ceramic materials:

(1) The detected depth is limited. When the Al K_α radiation is used as the X-ray source, the maximum accessible depth is about 10 nm, which is actually quite shallow for a thick bulk material. Thus, one should be careful when it is necessary to distinguish the bulk properties and the surface effects.
(2) The surface under X-ray illumination must be conductive and sufficiently-well connected to the ground of the spectrometer when accurate binding energies are required. This is related to the reference issue of binding energies, which have already been introduced in Section 3.4.1. When the electrical connection between the sample and the spectrometer is not well established, the so-called charging effect would occur and shift the emission towards higher binding energy. This situation should be avoided as the information on the Fermi level position will get lost.

Figure 3.7 schematically gives four possible modes of XPS measurements regarding the conductivity problem of the samples. Figure 3.7(a, b) compares the situations using an electrically conductive bulk sample and an insulating bulk sample. Both of them are mounted on the top of a metallic sample holder, which is grounded together with the spectrometer. The accumulation of positive charges on the sample surface due to the emission of photoelectrons should be compensated by external source of negative charges in order to avoid the charging effect. The conductive sample can easily provide a path for such a compensating current from the ground to the sample surface (following the black arrow), whereas the thick insulator can not. Normally, there are several strategies to minimize the effect of the surface charging, including using a neutralizer or flood gun, or making the insulator of interest a thin film sitting on the top of a conductive substrate (see Figure 3.7(c)). As for the usage of thin film insulator, one should be careful because both the macroscopic properties and microscopic structures of a thin film could strongly deviate from those of a bulk sample. Another strategy to avoid the charging effect on insulators is shown in Figure 3.7(d), where a conductive thin film top layer can be coated on

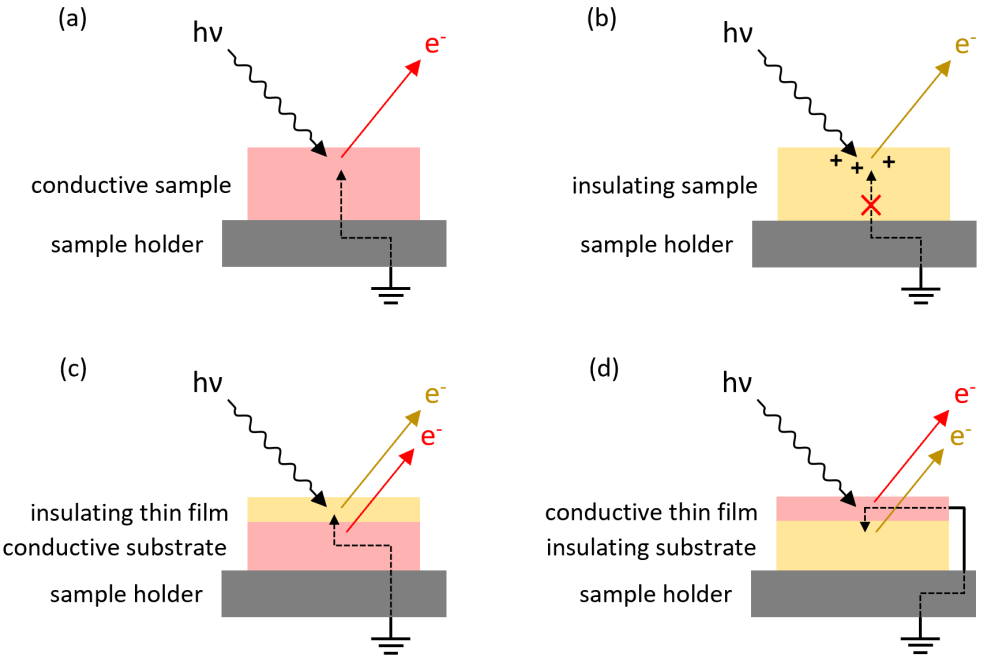

Figure 3.7.: Schematics for different modes of samples used for XPS measurement. (a) A conductive bulk sample; (b) an insulating bulk sample; (c) an insulating thin film sample coated on a conductive substrate; (d) an insulating bulk sample coated with a conductive thin film top layer/electrode.

the insulator. The top layer should be firstly thin enough so that the photoelectrons emitted from the substrate can still be detected, and it should also be well connected to the metallic sample holder via some extra structures, for example a wire or a mask made of metal, as indicated by the black solid line in Figure 3.7(d). It should be noted that this geometry actually studies the interface between the insulator and the top layer, rather than the pure information from the insulator. For instance, the Schottky barrier heights at the electrode/dielectric interfaces can be characterized by this method [216].

3.4.3. Thin film depositions and general procedures for XPS measurements

All depositions of thin film top electrodes and the subsequent XPS studies were performed in the DArmstadt Integrated SYstem for MATerials Research (DAISY-MAT). Prior to the depositions, a series of standard treatments were done on the ceramic pellets (grinding, polishing, cleaning, and annealing). Relevant details will be given in Sections 3.4.5 and 3.4.6 together with the procedures of the two in situ XPS methods. This section will only involve the general procedures for thin film depositions and XPS measurements.

The DAISY-MAT system combines a Physical Electronic PHI 5700 multi-technique surface analysis system (Physical Electronics, Inc., USA) and several chambers for thin film deposition with different methods, as shown in Figure 3.8. All chambers are connected together, which provides the possibility to transfer samples in the whole system without breaking the ultrahigh vacuum atmosphere. In this work, only

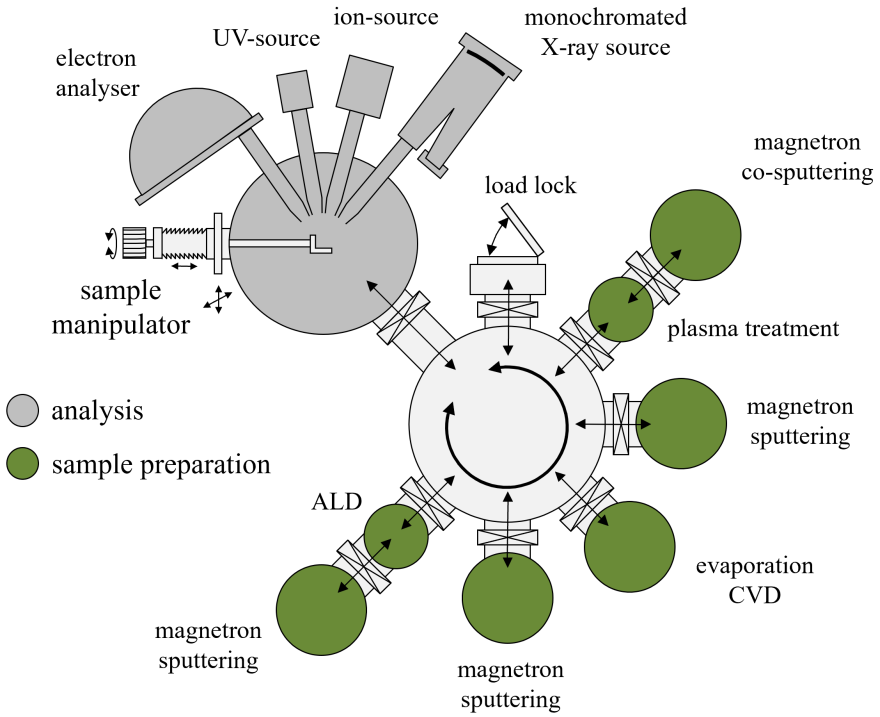

Figure 3.8.: Schematic of the DArmstadt Integrated SYstem for MATerials Research (DAISY-MAT).

two chambers for magnetron sputtering and the XPS part of the system were used.

Two types of top electrode materials were utilized for this work: RuO_2 and Sn-doped In_2O_3 (ITO). The selection of these two oxides has the following four aspects of considerations:

(1) To realize the geometry shown in Figure 3.7(d), inert metals could be good candidates for such thin film top layer. However, a partial reduction of the oxide substrate may already happen during the sputtering of the metal. There are some examples where the formation of metallic Pb was observed at the interfaces of PZT/Cu, PZT/Ag, and PZT/Pt in the course of deposition [217, 218]. This effect is not wanted and would cause inconvenience and confusion in further analysis. To avoid such problem, oxide top layers may be better choices because they are considered to be sufficiently oxidized and have no/less tendency to reduce the oxide substrates.

(2) Both RuO_2 and ITO are known as good electrode materials [219, 220]. RuO_2 is a metallic-like conductor [221, 222] with a conductivity of about 3×10^4 S/cm at room temperature [223]. ITO is an n-type degenerate semiconductor [224] with a conductivity up to 1×10^4 S/cm [225]. Following the strategy shown in Figure 3.7(d), the top layer should be at most 3–5 nm thick in order to make the photoelectrons emitted from the substrate detectable. With such a small thickness, both of these two oxides are still expected to be conductive enough for a valid binding energy determination by XPS interface measurement. However, for the two kinds of in situ XPS experiments conducted in this work, such thin layers were also designed to act as real electrodes of capacitor structures. The quality and validity of these electrodes will be tested and compared in Chapters 6 and 7.

(3) RuO_2 and ITO have obviously different work functions (RuO_2: ∼5.6 eV [226]; ITO: ∼4.5 eV [227]). Using a top layer with relatively high work function, the Fermi level of the substrate

material at the interface could be pulled towards the valence band. Similarly, using a top layer with relatively low work function could lead to the opposite effect. Based on such considerations, energy band alignment studies can be performed [228, 229] and possible pinning behaviors of the Fermi level could be observed.

(4) In ITO, the concentration of free charge carriers (electrons), which determines the electrical conductivity and the Fermi level position, can be tuned by the oxygen content [230–232]. This is because the doping effect of Sn donors can be compensated by excess oxygen, which tends to form electrically neutral defect complexes $(2Sn_{In}^{\cdot}O_i'')^{\times}$ [233, 234]. Such feature makes it possible to modify the Fermi level at the interface between ITO and another substance through the oxidation or reduction of ITO.

More details about the hypotheses or expected effects when using RuO_2 and ITO electrodes in the in situ XPS experiments will be described in Sections 3.4.5 and 3.4.6.

Both RuO_2 and ITO top electrodes were deposited by magnetron sputtering. The RuO_2 films were deposited with a reactive sputtering. A metallic Ru target was used, and the sputtering was performed with a 10 W dc power in a mixed atmosphere of Ar/O_2 (92.5/7.5). No substrate heating was applied during the deposition. The ITO films were sputtered from a ceramic ITO target (10 wt.% SnO_2) with a 25 W radio frequency (RF) power. The sputtering was carried out in pure Ar and the substrate temperature was set to be 350°C or 400°C. All deposition parameters for these two electrode materials are listed in Table 3.4. More detailed information for every sample involved in the two types of XPS experiments will be given in Table 3.5 of Section 3.4.5 and Table 3.6 of Section 3.4.6, respectively.

Table 3.4.: Deposition parameters for RuO_2 and ITO thin film top electrodes.

Deposition parameters	Top electrode materials	
	RuO_2	ITO
Temperature (°C)	25	350 or 400
dc/RF	dc	RF
Power (W)	10	25
Ar flow (sccm)	9.25	6.60
O_2 flow (sccm)	0.75	0
Pressure (Pa)	1.0	0.5
Target-sample distance (cm)	9.4	10.0
Deposition rate (nm/min)	3.0–3.3	3.6–4.3

All XP spectra in this work were measured with a monochromatic Al K_α radiation (1486.6 eV) and at a take-off angle of 45°. A general measuring procedure on each sample includes a survey scan and several detail scans on the specific emissions (the core-levels and the valence band) of interest to us. The survey spectra were measured with a pass energy of 187.85 eV and a step width of 0.8 eV. The subsequent detail spectra for the core-level emissions were acquired with a pass energy of 5.85 eV and a step width of 0.05 eV, leading to an overall energy resolution of about 0.4 eV, which was determined by the Gaussian broadening of the Fermi edge of a sputter cleaned Ag sample. With such a resolution, the accuracy of the acquired core-level binding energies can be <20 meV. All binding energies were

calibrated by using a sputter cleaned Ag standard sample and setting either its Fermi edge to 0 eV or its Ag $3d_{5/2}$ core-level peak to 368.26 eV (Ag $3d_{5/2}$ was used throughout this work). Moreover, the pressure in the XPS chamber was always lower than 2×10^{-9} Torr during the XPS measurements.

3.4.4. Sample geometry, sample holder, and heating stage for XPS measurements

Both types of in situ XPS experiments involved applying voltages and heating inside the XPS chamber. Thus, special sample holders and corresponding sample geometries were used.

There were two kinds of geometries for the relevant ceramic samples, as schematically shown in Figure 3.9(a, b). For both cases, the basic structure of the sample was a ceramic pellet sandwiched by two electrodes, forming a parallel-plate capacitor. The bottom electrode used for applying voltages was a thick Pt layer prepared by sputtering (Quorum Q300T D, Quorum Technologies Ltd., UK). The top electrode, where the XPS was measured, was a thin film of either RuO_2 or ITO, which was prepared by sputtering in DAISY-MAT (see Table 3.4). The thickness of the thin film top electrode should satisfy the two aspects of considerations. On the one hand, the emitted photoelectrons from both the top electrode and the bulk ceramic must be detectable, which required the top layer to be only several nanometers thick. On the other hand, the thickness of the sputtered electrode should ensure a sufficient conductivity as well as a full-established contact. Therefore, the thicknesses of RuO_2 and ITO thin film electrodes were decided to be 5 nm and 3–4 nm, respectively. In the case shown in Figure 3.9(a), an extra thick Pt layer was applied on the top of the RuO_2 or ITO top electrode, so that the electrical potential on the top side of the sample could manifest a more homogeneous distribution. A square-shape hole (2.5×2.5 mm^2) was remained in the center of the Pt layer to allow the XPS detection directly at the interface

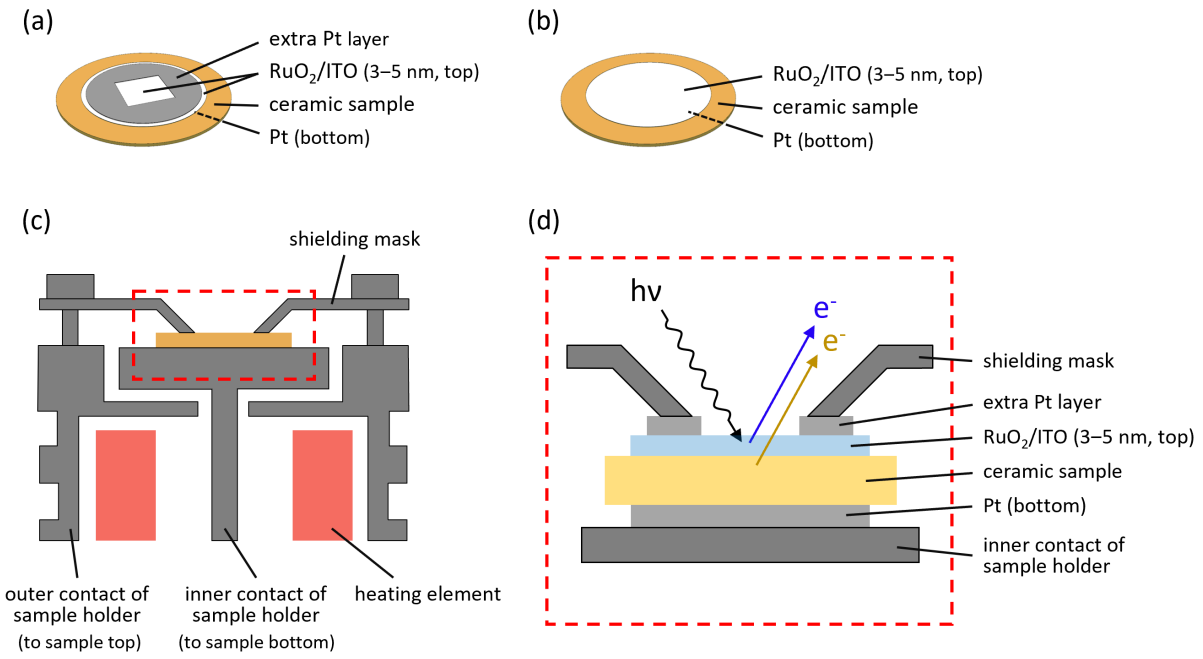

Figure 3.9.: Schematic diagrams of (a, b) sample geometries and (c, d) sample holder for the in situ XPS measurements.

between the ceramic and the RuO_2 or ITO electrode. The special shape of this reinforcement Pt layer was formed by two subsequent depositions between which the specifically designed deposition mask with a radial shielding strip (2.5 mm wide) was rotated by 90°. Despite the usage of the extra Pt layer, the main interface under investigation in such geometry was still the one between the ceramic bulk and the thin film of RuO_2 or ITO. By contrast, the geometry given in Figure 3.9(b) was a simplified version without the extra Pt layer, which was mainly adopted in the first type of in situ XPS experiments. More information about the choice of sample geometries and the details of sample preparations will be described in Sections 3.4.5 and 3.4.6.

Figure 3.9(c) illustrates how the samples were mounted in the stainless-steel sample holder that allowed separate contacts to both electrodes of the sample. The core part indicated by a red dashed rectangle is enlarged and shown in Figure 3.9(d) with more details. The outer and the inner metallic components were connected to the top and the bottom electrodes, respectively. Between the two metallic parts there were Al_2O_3 split bushes for electrical insulation (omitted in the schematic figure). Additionally, a shielding mask also made of stainless steel was used to connect the top surface of the sample (with the electrode) and the outer metallic part of the holder. The latter was always well connected to the ground, so it was possible to measure XPS on the top side of the sample corresponding to the reference of the spectrometer. Besides, by using such a shielding mask, the very high applied electric fields near the edge of the ceramic pellet and between the gap of two metallic components (high voltages up to ca. 930 V have been tried in this work), which could strongly affect the kinetic energy of the emitted photoelectrons, were well screened. As shown in Figure 3.9(d), the shielding mask should connect to the extra Pt layer if the sample geometry in Figure 3.9(a) was used. In the case without the extra Pt layer, the shielding mask was directly connected to the RuO_2 or ITO top electrode.

The sample holder was placed on a heating stage installed inside the XPS chamber, with which high-temperature XPS measurements became possible. The operating temperature of the sample could not be directly measured during the experiments. Therefore, the thermocouple attached to the heating stage was used and the sample temperature was calibrated with a quartz substrate. The construction and assembly of the heating stage were finished during this work. Figure 3.10 shows the photographs of the heating stage and the special sample holder for the in situ XPS measurements.

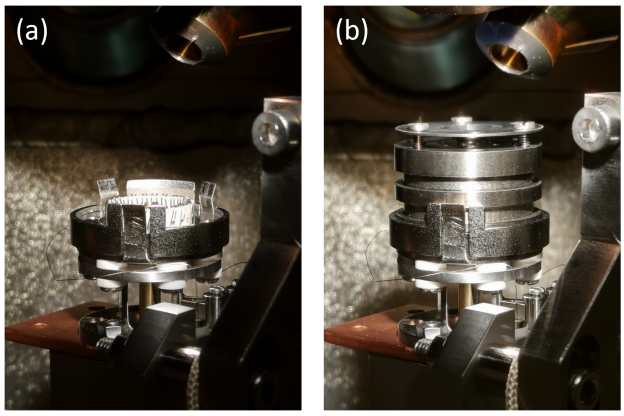

Figure 3.10.: Photographs of the heating stage in the XPS chamber: (a) without and (b) with the sample holder for applying voltages.

3.4.5. In situ XPS at the interfaces with electrochemical oxidation and reduction

Principle and hypothesis of the experiment

According to the theory mentioned in Section 2.4.2, trapping states for electrons and holes can result in the Fermi level confinement within the band gap of a material. Analogous description can be found in electrochemistry where the trapping processes of electrons and holes correspond to the electrochemical reduction and oxidation, respectively [235]. For determining the reduction and oxidation potentials, which are used to predict the stability of substances, XPS technique shows particular advantages because it can measure the chemical state and the Fermi level at the same time. There have been several examples of XPS studies carried out in DAISY-MAT that successfully detected the correlation between the electrochemical reduction and the Fermi level variation, including the observation of Fe^{2+} in α-Fe_2O_3 after the deposition of ITO top layer [236], Bi^0 in $BiVO_4$ [237] and both Bi^0 and Fe^{2+} in $BiFeO_3$ [238] after water exposure treatment on the surfaces. These XPS studies were based on the samples that were either sufficiently conductive or in the form of thin film deposited on conductive substrate (see Figure 3.7(a, c)). However, this is not possible for the present work on the PZ-based FEs and AFEs because we have only insulating ceramic bulk samples. Therefore, a new strategy for in situ XPS experiments was established. It should be noted that the trapping states and the corresponding Fermi level confinement/limitation addressed in this work can be used to describe the bulk properties of the dielectrics even though the experimental method itself was interface-based.

The basic principle and hypothesis of this experiment are schematically shown in Figure 3.11. The main idea was to modify the Fermi level position at the electrode interface of a solid electrolyte cell where the ceramic pellet acted as the electrolyte. The top electrode of the cell was a thin film whose interface with the bulk ceramic was utilized for XPS measurement, and the bottom electrode was always a thick Pt layer. Figure 3.11(a, c) illustrates two operating cases of the cell where the top electrodes are used as cathode and anode, respectively. It has been already mentioned in Section 2.4.1 that certain amounts of oxygen vacancies are usually believed to exist in PZT materials even if they are donor-doped. Hence, it is expected that the oxygen vacancies/ions in the bulk ceramic can migrate towards the cathode/anode under an applied electric field and at a sufficiently high temperature that makes the ionic species mobile, as during the process of resistance degradation. Using the case in Figure 3.11(a) as an example, when the thin film top electrode is used as cathode, the migration of the oxygen species will lead to a state with a concentration gradient within the cell, namely an oxygen-poor (reduced) cathodic region on the top plus an oxygen-rich (oxidized) anodic region at the bottom. In this case, the XPS can be used to monitor the reduction process at the top electrode interface. Also, it should be noted that such process could reduce the dielectric near the cathodic interface, the cathode, or both of them [148, 239–241]. In the schematic structure in Figure 3.11(a), the cathodic region is then labeled as “reduced zone”. Corresponding band diagram for the top electrode interface under the cathodic polarization is given in Figure 3.11(b), where the Fermi level position in the cathode material is assumed to rise if the cathode itself is reduced to some extent (see the red arrow). It is known that the Fermi level at the interface between an insulating dielectric and a conductive electrode should be fixed by the Fermi level of the latter. Therefore, during the operation of the electrolyte cell, the upward shift of the Fermi level position of the cathode layer by its reduction is expected to raise the Fermi level of the dielectric material (at least the narrow part adjacent to the cathodic interface). According to the theory related to Figure 2.13, we assume that the Fermi level of the dielectric has an accessible range within its band gap whose upper and lower limits are decided by trap levels which involve valence state transitions on host ions, as labeled with “transition level 1” and “transition level 2” in Figure 3.11(b), respectively. In the course of a continuous reduction at the cathodic interface, the upper limit of the Fermi level (“transition level

1") may be determined at the position where the Fermi level variation shows a clear pinning effect accompanied by a change in the valence state of one of the constituent elements. Analogous to the case that identifies the upper limit by studying the cathodic interface, the process to explore the lower limit of the Fermi level of the dielectric is shown in Figure 3.11(c, d), where the Fermi level in the anode should drop due to the oxidation process until approaching a pinning position ("transition level 2").

Similar in situ XPS experiments based on solid electrolyte cells can be found in the literature as well [240, 242–244]. In these reports, the top electrode materials were studied by XPS, while the solid electrolyte, usually a single crystal of Yttria-stabilized zirconia (YSZ), only acted as an ionic conductor with mobile oxygen species. Differently, this work is going to investigate the electrolyte material within the electrochemical cell by utilizing the feature of the top electrode. Another difference between the present work and the ones reported in the literature is the type of XPS technique. The electrochemical studies in Ref. [240, 242–244] mainly utilized ambient pressure XPS (AP-XPS) or near ambient pressure XPS (NAP-XPS). By contrast, only the conventional XPS operated in ultra-high vacuum (UHV-XPS) has been used in the present work. Thus, possible effects of the high vacuum on both the top electrode and the electrolyte should be particularly taken into account.

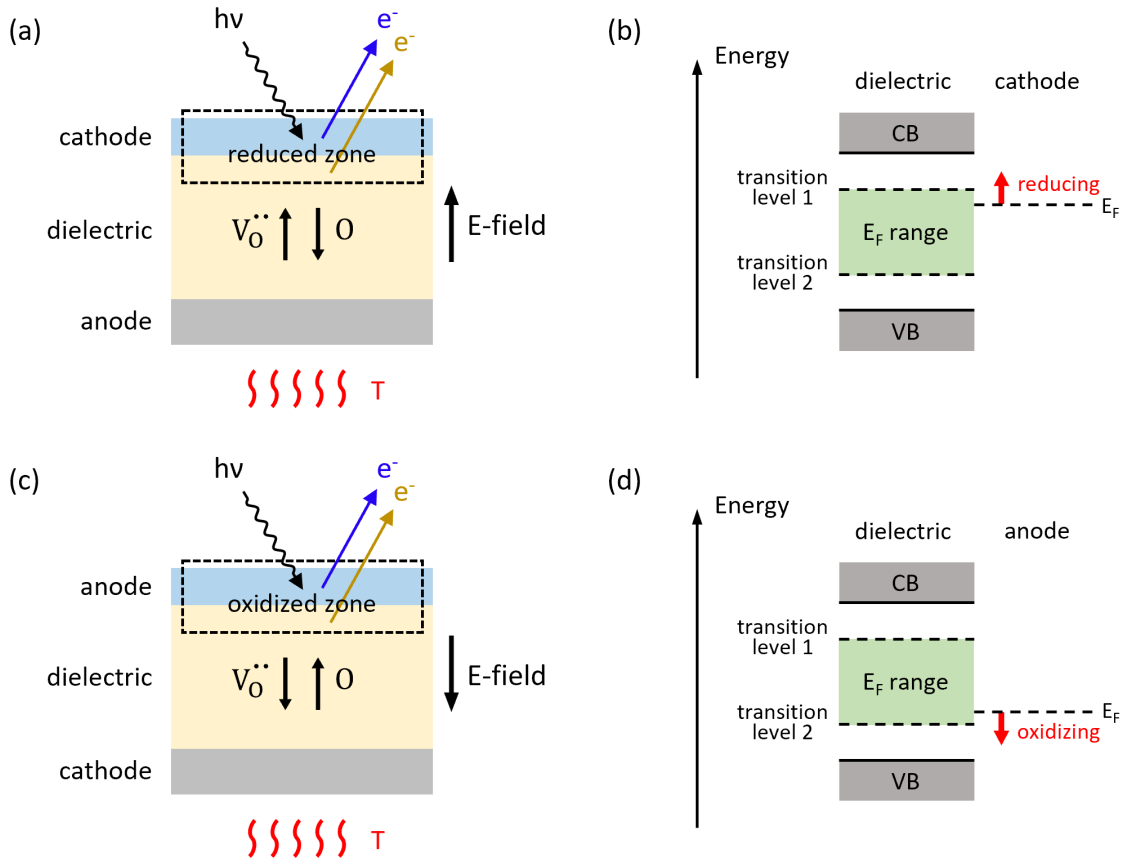

Figure 3.11.: Principle and hypothesis of the in situ XPS experiments with electrochemical reduction and oxidation that determine the trap states and the Fermi level limitations of dielectric bulk materials. (a, b) Exploring the upper limit of Fermi level using a low-work-function top electrode with cathodic polarization; (c, d) exploring the lower limit of Fermi level using a high-work-function top electrode with anodic polarization.

Experimental procedures

Three PLZST-related compositions were selected for this experimental method: C09, X01, and A02. Composition C09, as a standard room-temperature AFE material in this work, was expected to have very low $[V_O^{\cdot\cdot}]$ due to the donor doping. Compositions X01 and A02 modified the net doping concentrations based on composition C09, which should lead to obvious changes in $[V_O^{\cdot\cdot}]$. Because the mobile oxygen species is the core of operating the electrochemical cell designed for this study, the selected three compositions may give a good comparison with respect to the effects of oxygen transport, scientifically and technically. Apart from the PLZST-related compositions, several other ceramic samples were used for further comparisons, including PIC 151, PZT53/47, and PMN.

The sample geometry for this part basically followed the style in Figure 3.9(b). The ceramic pellets were firstly ground with sandpaper (#1200, #2400) into a suitable thickness of 0.15–0.26 mm. After necessary cleaning and annealing steps on the pellets, the top electrodes were deposited by magnetron sputtering in DAISY-MAT. ITO with a low work function was chosen to be the top cathode of the electrochemical cell for exploring the upper limit of the Fermi level variation because it was expected to create a relatively high starting point of the Fermi level position at its interface with the bulk dielectric material, which might render the further electrochemical reduction at the cathodic region easier to happen (corresponding to the case in Figure 3.11(a, b)). Similarly, using the high-work-function RuO_2 as the top anode material may benefit the lower limit identification due to the relatively low starting point of the Fermi level at the interface (corresponding to the case in Figure 3.11(c, d)). Prior to the

Table 3.5.: Information for top electrode preparations of the samples used for the in situ XPS experiments at the interfaces with electrochemical oxidation and reduction.

Sample No.	Bulk material	Surface cleaning	Top electrode deposition		
		Temp. (°C)	Material	Temp. (°C)	Thickness (nm)
BHX01X01	X01	350	RuO_2	RT	5
BHC09X13	C09	350	RuO_2	RT	5
BHA02X01	A02	350	RuO_2	RT	5
BHA02X02	A02	350	RuO_2	RT	5
BHPZT41	PIC 151	350	RuO_2	RT	5
BHPZT46	PIC 151	350	RuO_2	RT	5
BHX01X02	X01	350	ITO	350	4
BHC09X14	C09	350	ITO	350	4
BHA02X04	A02	350	ITO	350	4
BHPZT42	PIC 151	350	ITO	350	4
BHPZT43	PIC 151	350	ITO	350	4
PH004	PZT53/47	400	ITO	400	4
BHPMN8_10	PMN	350	ITO	350	4

sputtering of ITO and RuO_2 top layers, a step of surface cleaning was always carried out inside the sputter chamber by heating the ceramic samples in O_2 (0.5 Pa, 350°C–400°C, ca. 1 hour) to get rid of adventitious carbon species. The sputtering parameters for the two top electrode materials have been given in Table 3.4. A more detailed list of all relevant samples and the information of their top electrode preparation are shown in Table 3.5. After the deposition of top sides in DAISY-MAT, the ceramic samples were taken out of the system and the bottom Pt electrodes were subsequently prepared with the sputter coater Quorum Q300T D (Quorum Technologies Ltd., UK).

Figure 3.12 shows the schematic circuit for this type of in situ XPS measurements. The top electrode of the sample was used for XPS, so it was connected to the ground (the reference level of the spectrometer) via an picoammeter (Keithley 6487, Tektronix, Inc., USA). The dc bias was applied by the built-in voltage source of the picoammeter to the cell through the bottom electrode. This configuration ensured synchronous measurements of XPS and the leakage current of the sample. Actually, the obtained current signal consisted of two parts: the leakage current through the cell and the emission current due to X-ray illumination. More details will be displayed in the relevant results in Chapter 6.

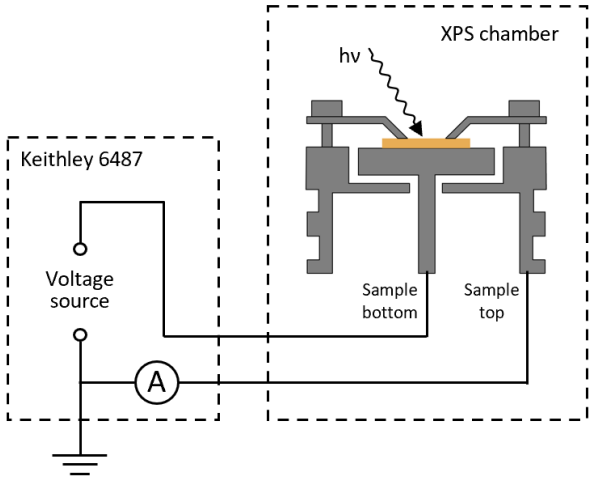

Figure 3.12.: Schematic diagram of the setup used for the in situ XPS at the interfaces with electrochemical oxidation and reduction.

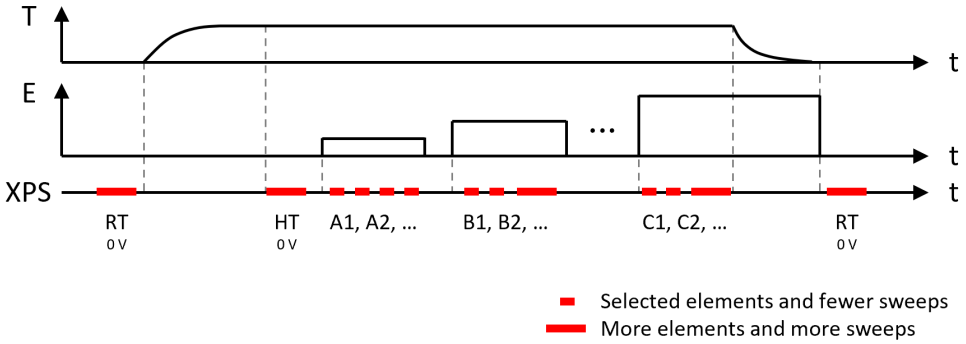

Figure 3.13.: Procedure of the in situ XPS at the interfaces with electrochemical oxidation and reduction.

Figure 3.13 demonstrates the procedure of a complete process of this operando method. Three aspects should be controlled simultaneously: the sample temperature inside the XPS chamber, the external electric field applied between the top and bottom electrodes, and the XPS acquisition. The times when XPS was running are indicated by thick red lines along the time axis. First of all, a careful XPS measurement should be carried out at room temperature without any applied voltage in order to know the initial states of all elements of interest. After that, the sample was heated up to the desired temperature. It usually took ca. 30 minutes for the heating stage inside the XPS chamber to reach a temperature that was sufficiently close to the setpoint (200°C–300°C) when the heating current was fixed. In this work, we always waited for another 30 minutes to get a more stable condition of the sample. When the temperature was ready, a complete XPS measurement with all relevant elements was done again without electric field. This step might reveal the effect of heating at the interface. Subsequently, a series of electric fields were applied to the sample and the corresponding currents flowing through the cell were recorded meanwhile by the picoammeter. As shown schematically in Figure 3.13, the field should rise stepwise. It is necessary to note that short interruptions of the electrical measurement were required in order to change the applied field. During each current acquisition, XPS measurement was carried out one after another until a higher field was selected. Two modes of XPS measurements were recommended: (i) a complete and careful scanning of all relevant core level emissions as previously done when the sample became relatively stable; (ii) only doing fewer sweeps on selected elements of interest in order to shorten the acquisition time, which could help to monitor a fast development of the situation more easily. Choice between these two modes depended on different samples and external conditions. Figure 3.13 just gives an example, but some flexibility was always required in real practice. Once all high-temperature tasks were finished, the heater was switched off. During cooling-down, the electric field should be maintained until the sample reached room temperature. Lastly, the XPS measurement was carried out once more at room temperature after the removal of bias.

In addition, every XPS step, marked by the thick red lines in Figure 3.13, is labeled with a letter followed by an ordinal integer number, which is the general way of naming spectra throughout all such experiments in this work. The letters denote the applied electric fields, and the numbers correspond to the XPS sequence. It should be noted that all core-level emissions within one XPS acquisition are assumed to take place at the same time. For example, there could be two core levels, first Pb 4f and then Zr 3d, measured within the same acquiring step of “A1”. They will be technically regarded as synchronous for simplification of timekeeping although the Zr 3d is actually scanned later than the Pb 4f to some degree. One should keep this in mind, especially when two successive XPS measurements need to be compared and the previous one lasts for a long time.

All results belonging to this experimental method will be given in Chapter 6.

3.4.6. In situ XPS at the interfaces with ferroelectric polarization

Principle and hypothesis of the experiment

In contrast to the previous in situ XPS approach introduced in Section 3.4.5, which is used to identify the Fermi energy limits of the materials, the experiment in this section will focus on the bound and free charges located around the electrode/dielectric interfaces within FE- or AFE-based capacitors, which can be regarded as a real interfacial behavior. The principle of this experimental method is mainly based on the screening theory described in Section 2.6.

It is expected that a step-like variation of electrostatic potential can be established at the electrode/FE interface when the FE-based capacitor has imperfect screening. This kind of potential modification depends on the applied electric field across the capacitor and it can change the SBHs according to Equations 2.39 and 2.40. Since XPS is usually an appropriate technique to characterize Schottky barriers, here we will develop another in situ XPS approach with which the field-dependent SBH modifications for both FE- and AFE-based capacitors can be studied. Based on Figure 2.20, the expected variations in XP spectra, principally in the form of binding energy shifts, of the elements belonging to the top electrode and the FE bulk material at five steps along a typical P–E loop are schematically demonstrated in Figure 3.14. Again, a simplified capacitor model is used here in which the FE layer is assumed to be a single

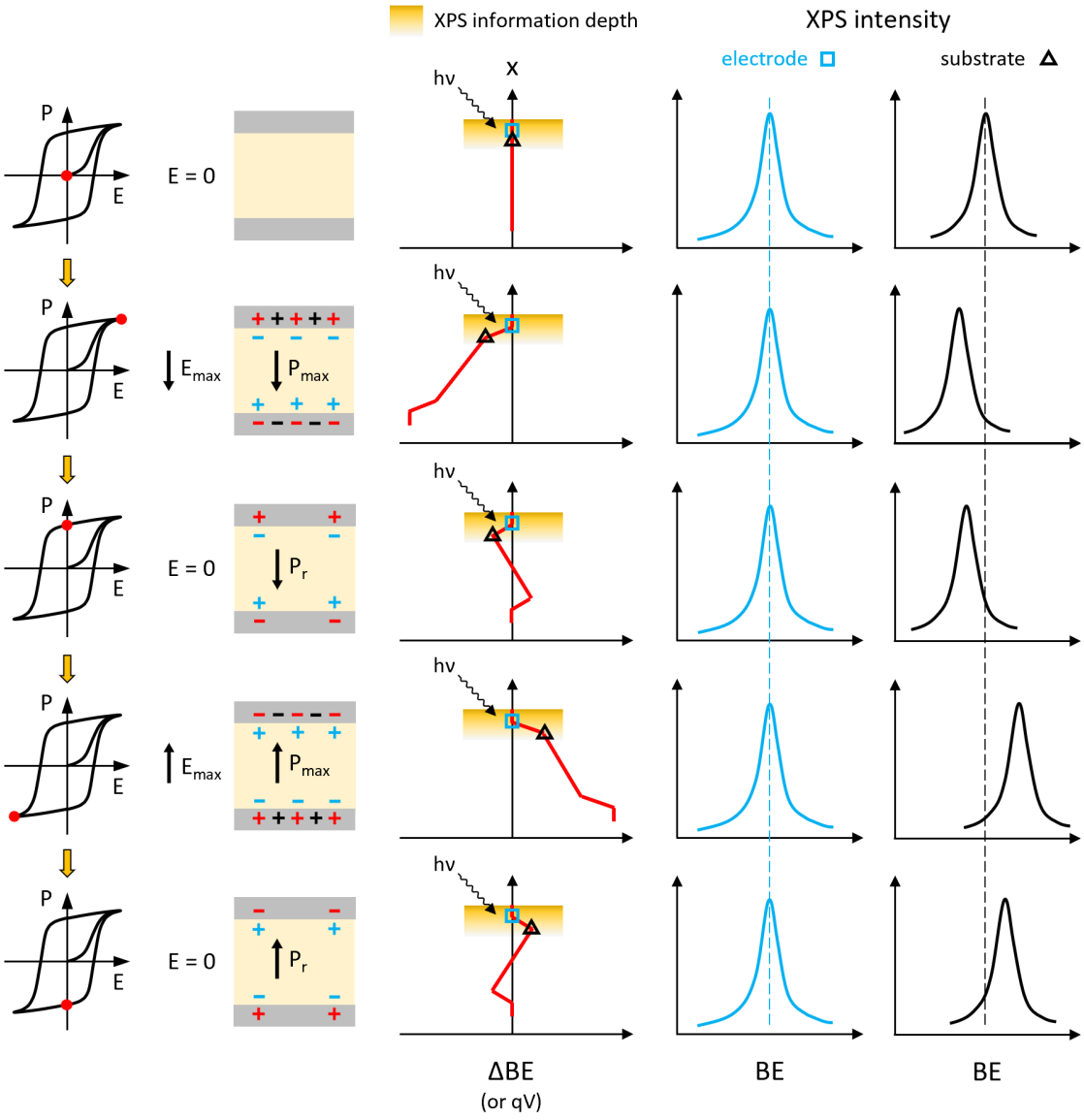

Figure 3.14.: Field-dependent electric potential profile along the thickness direction of a FE-based capacitor and its impact on the binding energies measured by XPS at the top electrode interface. The capacitor model is simplified by assuming a homogeneous polarization in the FE layer. Only the interface configuration with imperfect screening is considered here.

domain with homogeneous polarization. Ideally, the shift of binding energies should be proportional to the change in electric potential along the thickness of the capacitor structure (see the ΔBE–x or qV–x plots). When the X-ray illuminates the top side of the capacitor, information from a certain depth (ca. 10 nm) can be detected by XPS, indicated by the yellow bars in the ΔBE–x plots. Within such an XPS information depth, the top electrode (3–5 nm) is always electrically connected to ground (the reference of spectrometer), which fixes its electric potential and therefore no binding energy shift is expected (see the blue squares). By contrast, the uppermost layer of the FE substrate, which is closely contacted with the top electrode, will manifest a shift in binding energy due to the step-like potential modification if the effective screening length λ_{eff} is located within the depth of the remaining several nanometers for the XPS detection (see the black triangles). The last two columns on the right side of Figure 3.14 schematically show the expected shifts of XPS emissions corresponding to the situations given in the ΔBE–x plots. For example, when the top electrode is under anodic polarization (the case in the second row), the XPS emission of the FE material should shift toward lower binding energy. By this means, any FE polarization existing in the vicinity of the top electrode interface could be detected by the XPS technique. It should be noted that the binding energies are plotted here in such a way where higher values are on the right side of the axis. However, all XPS emissions in the result chapters will be plotted the other way around.

Experimental procedures

This in situ XPS method has been used in DAISY-MAT to study the screening behaviors of BTO single crystals [245, 246]. Similar operando XPS studies with in situ control of polarization were also reported for BTO thin films [247] and relaxor FE PMN-PT single crystals [248]. In this work, the same experimental strategy as that in Ref. [245, 246] will be applied to both FE and AFE ceramics for a comparison. The main technical difficulty for the studies on AFE ceramics is the relatively higher electric field that is needed to trigger the AFE-to-FE phase transitions. Hence, an upgraded equipment was utilized here.

Three PLZST compositions were selected for this experimental method: C09, C10, and C11. These three compositions were expected to display a gradual transition in the shape of P–E loop from AFE to FE at room temperature (see Section 4.1.1), which were intended for a comparison of the screening behaviors between the AFE and FE materials, or more accurately, between the FE phase induced by a reversible AFE-to-FE transition and the FE phase that can stably stay in a FE state when the external electric condition changes. Apart from the three PLZST compositions, the commercial PZT composition PIC 151 was also used in this work as a reference material. Besides, several PMN-PT ceramics (provided by Prof. Dr. Tadej Rojac of Jožef Stefan Institute, Ljubljana, Slovenia) were studied with the same method in the Bachelor thesis of Johanna Steinmann [249].

The sample geometry used this part basically followed the style in Figure 3.9(a) except for the cases of PIC 151 with ITO top electrode which followed Figure 3.9(b). The ceramic pellets were firstly ground with sandpaper (#1200, #2400, #4000) and then polished with polishing disk and diamond paste (6μm, 3μm, 1μm, 1/4μm). The thicknesses of the ceramic pellets were 0.12–0.16 mm, which depended on the needed electric fields, the maximum operating voltage of the voltage source, and the mechanical strength of the ceramic disks. After standard cleaning and annealing steps on the as-polished pellets, the top electrodes (RuO_2 or ITO) were prepared by magnetron sputtering technique in DAISY-MAT. A surface cleaning step was always carried out right before each film deposition by heating the ceramic sample in O_2 (0.5 Pa, 350°C–400°C, ca. 1 hour) inside the sputter chamber. The sputtering parameters for RuO_2 and ITO top electrodes can be found in Table 3.4. Table 3.6 gives a detailed list of all relevant

Table 3.6.: Information for top electrode preparations of the samples used for the in situ XPS experiments at the interfaces with ferroelectric polarization.

Sample No.	Bulk material	Surface cleaning	Top electrode deposition			
		Temp. (°C)	Material	Temp. (°C)	Thickness (nm)	Extra Pt layer
BHPZT13	PIC 151	350	RuO_2	RT	5	yes
BHC11X10	C11	350	RuO_2	RT	5	yes
BHC10X03	C10	350	RuO_2	RT	5	yes
BHC09X09	C09	350	RuO_2	RT	5	yes
BHPZT30	PIC 151	350	ITO	350	3	no
BHPZT31	PIC 151	350	ITO	350	3	no
BHC11X07	C11	400	ITO	400	4	yes
BHC09X05	C09	400	ITO	400	4	yes

samples in this part and the information of their top electrode preparation. After the deposition of RuO_2 or ITO layer, the bottom Pt electrodes and the reinforcement Pt layers on the top sides were prepared with the sputter coater Quorum Q300T D (Quorum Technologies Ltd., UK).

Figure 3.15 gives the schematic diagrams for this type of experiments, where two measuring modes are involved. The first mode is the P–E mode, which was based on the Sawyer-Tower circuit shown in Figure 3.3 and utilized to acquire the P–E hysteresis loops inside the XPS chamber. The second mode is the dc mode, with which a constant dc bias can be applied to the sample during the operation of XPS. As the X-ray photoemission took place on the top side of the sample, the top electrode should be sufficiently well connected to the ground (the reference of spectrometer). A moderate resistor R_{pr} (100 kΩ) was used here to protect the circuit against the sudden breakdown of the sample when a very high voltage was operating. This protective resistor was small enough to ensure both an accurate determination of binding energies and a nearly complete voltage drop on the highly resistive ceramic sample, which have been verified throughout relevant experiments. Different from the top electrode of RuO_2 or ITO, the bottom Pt electrode was always used for applying high voltages (both polarities) that generated and controlled electric fields through the capacitor and changing the polarization states within the dielectric. The high-voltage amplifier used in both modes in Figure 3.15 was model 1HVA24-BP1-F (Advanced Energy Industries, Inc., USA), which supported dc voltages up to $\pm$1 kV. The generation and acquisition of electric signals via the external circuit were realized by the I/O device USB-6211 combined with a LabVIEW program (National Instruments, USA). Moreover, it is also possible to carry out such in situ XPS measurements at elevated temperatures by using the heating function of the newly installed sample stage described in Section 3.4.4.

Figure 3.16 demonstrates the procedure of a complete process of this operando method, where the thick red lines along the time axis indicate the times when XPS was measured. First of all, a careful XPS measurement including both survey and detail spectra was carried out in the dc mode but with no bias applied, which characterized the initial or unpoled state of each sample. Secondly, the setup was switched to the P–E mode and the hysteresis loops were measured with triangular waveform. Usually, at least two cycles of P–E measurement were needed to polarize the sample into a “developed” state. Subsequently, a series of XPS acquisitions were performed in the dc mode under a sequence of electric

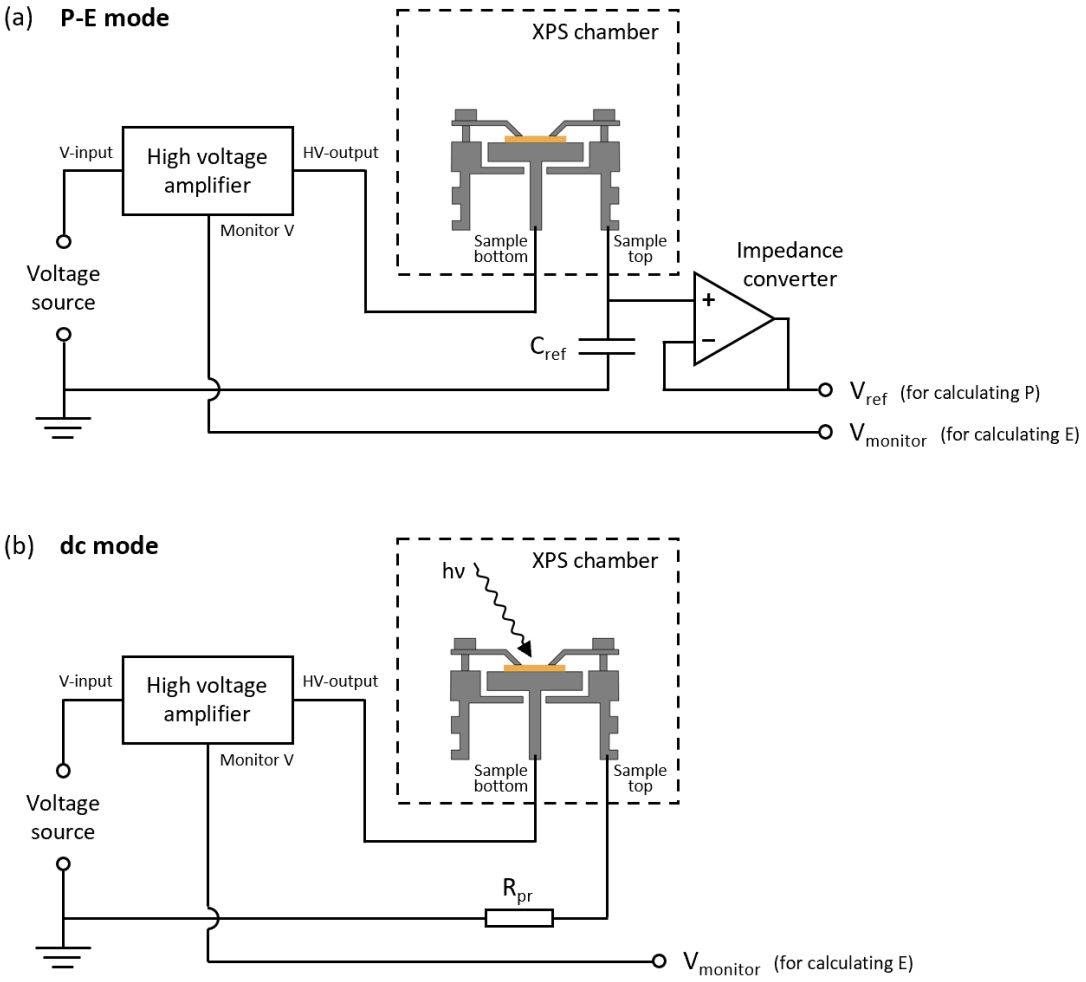

Figure 3.15.: Schematic diagram of the setup used for the in situ XPS at the interfaces with ferroelectric polarization: (a) *P–E* mode; (b) dc mode.

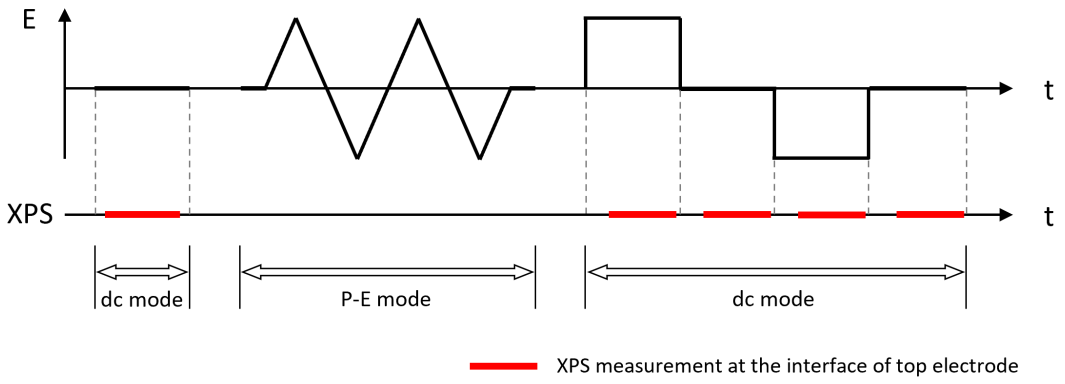

Figure 3.16.: Procedure of the in situ XPS at the interfaces with ferroelectric polarization.

fields that correspond to $P_{\mathrm{max}} \rightarrow P_{\mathrm{r}} \rightarrow -P_{\mathrm{max}} \rightarrow -P_{\mathrm{r}}$. Within each step, the core-level scanning of XPS was always started at least one minute later than the moment when the applied voltage was changed, so that the charging or discharging effect of the capacitor on the measured spectra was expected to be sufficiently reduced.

All results belonging to this experimental method will be given in Chapter 7.

3.5. Other characterizations

Apart from the experimental methods described in Sections 3.2–3.4, the PLZST ceramic samples have also been shared within the LOEWE project FLAME (funded by the State of Hesse, Germany) for other characterizations. Two relevant doctoral dissertations are listed here for reference:

(1) Ding, Hui. *Domain morphology and atomic structure of antiferroelectric perovskites* PhD thesis (Technische Universität Darmstadt, 2022).
Domain morphology and atomic structure of PLZST compositions C09, C10, and C11 characterized by transmission electron microscopy [250].

(2) Egert, Sonja. *Local structure-property relations in antiferroelectric oxides* PhD thesis (Technische Universität Darmstadt, 2022).
Local Structure of compositions X01, C00, C08, C09, and C11 characterized by nuclear magnetic resonance spectroscopy [251].

4. Basic Characterizations of Ceramic Samples

After the synthesis of ceramic pellets, several basic characterizations have been carried out based on the procedures given in Section 3.2. This chapter will focus on the main dielectric properties (hysteresis loops in Section 4.1 and dielectric permittivities in Section 4.2), the crystalline structures examined by XRD (Section 4.3), and the microstructures characterized by SEM (Section 4.4). Other necessary features of the as-sintered samples are given in the appendices, including the appearance and densification of ceramic pellets (Appendix A.4). In addition, some extended results of the above-mentioned sections can be found in the appendices as well (Appendices A.1, A.2, and A.3). Table 4.1 is a list of relevant data of all compositions sorted by different methods. As most of the compositions have been reported in the literature, the results in this chapter are given basically just for reference.

Table 4.1.: List of all methods of basic characterizations on the ceramic samples sintered for this work.

Method	Composition (Section in this work)
P–E & S–E loop (room temperature)	all C-, X-, and A-series (Section 4.1.1 & Appendix A.1)
P–E (varying temperature)	C09, C10, C11 (Section 4.1.2); X01, X02, X03 (Appendix A.1)
ε_r–T & $\tan\delta$–T	all C-, X-, and A-series (Section 4.2.1 & Appendix A.1)
ε_r–E (varying temperature)	C09, C10, C11 (Section 4.2.2)
XRD on unpoled pellets	all C-, X-, and A-series (Section 4.3 & Appendix A.2)
XRD on poled pellets	C09, C10, C11 (Appendix A.2)
XRD on powders	C08, C09, C10, C11 (Appendix A.2)
SEM	C00, C09, C11, X01, A02 (Section 4.4 & Appendix A.3)
Radial shrinkage	all C-, X-, and A-series (Appendix A.4)
Density by Archimedes' method	all C-, X-, and A-series (Appendix A.4)

4.1. Hysteresis loops

4.1.1. Hysteresis loops at room temperature

Representative room-temperature P–E loops of all synthesized compositions are displayed in Figure 4.1. All loops shown here followed the similar measuring procedure. A bipolar triangular waveform

with small amplitude was applied to the sample first for a test. If the used field was not high enough to open a loop, the amplitude would be increased stepwise. Every sample was annealed before the first test to remove the remanent polarization induced in any previous measurement, but there was no more heat treatment during the stepwise cycles with increasing amplitude. Compositions C00, C04,

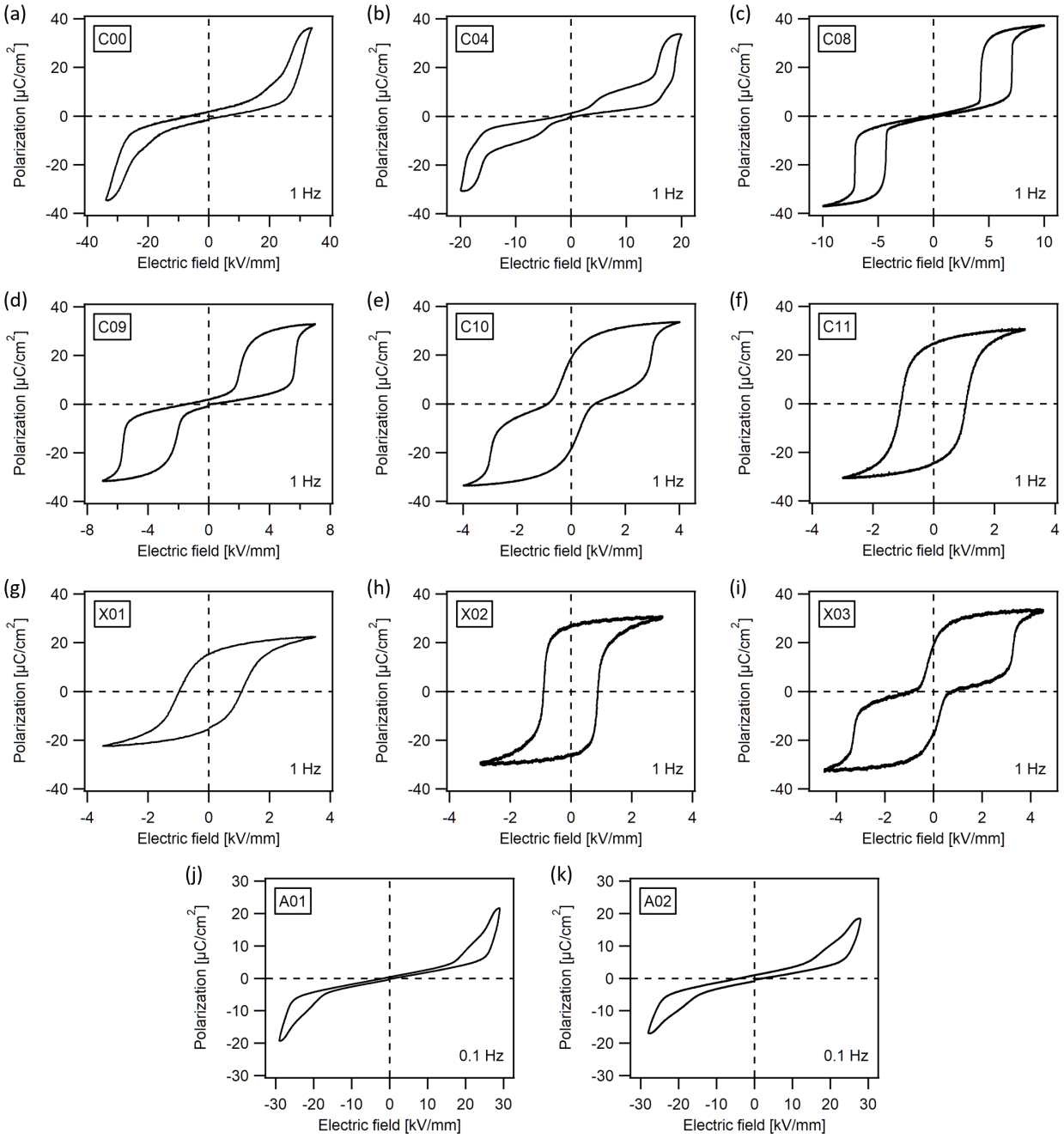

Figure 4.1.: Polarization versus electric field hysteresis loops of all C-, X-, and A-series compositions at room temperature. The C- and X-series samples were measured at 1 Hz and the A-series were measured at 0.1 Hz.

A01, and A02 were measured until breakdown, and their last effective loops before the breakdown are plotted in Figure 4.1. For the other compositions, the measurements were finished without getting a final breakdown because sufficiently opened loops had already been observed. Figure 4.1 only displays the loops of their last steps. Besides, there is another general concern in this figure about the difference between the first and the second loops successively measured at the same field if the sample has never suffered such a high field before. This phenomenon has been mentioned in Section 2.2.2, and it can be usually observed in both FEs and AFEs. In this work, the first and the second loops will be described as "initial" and "developed", respectively. Those initial loops are not included in Figure 4.1 because the applied fields were stepwise increased. With such procedure, the information of the initial states of the samples was lost. Therefore, only the fully developed loops are plotted at present. As for the initial ones, there will be separate description later in this section. In addition, the samples of C04, C08–C11, and X01–X03 belong to scenario (1) described in Section 3.2.1, while C00, A01, and A02 should follow scenario (2). Sample preparations of these two groups were therefore different according to Table 3.3. Furthermore, a direct comparison of the developed P–E loops within each series can be found in Figure A.1 in Appendix A.1, where the compositions belonging to the same series are plotted together.

C-series have the same La and Zr contents, so the effect of the Ti/Sn ratio can be studied. The opened loops in Figure 4.1(a–f) show a clear tendency. Composition C11, with the highest Ti concentration (11% on the B-site), possesses a stable FE loop once it is fully developed. With the decrease of Ti content, the samples tend to become AFE. Composition C09 (9% Ti on the B-site) already shows a complete AFE hysteresis behavior. The forward AFE-to-FE transition fields (positions with the largest slopes) increase remarkably when the Ti content is reduced, from about 5.7 kV/mm for composition C09 to about 31.5 kV/mm for composition C00 (no Ti). Composition C10 exhibits a so-called pinched loop which is normally regarded as an intermediate state between AFE and FE. According to the PLZST phase diagram given in Figure 3.1 [23], the phase boundary between A_T and $F_{R(LT)}$ should be located at the point of 10–11% Ti in the case of 75% Zr, which is basically consistent with our observations. Moreover, the two Ti-poor compositions C00 and C04 manifest double loops with the feature of so-called field-induced multiphase transitions where the ascending segment in Quadrant I shows two different slopes and the descending part shows distinguishable steps (same in Quadrant III but with opposite signs). This is in accordance with the studies in the literature on similar Ti-poor compositions in PLZST [92] and PNZST [252]. Such phenomenon has also been reported in PLZT [253] and PZ [254]. Additionally, the dependence of the AFE-to-FE transition field on the Ti content within the C-series is given in Figure A.2 in Appendix A.1.

X-series keep the same B-site ratios as that of composition C09 but modifying the La content. As can be seen in Figure 4.1(d, g–i), with a decreasing La content, the transition from the AFE loop of composition C09 (2% La on the A-site) to a typical FE loop of composition X01 (no La) can be observed. Between C09 and X01, composition X02 with 1% La shows a stable FE loop once it is fully opened, analogous to the case of C11. Also, pinched loop like composition C10 is found in X03 with 1.5% La. By comparing X- and C-series, a preliminary speculation could be that the A-site aliovalent and the B-site isovalent modifications probably possess similar influences on the balance between the AFE and the FE phases.

Compositions A01 and A02 are doped with Fe based on composition C00, so they are expected to have more oxygen vacancies and be electrically leakier than C00. The possible effects of leakage within the bulks on the AFE features can thereby be investigated. During the P–E loop tests, these two compositions were very easy to encounter breakdown once the AFE-to-FE transition fields were approached, which indicated the contribution either from a bulk leakage or from an issue on the electrode interface. In order to determine whether these two compositions are AFEs, both higher and lower frequencies were

utilized in their P–E loop measurements, compared to the normal value of 1 Hz for the other samples. A lower frequency (0.1 Hz) turned out to be a better choice for measuring the loops of compositions A01 and A02, as shown in Figure 4.1(j, k). On the one hand, lowering the measuring frequency would decrease the charging and discharging currents at the electrodes. On the other hand, it extends the time when the electric field is applied to the sample, which could enlarge the leakage effect through the whole sample. If a lower frequency can help to avoid breakdown, it may imply that the breakdown in the A-series samples could be more related to an interface issue than to a bulk leakage. Concerning the measured P–E loops of compositions A01 and A02, it should be noted that the scales of polarization in Figure 4.1(j, k) are different from the others. Apparently, these two loops are not fully opened, which makes the determination of transition fields difficult. However, it can be obviously concluded that the A-series are still AFE and the shapes of their loops are quite similar to that of composition C00, showing the characters of the above-mentioned field-induced multiphase transition.

Figure 4.2 displays the S–E loops measured together with the room-temperature P–E loops according to the description of scenario (1) in Section 3.2.1. Compositions C00, A01, and A02 are not included

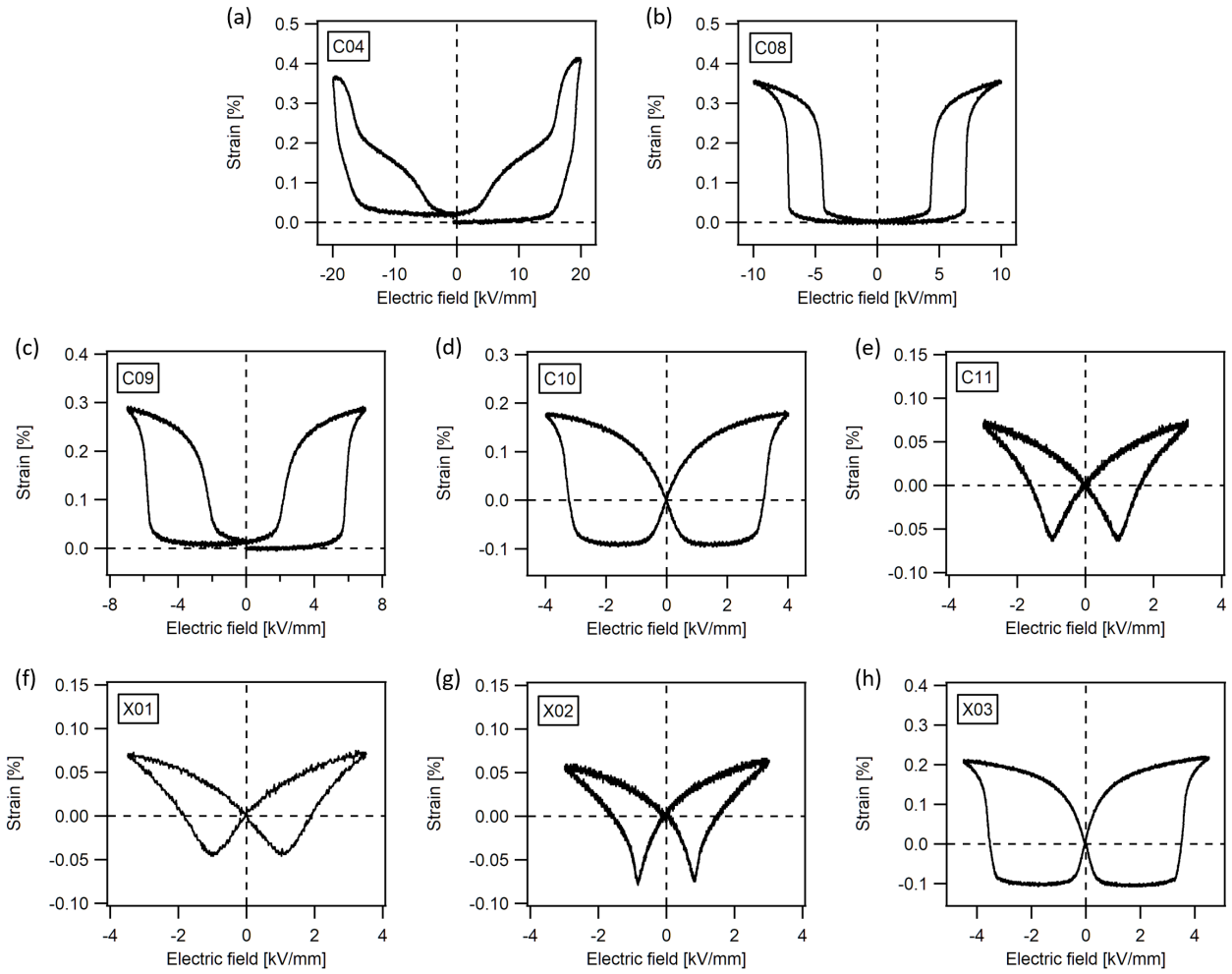

Figure 4.2.: Longitudinal strain versus electric field hysteresis loops of selected C- and X-series compositions at room temperature. All loops displayed here were measured at 1 Hz.

here because their special sample geometry was incompatible with the holder for longitudinal strain measurement (see scenario (2)). By taking the strain at zero electric field as the new origin, all loops are shifted along the vertical direction. As can be seen, the shapes of S–E loops correspond well to the P–E features plotted in Figure 4.1. Compositions C08 and C09 show the typical shapes consistent with the schematic in Figure 2.5(b), and composition C04 exhibits a clear AFE strain feature of the field-induced multiphase transition [252, 253]. By contrast, typical S–E loops of FE materials are obtained for compositions C11, X01, and X02 after they are sufficiently opened. Compositions C10 and X03, which are located between AFE and FE states, also possess an intermediate shape in S–E loops where the residual strain does not drop to a negligibly low level when the decreasing field already approaches zero. Moreover, the magnitudes of the longitudinal strain (from minimum to maximum) can reach about 0.3–0.4% for the AFE compositions, while the ones for the FE-like loops mostly remain not greater than 0.15%. It can also be imagined that the strains would be a little larger if rigorous saturations in the field-induced polarization can be realized without breakdown. Nevertheless, the magnitudes of strain shown in Figure 4.2 are within a reasonable range for these compositions compared to the values in the literature [23, 255].

Frequency dependence of hysteresis behaviors

As for the hysteresis loop measurement, there are two other important points with respect to the material properties of FEs and AFEs: the frequency dependence, and the comparison between the initial and the developed states.

Figure 4.3 gives some examples about the P–E and S–E loops acquired at different frequencies. In Figure 4.3(a, d), it can be seen that composition C09, which has a standard AFE hysteresis behavior,

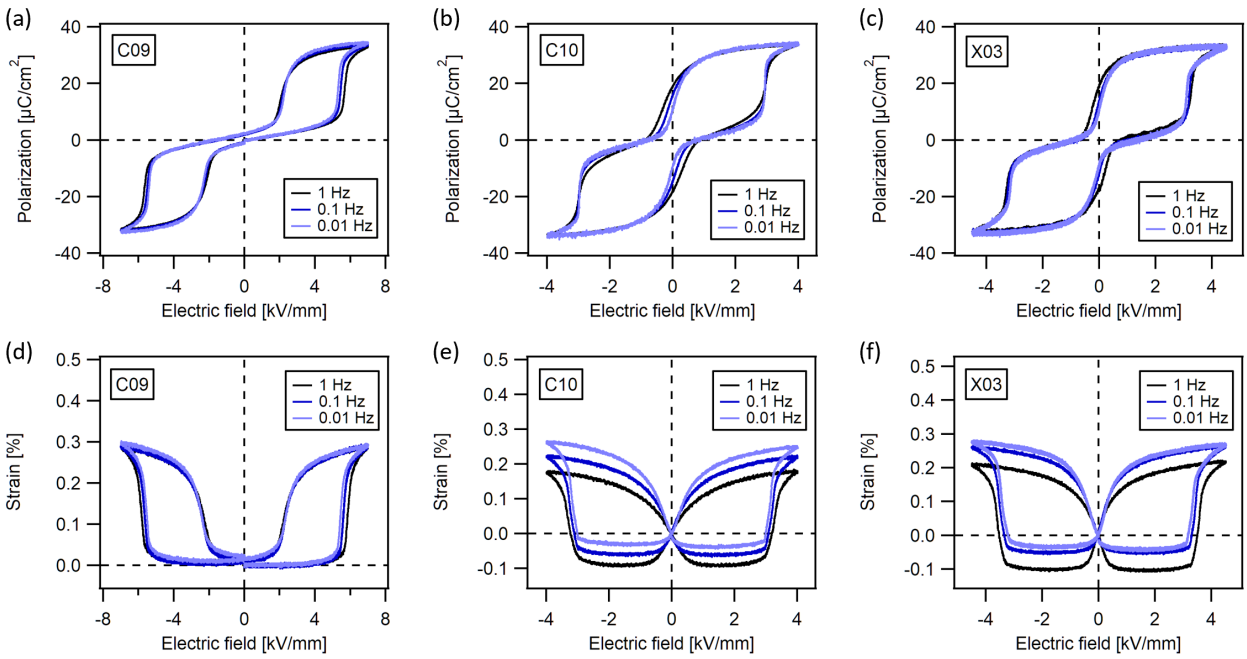

Figure 4.3.: Frequency-dependent hysteresis loops of selected compositions. (a–c) Polarization versus electric field loops; (d–f) strain versus electric field loops.

undergoes both the forward AFE-to-FE and the backward FE-to-AFE transitions slightly earlier in the scale of field at lower frequencies. The difference is small but still noticeable. This indicates that the dynamics of the phase transitions and domain re-orientation should be taken into consideration for such AFE compositions. Composition C10, which is regarded to have an intermediate state between AFE and FE at room temperature, shows an enlarged dynamic effect in Figure 4.3(b, e). The dissipation of the remanent polarization and strain at zero electric field is more noticeable when lower frequencies are utilized. In Figure 4.3(c, f), composition X03 shows basically the same phenomena as composition C10, except that the difference between using 0.1 Hz and 0.01 Hz is smaller in composition X03 than in C10. Despite this, the similarity in the frequency dependence between X03 and C10 again implies the similar effect of A-site aliovalent and B-site isovalent substitutions in such material system.

The initial loop versus the developed loop

As mentioned in Section 2.2.2 and also in the first paragraph of the current section, there are clear distinctions between the initial loop and the developed loop within FE and AFE materials. Some compositions are selected in Figure 4.4 to show such differences. The room-temperature P–E loops measured during temperature-dependent studies are plotted here, so all these samples were prepared following scenario (3) in Section 3.2.1. Before the P–E loop measurements, they were all annealed above T_C so that they should be at the unpoled states with no remanent polarization.

According to the developed loops (labeled with "2nd") in Figure 4.4(a–c), compositions C09, C10, and C11 are thought to be AFE, something between AFE and FE, and FE, respectively. However, their initial

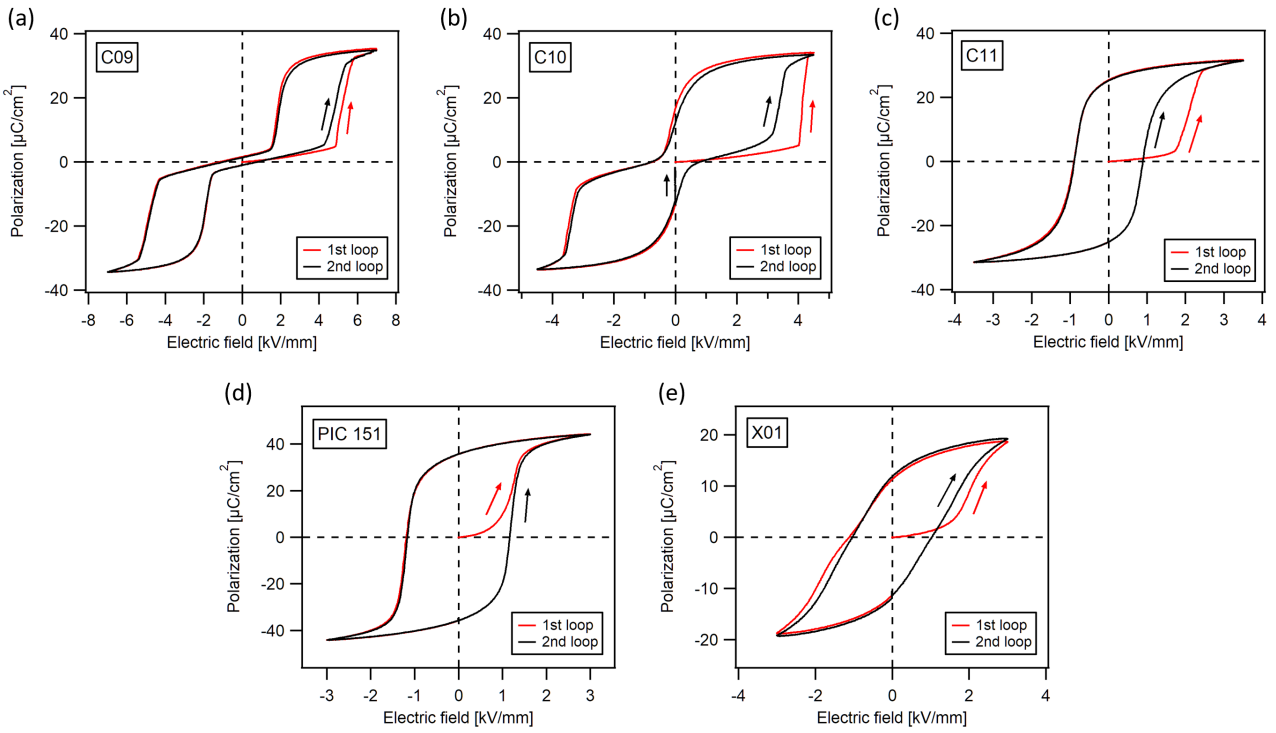

Figure 4.4.: Selected examples for the comparison between the initial (1st) and the developed (2nd) hysteresis loops of polarization versus electric field. All loops were measured at 1 Hz.

loops (labeled with “1st”) exhibit apparent deviations from the second cycles, mostly in Quadrant I. In the initial loops, they all experience “AFE-to-FE”-like transitions during which a large polarization develops very quickly. The corresponding transition fields in their initial loops are always higher than their switching or coercive fields extracted from the developed ones. Such initial states, especially in the compositions very close to the AFE–FE phase boundary (e.g. compositions C10 and C11 in this work), are usually defined as an initial AFE state that can be irreversibly transformed into a FE state during the first application of a sufficiently high electric field (see the description on Figure 2.12 in Section 2.3.2). Here it is noteworthy that composition C09 also shows such deviation in the initial loop even though it is “safely” expected to be AFE. In the other words, the AFE states before and after poling of composition C09 (or other AFE compositions not involved here) might not be identical as well. The re-orientation of AFE domains in the early stage under applied electric field reported by Park *et al.* may interpret such phenomenon [51] (see step 1 in Figure 2.6). Moreover, another detail in Figure 4.4(b) should be mentioned here. As for the intermediate compositions like C10, the attenuation of the remanent polarization after the removal of electric field could be monitored because the measurement program we used actually operated for an extra period of time (ca. 1 second) after the cycles of the triangular waveform were completed. During this period, zero voltage was applied to the sample but the current was still being acquired. In Figure 4.4(b), the decay of the remanent polarization is the vertical segment in the developed loop indicated by a black arrow along P-axis. This phenomenon reveals that the induced FE phase in such compositions is not stable and the material will recover its AFE phase to some extent very fast once the field is removed. Such behavior might also exist in other compositions, but the effect is usually very small and it can be neglected in most cases.

Two more examples with FE loops are displayed in Figure 4.4(d, e). PIC 151 is a commercial PZT ceramic composition. During the initial loop, its polarization starts to grow gradually and smoothly in Quadrant I within the region enclosed by its developed loop. Apart from the typical poling behavior of FE, no evidence of any specific transition field can be observed. In contrast to PIC 151, composition X01 undergoes a similar procedure to composition C11, where the red initial curve in Quadrant I (and even slightly in Quadrant III) leaves the area surrounded by the second loop. Since no AFE-related feature has been discovered on composition X01 throughout this work, such deviation could temporarily be attributed to a certain poling effect that is probably different from that of PIC 151.

Briefly, it can be noticed that the information carried by the initial hysteresis loops is quite worth measuring. Hence, they have always been acquired prior to the developed ones as long as the unpoled or recovered samples were accessible.

4.1.2. Temperature-dependent hysteresis loops

Considering that the compositions near the AFE–FE phase boundaries are sensitive to different external conditions due to their comparable free energies of different phases, the temperature dependence of hysteresis behaviors are necessary to be investigated. Figure 4.5 displays the P–E loops for compositions C09, C10, and C11 measured at several temperature steps. All samples were prepared following scenario (3) in Section 3.2.1. For each individual P–E plot, the initial (red) and developed (black) loops were measured successively, but the sample was always annealed over T_C before the first cycle. Some of the initial loops were missed due to the cooling down process, so only a single developed (black) loop is displayed there. Similar measurements were also performed on compositions X01, X02, and X03, and relevant data are shown in Figure A.3 in Appendix A.1.

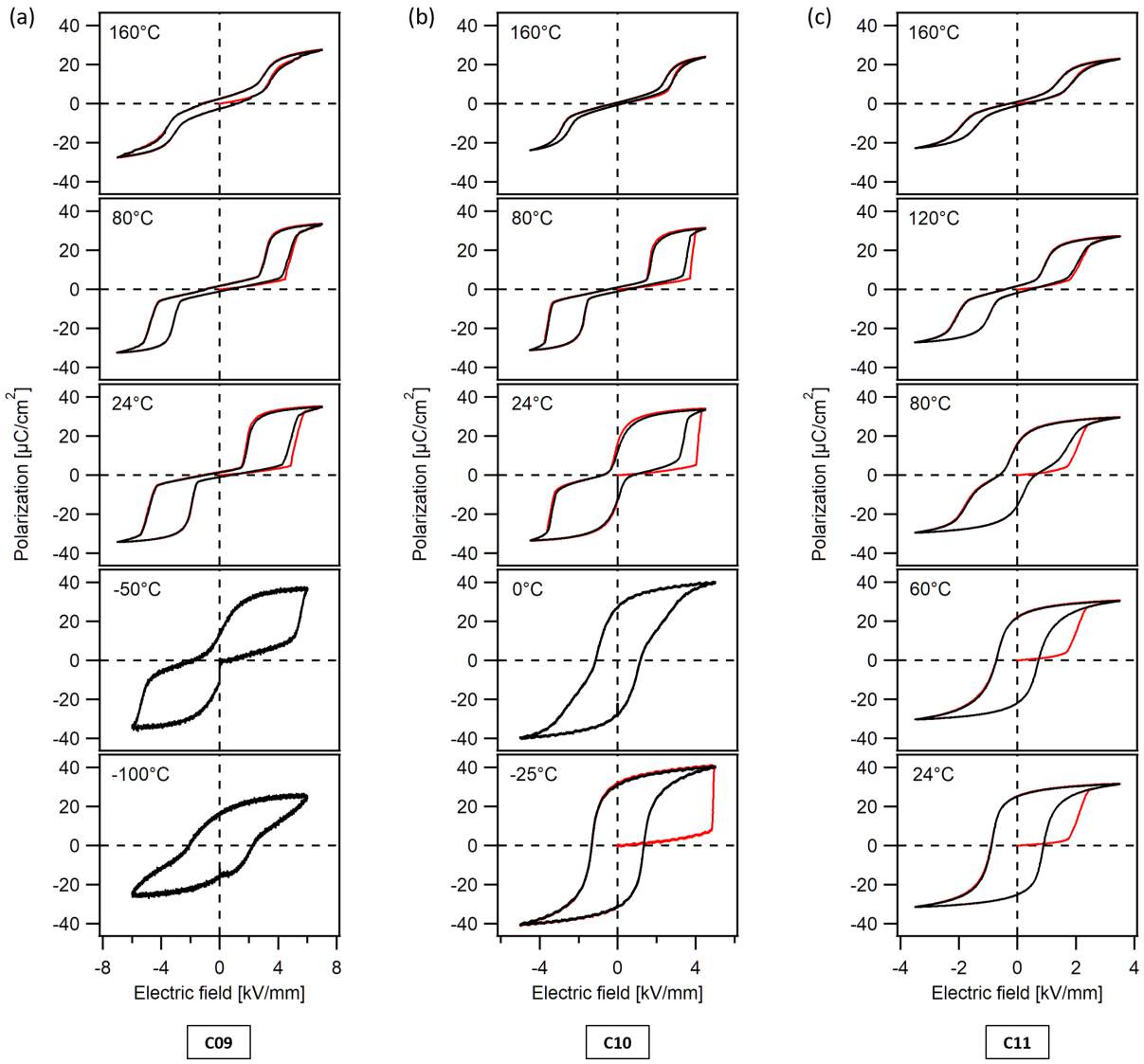

Figure 4.5.: Temperature-dependent polarization versus electric field hysteresis loops of compositions C09, C10, and C11. The red and black loops represent the initial and the developed ones, respectively. In several individual cases with extra cooling by liquid N_2, only the developed loops were acquired.

As can be seen in Figure 4.5, all these three C-series compositions exhibit the same tendency with the change of temperature although they possess distinct loop shapes at room temperature (24°C). All of them have AFE double hysteresis loops at higher temperatures and FE single loops at relatively lower temperatures. It seems that the most significant difference among these samples is the transition temperature between the AFE and the FE. Such AFE–FE transition normally spreads over a temperature range, in which the intermediate state of the material can be characterized by a pinched shape of the developed loop. For composition C11, this transition takes place at a temperature range around

80°C. With the decrease of Ti content, the transition temperature remarkably drops to around room temperature for composition C10, and further down to near −50°C for composition C09. The precise critical temperature can be determined by measuring the depolarization current during a slow heating-up on a pellet that has been poled beforehand at a sufficiently low temperature where it manifests a FE state. The peak occurring in the depolarization current reflects the transition temperature. These data are not given in this work.

Another noteworthy difference among these three compositions is the variation of their transition field of the initial loops in Quadrant I. It can be clearly seen in composition C10 that the electric field where a rapid growth of polarization takes place increases with the decrease of temperature. This implies either a temperature-sensitive dynamic effect or a strong temperature-dependent variation of free energy difference between the states before and after the transition. In composition C11, there is only a tiny temperature dependence of the transition fields in the initial loops in Quadrant I. Composition C09, which had unfortunately two temperature steps with missed initial loop information, shows a similar difference of the initial transition fields between 24°C and 80°C compared to composition C10. Such temperature dependence is shown in Figure 4.6, where the data points of compositions X02 and X03 extracted from Figure A.3 are also involved for a direct comparison. Interestingly, it can be noticed that the temperature dependence of the transition field of the initial P–E loop becomes less obvious when the transition fields are effectively lowered by compositional modifications in these materials.

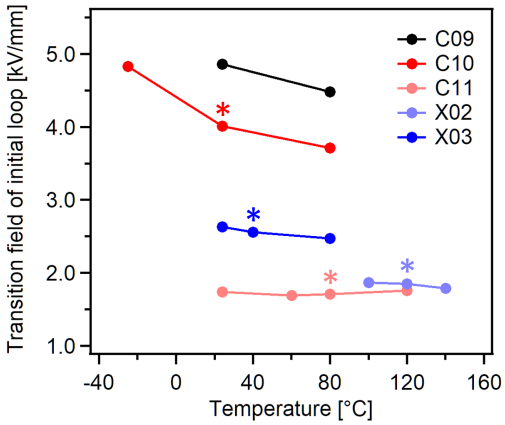

Figure 4.6.: Variation of the transition field extracted from the initial polarization versus field loops that are measured at different temperatures for compositions C09, C10, C11, X02, and X03. The asterisks indicate the measurement steps that are closest to the temperature-induced AFE−FE transition states of the materials (showing pinched developed loops).

Furthermore, it can be observed in Figure 4.5(a) that the low-temperature loops of composition C09, especially the one at −100°C, exhibit also a slightly pinched shape with FE feature. This phenomenon may indicate a strongly suppressed dynamic of domain switching at extremely low temperatures. Alternatively, it could be attributed to a partially AFE-to-FE transition due to the limit of applying sufficiently high electric field with the currently used equipment. According to the tendency shown in Figure 4.6, one may estimate that the field required for a full AFE-to-FE transition (during the initial loop) of the C09 sample at −100°C could be about 7 kV/mm or even higher, which has not been reached in this experiment.

4.2. Dielectric permittivity

4.2.1. Dielectric permittivity versus temperature

This section describes the temperature-dependent dielectric permittivity of the PLZST-related compositions listed in Table 3.1. The main purpose is to know their T_C according to the description in Section 2.2.2. The information of T_C is necessary for the post-annealing treatments of all samples (after mechanical grinding/polishing or electrical poling) and for the studies carried out at elevated temperatures.

Figure 4.7 provides typical examples for such dielectric measurements on compositions C08 and X01. For each sample, both relative dielectric permittivity and dielectric loss tangent are plotted against temperature (only during heating-up), and the data acquired at a series of frequencies are displayed together. As can be seen in Figure 4.7(a), the room-temperature AFE composition C08 has very little frequency dependence in its permittivity vs. temperature relation. At each frequency involved here, the permittivity curve generally exhibits a peak at around 200°C (identified as T_C). The peak is not as sharp as the schematic case in Figure 2.8, but it is characteristic for the PLZST materials [94, 96, 208, 209]. Corresponding to the peak in the permittivity plot, a small maximum/fluctuation can always be found in the loss curve in Figure 4.7(b) at around 200°C except for the case of 10^6 Hz, where a much larger peak appears and its shape looks similar to the permittivity curve. This phenomenon is related to the electrical resonance in the circuit, which can be verified by measuring the loss tangent of a sample against frequency at fixed temperatures. The resonance takes place usually at around 10^7 Hz for these

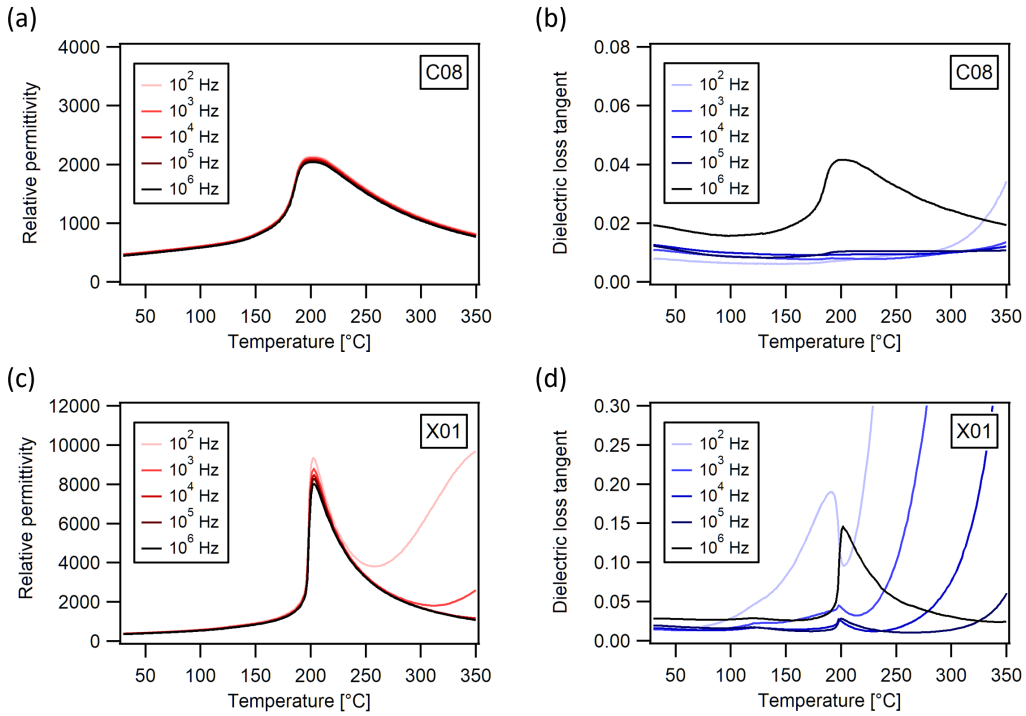

Figure 4.7.: Typical examples for the temperature-dependent (a, c) relative permittivity and (b, d) dielectric loss tangent. The measurements were performed at a series of frequencies.

PLZST ceramic pellets and the loss tangent vs. frequency curves are already in a considerably rising stage at 10^6 Hz. This leads to a rapidly amplified signal of loss tangent at such a high frequency. For the frequencies $\leqslant 10^5$ Hz, all the loss curves of this C08 sample basically remain at very low magnitude around 0.01 over the whole range from room temperature to 350°C. Only the curve of 100 Hz increases at ca. 300°C, indicating an onset of conductivity. In contrast to composition C08, the FE composition X01 exhibits much sharper permittivity peaks at all frequencies, as shown in Figure 4.7(c). Besides, a clear frequency dependence can be noticed in both the permittivity and the loss plots, which can be regarded as a characteristic symbol for a higher conductivity of this sample. Moreover, the obvious loss peak that could be assigned to the resonance effect can also be noticed at 10^6 Hz for the X01 sample. Since the dielectric loss exhibits more complicated variations with the change of temperature and frequency, which are difficult to analyze without the help of other techniques, we will mainly focus on the permittivity plots here and only display the loss data for reference.

Figure 4.8 compares the relative dielectric permittivity and loss tangent as a function of temperature within the C-, X-, and A-series, respectively. As C09 is the basic composition of X-series (with the same B-site ratio), it is also added into Figure 4.8(c, d) for a direct comparison. The data of composition C00 are also included in Figure 4.8(e, f). All the curves plotted here are acquired at 10^3 Hz. More complete results of all the relevant compositions showing the dependence on frequency can be found in Figures A.4 and A.5 of Appendix A.1.

As can be seen in Figure 4.8(a, b), the C-series compositions possess an obvious tendency when the Ti content changes. Composition C11, which has the highest Ti concentration (11% on the B-site), exhibits the sharpest peak and the highest values of relative permittivity in the whole temperature range up to 350°C. With a gradual decrease of the Ti content, the peak that indicates the position of T_C becomes blunter, and the permittivity significantly decreases in the whole temperature range. If one only regards the temperature corresponding to the maximum of the peak as T_C, it can be seen that lowering the Ti content increases T_C, from ca. 188°C for composition C11 to ca. 202°C for composition C08. These phenomena are basically in agreement with what has been reported in literature [94, 208, 209]. As for the two compositions with the lowest Ti concentrations, C04 and C00 (4% and 0% on the B-site, respectively), the main peaks are strongly blunted and reduced, showing a plateau-like region roughly between 200°C and 300°C. In PLZT-, PLZST- or PNZST-related materials, such dielectric plateau has been assigned to a so-called multicell cubic (MCC) state [92, 102, 256]. The presence of a clear MCC region will make it difficult to determine the T_C by just reading the maximum on the permittivity curve. Hence, any annealing treatment or high-temperature measurement in the rest of this work on the samples showing MCC feature should avoid the temperatures corresponding to the plateau range. Besides, another dielectric peak (or shoulder) can be noticed in compositions C04 and C00 on the left-hand side of the main permittivity peak, which indicates the existence of another structural phase transition at a lower temperature. This could also be related to the special shape of their P–E loops that show the feature of field-induced multiphase transitions (see Figure 4.1(a, b)). Different from compositions C00 and C04, there is no recognizable phase transition for composition C11 between 60°C and 120°C according to its permittivity curve although the temperature-dependent P–E loops indicate a clear transition from FE to AFE behavior (see Figure 4.5(c)). Since the permittivity measurements displayed here always use unpoled samples, it can be known that the unpoled C11 sample should be always in an AFE state within the whole temperature range below T_C and its temperature-related transition from FE to AFE only refers to the states under electric fields. Therefore, it is expected to observe an extra step in the permittivity vs. temperature curve of composition C11 if the permittivity is measured either with an additional dc field or on a poled sample. Similar examples have been reported in Refs. [96, 257].

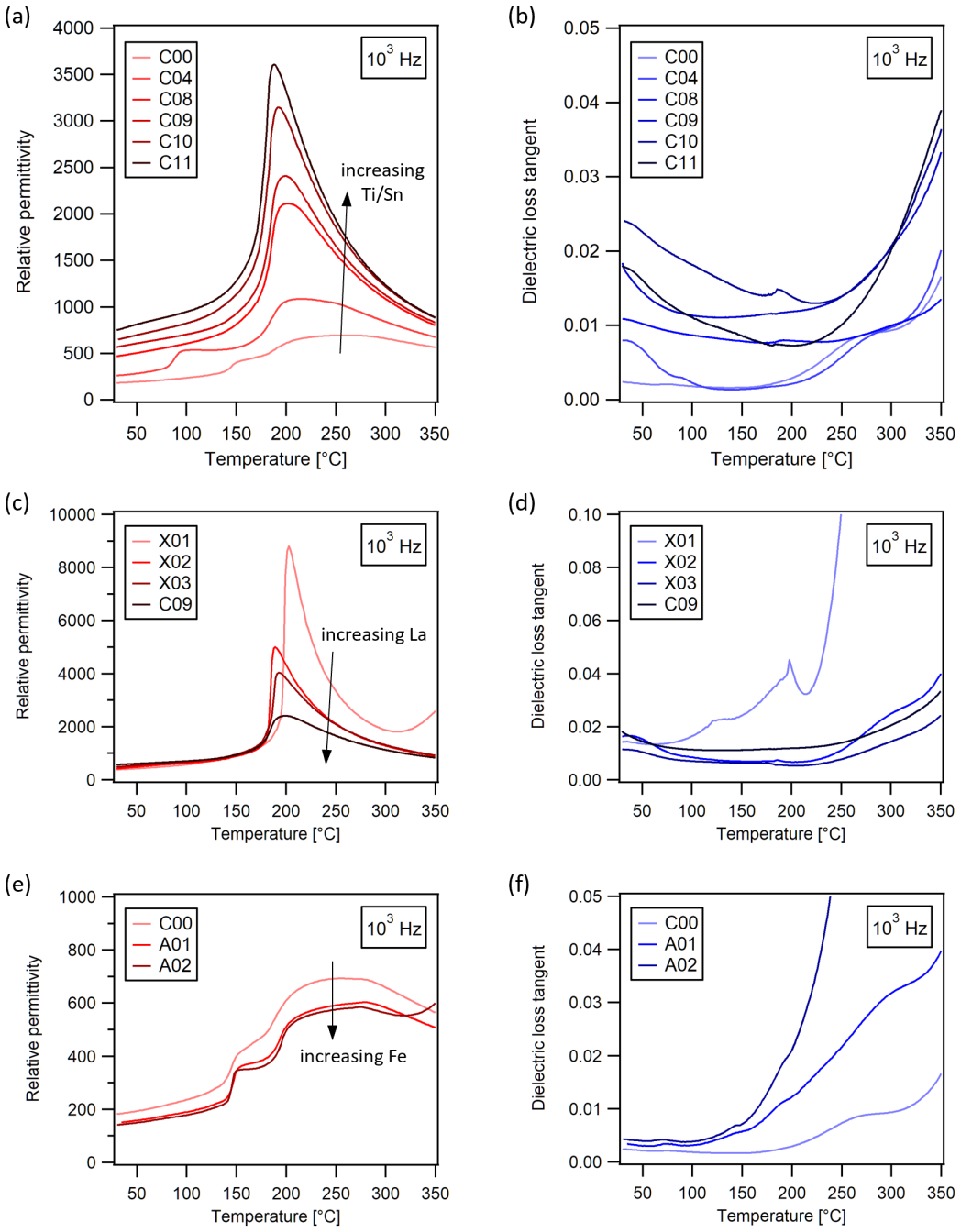

Figure 4.8.: Comparisons of the temperature-dependent relative permittivity and loss tangent within (a, b) C-series, (c, d) X-series (composition C09 appended), and (e, f) A-series (composition C00 appended). All curves were measured at 10^3 Hz.

The effect of La doping concentration in the PLZST materials can be seen in Figure 4.8(c, d). The undoped X01 has the sharpest and highest peak among the four compositions. With increasing La doping concentration, the permittivity peak becomes blunter and lower. It should be noticed that the peak shift resulting from the La doping is not monotonic. Composition X01 has the highest T_C at ca.

203°C. When 1% La is added to the A-site, the T_C of composition X02 is reduced to ca. 189°C, which is the lowest value among the four compositions. Afterwards, the peak maximum gradually shifts back to higher values. For composition C09, it reaches ca. 200°C. Such tendency is basically similar to the results in Ref. [96]. Moreover, only composition X01 exhibits some leakage at temperatures >300°C, and adding only 1% La can already eliminate the leaky characteristic in the temperature range up to 350°C. Actually, both compositions X02 and X03 possess nearly no frequency dependence of the permittivity, as shown in Figure A.5(c, e) in Appendix A.1.

The situation with co-doping of La and Fe is shown in Figure 4.8(e, f). The two samples with Fe content exhibit basically similar shapes of the permittivity curves compared to the case of composition C00, which implies that adding acceptor Fe ($\leqslant$2% on the B-site) might not induce very remarkable change in the dielectric properties of such donor-doped materials. This impression may also be supported by the previous P–E loop measurements, in which similar loop shapes have been obtained in these three compositions (see Figure 4.1(a, j, k)). According to the positions of the permittivity plateaus, one could say that for all the three compositions the temperature range $\geqslant$300°C should be sufficiently high to ensure a paraelectric state. Besides, the permittivity of the two A-series compositions is clearly reduced compared to composition C00, but the difference between A01 and A02 is quite small at $\lesssim$300°C. After reaching ca. 300°C, composition A02 with the higher Fe concentration exhibits an increase in its permittivity, overtaking that of composition A01. Furthermore, it is easy to see in Figure 4.8(f) that the loss tangent curves of the A-series samples show more and more leaky characteristic with increasing Fe doping concentration.

4.2.2. Dielectric permittivity versus electric field at varying temperature

According to the theory described in Section 2.2.2 and the experimental procedure given in Section 3.2.2, this part displays the electric-field dependence of dielectric permittivity measured on compositions C09, C10, and C11. For each sample, the permittivity measurements were carried out at stepwise varying temperatures, which generally correspond to the temperature steps involved in the P–E hysteresis loop studies in Figure 4.5. Combining the polarization and the permittivity measured under large electric fields may provide more information with respect to the domain switching in FEs and the AFE-to-FE phase transition in AFEs. Figure 4.9(a–c) shows the permittivity vs. field loops obtained at five temperature steps of compositions C09, C10, and C11, respectively. Basically, all the observed loops can be classified into four types:

(1) The FE type as sketched in Figure 2.7(c), e.g. the C10 at $\leqslant$0°C and the C11 at $\leqslant$60°C.
(2) The AFE type as sketched in Figure 2.7(d), e.g. the C09 at 25°C and 80°C, the C10 at 80°C, and the C11 at 120°C. In most of these cases, only limited increase of the permittivity can be observed when the applied field is rising within the AFE region. The C10 sample shows an exception at 80°C, in which the permittivity slightly decreases with the field before its AFE-to-FE transition point. For all these cases, the permittivity drops significantly (always by about 50%) as soon as the material is transformed into a FE phase.
(3) The intermediate type between types (1) and (2), e.g. the C09 at −50°C, the C10 at 25°C, and the C11 at 80°C. Unlike the situation of type (2), these curves always experience relatively flat stages before their AFE-to-FE transition fields. It should also be noticed that in these cases the permittivity can almost recover the initial level when the applied field goes back to zero. This should be attributed to the very low frequency of the triangular waveforms (only 5 mHz) utilized here by the high voltage amplifier, which is much slower than the frequency used for the P–E

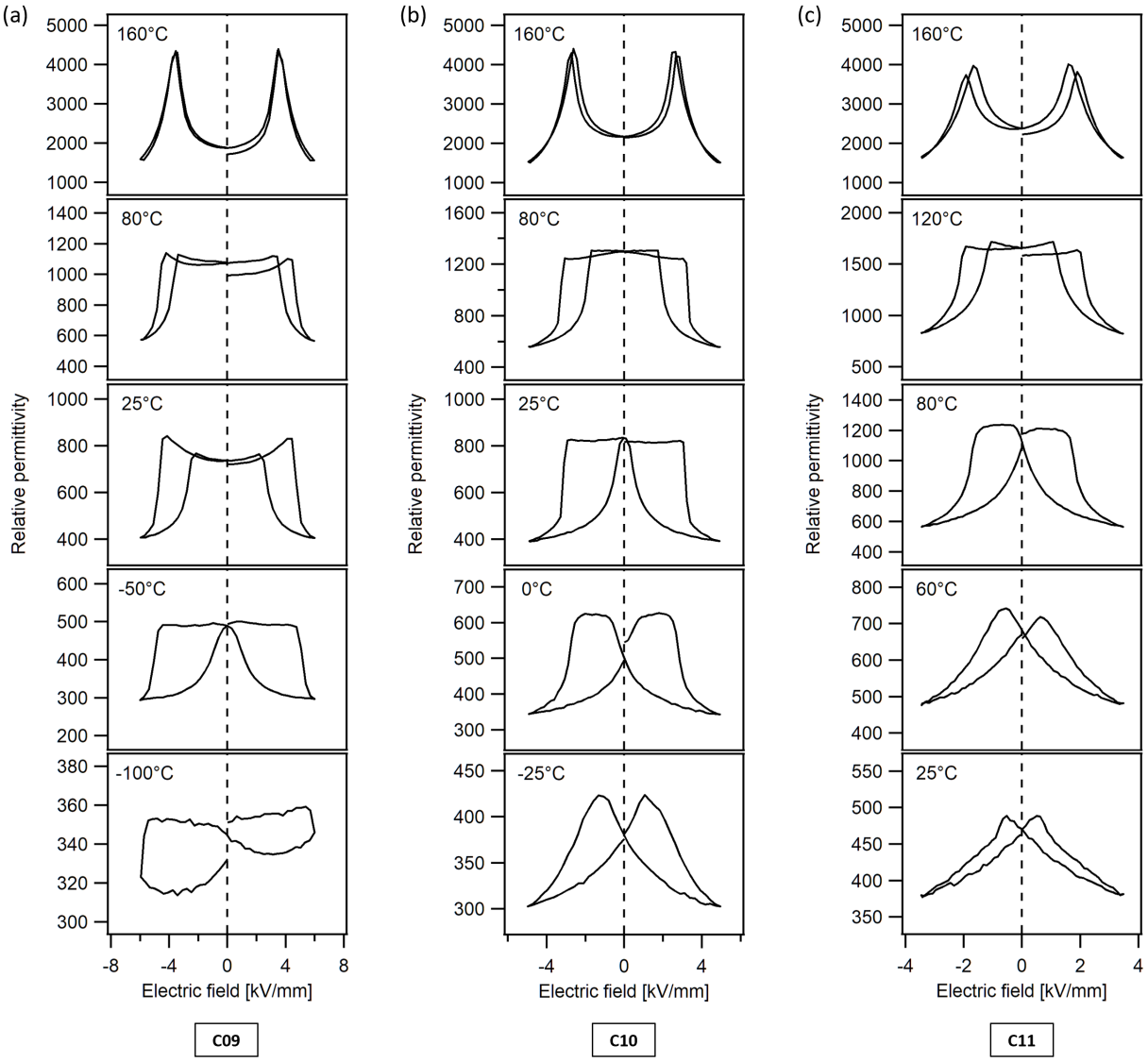

Figure 4.9.: Electric-field-dependent relative dielectric permittivity of compositions C09, C10, and C11 measured at different temperatures.

loop measurements (normally 1 Hz). When such samples are in their respective intermediate states between low-temperature FE and high-temperature AFE, they are expected to exhibit more obvious frequency-dependent hysteresis characteristic (see the P–E loops in Figure 4.3).

(4) The AFE type as sketched in Figure 2.7(b), e.g. all the curves at 160°C for compositions C09, C10, and C11. Although these curves were measured with the so-called incremental method, they seem quite similar to the style normally obtained with the differential method (see Figure 2.7). Considering that the corresponding P–E double loops of these three compositions at 160°C also show different shapes (slim and slanted) compared to the lower-temperature ones, it is reasonable to assume that the materials undergo a special structure-related variation within a

narrow temperature range just below the T_C (160°C is already close to their T_C, see Figure 4.8(a)). Such an intermediate state might be able to explain both the remarkable permittivity rise with the increasing field and the subsequent sharp peak in the permittivity vs. field plots at 160°C. However, this speculation is so far not clear.

Apart from the four types mentioned above, the curve of the C09 sample at -100°C shows a strange shape, in which the change of permittivity seems to be severely limited (changed by only about 40). This phenomenon matches the pinched and confined FE P–E loop of this sample measured at the same temperature (see Figure 4.5(a)), and it might be again attributed to either a strong suppression of domain switching at very low temperatures or an incomplete field-induced AFE-to-FE transition.

4.3. Crystalline structure analysis

The XRD patterns measured on the ceramic pellets of all compositions (C-, X-, and A-series) are given in this section. Relevant experimental details can be found in Section 3.2.3. According to the phase diagram of the PLZST materials (see Figure 2.11(b)), it has been known that the relevant crystalline structures could be tetragonal AFE (A_T), orthorhombic AFE (A_O), or rhombohedral FE (F_R). Most of the C-series compositions should be located in the A_T or the A_O region. The two compositions with the highest Ti content (C10 and C11) may tend to possess some FE features because they are very close to the phase boundary between A_T and F_R. This expectation has been verified during the previous P–E loop measurements in Section 4.1. By contrast, the two compositions with the lowest Ti content (C00 and C04) are expected to stay certainly in the A_O region. This has also been proven by their special shapes of P–E loops, which exhibit the feature of field-induced multiphase transition and are clearly different from those of compositions C08 and C09. It should be noted that the "tetragonal" in the A_T phase does not refer to a single tetragonal perovskite unit cell. Rather, it also means a supercell structure that is comprised of some tetragonal perovskite cells, similar to the A_O phase. The earliest description and definition of the A_T phase, to the best of the author's knowledge, can be found in Refs. [23, 39, 90]. Concerning the full symmetry of these modified PZ-based AFE materials, there are usually at least two aspects of difficulties. On the one hand, the conventional XRD is not sensitive enough to identify the small reflections caused by the supercell structures [51, 107, 258]. On the other hand, the existence of incommensurate modulation can enlarge the complexity of the reflections. Therefore, here we adopt the general strategy in the relevant literature when characterizing the crystalline structure of such materials based on the conventional XRD patterns: only to check the tetragonal perovskite unit cell for both A_T and A_O phases [51, 92, 96, 258].

Figure 4.10 displays the patterns within the 2θ range between 20° and 70°. The important reflections are labeled in blue, which are shared by all samples. It should be noted that the pseudo-cubic index of a perovskite unit cell is always used for convenience. Apparently, all these compositions have similar distributions of the main reflections that can be assigned to perovskite structures. Besides, several reflections with very low intensities can be observed in most of the samples, indicating the existence of superlattices. The most obvious examples are the small tips between {200} and {211} peaks except the one already labeled as {210} [259]. Among all these patterns, only composition X01 has no such superlattice reflection between {200} and {211} peaks, which is in agreement with that this undoped PZST sample is purely FE.

In order to extract more structural information from the XRD patterns, Figure 4.11 compares the {110},

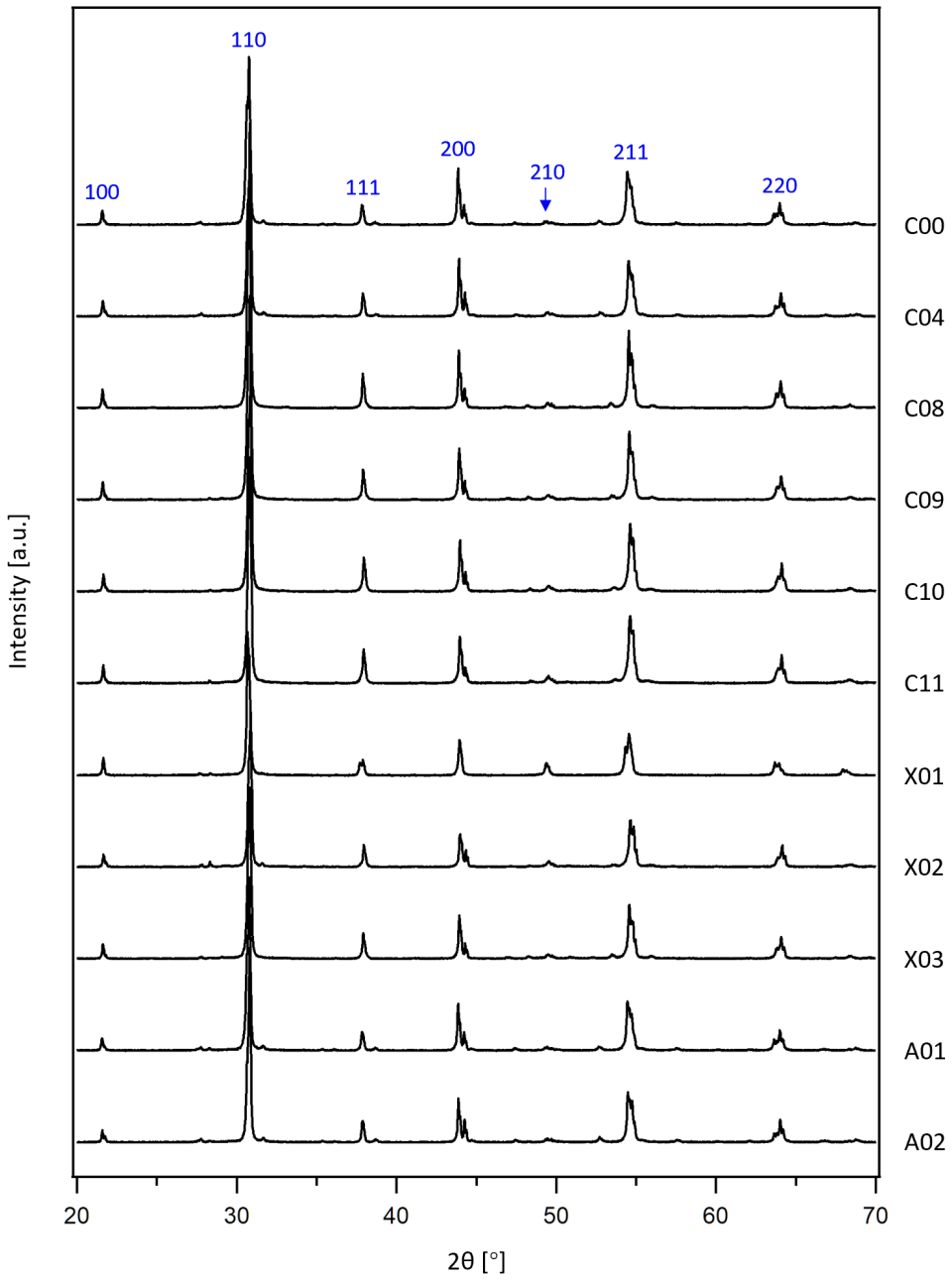

Figure 4.10.: X-ray diffraction patterns in the 2θ range from 20° to 70° of all C-, X-, and A-series compositions. Pseudo-cubic index of perovskite unit cell is used to indicate the reflections.

{111}, and {200} peaks within each series separately. Here all the reflections still utilize the pseudo-cubic index for convenience. The reflections belonging to $K_{\alpha 1}$ radiation are marked schematically with short blue lines, and the signals from $K_{\alpha 2}$ are marked with brown arrows if they are recognizable. In addition, only the first pattern from the top of each plot will be labeled when the following ones show basically the similar features. It is well known that a perovskite PZT with tetragonal symmetry should show splitting of the {200} reflection at $2\theta \approx 44°$ into (200) and (002) peaks and show no splitting of the {111} at $2\theta \approx 38°$. By contrast, the rhombohedral phase is expected to have splitting of the {111}

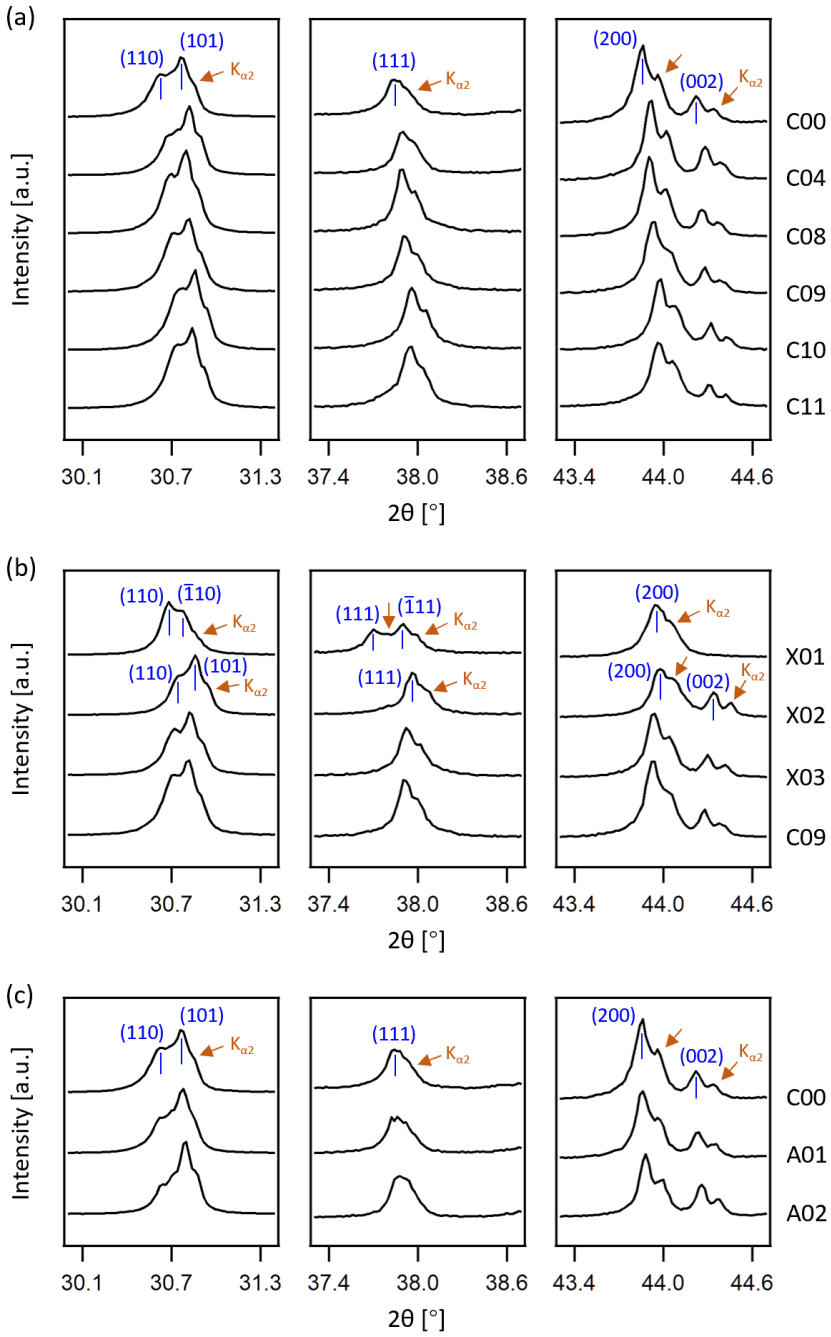

Figure 4.11.: {110}, {111}, and {200} peaks in the X-ray diffraction patterns of (a) C-series, (b) X-series (composition C09 appended), and (c) A-series (composition C00 appended). Pseudo-cubic index of perovskite unit cell is used to indicate the reflections.

reflection into (111) and ($\bar{1}$11) but no splitting of the {200} peak [51, 258]. As can be seen in Figure 4.11(a), all the C-series samples display very similar patterns, where the split (200) and (002) peaks indicate a tetragonal perovskite unit cell with $a = b > c$. Hence, the whole C-series can be assigned to either the A_T or the A_O phase. It should be noted that all XRD patterns given here were measured on the unpoled samples. As it has been reported in the literature that exposure to external electric field

can result in certain variations of the crystalline structures [51, 52, 110, 258], additional experiments have been performed in this work where the unpoled and poled states can be compared directly on the same ceramic pellets that were coated with electrodes. The results clearly show that after poling a rhombohedral FE phase has been induced in the C11 sample although its unpoled state displays a tetragonal structure very similar to the other C-series compositions. Relevant data can be found in Figure A.6 in Appendix A.2.

Another important information in Figure 4.11(a) is the intensity ratio between the (200) and (002) reflections, which should be ideally $2:1$ for a tetragonal polycrystalline material with $a = b > c$. However, the ratio shown here is obviously larger than $2:1$. In this work, powder diffraction has also been done for compositions C08–C11, where the intensity ratios of (200) and (002) reflections are much closer to $2:1$. The discrepancy between the patterns obtained on pellets and powders undoubtedly indicates the existence of texture/preferred domain orientation of the tetragonal structure in the ceramic pellets, where the ab-planes tend to tilt out of the plane of the disk. Considering that all the pellets had been ground (top and bottom surfaces) and annealed beforehand, i.e. the XRD measurements were carried out on the inner bulks instead of on the as-sintered surfaces, it can be speculated that such texture should form most probably during the annealing step after the grinding (more exactly, during the cooling-down through T_C) prior to the XRD measurement. Relevant data and comparison can be found in Figure A.7 in Appendix A.2.

Different from the C-series where the Ti/Sn ratio varies, Figure 4.11(b, c) presents the effects of doping. For a better comparison, compositions C09 and C00 are added to the X- and A-series, respectively. As can be seen in Figure 4.11(b), compositions X02 and X03 possess similar patterns to that of C09 (tetragonal perovskite unit cell), whereas composition X01 shows a different crystalline structure that can be indexed to a rhombohedral phase due to the clear splitting of the {111} reflection. The similarity in the tetragonal characteristic of compositions X02 and C09 implies that at room temperature only 1% of La donor on the A-site can already effectively stabilize the AFE phase. Nevertheless, composition X02 still exhibits a field-induced AFE-to-FE transition in its initial P–E loop and a FE behavior in its developed loop at the room temperature, which is different from the case of composition C09 but is very similar to C11. Regarding the effect of extra acceptor Fe in PLZS, no significant discrepancy in terms of peak splitting can be found between the two A-series samples and composition C00, as shown in Figure 4.11(c). This observation reveals that the compensating acceptor in the donor-doped composition cannot convert the AFE crystalline structure into a FE one, which is in agreement with the very similar P–E loops of compositions C00, A01, and A02. However, such statement may be only valid for low-Ti compositions. It should be noted that their orthorhombic structures are relatively close to that of the undoped PZ, which is originally an AFE. About the effect of compensation between donor and acceptor on the compositions with higher Ti content, no study has been done in this work.

Apart from the splitting of reflections that helps to qualitatively identify the lattice symmetry, more information, such as the lattice constants of the perovskite unit cells, can be extracted from the XRD patterns as well. With the lattice constants, one can calculate the theoretical density of the material and further determine the relative density of the sintered ceramic sample. Relevant descriptions and data can be found in Appendices A.2 and A.4.

4.4. Microstructure characterization

The microstructures of the sintered ceramic samples were studied by SEM technique. Figure 4.12 displays the SEM images of five selected compositions: C00, C09, C11, X01, and A02. Compositions C09 and C11 are the most important PLZST ones near the phase boundary between the A_T and the $F_{R(LT)}$ regions. Composition C00 has the lowest Ti concentration (0%) in the C-series, far away from C09 and C11. Compositions X01 and A02 are actually the variants of C09 and C00, respectively. These five selected compositions are located at the ends or intersections of the three series as shown in schematic of Figure 3.1(b). Therefore, characterizing these samples is expected to provide an overall impression of the morphology of all relevant compositions.

According to the experimental procedures given in Section 3.2.4, two types of SEM microstructures were obtained. In the left column of Figure 4.12, one can find the micrographs of the as-sintered ceramic surfaces. It should be noted that the scale bar used for the A02 sample (Figure 4.12(i)) is different from the others. It is easy to see that composition A02 has the largest grain size on the surface. Besides, no obvious abnormal growth of the grains can be discovered in any of the five cases. Nevertheless, it cannot be denied that these microstructures belong to the ceramic surfaces, which was in contact with the packing powder inevitably during the high-temperature sintering process. Hence, it is imaginable that such surfaces would manifest discrepant morphology compared to the bulk. Here the surface images are provided just for reference.

The inner bulk microstructures of the five compositions are presented in the right column of Figure 4.12. All the samples were ground and polished so that the interior of the bulk materials can be characterized. Among them, the C09 and C11 samples were thermally etched at 900°C after the polishing in order to render their grain boundaries more identifiable. The attempts to etch these samples were not ideal, and two examples that did not fully meet expectations are given in Appendix A.3. Despite the technical difficulties, we still show the unsatisfactory images of the etched samples in Figure 4.12(d, f). For the other compositions, no thermal etching was carried out and sufficiently good contrast, with which the neighboring grains can be distinguished, was achieved by means of using a smaller accelerating voltage (15.0 kV for compositions C09 and C11, but 8.0 kV for the others). In addition, it should be noted that the A02 sample again utilizes a different scale bar compared to the rest (Figure 4.12(j)). At least three aspects of information can be obtained from these microstructure images:

(1) Some very dark hole-like regions with comparable dimensions to the normal grains can be observed in all samples. They do not appear on the as-sintered surfaces and can be mostly assigned to the so-called pull-outs (lost grains) during the polishing process. However, the situation of composition A02 would be an exception. Since the A02 sample has the lowest relative density (only 90.97%) among all the sintered ceramics in this work (see Table A.2 in Appendix A.4), it can be speculated that some of the black holes in Figure 4.12(j) might be pores, which formed during the sintering process.
(2) There are irregularities at the triple junctions of the grain boundaries. In the C00 and X01 samples, these positions are manifest in dark colors, but they do not seem to be vacant. Similar things are recognizable in composition A02, but they have brighter color and look much larger in size. In the two etched samples C09 and C11, such irregularities are also believed to be existing. Since they are indeed constituent parts of the grain boundaries, these small positions have been etched as well and thereby become difficult to be identified. The origin of this phenomenon is most probably the 2% excess PbO content added during the ceramic preparation for all relevant samples. It has

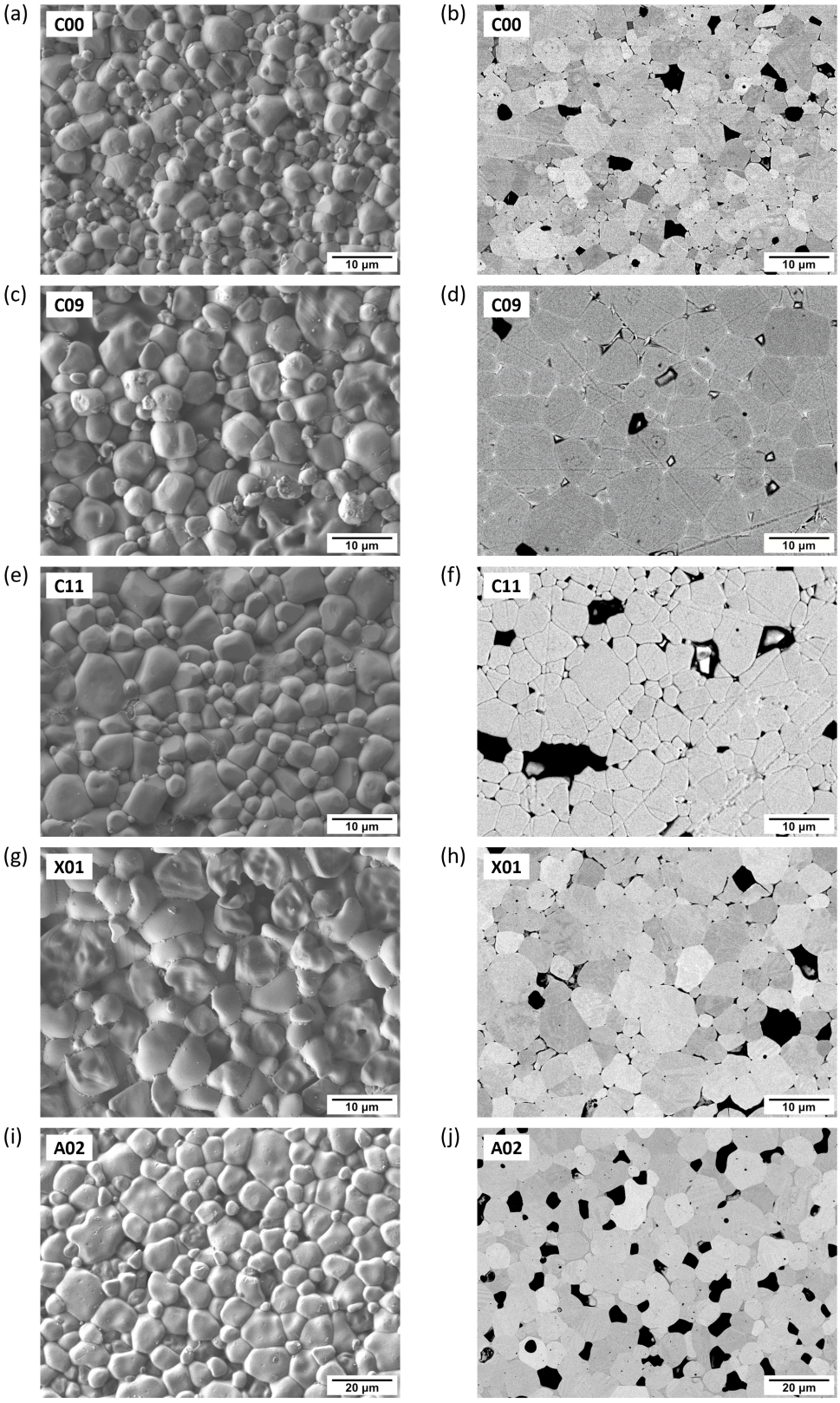

Figure 4.12.: Scanning electron microscopic images of selected compositions. Left column: as-sintered surfaces; right column: interior morphology after grinding and polishing (the C09 and C11 samples had an extra step of thermal etching after the surface polishing).

been reported in the literature that a PbO-rich liquid phase is usually expected in PZT ceramics with PbO excess, which appears at the grain boundaries (both the 2-dimensional layers and the triple junctions) and can influence the densification process during sintering [260–263].

(3) The grain size can be quantified by using the image processing and analyzing software ImageJ [211]. An example of the way how the grains are recognized by ImageJ is given in Appendix A.3. Figure 4.13 shows the statistical distributions of the grain size in four compositions. For each composition, 2–3 regions which contain more than 200 grains in total were selected for doing the statistics. The mean value of grain size $\bar{d}$, the standard deviation σ, and the number of selected grains N are inserted in the plots. Obviously, no bimodal distribution can be noticed in all these compositions, indicating sufficiently good homogeneity of the grain growth. Besides, the A02 sample exhibits the largest average grain size among these compositions, which could be regarded as one of the effects of the additional Fe doping in such La-doped PZT-related materials in the viewpoint of ceramic sintering.

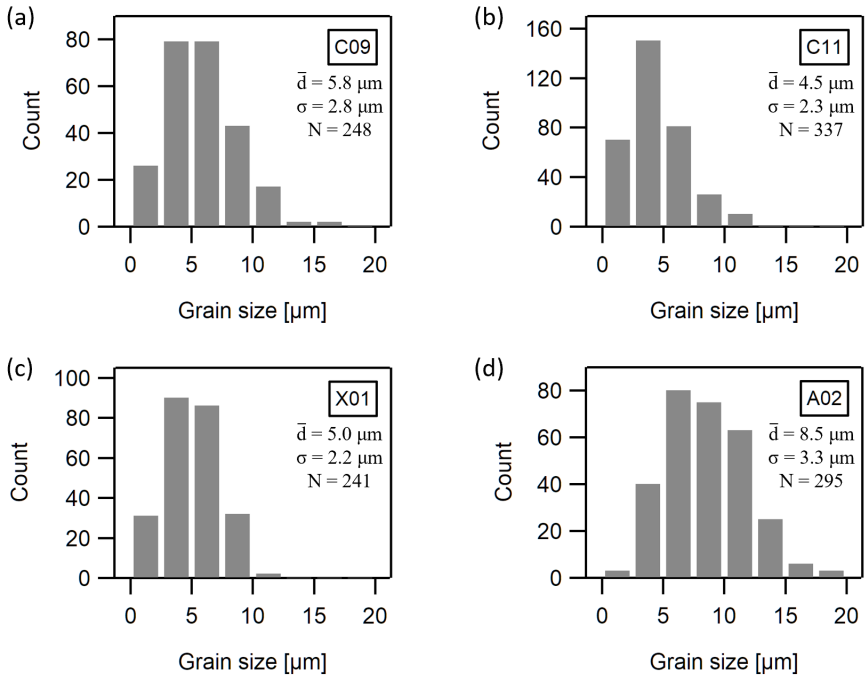

Figure 4.13.: Grain size distributions of compositions C09, C11, X01, and A02.

4.5. Summary

This chapter described the basic characterizations of the three series of ceramic samples after the sintering. The hysteresis loops, which are the most important properties of these FE and AFE materials, have been measured at different frequencies and temperatures. Based on the obtained P–E loops, suitable compositions can be selected for the subsequent conductivity and XPS experiments, where the behaviors of such materials under various thermal and electrical conditions will be investigated. Apart from the hysteresis loops, we have also studied the dielectric permittivities, the crystalline structures, and the microstructures of relevant compositions, which provide basic information of the materials.

5. Electrical Conductivity

This chapter will show the results of dc conductivity tests on different compositions according to the experimental strategies described in Section 3.3. The studies are divided into two parts, which utilize the so-called static and dynamic methods, respectively. For the static method, the electrical measurements were always performed at fixed temperatures. In Section 5.1.1, the electric-field-dependent dc conductivity is investigated for most of the compositions synthesized for this work. Such field-dependence is measured at several temperature levels for each sample, so that an overview of the conduction behaviors under the two common external conditions, the electric field and the temperature, can be preliminarily learned. Based on this, the conductivities of the original AFE and the field-induced FE states of a single AFE composition can be compared, as shown in Section 5.1.2. In contrast to the static method, the dynamic one involves the ramping of temperature when a constant dc bias is applied to the sample. By such method, the activation energies of the materials can be obtained. Section 5.2.1 first describes the way how to extract information from the Arrhenius plots using composition C09 as an example, and then shows a comparison of the conductivities and activation energies among all relevant compositions. Additionally, more dynamic measurements carried out with multiple thermal cycling are described in Appendix B.2, which demonstrates the problem and limitation of such experiments. Based on the observations in this chapter, some discussion on the conduction mechanisms of these Pb-based FEs and AFEs will be given in Chapter 8. For convenience, Table 5.1 lists all types of experiments in this part.

Table 5.1.: List of electrical conductivity experiments carried out on different compositions.

Composition	Static method		Dynamic method	
	$\sigma(E,T)$ (Section 5.1.1)	AFE vs. FE (Section 5.1.2)	Single cycling (Section 5.2)	Multiple cycling (Appendix B.2)
C00	✓	×	✓	✓
C09	✓	✓	✓	✓
C10	×	×	×	✓
C11	✓	✓	✓	✓
X01	✓	×	✓	✓
X02	✓	×	✓	✓
X03	×	×	×	✓
A01	✓	×	✓	×
A02	✓	×	✓	×
PIC 151	×	×	×	✓

5.1. Electrical conductivity by static dc method

5.1.1. Electric-field- and temperature-dependent dc conductivity

First of all, an example of such conductivity measurement is demonstrated in detail based on the important composition C09 that possesses a clear AFE behavior at room temperature. Figure 5.1(a) gives the schematic measuring procedure in terms of the controlling of temperature and electric field (or dc voltage). The main idea is to apply a series of electric fields at each temperature level and read the current signals, which has been described already in Section 3.3.2. Here the same field profile will be applied to the sample at five temperature levels (RT, T1–T4), indicated by the gray shaded fields. Extra steps of annealing are performed at sufficiently high temperature (usually tens of degrees higher than T_C, marked by the asterisks) prior to the following temperature level. However, such extra annealing is not needed when the next temperature level is already higher than the annealing temperature. In this case, the electrical measurements can be started directly after the temperature becomes stable for 20 min (steps T3 and T4 in the schematic here). Figure 5.1(b) displays the conduction behavior of composition C09 at room temperature, 100°C, 200°C, 300°C, and 400°C, respectively. The conductivity values are calculated by the two-point method according to Equation 3.4. For such measurements, all samples have similar thicknesses (0.14–0.15 mm), so we usually controlled the voltage rather than the electric field for convenience. The applied voltages on this C09 pellet are labeled in red in the field plot, where the fields are calculated values that provide information about the orders of magnitude. Besides, the duration of each step of applying voltage is 10 min in this sets of experiments.

At lower temperatures, e.g. 24°C and 100°C, reasonably smooth current signals ($>10^{-12}$ A) are accessible only under higher electric fields. The signals acquired at lower fields are full of noise, which is expected

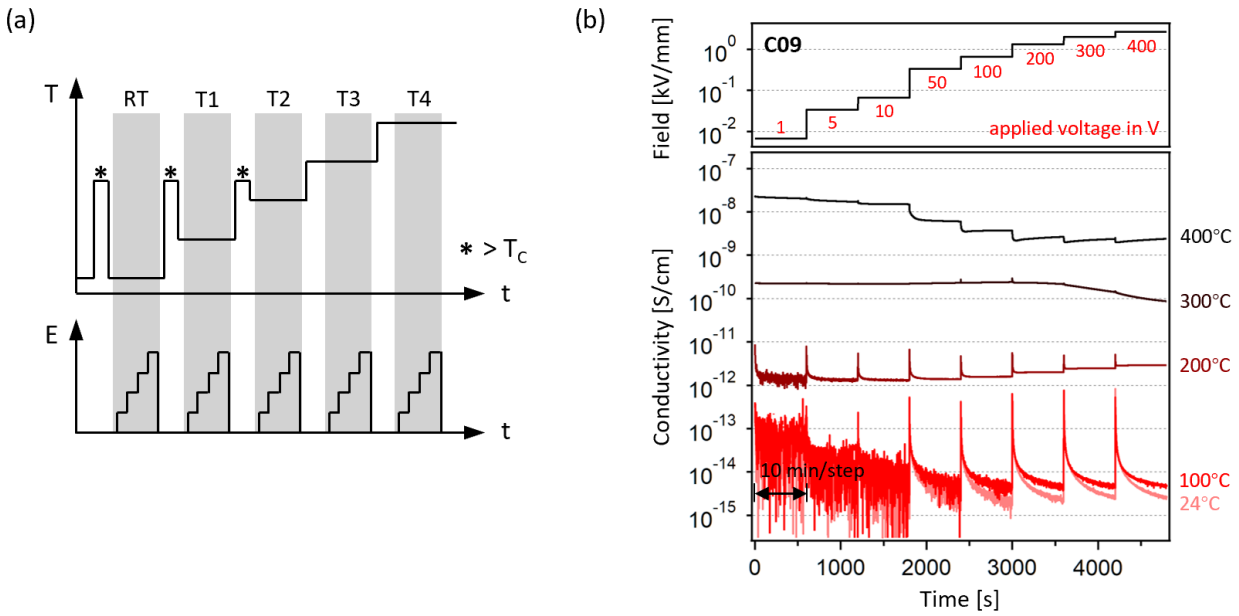

Figure 5.1.: Example of measurement for the electric-field- and temperature-dependent dc conductivity. (a) Schematic measuring procedures; (b) data of composition C09 as an example.

to cause severe deviation and becomes unusable. According to the data obtained with fields >0.1 kV/mm, this sample can be considered to have a conductivity lower than 10^{-14} S/cm in the temperature range between 24°C and 100°C. Another noticeable issue for the lower-temperature measurements is the relaxation feature of the capacitive device, namely the unsaturated charging or discharging current within a relatively short period after a rapid change of the dc voltage. In Figure 5.1(b), it is obvious that the duration of 10 min is insufficient for the current signals to approach stable magnitudes under any applied field at both 24°C and 100°C, which indicates the necessity of a longer duration of each voltage step if one wants to strictly use the saturated values to quantify the leakage of the sample. The above-mentioned difficulties of measuring conductivities on such highly insulating materials are less severe with the increase of temperature. At 200°C, it can be seen that the measured signal easily gets saturated after a very short charging period at any electric field used here. Also, the calculated conductivity slightly increases with the field, which manifests a non-linear I–V relationship. At even higher temperatures, the field-dependent conductivity exhibits more complicated variations, including the decrease of conductivity within each voltage step (e.g. ⩾300 V at 300°C), the sudden drop of conductivity when higher voltages are applied (e.g. 50 V and 100 V at 400°C), and the resistance degradation with very mild rise of conductivity (e.g. ⩾200 V at 400°C). The most interesting feature shown here is the decreasing tendency of the conductivity at higher field and higher temperature, which emerges remarkably at the top-right corner of the conductivity plot in Figure 5.1(b). This phenomenon will be observed again on other samples, and it will be verified by the dynamic method and discussed in more detail in Section 5.2.

Back to the issue of long charging time of the capacitive samples at lower temperatures, Figure 5.2 gives a comparison based on composition C09 when its lower-temperature conductivity is measured with different durations of each voltage step. Following the procedure in Figure 5.1(b), a similar experiment has been carried out and plotted in Figure 5.2(a), where the duration of each voltage step is extended to 90 min. The effect of the longer duration is very clear. Within each voltage step, the signal is still

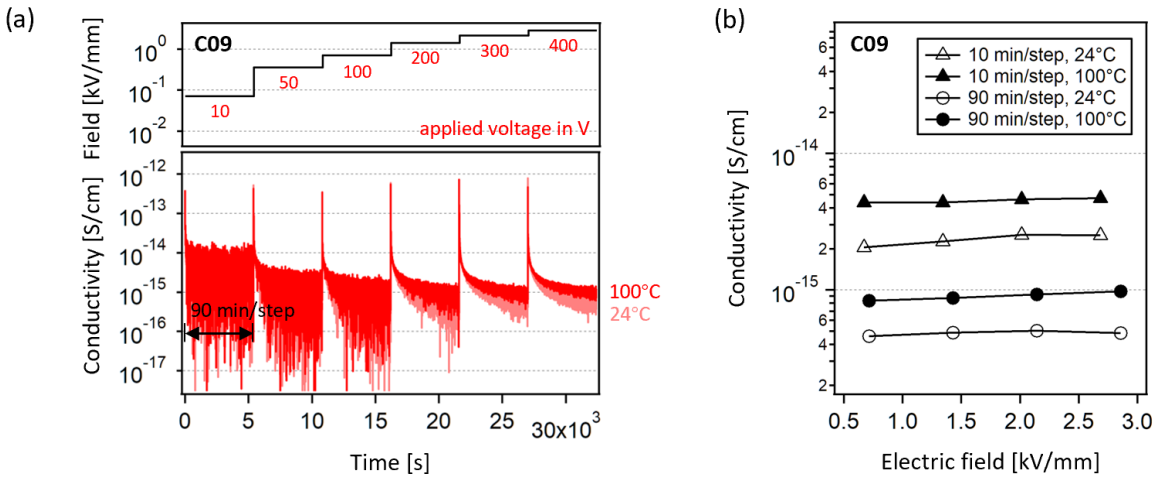

Figure 5.2.: (a) Electric-field-dependent dc conductivity of composition C09 measured at room temperature and 100°C with longer duration of each voltage step (90 min/step). (b) Comparison of the conductivity of composition C09 measured with different durations of each voltage step.

decreasing even after 90 min. Figure 5.2(b) compares the final conductivity values extracted from the last few voltage steps of the two cases using 10 min/step and 90 min/step. The earlier steps measured with lower fields are not included in the comparison mainly because they are too noisy. It is easy to notice that the extracted conductivity values can further decrease down to the magnitudes lower than 10^{-15} S/cm for both 24°C and 100°C, just by waiting for 80 min longer for each step. Therefore, one should always keep in mind that such experimental method may take very long time to reach saturation. The continuous decrease in the acquired current signals, which would induce an error in the determination of the leakage level, might be attributed to many factors, for example the minor movement of FE domain walls/AFE domain boundaries, the migration of charged defects, some interface effects related to grain boundaries, or the leakage within the measurement circuit. Nevertheless, one could decide a sufficiently suitable waiting time in practice, keeping a balance between the accuracy and the total measuring time. In the present work, an overview of the electric-field- and temperature-dependent conductivity is needed, so the duration of 10 min for each voltage step is always applied to the other samples, same as the case in Figure 5.1(b).

Using the same procedure as for composition C09, the electric-field- and temperature-dependent dc conductivities of the selected samples of the C-series (C00 and C11), X-series (X01 and X02), and A-series (A01 and A02) are displayed in Figures 5.3, 5.4, and 5.5, respectively.

The dependence of conductivity of compositions C00 and C11 is similar to that of C09. Composition C00, which has the lowest Ti content (0%) in the C-series, shows slightly lower conductivities than those of C09 and C11 at all temperatures from 100°C to 400°C. Surprisingly, the room-temperature conductivity of composition C00 seems to be higher than at 100°C. As for composition C11, the most obvious difference is the curves at the bottom-right corner of the conductivity plot, where the conductivity is significantly high at 200–400 V (1.37–2.74 kV/mm) at both room temperature and 100°C. From the P–E loops given in Figure 4.5, it is known that for composition C11 such high electric fields are already

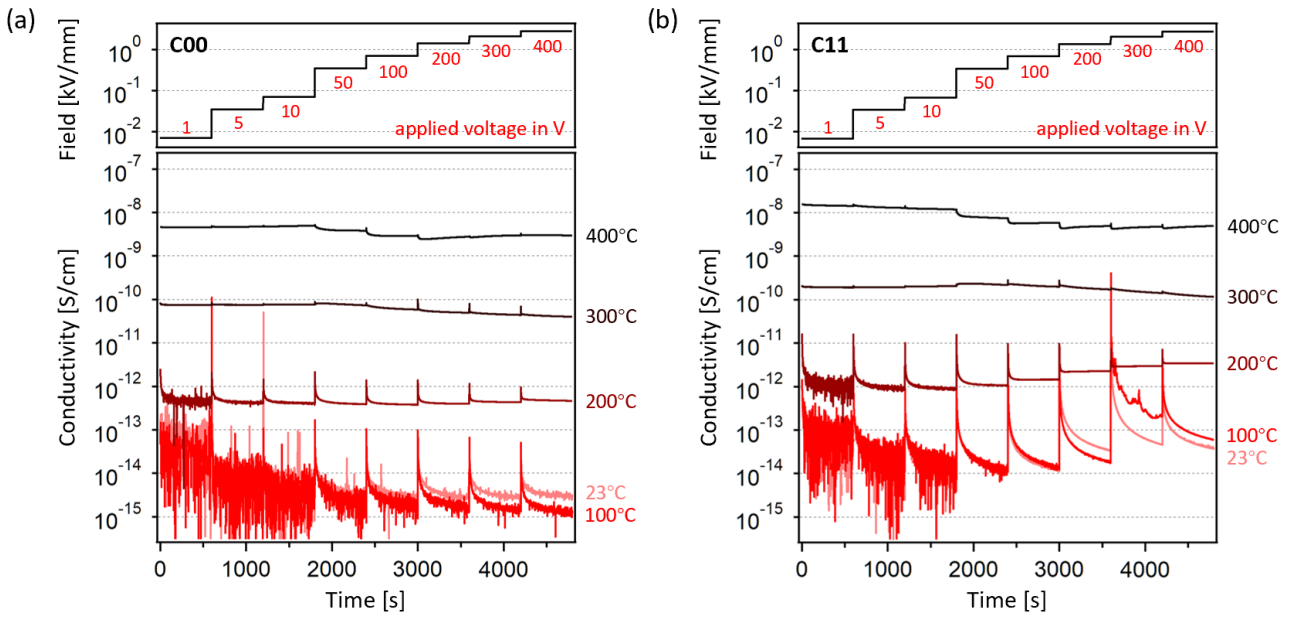

Figure 5.3.: Electric-field- and temperature-dependent dc conductivities of compositions C00 and C11.

sufficient to induce a considerable amount of FE polarization at these temperatures, which is thought to cause the particular variation of the conductivity curves.

Compositions X01 and X02 have less La content than C09 and are expected to show the effect of the La dopant on the electrical conductivity. Composition X02, which contains only 1% La on the A-site, has slightly higher conductivities at all investigated temperatures compared with the 2% La composition C09. The curves at the bottom-right corner of its conductivity plot possess the similar feature to the case of composition C11, which is again attributed to the formation of FE polarization under such conditions (see the P–E loops in Figure A.3). Besides, the X02 sample exhibits a fast increase of conductivity at 400°C when 200 V (1.33 kV/mm) is applied. Such breakdown phenomenon has not been observed in any C-series sample under the same testing conditions. In contrast to composition X02, the X01 sample shows a totally different field and temperature dependence of the conductivity. The measurement is ended at only 200°C and 200 V (1.42 kV/mm) due to the severe instability and subsequent breakdown of the sample. All conductivities measured at 23°C, 100°C, and 200°C are several orders of magnitude higher than those of composition X02. Moreover, the X01 sample experiences more obvious resistance degradation at both 100°C and 200°C, which indicates the existence of more $V_O^{\cdot\cdot}$ in this composition.

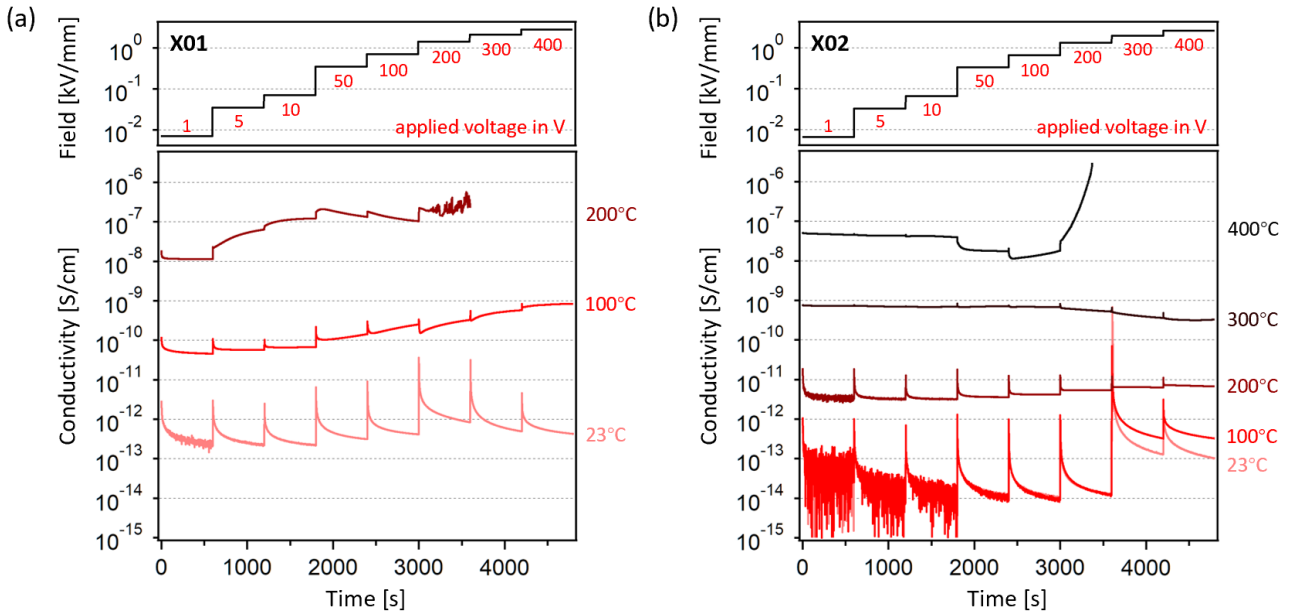

Figure 5.4.: Electric-field- and temperature-dependent dc conductivities of compositions X01 and X02.

Compositions A01 and A02 have extra Fe doping content based on C00, which can further tune the concentrations of relevant point defects, for example $V_O^{\cdot\cdot}$ and V_{Pb}''. Although the conductivities of composition A01 measured at 200°C, 300°C, and 400°C are all slightly higher than those of C00 because of the 1% Fe content on the B-site, the overall field- and temperature-dependence is very similar to that of C00. Besides, the room-temperature conductivity of the A01 sample is also slightly higher than the level at 100°C, same as composition C00. Regarding composition A02, the conductivity curves of all temperatures exhibit further upward shifts compared to the case of A01. A considerable difference between the curves of room temperature and 100°C can be clearly seen. Also, this sample undergoes resistance degradation at 200°C or higher temperatures, much more obvious than the A01 sample. For

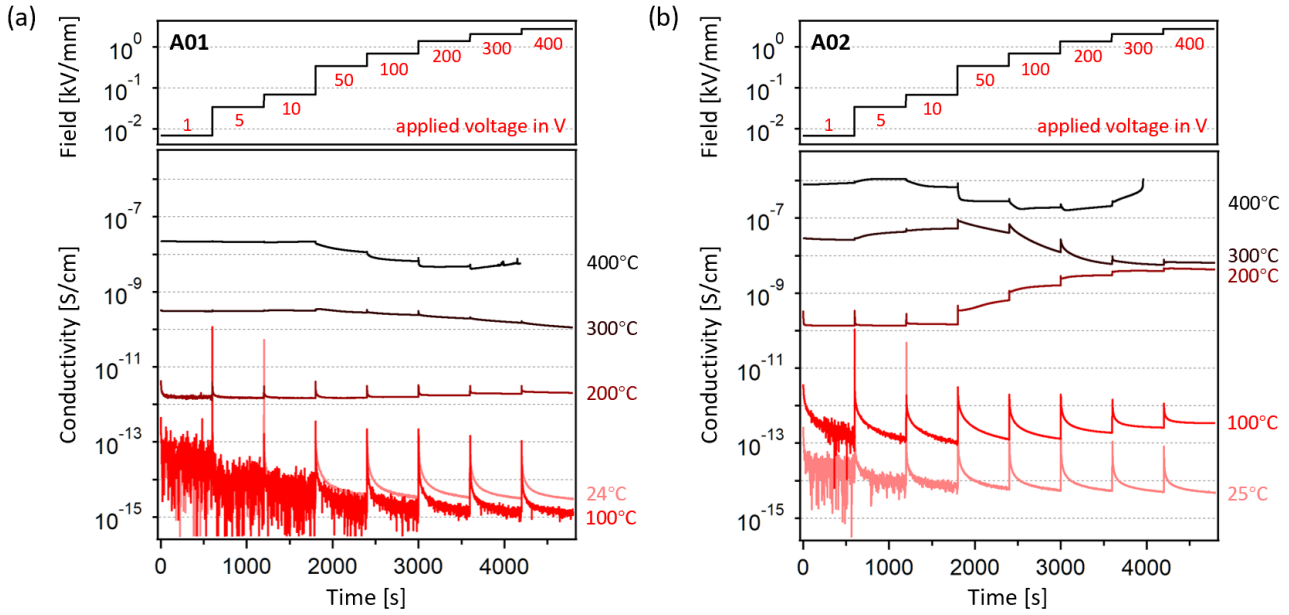

Figure 5.5.: Electric-field- and temperature-dependent dc conductivities of compositions A01 and A02.

both A-series compositions, the experiments are ended with breakdown at 400°C. Moreover, it is very interesting that the field-induced decreasing tendency of conductivity at higher temperatures, which has been already mentioned in the case of C09, can be actually discovered in all compositions involved in the present section.

This part is intended for obtaining an overall impression of the conductivity of the ceramic samples under different conditions of electric field and temperature, which will be used principally as a basis and a reference for the following parts of this work.

5.1.2. Comparison of electrical conductivity between the ferroelectric and antiferroelectric phases of the same composition

One of the core topics of AFE materials is the transition between the ground-state AFE phase and the electric-field-induced FE phase. The purpose of this section is to investigate the difference between these two phases in terms of electrical conductivity. Based on the experience obtained from the field- and temperature-dependent conductivity measurements in Section 5.1.1, the following technical issues should be carefully considered in order to realize such study:

(1) In order to measure the conductivity on the field-induced FE phase by dc method, a sufficiently high field that exceeds the AFE-to-FE transition field is needed. This is why the conductivity measurements with dc 400 V (generating 2.67–2.86 kV/mm through the pellets with thicknesses of 0.14–0.15 mm) have been tested in Section 5.1.1.
(2) The comparison between the AFE and FE phases needs the conductivity value measured on the AFE phase, which still requires a relatively low electric field. It has been observed in Section 5.1.1 that measuring at lower fields and at room temperature cannot generate usable data without

severe noise. Therefore, higher temperature would be better for the acquisition of current signals.

(3) To keep the AFE or FE state of these materials, the temperature should not exceed their T_C. Besides, the elevated temperatures very close to the T_C should also be avoided because of their intermediate or metastable characteristics, which might result in specific domain evolutions accompanied by complex charge movements. Hence, the temperature used for such conductivity measurements should not be too high.

(4) The charging process usually takes very long time in the capacitive devices, especially in the ones with FE polarization. It has been described in Section 5.1.1 that the waiting time of 10 min or 90 min for each voltage step is not enough for detecting any tiny difference of leakage currents. A nearly perfect saturation of the current would be necessary for this purpose.

Taking all these points into consideration, two compositions, C09 and C11, have been selected in this section for comparing the dc conductivities of the AFE and FE phases. Figure 5.6(a) gives the schematic conditions of temperature and applied voltage for each sample. The conductivity measurements were carried out at 140°C. The sequence of applying dc voltage is 100 V → 400 V → 100 V, and each voltage step takes 5 hours. At 140°C, compositions C09 and C11 both exhibit AFE characteristic, whose P–E loops (only half of the initial loops in Quadrant I, measured at 1 Hz) are plotted in Figure 5.6(b, c). For the C09 sample (0.14 mm thick), the applied 100 V and 400 V correspond to the electric fields of ca. 0.71 kV/mm and 2.86 kV/mm (labeled as E1 and E2), respectively. Both of them are located on the left side of the AFE-to-FE transition field. Under these fields, the material is expected to stay in the AFE phase, so the conductivity of two AFE states of the same composition can be compared. For the C11 sample (0.136 mm thick), the applied 100 V and 400 V induce the fields of ca 0.74 kV/mm and 2.94 kV/mm (labeled as E3 and E4), respectively. Different from the case of C09, here the field E3 is still in the AFE region but E4 corresponds to a field-induced FE state. Thus, the conductivities belonging to the AFE and FE phases can be compared on the same sample. In addition, larger ceramic pellets and correspondingly larger electrode diameter (⌀6.5 mm) are utilized here in order to acquire higher and therefore more stable current signals.

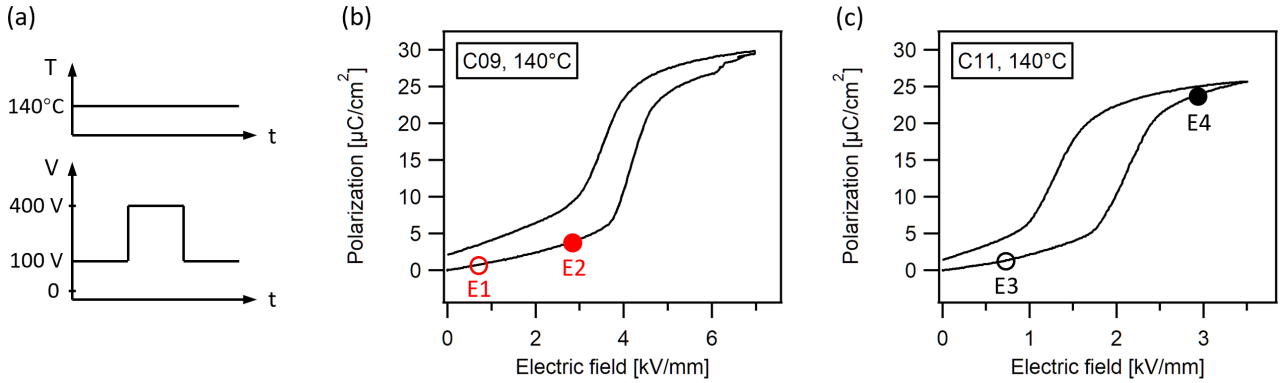

Figure 5.6.: Procedures for measuring the electrical conductivity of the ferroelectric and antiferroelectric phases. (a) Schematic conditions of temperature and applied voltage for each sample; (b) the initial *P*–*E* loop of composition C09 measured at 140°C and two electric fields E1 and E2 used for the dc conductivity measurement; (c) the initial *P*–*E* loop of composition C11 measured at 140°C and two electric fields E3 and E4 used for the dc conductivity measurement.

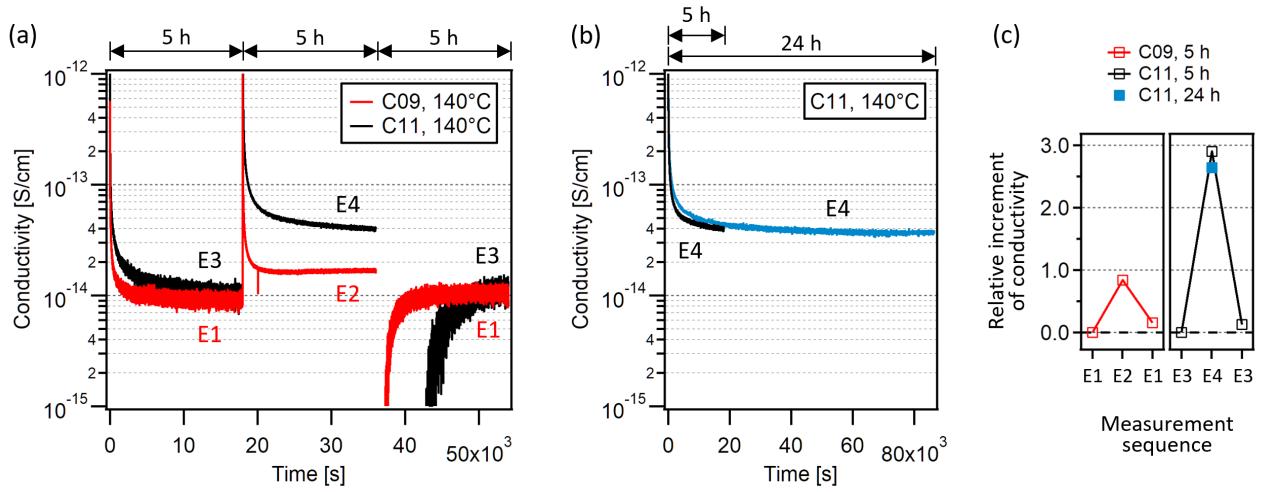

Figure 5.7.: Comparison of the electrical conductivity of the ferroelectric and antiferroelectric phases. (a) The conductivity curves measured at 140°C with the electric field sequence E1→E2→E1 for composition C09 and with the electric field sequence E3→E4→E3 for composition C11; (b) additional conductivity measurement performed on the C11 sample at the field E4 but with a longer waiting duration of 24 hours; (c) evolution of the final conductivity values of each voltage step throughout the measurements on compositions C09 and C11.

Figure 5.7(a) displays the conductivity curves measured on the two compositions. It can be seen that a duration of 5 hours is sufficiently good for most of the voltage steps to reach nearly saturated levels in both samples except the one of composition C11 measured with field E4, where the signal is still recognizably going downward. In order to figure out how long such decrease would last, an additional measurement has been performed that keeps all conditions unchanged but extends the waiting duration up to 24 hours, as shown by the blue curve in Figure 5.7(b). It is clear that the blue curve stops decreasing after about 20 hours, and the difference between the final conductivity levels obtained after 5 hours and 24 hours is sufficiently small (decreased by 15%) compared to the differences among the voltage steps shown in Figure 5.7(a). Besides, there are some other details that can be noticed in Figure 5.7(a). For example, the step measured with field E2 of composition C09 experiences a slight increase after about 2 hours, which might be assigned to a mild resistance degradation due to the long-term stress of high electric field at elevated temperature. Another notable point is the discrepancy in the charging/discharging process between the C09 and C11 samples. (The missing parts on the two conductivity curves in logarithmic scale are caused by the negative discharging current when the voltage is switched from 400 V back to 100 V.) It is evident that the C11 sample needs longer time than C09 to finish charging/discharging. This phenomenon is mainly attributed to the high polarization of the field-induced FE state and is not difficult to understand.

The most important information in Figure 5.7(a) is the final conductivity value at each voltage step if we can assume that sufficiently good saturations have been reached. Figure 5.7(c) shows the evolution of such final conductivity values extracted from the curves in Figure 5.7(a, b). For each sample, the change of conductivity is now expressed by the increment value relative to the first data point. It can be observed that the higher electric field leads to larger conductivity value, which is true for both samples and also in good agreement with the data measured at the temperatures $\leqslant$200°C in Section 5.1.1.

Interestingly, strong difference can be found if one compares the second data points in the two plots of Figure 5.7(c). The field E2, which still keeps the C09 sample in its AFE state, can only increase the conductivity by less than 100% relative to the lower-field value. By contrast, the field E4, which has a comparable magnitude as the field E2 in the case of composition C09 but transforms the C11 sample into a FE state, can increase the conductivity of C11 by more than 250% compared to the value of an AFE state. The data point of composition C11 with the 24-hour waiting duration is also appended to the plot, which shows only a minor downward correction with respect to the 5-hour value and does not change the tendency. Because the C09 and C11 samples have close compositions (only 2% difference in the Ti content) and similar high-temperature conductivity features (see Section 5.1.1), they are expected to have similar field dependence of conductivity at lower temperatures as well. However, Figure 5.7 demonstrates a totally different situation, which could be most probably attributed to the FE phase of the C11 sample induced by the field E4.

Based on this discovery, it is reasonable to speculate that the electric-field-induced FE phase of an AFE material would have a higher electrical conductivity than its original AFE phase. One of the possible interpretations would be the charged domain wall in FEs (see Section 2.5.1). The observation shown here could be thereby regarded as a preliminary evidence of the existence of charged domain walls in the PLZST system. Furthermore, the extremely low conductivity of such PLZST samples technically provides a distinct advantage for detecting tiny extrinsic conductive contributions, for example related to the domain configurations in FEs and AFEs.

5.2. Electrical conductivity by dynamic dc method

5.2.1. Conductivity under thermal cycling

The original purpose of this part is to determine the activation energies of relevant ceramic samples. This needs the electrical conductivity as a function of temperature, but the conductivity is usually acquired isothermally, just like each segment of the static measurement (with constant dc voltage and at fixed temperature) shown in Section 5.1.1. However, huge complexity of the conduction behaviors under different thermal and electrical conditions has been found on the Pb-containing ceramic samples, as already described in Section 5.1.1. Under a given condition combining temperature and electric field, the conductivity usually does not remain constant with time. Instead, a rise, a drop, or a mixture of the previous two may take place, mostly depending on the defect chemistry of the material. Therefore, the isothermal measuring strategy has also a technical limitation that would miss some important evolution of the sample and lead to deviations for the conductivity measurement.

In this section, the conduction behaviors are studied by the dynamic dc method, where the temperature condition consists of thermal cycles. The ramping rate for heating and cooling is set to be moderate so that monitoring samples' gradual changes due to the application of temperature and electric field becomes possible by means of analyzing the shape and slope of the Arrhenius plot (see Section 3.3.3). This part has the following two main tasks: (i) to supplement the investigation of Section 5.1.1; (ii) to determine the activation energies of different compositions. It should be noted that using this method would unavoidably encounter problems related to the non-equilibrium states and processes of the samples although the measurement itself seems to be more time-saving than the isothermal strategy. The non-equilibrium issues include at least the varying capacitive contribution of the samples during the temperature ramping and the effect of migrating charged point defects under electric fields at elevated

temperatures (similar to the resistance degradation). The former will be discussed in detail later in this section, and the latter will be described with more examples in Appendix B.2.

Figure 5.8 illustrates an example of the dynamic conductivity measurement under thermal cycling based on a C09 sample. Figure 5.8(a) sketches the conditions of temperature and voltage. A dc voltage of 5 V is applied to the sample throughout the experiment, generating an electric field of ca. 0.036 kV/mm (sample thickness 0.139 mm). At the same time, the temperature profile of one cycle consists of three stages: heating-up (with a rate of 2.5°C/min from room temperature to 400°C), dwelling (at the maximum temperature for 30 min), and cooling-down (with a rate of 2.5°C/min back to room temperature). The dwelling duration and the number of cycles can be modified for different purposes. The conductivity measured during the second thermal cycle of this C09 sample is displayed in Figure 5.8(b) as an example, where the conductivity curve can be divided into three segments (labeled as I, II, and III) that correspond to the three stages in the temperature profile. Generally, the conductivity

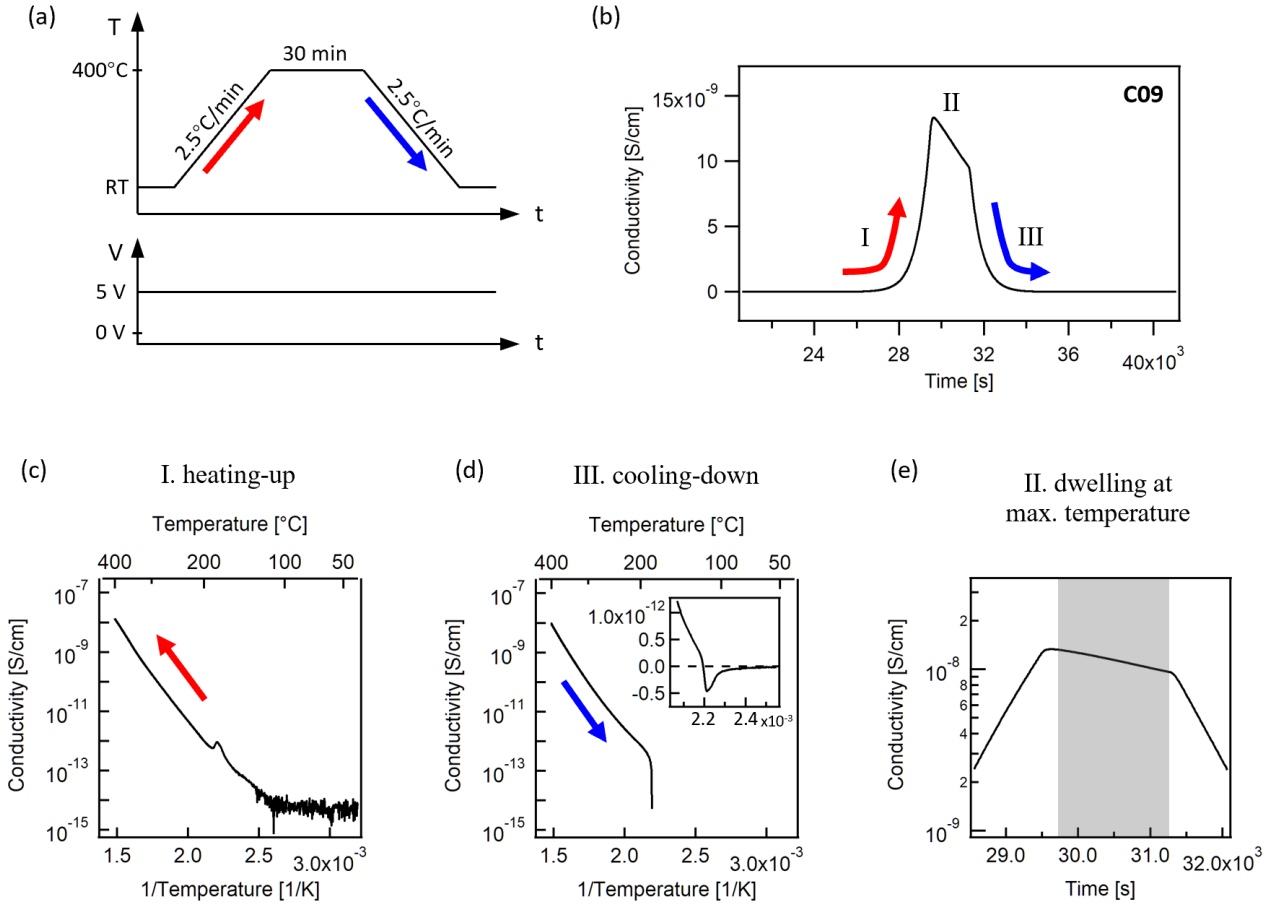

Figure 5.8.: Example of conductivity measurement under thermal cycling on a sample of composition C09. (a) Schematic measuring procedures; (b) a segment of the curve of conductivity vs. time corresponding to a single thermal cycle; (c) the Arrhenius plot of the heating-up stage; (d) the Arrhenius plot of the cooling-down stage; (e) the change of conductivity in the dwelling stage at the maximum temperature (the part with gray background).

increases in the heating-up stage and decreases during the cooling-down. In addition, the 30-min dwelling at 400°C results in a clear decrease of the conductivity as well, which can be actually regarded as a static measurement exactly like what have been done in Section 5.1.1. Such decrease of conductivity implies either an non-equilibrium between the bulk material and the atmosphere or a slow internal redistribution of certain charge carriers or charged defects under the present conditions. Figure 5.8(c, d) gives the Arrhenius plots for the heating-up and the cooling-down segments, respectively. The evolution of conductivity follows the red arrow during the heating-up and the blue arrow during the cooling-down. In this case, the measured current in the heating-up stage is always positive, while the one in the cooling-down stage becomes negative at lower temperatures. This is the reason why some part of the conductivity curve does not appear in the logarithmic plot. (The insert of Figure 5.8(d) plots the negative part in the linear scale.) Figure 5.8(e) magnifies the region near segment II in the conductivity–time plot of Figure 5.8(b). In Appendix B.2, the dwelling segments of conductivity will be described in more detail and they will be separately plotted in logarithm against time.

Prior to the comparisons of obtained conductivity curves among various ceramic samples, it is necessary to figure out what information the Arrhenius plot of such materials could tell us. The Arrhenius plot of another C09 sample is given as an example in Figure 5.9. This sample is basically similar to the previous one. Only one thermal cycle up to 400°C is carried out here with a very short dwelling time (only 5 min long). The heating-up and cooling-down segments are drawn in red and blue, respectively. On the heating-up curve, a small peak can be observed in Figure 5.9(a) at ca. 181°C, which is related to the T_C of the material. According to the position of T_C, the whole thermal process can be generally divided into a higher-temperature region where no FE or AFE domain exists and a lower-temperature region where the FE or AFE characteristics may influence the current measurement with a change of temperature. The situations within these two regions should be investigated separately.

The higher-temperature region is magnified in Figure 5.9(b). Interestingly, the heating-up and the cooling-down curves cross over at ca. 312°C in this example. It can be easily noticed that within the temperature range approximately from 280°C to 340°C (indicated by the red shaded area) there is an obvious drop on the slope of the heating-up curve, which reverses the relative positions of the

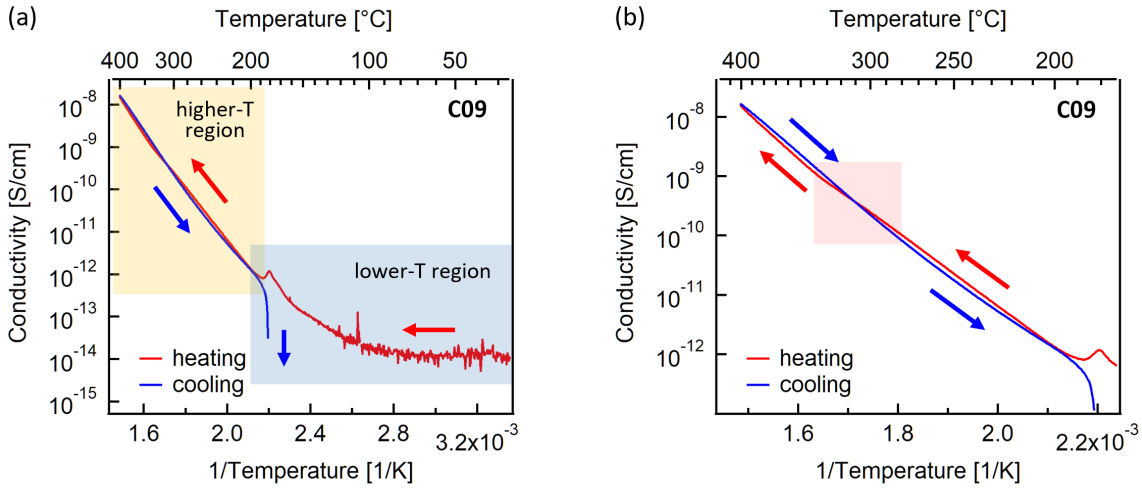

Figure 5.9.: Example of the Arrhenius plot of a sample of composition C09. (a) The higher-temperature and the lower-temperature regions; (b) the magnified higher-temperature region.

two curves. Hence, it becomes important to learn the temperature-dependent slope of the Arrhenius plot (for calculating activation energies) along both the heating-up and the cooling-down curves. The phenomenon that the slope during the heating-up manifests a drop at around 300°C has been observed in most of the relevant ceramic samples in this work. Such effect could most probably be assigned to the previously mentioned resistance-degradation-like evolution of the sample under the external electric field at high temperatures. More details will be given in Appendix B.2.

Regarding the lower-temperature region marked in Figure 5.9(a), the shape of the conductivity curve is worth a discussion. As mentioned before, part of the conductivity curve measured during the cooling-down does not show up in the Arrhenius plot because of the negative current. The negative peak usually occurs also near the T_C, which indicates that it should be caused by the significant change in the capacitance of the sample, same as the case with the positive peak during heating-up. Since the negative values are not present in the Arrhenius plot, one may attempt to do more analysis on the heating-up curve, for example quantifying the slope at different temperatures and then calculating the activation energy. However, this might cause misleading conclusions if the dynamic dc method with a ramping of temperature is adopted. The problem is described in Figure 5.10 with the help of a simplified simulation. In Figure 5.10(a), the experimentally measured Arrhenius plot of a C09 sample (same as the one in Figure 5.9) is drawn in blue dots. Besides the positive peak related to the T_C (labeled as "ii"), there are three segments along the heating-up branch where it seems to be possible to determine some activation energies (labeled as "i", "iii", and "iv"). Segment "i" can be assigned approximately to the contribution of the sample leakage, which is worth a careful quantification of the activation energy. Segments "iii" and "iv" with much smaller slopes, however, should have no direct correlation with smaller activation energies. Rather, their slopes are closely related to the way how such dc measurements are performed. The main idea for the simulation is to involve the charging and discharging currents of the capacitor when analyzing the Arrhenius plot. There are basically two reasons why the capacitive contribution of the acquired current signal should not be ignored. First, these FE or AFE samples usually possess a significant change in the dielectric permittivity (and thereby the capacitance) with temperature, so there must be a charging current when the capacitance increases and a discharging current when the capacitance decreases. Second, it is noticed that the conductivities of these Pb-based samples are indeed quite low, and the low leakage current might render the capacitive signal more conspicuous and recognizable.

For the simulation, we first suppose an ideal leakage component, namely a straight line in the Arrhenius plot with a constant slope (see the black lines in Figure 5.10). The position of this straight line can be adjusted by setting its conductivity value at room temperature. Afterwards, we take the permittivity–temperature relation of the relevant composition, which has already been studied in Section 4.2.1, to simulate the change of sample's capacitance with time during the temperature ramping process. It should be noted that the dielectric permittivity is normally measured at different frequencies via ac method, but here we treat dc data. Considering that composition C09 has a relatively weak frequency dependence of permittivity (see Figure A.4(g)), we just simply adopt the permittivity–temperature curve obtained at the minimum frequency 100 Hz. Additionally, we should assume that the permittivity–temperature relation is not dependent on the ramping rate of temperature in Section 4.2.1. In the simulation, the ramping rate of temperature (T–t) can be tuned in order to fit any extra current induced by the change of capacitance ($\mathrm{d}C/\mathrm{d}t$), but the capacitance–temperature relation (C–T) will be always fixed. Now we can calculate the charging and discharging currents by

$$I = \frac{\mathrm{d}Q}{\mathrm{d}t} = C \cdot \frac{\mathrm{d}U}{\mathrm{d}t} + U \cdot \frac{\mathrm{d}C}{\mathrm{d}t}. \tag{5.1}$$

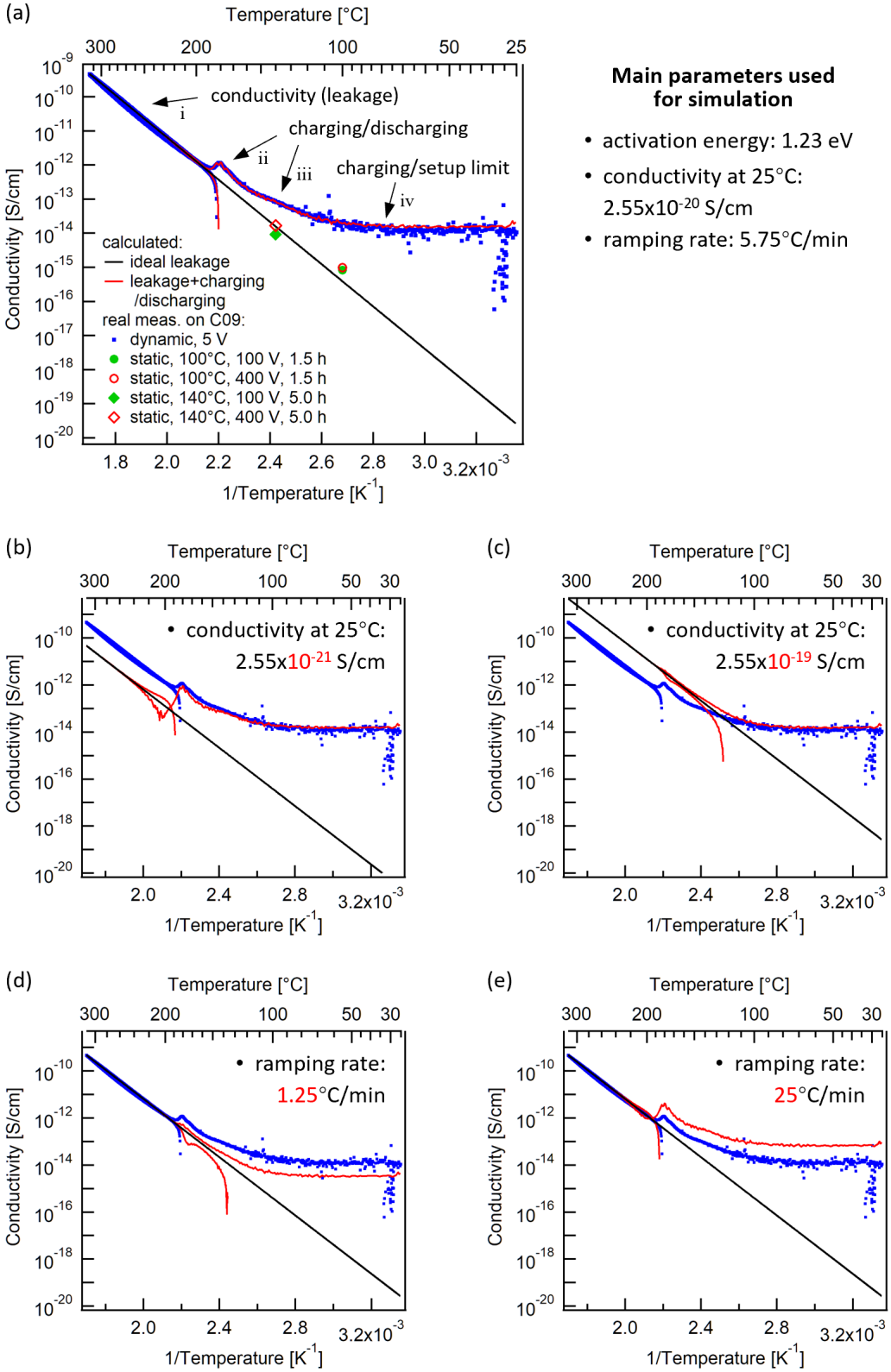

Figure 5.10.: Simulation of the Arrhenius plot of a C09 sample in the lower-temperature region by considering the charging and discharging currents of the capacitive device during a dynamic dc conductivity measurement.

Since the dc bias is constant throughout the measurement ($\mathrm{d}U/\mathrm{d}t = 0$), we have

$$I = U \cdot \frac{\mathrm{d}C}{\mathrm{d}t}. \tag{5.2}$$

Such extra current should be superimposed on the ideal leakage signal, i.e. the total conductivity measured by this dc method is comprised of the leakage and the capacitive components. According to Equation 3.4, the extra capacitive component of electrical conductivity σ_c can be therefore calculated by

$$\sigma_\mathrm{c} = \frac{I \cdot d}{U \cdot A} = \frac{\mathrm{d}C}{\mathrm{d}t} \cdot \frac{d}{A} = \frac{\varepsilon_0 \frac{A}{d} \cdot \mathrm{d}\varepsilon_\mathrm{r}}{\mathrm{d}t} \cdot \frac{d}{A} = \varepsilon_0 \cdot \frac{\mathrm{d}\varepsilon_\mathrm{r}}{\mathrm{d}t}. \tag{5.3}$$

The sum of the ideal leakage and the capacitive components is plotted in Figure 5.10 with red curves, which is expected to simulate the Arrhenius plot of conductivity by using the dynamic dc method described in this section. Figure 5.10(a) displays a simulated result, in which a set of parameters (the activation energy, the conductivity at 25°C, and the temperature ramping rate) are utilized to depict the real measurement of the C09 sample. It is obvious that the shape of the whole conductivity curve within the lower-temperature region, including segments “ii”–“iv”, can be described sufficiently well by taking the charging/discharging currents into account. It should be noted that the ramping rate used to fit the real measurement data is 5.75°C/min, which is higher than what is actually applied (2.5°C/min). This non-negligible deviation might be related to the fact that the permittivity–temperature relation used for the simulation of the Arrhenius plot is obtained by ac method (100 Hz) but the simulated ramping itself is actually a dc process. Figure 5.10(b, c) shows the two simulated cases (still see the red curves) where the ideal leakage component of conductivity is shifted by one order of magnitude downward and upward, respectively. For segments “ii” and “iii” remarkable change in the curve shape can be observed. By contrast, segment “iv” still remains almost horizontal, and its magnitude shows no obvious difference. Figure 5.10(d, e) gives two more simulated cases where the temperature ramping is decelerated and accelerated, respectively. Both of them exhibit not only a variation on the shape of segment “ii” but also a clear change in the magnitude of segment “iv”. By comparing the four cases shown in Figure 5.10(b–e), one can conclude that the shape and position of segments “ii”–“iv” on the conductivity curve closely depend on the room-temperature conductivity and the temperature ramping rate. Compared to the ideal leakage component, the much higher capacitive contribution, which could be considerably enhanced by a faster ramping, would dominate the acquired current signal, concealing most details in terms of the leakage behaviors in the lower-temperature region. Therefore, quantifying the activation energies of segments “iii” and “iv” actually has no scientific meaning. Moreover, the very low conductivity 2.55×10^{-20} S/cm at room temperature, which is approximately determined by an extension of the higher-temperature part (segment “i”), should correspond to a current in the order of 10^{-19} A when 5 V is applied to this sample. Such a low current is far beyond the measuring range of a picoammeter. That is to say, the setup used in this work has a limitation to measure the real conductivity of such highly insulating materials around room temperature. Even with the static dc method in the Section 5.1, the same limitation would also be expected. Nevertheless, applying higher voltage (field) or heating the sample up is expected to effectively increase the acquired current signals, which would help the determination of the conductivity. In Figure 5.10(a), four conductivity data points at 100°C and 140°C extracted from the previous static measurements in Figures 5.2(b) and 5.7(a) are appended for a comparison. It is clear that they are all located near the black straight line that denotes the ideal leakage component, rather than along the curve of the real dynamic measurement (blue dots).

5.2.2. Comparison of the Arrhenius plots of different compositions and determination of the activation energies

With the general impression of the features of the Arrhenius plots for composition C09, a comparison among a wider range of relevant materials can be performed. The measuring procedures basically follow the schematic in Figure 5.8(a). The ramping rate of temperature is always 2.5°C/min for both heating-up and cooling-down stages, and the dwelling time at the maximum temperature 400°C is set to be only 5 min here. The applied voltage for the electrical measurement is 5 V for most samples except the two compositions that are expected to have much higher conductivities (0.1 V for X01, and 0.5 V for A02). It should be noted that the ceramic pellets are 0.13–0.15 mm thick, which leads to slightly different electric fields even if the applied voltages are the same. Table B.1 in Appendix B.1 lists the thicknesses, the applied voltages, and the corresponding fields of relevant samples. Moreover, every sample has been annealed at the temperature higher than its T_C before the conductivity experiment. Figure 5.11(a–c) shows the comparison among selected compositions of C-, X-, and A-series, respectively. For these dynamic dc measurements, the Arrhenius plots only belonging to the first thermal cycles are displayed. In addition, the conductivity values measured with the static method at 200°C, 300°C, and 400°C that are extracted from Figures 5.1, 5.3, 5.4 and 5.5 in Section 5.1.1 are also added to the plots in Figure 5.11. These discrete data points are the final conductivity values after 10 min of selected voltage steps (the steps with 1 V for compositions X01 and A02; the steps with 5 V for all the rest). Relevant sample details are also given in Table B.1 in Appendix B.1. Here in Figure 5.11, we will principally focus on the Arrhenius relations within the higher-temperature region as defined in Figure 5.9(a).

As can be noticed in Figure 5.11(a), all discrete data points of the static method are situated very close to the continuous conductivity curves obtained with the dynamic method, i.e. the two methods can depict very similar tendencies of the Arrhenius relation in the higher-temperature region. Obviously, the temperature-dependent conductivities of the three C-series compositions are generally similar at the temperatures >200°C except that the C11 sample manifests a relatively steeper curve between 200°C and 300°C. Among these three compositions, the C00 sample exhibits the lowest conductivity in the whole temperature range. This phenomenon might be related to the fact that composition C00 has the lowest Ti content (0%) in the C-series.

Figure 5.11(b) compares the two X-series compositions X01 and X02 with composition C09. These three samples share the same B-site ratio, and their La concentrations on the A-site are 0%, 1%, and 2%, respectively. It is clear that more La dopant would lead to a decrease of the conductivity in the higher-temperature region, but such doping effect tends to a saturation when the donor content reaches 1% (as composition X02). This observation is basically in line with the description in Ref. [45] that 1% donor content in PZT (intrinsically p-type) can reduce the conductivity by about three orders of magnitude but more donor over 1% does not further modify the conductivity noticeably. Another remarkable feature in Figure 5.11(b) is the shape of the conductivity curve of composition X01. Its heating-up and cooling-down segments possess such a large distinction that the activation energies within the higher-temperature region become quite indeterminate. Besides, the only discrete data point of conductivity obtained through the static method at 200°C (no available data at higher temperatures due to breakdown) stays near the heating-up curve, which implies certain irreversible changes of this sample happening at elevated temperatures and under the applied dc bias. The electrochemical instability of composition X01 (severe reduction on the Pb-site at cathodic interface) observed during the in situ XPS experiment in Chapter 6 may provide an interpretation for this issue (see Section 6.2.1). In contrast to composition X01, the difference between the dynamic and static methods seems to be

not obvious for composition X02, which is similar to the case of C09. With respect to the special curve shape of the X01 sample, which might be attributed to an evolution like resistance degradation, some descriptions will be provided in Appendix B.2.

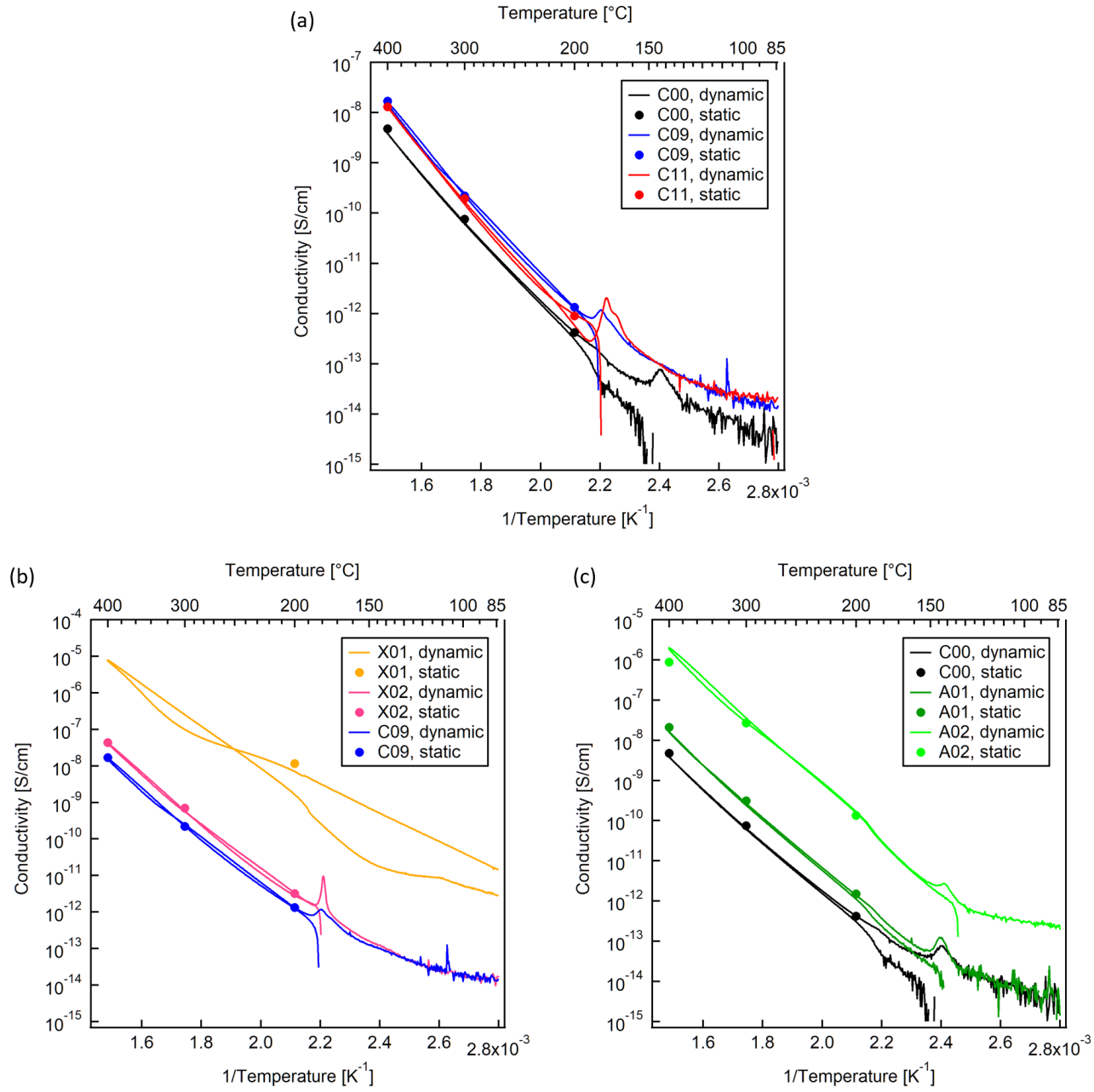

Figure 5.11.: Comparisons of the Arrhenius plots of various compositions measured with the dynamic dc method. (a) Selected compositions of the C-series; (b) selected compositions of the X-series, and composition C09 is appended; (c) the A-series, and composition C00 is appended. Some conductivity data points measured at 200°C, 300°C, and 400°C with the static dc method in Section 5.1.1 are also included for comparisons.

Figure 5.11(c) compares the two A-series compositions A01 and A02 with composition C00. These three samples have the same A-site ratio (2% La) but different Fe content on the B-site (0%, 1%, and 2% Fe for compositions C00, A01, and A02, respectively). Fe dopant is an acceptor, which should be able to counteract the doping effect of La donor. As expected, the conductivity increases with the increasing Fe concentration. It should also be noticed that the conductivity increment from A01 to A02 (1% more Fe) is much greater than that from C00 to A01 (also 1% more Fe), which is very similar to what have been found previously in the case of La doping in Figure 5.11(b). One could say that Figure 5.11(b) compares different donor-doping effects, while Figure 5.11(c) indeed treats different "net-donor" concentrations. Moreover, the Arrhenius plots of these three samples are basically parallel between 200°C and 400°C. The only exception is the heating-up curve of the A02 sample where a slight drop of the slope can be observed at around 300°C, similar to the case in Figure 5.9(b).

Figure 5.12 makes a direct comparison of the conductivities at 300°C and 400°C of these compositions. The data points measured with both the dynamic and the static methods are included. Composition X01 is not displayed here because of the lack of the static data at these temperatures and the strong non-equilibrium shape in its Arrhenius plot. The three groups of comparison displayed in Figures 5.11 and 5.12 could provide a preliminary impression of the temperature-dependent conductivities of all the three ceramic series. On the one hand, the influence of doping (or co-doping) on the electrical conductivity can be characterized on the higher-temperature side of the Arrhenius plots. On the other hand, it can be noticed that most of these Pb-containing compositions exhibit nearly parallel Arrhenius relations at the temperatures >200°C except the undoped PZST composition X01. This indicates a strong similarity in the conduction mechanism of these materials. Thus, a detailed study on the activation energies of such Arrhenius plots is necessary.

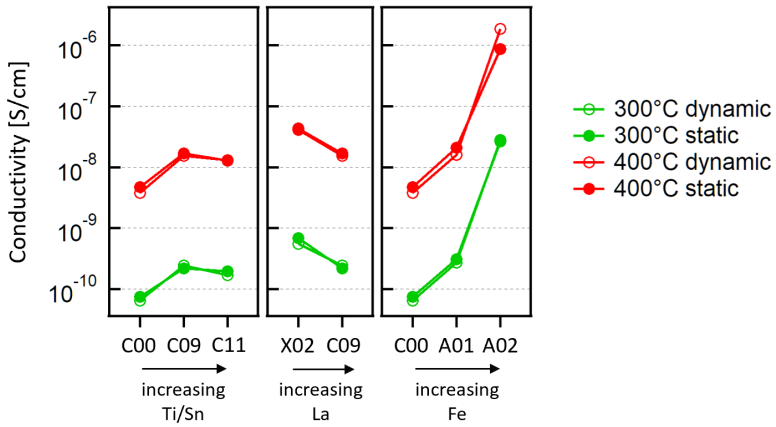

Figure 5.12.: Comparison of the conductivities of relevant compositions at 300°C and 400°C measured with the dynamic and the static dc methods, respectively.

Figure 5.13 compares the activation energies of different compositions extracted from the temperature-dependent conductivity measurements shown in Figure 5.11. For the static method, the activation energy is calculated from the slope of the straight line through the two data points at 300°C and 400°C. For the dynamic method, only the narrow region near the maximum temperature 400°C is used to determine the activation energy, and the data belonging to both the heating-up and cooling-down segments are provided for each composition. It can be noticed that the heating-up and cooling-down values always show clear difference in most cases except composition C00. For compositions C09 and

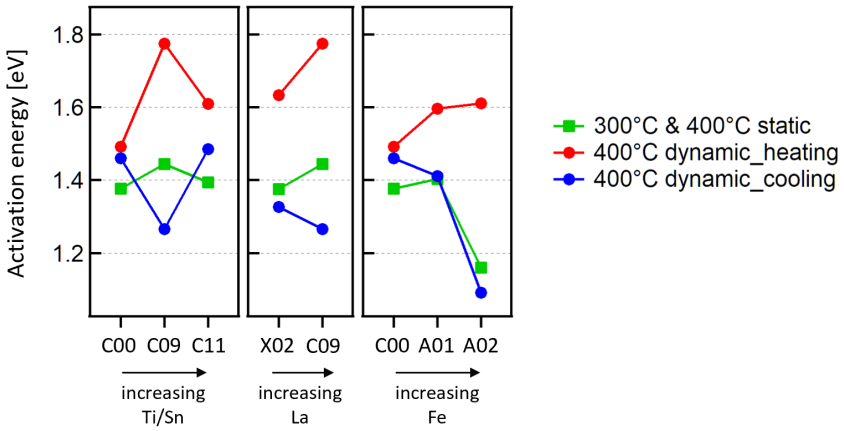

Figure 5.13.: Comparison of the activation energies of relevant compositions at 300°C and 400°C extracted from the dynamic and the static dc conductivity measurements.

A02, such differences can be up to 0.5 eV, which brings difficulty of determining the reliable activation energies based on the method presented here. The problem originates from the fact that conductivity curves in the heating-up and cooling-down stages do not coincide with each other, which is very obvious in compositions X01, A02, and C09 (see Figure 5.11). Such phenomenon could be very probably related to the migration and redistribution of charged point defects or the re-orientation of defect dipoles under electric field and at elevated temperature. More details about this "resistance-degradation-like" behavior will be given in Appendix B.2. In contrast to the dynamic method, which shows considerable uncertainty in the determination of activation energies, the static strategy seems to be more straightforward to depict the temperature dependence of conductivity. One should also keep in mind that appropriate measuring conditions (temperature and electric field) are still needed for the static dc measurements because any severe resistance degradation of the sample, which will give rise to an increase of the acquired conductivity, should be avoided. According to the static data points given in Figure 5.13, the activation energies between 300°C and 400°C of these materials are always located around 1.4 eV except for the cases of compositions A02 and X01 (X01 is not given here). The strongly deviating conductivity–temperature relations or activation energies of these two compositions may also be caused by the resistance degradation happening already at 200°C, which indicates the high $[V_O^{\cdot\cdot}]$ in the materials due to their lower "net-donor" doping concentrations.

5.3. Summary

The dc conductivities of various Pb-based FE and AFE ceramics, which are expected to be very good insulators, have been studied by static and dynamic methods. The static method measures the conductivity at fixed temperatures, while the dynamic experiments are performed with the ramping of temperature.

In Section 5.1.1, the conductivities have been measured at different electric fields and temperatures by the static method. Such measurement can provide a fast overview of the conduction behavior of the sample. However, it has some limitations when the studied materials are insulating dielectrics. On the one hand, the waiting time of each voltage step should be sufficiently long, otherwise the continuously decreasing current (discharging of the dielectric) would lead to a deviation of the conductivity. On the

other hand, it has been noticed that the previous measuring steps, i.e. the history of the sample, could influence the subsequent ones. Nevertheless, useful information can still be extracted from these tests. For some compositions, an increase of the conductivity can be seen at elevated temperatures, similar to the resistance degradation of STO. Besides, for most of the samples involved in this work, a decreasing tendency of the conductivity can clearly be observed at $\geqslant$300°C when higher fields are applied. This would also be attributed to a redistribution of mobile charged defects, for example $V_O^{\cdot\cdot}$ and even V_{Pb}'', within the bulk samples. The origin of this phenomenon is not yet clear.

In Section 5.1.2, the conductivities belonging to the AFE and the FE phases have been directly compared. This can be realized by applying two different electric fields to the same piece of sample. The lower field does not exceed the AFE-to-FE transition point of the AFE material, but the higher field does. Much longer waiting time for each voltage step has been used in this experiment compared to that of Section 5.1.1 in order to obtain better saturation of the leakage currents and thereby more reliable comparison of the conductivities. It has been found that the high-field-induced FE phase is somehow more conductive than the unswitched AFE phase. The difference is not very noticeable, so it is very likely hidden by the relatively higher leakage background in most materials. The extremely high resistivity of the PLZST compositions gives the chance to observe such a small discrepancy. The origin of this observation might be the intrinsic difference of the bulk (contribution of the lattice) or the existence of charged domain walls/boundaries. The other candidates, such as grain boundaries, are likely not related as they are usually not expected to do anything electrically during the AFE-to-FE phase transition and the FE domain switching. However, this is speculative and further investigation is still needed.

In Section 5.2, the dynamic method has been applied. From the technical point of view, this type of conductivity measurement with ramping of temperature can save time, and it can also record the continuous variation of the sample during the heating-up and cooling-down stages. However, such variation, which can be most likely assigned to certain non-equilibrium processes (e.g. resistance degradation), will modify the shape of the Arrhenius plots and therefore influence the determination of activation energies (relevant descriptions given in Appendix B.2). Besides, the charging and discharging currents induced by the significant change of the dielectric permittivity (thereby the capacitance) in the FEs and AFEs at T_C will be superimposed on the Arrhenius plot. Such effect will become non-negligible or even fatal if the intrinsic leakage of the sample is extremely low. In this case, the Arrhenius plot near and below the T_C is not worth an analysis. Nevertheless, the higher-temperature region of the Arrhenius plot seems to be in good agreement with the data extracted from the static measurements for most compositions in this work. For the C-series, where the Ti/Sn ratio is varying, it has been observed that the lower Ti content may result in lower conductivity. For the X- and A-series, one may conclude that the donor (or "net-donor") doping can effectively decrease the conductivity. More importantly, it can be noticed that the compositional modifications do not seem to affect the slope of the Arrhenius plot (activation energy) although these materials exhibit clear difference in the magnitude of the conductivity. With respect to the activation energy, values around 1.4 eV seem to be a common characteristic of these materials at temperatures between 300°C–400°C. More discussion about this value and the possible conduction mechanism of these Pb-based ceramics will be given in Chapter 8.

6. In Situ X-Ray Photoelectron Spectroscopy at Interfaces with Electrochemical Oxidation and Reduction

This chapter describes detailed measurement sequences and results according to the in situ XPS approach introduced in Section 3.4.5. Two types of top electrodes, RuO_2 and ITO, are applied to different Pb-based ceramics in order to search for the lower- and the upper limits of the Fermi level in such dielectrics, respectively. In Section 6.1, two cases with RuO_2 anode will be demonstrated and the limitation of RuO_2 used for our purpose will be discussed. In Section 6.2, more experiments with ITO cathodes in different Pb-containing dielectric materials will be described and compared in terms of the occurrence or absence of reduced Pb species. Using this approach, a transition level of $Pb^{2+/0}$, which acts as a trap for electrons, can be determined quantitatively for some of the studied compositions. This indicates the existence of an upper limit of the Fermi level in these Pb-containing FEs and AFEs. For convenience,

Table 6.1.: Pb-containing ceramic samples used for the in situ XPS experiments for determining Fermi level limitation at electrochemically polarized interfaces.

Sample No.	Bulk material	Top electrode		Temperature	Relevant content in this work
		Material	Polarity		
BHX01X01	X01	RuO_2	anode	250°C	Section 6.1.1 & 6.1.2
BHC09X13	C09	RuO_2	/	250°C	Section 6.1.2
BHA02X01	A02	RuO_2	/	200°C	Section 6.1.2
BHA02X02	A02	RuO_2	anode	300°C	Section 6.1.2 & Appendix C.1.1
BHPZT41	PIC 151	RuO_2	anode	300°C	Section 6.1.1 & 6.1.2
BHPZT46	PIC 151	RuO_2	anode	200°C	Section 6.1.2
BHX01X02	X01	ITO	cathode	250°C	Section 6.2.1 & 6.2.2
BHC09X14	C09	ITO	cathode	250°C	Section 6.2.1 & 6.2.2
BHA02X04	A02	ITO	cathode	300°C	Section 6.2.2 & Appendix C.1.2
BHPZT42	PIC 151	ITO	cathode	300°C	Section 6.2.1 & 6.2.2
BHPZT43	PIC 151	ITO	cathode	300°C	Appendix C.1.4
PH004	PZT53/47	ITO	cathode	250°C	Section 6.2.2 & Appendix C.1.3
BHPMN8_10	PMN	ITO	cathode	250°C	Section 6.2.2 & Appendix C.1.5

Table 6.1 gives a list of all samples used in this part. Their relevant experimental procedures and results can be found either in the current chapter or in Appendix C.1.

6.1. Interfaces with RuO_2 anode

RuO_2 was selected as the first electrode material to test the in situ XPS approach in this chapter. As introduced in Section 3.4.5, RuO_2 with a high work function is expected to realize a relatively low starting point of the Fermi level position at the interface with a dielectric. This has an advantage when exploring the lower limitation of Fermi level within the band gap of the dielectric by operating a solid electrochemical cell at elevated temperature and monitoring the anodic interface. In this section, detailed description of the steps and data for this type of measurement will be given in specific examples. The subsequent experiments, including the ITO-cathode cases in Section 6.2 and all extended results in Appendix C.1, will basically follow the similar presenting styles as demonstrated in this part.

6.1.1. Typical results with detailed procedures

Case 1. PIC 151 with RuO_2 anode at 300°C

Early attempts were carried out on the commercial modified PZT composition PIC 151. A typical example operated at 300°C is given here first. The sample was a 0.15 mm thick ceramic pellet, with a 5 nm thin RuO_2 top electrode and a thick Pt bottom electrode. According to the circuit shown in Figure 3.12,

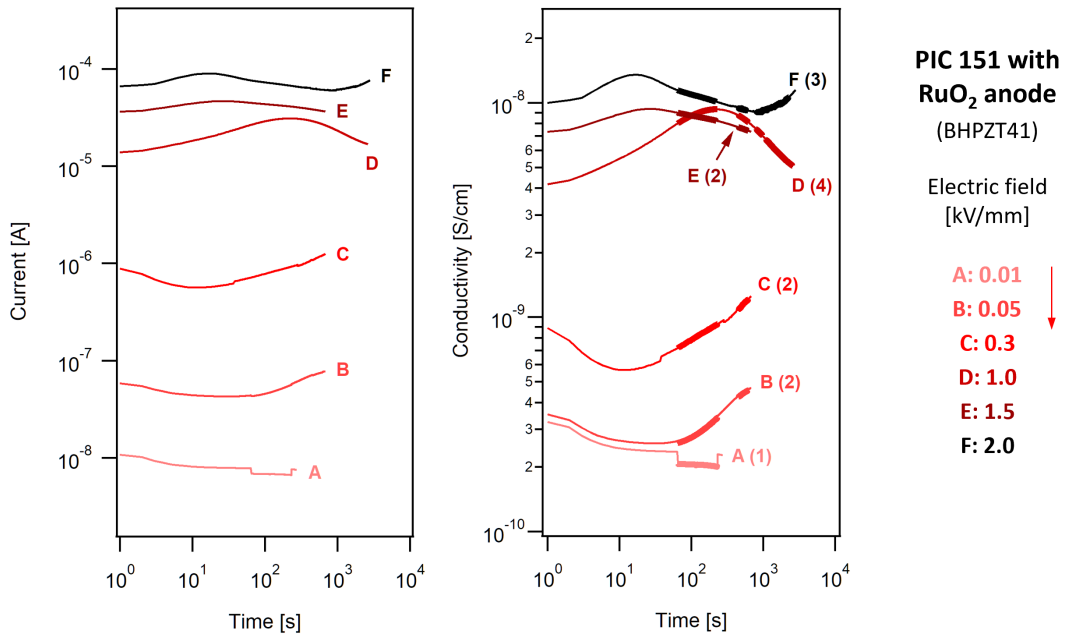

Figure 6.1.: Measured currents and calculated conductivities at 300°C and at stepwise increasing applied electric fields for a PIC 151 sample with RuO_2 anode (sample No. BHPZT41).

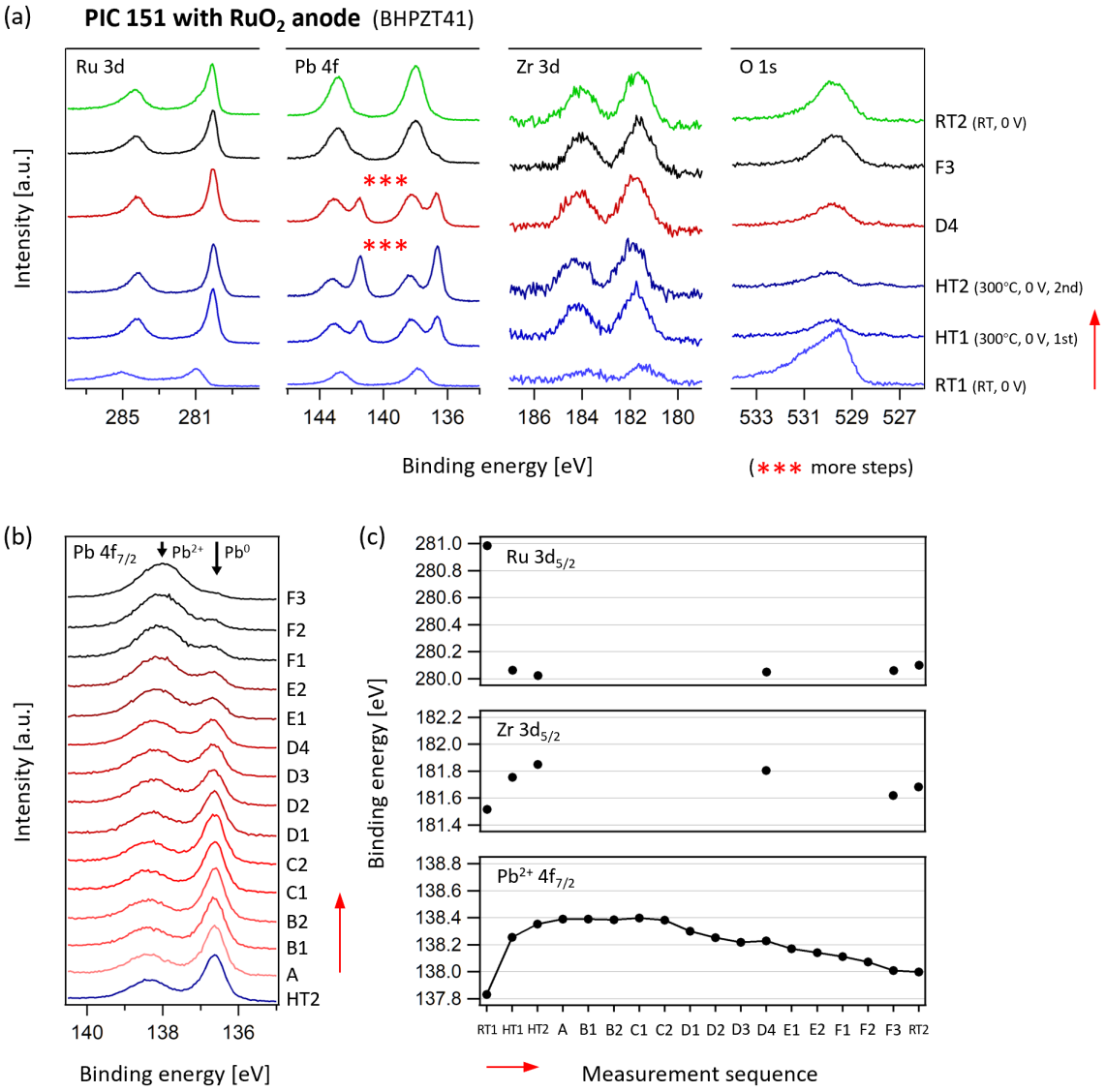

Figure 6.2.: XP spectra recorded at the interface between PIC 151 and RuO_2 anode during the application of stepwise increasing electric fields (sample No. BHPZT41). (a) Ru 3d, Pb 4f, Zr 3d, and O 1s core level spectra in several key steps. (b) Pb $4f_{7/2}$ spectra in detailed measurement sequence at 300°C. (c) Binding energies of Ru $3d_{5/2}$, Zr $3d_{5/2}$, and Pb^{2+} $4f_{7/2}$ extracted from all relevant spectra in (a) and (b). The red arrows indicate the sequence of measurements.

negative voltages were applied to the Pt side, so the RuO_2 was used as anode. Figure 6.1 displays both the acquired current signals and the calculated conductivities when stepwise rising electric fields were applied between the top and the bottom electrodes at 300°C. Figure 6.2 shows the XPS data measured at the anodic interface between RuO_2 and PIC 151 bulk ceramic throughout the experimental procedure as described in Section 3.4.5. A combination of these two types of figures will be basically the standard way to describe the detailed results of such experiment.

In Figure 6.1, the currents measured at different electric fields are plotted in logarithmic scales and labeled with letters. The corresponding conductivities, which are extracted by 2-point method with the contact area and the sample thickness, are also displayed in the similar style. The applied electric fields (hereinafter referred to as "field A", "field B", etc.) are given on the right side with a red arrow indicating their sequence. Different leakage behaviors can be seen when the fields increase step by step, including the initial charging stage (at fields A–C), the resistance degradation process (at fields B–F), and the slight decrease of leakage after reaching a saturation (at fields D–F). In short, the electrical conductivity of this sample tends to increase with the increase of electric field, and the degradation can take place in some conditions most probably due to the existence and migration of oxygen vacancies. Although the field-dependent leakage behavior might have some links to the observations at the electrode interfaces, their origin is temporarily not the key point for detailed discussion in this context. Additionally, thick lines are used in the conductivity plot to indicate the periods when XPS measurements were carried out. The numbers in the parentheses after the letters denote the number of times for XPS acquisition in the course of each current curve. Another noticeable feature of these current or conductivity curves is the occurrence of a pair of abrupt steps, especially when the current measured by the picoammeter is relatively low. This is because the leakage current through the sample is superimposed by another small current that results from the photoelectron emission during XPS. When the magnitudes of these two currents are comparable, a pair of steps will be observed evidently on the current curve and thereby on the conductivity as well. In the present case where the grounded top electrode is used as anode, the two current components flow in opposite directions. Hence the overlapping leads to first a downward and then an upward step on the current, for example on the curves of field A. It should also be noticed that there are two steps on the curves of field C which seem to form wrong offset directions. Different from field A, field C possesses a period with an offset on the current or conductivity, which does not coincide with the period of any XPS measurement, as clearly shown in the conductivity plot. Therefore, similar situations to the steps on the curves of field C are not directly related to photoelectron emission and can be ascribed to some unavoidable stability problems from either the interface or the bulk material itself.

In Figure 6.2(a), the core level emissions of Ru 3d, Pb 4f, Zr 3d, and O 1s at several important steps are displayed. Following the red arrows that indicate the measurement sequence, these selected key steps are: (i) step RT1: at room temperature without applying any bias (light blue); (ii) step HT1: after 30 minutes being at 300°C without bias (medium blue); (iii) step HT2: an extra check after another 30 minutes staying at 300°C without bias (dark blue); (iv) step D4: the 4th XPS acquisition at field D (1.0 kV/mm) (dark red); (v) step F3: the 3rd XPS acquisition at field F (2.0 kV/mm) (black); (vi) step RT2: after cooling down to room temperature and removing the applied field (green). By comparing the spectra of steps RT1, HT1, and HT2, the effect of heating in the vacuum on the top interface between RuO_2 and PIC 151 can be investigated. Significant changes happen at 300°C with the increase of heating time. First of all, the Ru 3d emission experiences a clear reduction, indicated by a more symmetric peak shape and a decrease of binding energy from about 281.0 eV to 280.1 eV. It means that the RuO_2 thin top layer, which was deposited at room temperature, cannot sustain its oxidation state and tends to become metallic Ru in such a reducing condition. This can be also verified by the strongly decreased relative intensity of O 1s emission after the heating process at 300°C for the first 30 minutes. At the same time, the PIC 151 substrate undergoes an obvious reduction as well. The Pb 4f emission already shows two doublets after the first period of heating. The high binding energy doublet belongs to the oxidized state as before (Pb^{2+}), while the low binding energy doublet can be identified as a metallic state (Pb^0). Such reduction of a specific element cannot be found on Zr 3d, which only shows a shift to higher binding energy, similar to the behavior of Pb^{2+} component after some heating time. Step HT2 shows a further growth of Pb^0 component at the interface after another 30 minutes at 300°C. The

Ru $3d_{5/2}$ peak becomes more symmetric than that in step HT1. The binding energies of all core level emissions still have slight shifts following the previous tendencies. Hence it can be concluded that the heating in such a high vacuum has a continuous reducing effect on the interface between RuO_2 and PIC 151. The duration is at least 1 hour according to the present case. The problem resulting from the reduction of the interface only by heating in the vacuum will be discussed with more details in Section 6.1.2. Here we should decide a starting point for the further study on the effect of electric fields.

The strategy of XPS acquisition when dc bias is applied to the sample is to balance the quality of spectra and the real-time of monitoring fast changes, as described in Section 3.4.5. For this purpose, steps D4 and F3 in Figure 6.2(a) are the ones by careful sweeps and with all relevant elements involved. Only Pb 4f emissions are measured in a relatively faster way in the other steps during the application of both temperature and electric field. The symbols with three red asterisks in Figure 6.2(a) denote the places where more spectra have been measured repeatedly, and all omitted spectra in Figure 6.2(a) are plotted in Figure 6.2(b) in order to illustrate the complete evolution of the Pb 4f emission. Based on the theoretical prediction of such experiment introduced in Section 3.4.5, the applied electric field would induce an oxidation at the anodic interface of the solid electrolyte cell due to the migration of oxygen vacancies (or oxygen ions) inside the sample at elevated temperature. In this case, the RuO_{2-x} (previously reduced) anode, the PIC 151 substrate, or both of them, are expected to undergo oxidation once sufficiently high fields are applied. In Figure 6.2(a), the Ru $3d_{5/2}$ emission of step F3 shows again an asymmetry on the higher binding energy side when compared to the spectrum of step HT2. Also, the relative intensity of O 1s peak is gradually recovering. These phenomena indicate the re-oxidation of the previously reduced RuO_2 anode layer. As for the Pb 4f emissions displayed in Figure 6.2(b), a clear decline in the Pb^0 component accompanied by a recovery of Pb^{2+} intensity reveals the re-oxidation taking place on the side of PIC 151 as well when the applied field is going up stepwise. This is also consistent with the theories. Besides, it can be noticed that the concentration of metallic Pb actually does not stop growing until step B2. After reaching a maximum, it starts to drop when field C (0.3 kV/mm) is applied. The most evident decline occurs since step D1 where the field is 1.0 kV/mm. Here the relatively high applied fields and the fast decline of the Pb^0 component seem to be correlated because higher fields could enhance the migration of oxygen vacancies or ions. As for the modest growth of the Pb^0 peak at lower fields in the beginning, the above-mentioned effect of heating in the high vacuum should be taken into account. In other words, the reduction at the interface due to heating is very likely still ongoing and dominates the progress even though an electric field has been applied. Moreover, the Zr 3d emission does not show any obvious change in its shape throughout the re-oxidation at this anodic interface.

The high-temperature experiment with applied voltage is terminated after step F3 because here the peak of metallic Pb has already become fairly small. Also, the leakage current measured at field F (2.0 kV/mm) turns more noisy and starts to rise again after a period of decrease, which probably implies an upcoming breakdown or instability of the sample. During cooling-down, the maximum field 2.0 kV/mm is persistently applied on the sample until it reaches room temperature, so that the anodic interface can stay in the oxidized state rather than being reduced again in the high vacuum due to the residual heat. In the final step, all relevant core levels are measured again at room temperature and at zero electric field (step RT2). It can be found that the Ru 3d emission has been further oxidized compared to that in step F3. However, it does not recover the as-deposited state and its binding energy remains at about 280.1 eV. For the Pb 4f emission, the metallic component almost disappears. To summarize, the whole experiment demonstrates a process that consists of firstly the reduction at the top electrode interface due to heating in the high vacuum and the subsequent re-oxidation induced by an anodic polarization in a solid electrolyte cell at a sufficiently high temperature.

In Figure 6.2(c), the binding energies of the Ru 3d, Zr 3d, and Pb^{2+} 4f core levels are extracted from the spectra in Figure 6.2(a, b) and plotted along the whole set of the measurement sequence. It should be noted that the measurement sequence does not directly or linearly reflect the increments of electric fields. The detailed condition of applied field of each measurement step can be found in the current and conductivity plots (Figure 6.1). Here Figure 6.2(c) just provides a more straightforward way to compare the evolution of all binding energies. In the pure heating period, the severe reduction of both the top and the bulk layer corresponds to a strong shift of Ru 3d to lower binding energy and a comparable increase of the binding energies of Pb^{2+} 4f and Zr 3d. In the following re-oxidation stage with a series of applied fields, the Ru 3d peak remains at a relatively low level of binding energy, while the elements of the dielectric show a clear tendency to shift back. Furthermore, the variation of the Pb^{2+} 4f emission in the binding energy seems to be more intense than that of the Zr 3d. This might be related to the fact that the reduction takes place on the Pb-sites rather than on the Zr-sites within the bulk material.

Case 2. PZST X01 with RuO_2 anode at 250°C

The most noticeable feature of case 1 is the strongly reduced top electrode interface, which occurred already during the heating process before a voltage was applied. Here another case is given in which an X01 sample (nominally undoped PZST, FE hysteresis loop at room temperature) was selected and the solid electrolyte cell was operated at 250°C (higher than its T_C (see Figure 4.8), but 50°C lower than the temperature used in case 1). The sample was a 0.22 mm thick ceramic pellet, with a 5 nm thin RuO_2 top electrode and a thick Pt bottom electrode. The same setup and similar experimental procedure as case 1 were used. Figure 6.3 gives the current and conductivity plots corresponding to stepwise rising electric fields applied at 250°C. Figure 6.4 displays the XPS data measured at the anodic interface between RuO_2 and X01 ceramic throughout the experimental procedure as described in Section 3.4.5.

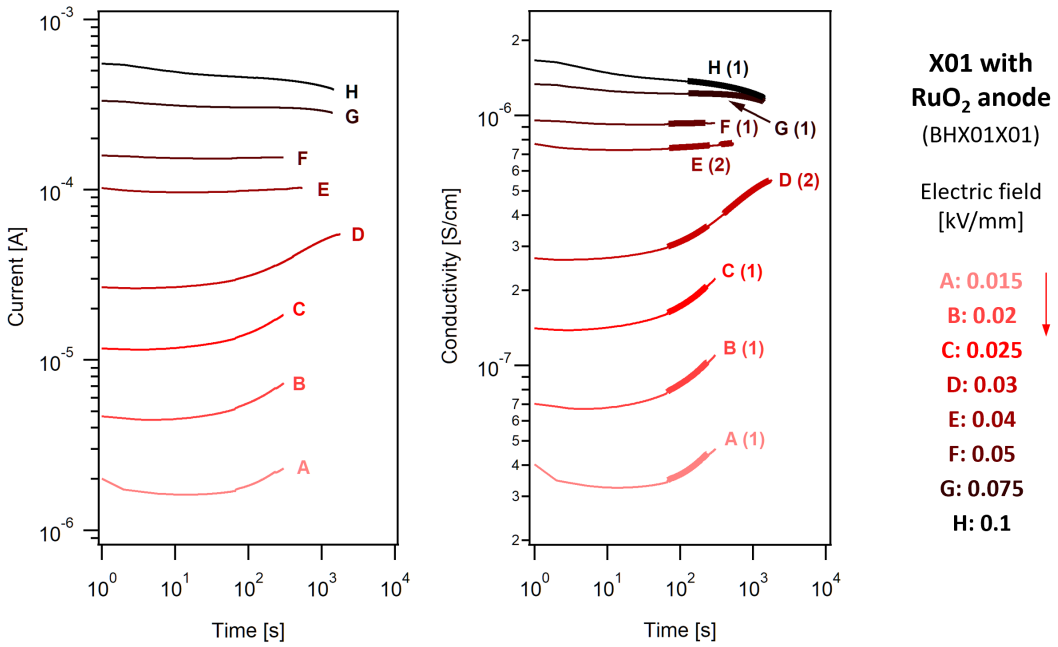

Figure 6.3.: Measured currents and calculated conductivities at 250°C and at stepwise increasing applied electric fields for an X01 sample with RuO_2 anode (sample No. BHX01X01).

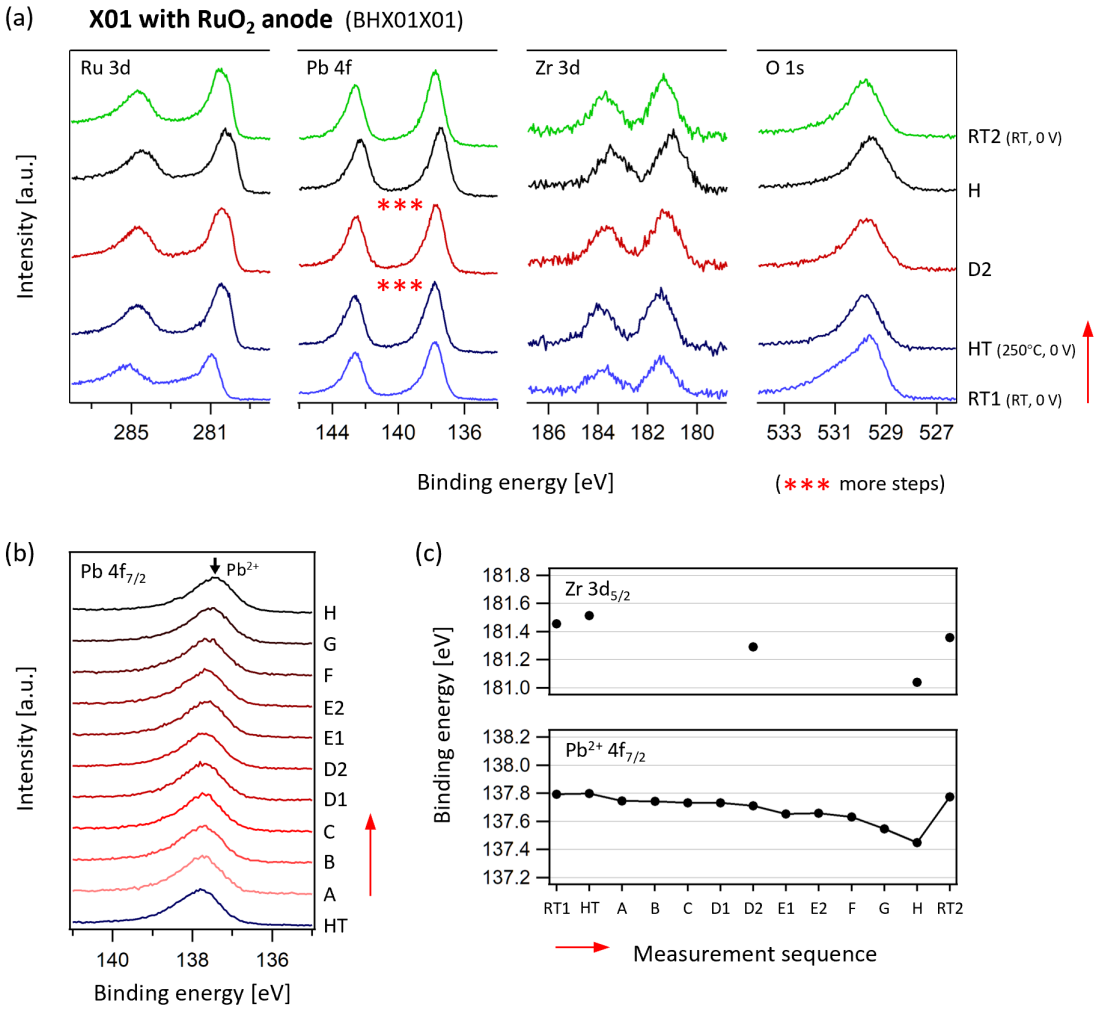

Figure 6.4.: XP spectra recorded at the interface between X01 and RuO_2 anode during the application of stepwise increasing electric fields (sample No. BHX01X01). (a) Ru 3d, Pb 4f, Zr 3d, and O 1s core level spectra in several key steps. (b) Pb $4f_{7/2}$ spectra in detailed measurement sequence at 250°C. (c) Binding energies of Zr $3d_{5/2}$, and Pb^{2+} $4f_{7/2}$ extracted from all relevant spectra in (a) and (b). The red arrows indicate the sequence of measurements.

The highest applied electric field in this experiment is much lower than that in case 1, but the electrical conductivities of the present sample already exhibit a similar dependence on field, varying in a range of nearly two orders of magnitude, as shown in the conductivity plot of Figure 6.3. At lower fields, the leakage currents always tend to rise with time, typical for resistance degradation. Once the applied field reaches a level about 0.05 kV/mm, however, the leakage currents show a saturation or even a slight decreasing tendency. Meanwhile, the increase of the calculated conductivities are also retarded when the applied field is rising step by step.

Figure 6.4(a) plots five important steps of the XP spectra, which are: (i) step RT1: at room temperature without applying any bias (light blue); (ii) step HT: after 30 minutes being at 250°C without bias

(dark blue); (iii) step D2: the 2nd XPS acquisition at field D (0.03 kV/mm) (dark red); (iv) step H: the only one XPS acquisition at field H (0.1 kV/mm) (black); (v) step RT2: after cooling down to room temperature and removing the applied field (green). Here the step after an extra annealing time before the application of electric field (step HT2 in case 1) is cancelled. The dc bias is applied to the sample right after the XPS measurement of step HT. Different from case 1, the interface between PZST X01 and RuO_2 shows only a mild/slow reduction by comparing steps RT1 and HT in the present case. After 30-minute annealing at 250°C without bias in the vacuum, the Pb 4f emission does not show any obvious change in its position and shape, while part of the Ru 3d emission displays a lowered binding energy, which implies a partial reduction of RuO_2 leading to a broadening of the peak. Comparing cases 1 and 2, it can be speculated that the reduction at the interface with RuO_2 induced by just heating in vacuum strongly depends on the substrate material or the temperature. This uncertainty would cause complexity and difficulty in such experiments, which will be discussed for more cases in Section 6.1.2.

Regarding the course of applying electric fields, the spectra of all relevant elements given in Figure 6.4(a) manifest the same tendency with gradually decreasing binding energies. From step D2 to step H, the peaks of Ru 3d, Pb 4f, and Zr 3d all shift to lower binding energies by about 0.25 eV. Such nearly parallel shifts could be attributed to either a lowering of Fermi level at the interface or a non-negligible voltage drop across the very thin top layer due to the comparatively high leakage current through the pellet. The first possibility would be in good agreement with the purpose of this study, i.e., the top electrode material being continuously oxidized under anodic polarization and its increasing work function correspondingly lowering the Fermi level at its interface with the dielectric bulk material. The RuO_{2-x} thin films grown by magnetron sputtering technique were previously studied in DAISY-MAT with respect to the dependence of their work function on the oxygen content in the Ar/O_2 sputter gas mixture [264]. Although an effective increase of the work function in oxygen-rich RuO_{2-x} films has been experimentally verified, it is still necessary to note that such work function modification of RuO_{2-x} should be accompanied by a distinguishable change in the Ru^{4+}/Ru^0 ratio in the Ru 3d emission, which can hardly be observed here by comparing steps D2 and H. Hence, the parallel shifts of the spectra of Ru 3d, Pb 4f, and Zr 3d could be dominated very likely by a voltage drop across the very thin top electrode. The backward shifts of relevant spectra after the removal of the high temperature and dc bias (step RT2), which was not observed in case 1, may also support this speculation. Besides the shift of the binding energies of core-level emissions, another vital observation in this case is the absence of any change in the shape of Pb 4f peak throughout the whole experiment (see Figure 6.4(a, b)), which is different from case 1. However, this can be intuitively interpreted by the fact that the starting point of the high-temperature process in this case (step HT) is already a fully oxidized and stable Pb^{2+} state where a further oxidation is not expected to take place easily. Moreover, the binding energies of the Zr 3d and Pb^{2+} 4f core levels extracted from Figure 6.4(a, b) are plotted versus the measurement sequence in Figure 6.4(c). The binding energy values of the Ru 3d emission are not involved here because of the difficulty in determining the exact positions of such heavily overlapping emission peaks from metallic and oxidized Ru.

6.1.2. Problem of the RuO_2 top electrode at elevated temperatures

According to the observations in the previous two cases, it can be noticed that varying degrees of reduction may occur at the interfaces between RuO_2 and Pb-containing dielectric ceramics under the combined conditions of high vacuum and elevated temperature. Such reduction prior to the application of dc bias leads to different starting points for operating the solid electrolyte cells, which makes the

further analysis on the Fermi level variation at the interfaces problematic. This section will provide some more examples so that the effects of the annealing temperature and the type of substrate material on the interfacial reduction can be demonstrated. All XP spectra displayed in this section have been normalized for convenient comparisons.

Figure 6.5(a, b) compares two PIC 151 ceramic samples both coated with 5 nm thick RuO_2, which were annealed inside the XPS chamber at 200°C and 300°C, respectively. The sample in Figure 6.5(b) has been already described in case 1 of Section 6.1.1, where the vacuum-annealing at 300°C results in severe reduction in both the RuO_2 layer ($Ru^{4+} \rightarrow Ru^0$) and the PZT substrate ($Pb^{2+} \rightarrow Pb^0$). Also, it can be seen that the formation of the reduced species lasts for at least 1 hour in the PZT substrate but gets almost saturated in the RuO_2 layer. This phenomenon implies that the heavily reduced RuO_{2-x} (or metallic Ru) could become permeable to oxygen migration. By contrast, the sample in Figure 6.5(a), which experiences a vacuum-annealing at 200°C also for 1 hour, only shows a partial reduction of the RuO_2 layer. The binding energy of the Ru 3d peak is always about 280.5 eV, still higher than that of metallic Ru. Concerning the Pb 4f emission in PZT, no reduced signal can be observed even after 1-hour annealing in the vacuum, which reveals that the oxygen migration through the RuO_{2-x} layer is effectively suppressed at lower annealing temperature. In addition to the evolution induced just by heating under zero bias, one more step of XP spectra obtained after applying a field of 2.4 kV/mm (RuO_2 as anode) for 1 hour 40 minutes are added to Figure 6.5(a). The appearance of a small shoulder at around 280.1 eV on the Ru 3d emission (see the red spectrum) indicates that the interfacial reduction can still be regarded as a slow process which might last for hours. In short, it can be concluded by comparing the two cases in Figure 6.5 that the annealing temperature is important when RuO_2 is used as anode material for such in situ XPS experiments. A similar comparison of two A02 samples (2% La and 2%

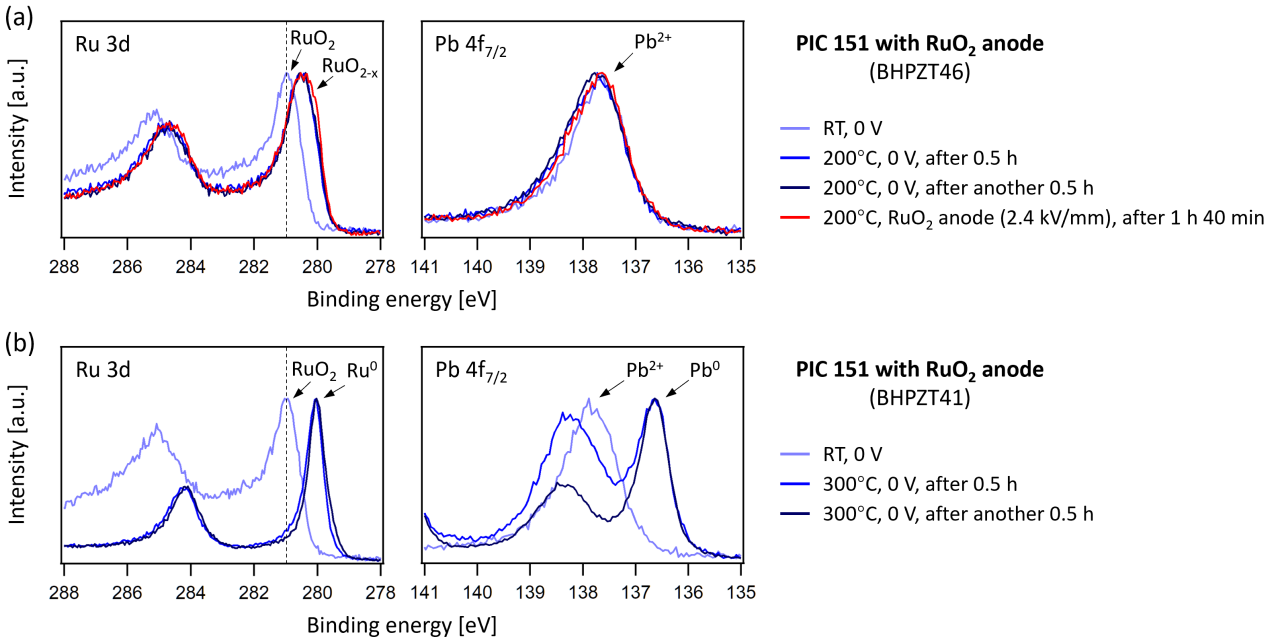

Figure 6.5.: Effect of temperature on the reduction at the interface between PIC 151 ceramic substrate and RuO_2 top layer during the annealing in the vacuum without applying dc bias: (a) annealing at 200°C; (b) annealing at 300°C.

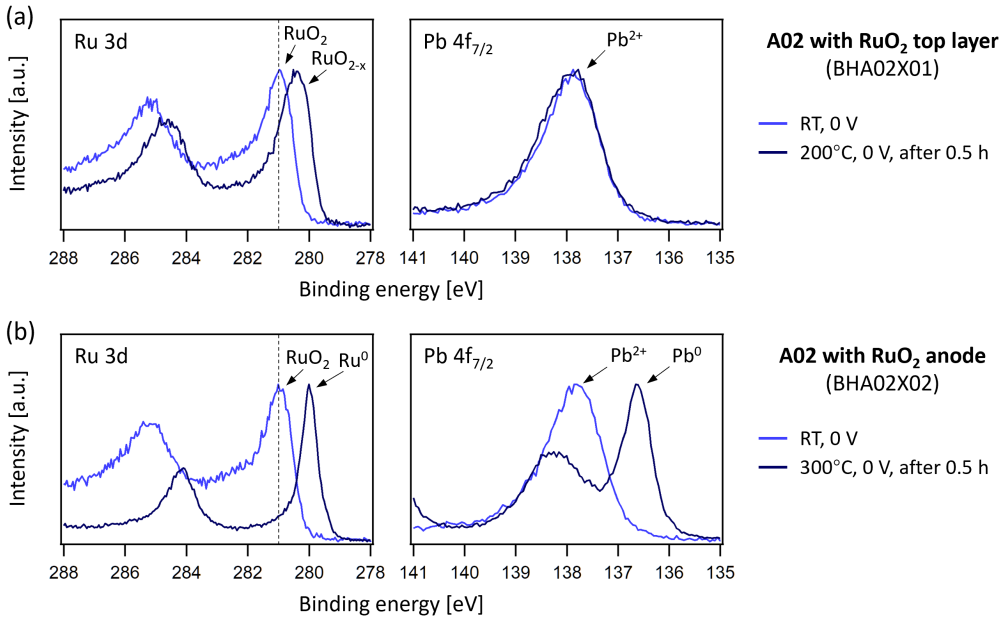

Figure 6.6.: Effect of temperature on the reduction at the interface between PLZSF A02 ceramic substrate and RuO_2 top layer during the annealing in the vacuum without applying dc bias: (a) annealing at 200°C; (b) annealing at 300°C.

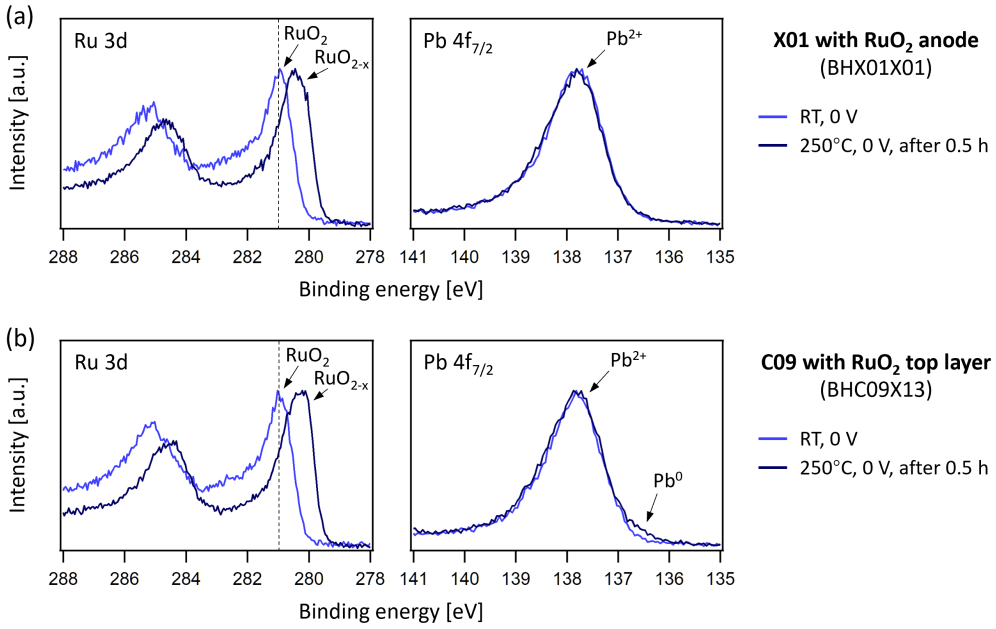

Figure 6.7.: Effect of substrate material on the reduction at the interface between ceramic substrate and RuO_2 top layer during the annealing in the vacuum without applying dc bias: (a) PZST composition X01 as substrate; (b) PLZST composition C09 as substrate.

Fe co-doped PLZSF) is given in Figure 6.6, which shows nearly the same tendency as that of the PIC 151 samples in Figure 6.5. One obvious difference is that the strongly reduced Pb 4f emission, which is observed on the A02 sample in Figure 6.6(b) after only 0.5 hour of a 300°C vacuum-annealing, cannot

be easily obtained on the PIC 151 in Figure 6.5(b) under the same conditions. This indicates evidently that the interfacial reduction also depends on the choice of substrate materials. The detailed measuring steps and data of the A02 sample in Figure 6.6(b) are given in Appendix C.1.1 for reference.

As for the effect of the substrate materials on the reduction at the interface with RuO_2 top layer, Figure 6.7(a, b) provides another comparison based on two different ceramics, X01 (nominally undoped PZST) and C09 (2% La doped PLZST), both of which were coated with 5 nm thick RuO_2 and heated inside the XPS chamber at 250°C. The sample in Figure 6.7(a) has been described in case 2 of Section 6.1.1. For both examples in Figure 6.7, the partial reduction within the RuO_2 layers can be identified. According to the different shapes of the Ru 3d emissions, the reduction in the PLZST C09 sample seems to be slightly heavier than that in the PZST X01 sample, which can be further verified by the formation of a Pb^0 shoulder at around 136.6 eV in the case of C09. The different degrees of the interfacial reduction behavior might result from different $[V''_{Pb}]$ and $[V_O^{\cdot\cdot}]$ in these two ceramics due to the La dopant.

For discussing the problem of using RuO_2 as top electrode for this type of in situ XPS experiment, schematic models of the top electrode interface between RuO_2 and the dielectric at three important steps are illustrated in Figure 6.8. A static and stable as-deposited situation is shown in Figure 6.8(a), corresponding to its schematic interfacial band diagram in Figure 6.8(d). One could firstly assume that the dielectric material has an accessible Fermi level range within its band gap and using the high-work-function RuO_2 top layer leads to a low starting point of the Fermi level position already close to the lower limit of the Fermi level range. Once the sample is heated up, the migration of oxygen species should be taken into consideration, which would transform the as-deposited RuO_2 into an oxygen-deficient state RuO_{2-x}. As shown in Figure 6.8(b), there could be at least three options for the oxygen migration: (i) oxygen leaving the RuO_2 layer and entering the high vacuum; (ii) oxygen moving from the dielectric into the RuO_{2-x}; (iii) oxygen moving from the RuO_{2-x} into the dielectric. Since the latter two options

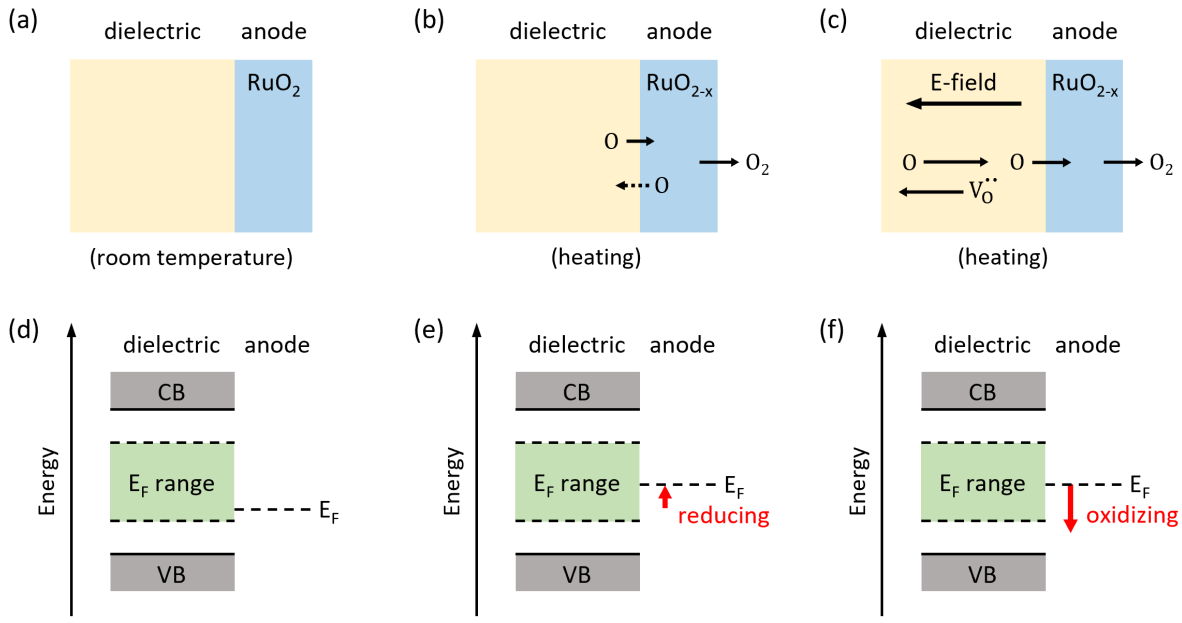

Figure 6.8.: Schematic models to depict the evolution of an interface between the thin-film RuO_2 anode and the dielectric bulk material at three steps during the in situ XPS study using the model of solid electrolyte cell.

are very unlikely to take place at the same time, the third one is marked with a dashed arrow. It can be expected that an equilibrium state of the oxygen content could be gradually established with time. If one assumes a net reduction within the RuO_{2-x} layer, the starting point of the Fermi level at the interface will be "modified" because the non-stoichiometry of RuO_2 usually gives rise to deviated work function [264]. This deviation is sketched in Figure 6.8(e). Figure 6.8(c) displays the situation when the oxygen ions or vacancies from the dielectric start to participate in the migrating process under the external electric field. New balance will be established and the RuO_{2-x} may have the chance to experience a mild re-oxidation that is expected to further shift the Fermi level, as depicted in Figure 6.8(f).

The above-mentioned complicated processes bring about significant uncertainty to the determination of the Fermi level limits with RuO_2 electrodes. The strategy of this type of in situ XPS study is to quantify the oxidation/reduction potential by performing electrochemical oxidation/reduction at the electrode interface. The major problem of using RuO_2 electrode is the unavoidable chemical reduction within both the RuO_2 and the dielectric just by heating the sample in the high vacuum of XPS chamber. Once the chemical reduction dominates the changes at the electrode interface, the equilibrium (both thermodynamic and kinetic) of the interfacial region should be taken into account, which could be strongly material-dependent and may sometimes take considerably long duration to reach. Any slow chemical process not being in equilibrium could induce problematic determination of the starting point of the Fermi level position. For example, the situations in Figure 6.8(b, c), which have too many possibilities of oxygen migration involved, would be very likely to encounter such problem. Furthermore, the identification of the Fermi level limits would make less sense if the dielectric materials of interest have been already strongly changed during the chemical oxidation or reduction.

In brief, the RuO_2 does not seem to be a suitable anode material for the exploration of the lower limit of the Fermi level by utilizing the present operando XPS method. The solution could be either searching for another anode material with higher stability in high vacuum atmosphere or performing such measurements in a NAP-XPS instead of the UHV-XPS system used in this work.

6.2. Interfaces with Sn-doped In_2O_3 cathode

According to the method introduced in Section 3.4.5, ITO was selected as the cathode material for the solid electrolyte cells, which could experience electrochemical reduction at the cathodic interface and help to identify the upper limit of the Fermi level within the band gap of the dielectric material. Three cases will be firstly given with detailed description of measuring steps and corresponding results. Subsequently, more materials will be involved for comprehensive comparisons and discussions.

6.2.1. Typical results with detailed procedures

Case 1. PZST X01 with ITO cathode at 250°C

Details of a PZST X01 sample (nominally undoped PZST, 9% Ti on the B-site, FE hysteresis loop at room temperature) are given here first. The sample was a 0.226 mm thick ceramic pellet, coated with a 4 nm thin ITO top electrode (deposition at 350°C) and a thick Pt bottom electrode. According to the circuit shown in Figure 3.12, positive voltages were applied to the Pt side, so the ITO was used as cathode. Figure 6.9 shows both the acquired currents and the calculated conductivities when stepwise increasing

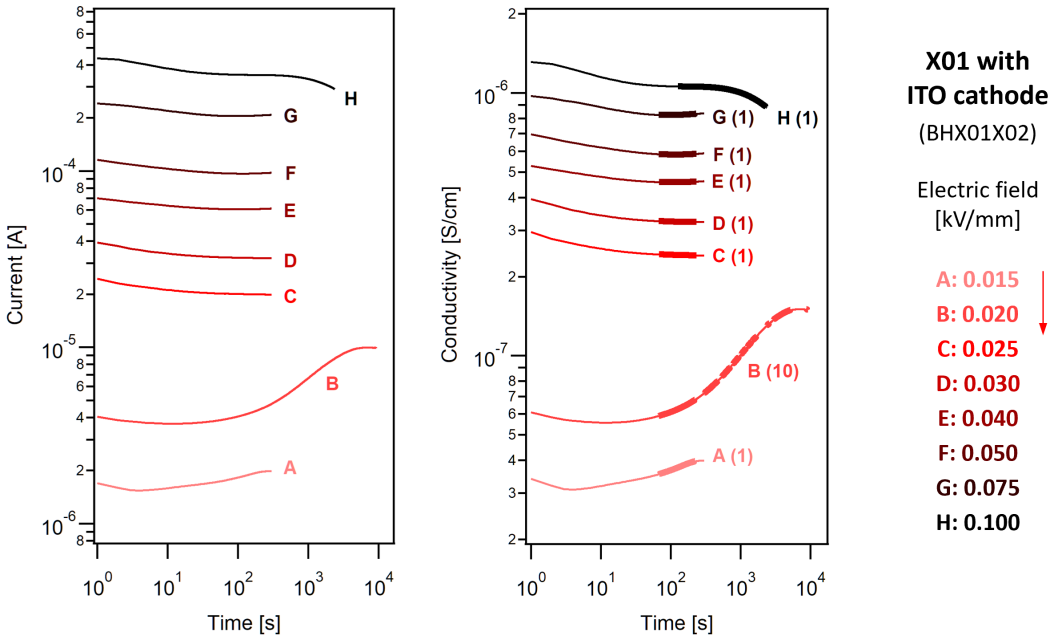

Figure 6.9.: Measured currents and calculated conductivities at 250°C and at stepwise increasing applied electric fields for an X01 sample with ITO cathode (sample No. BHX01X02).

electric fields were applied at 250°C. The temperature used here was higher than the T_C of the material (see Figure 4.8) so that any effect of the FE polarization can be excluded. Figure 6.10 displays the XPS data measured at the cathodic interface between the ITO and the PZST X01 bulk ceramic throughout the experimental procedure as described in Section 3.4.5.

In Figure 6.9, the current and conductivity plots basically possess a very similar tendency compared to the example of the same PZST X01 bulk material where RuO_2 was used as anode (case 2 in Section 6.1.1). This confirms that electrical transport is mostly a bulk property and not affected by the electrode material. At lower electric fields (fields A–B), the leakage currents increase with time, showing typical features of resistance degradation. When higher fields are applied (fields C–G), the leakage curves tend to become nearly saturated within the duration of the current measurement. The leakage current acquired at the highest electric field on this sample (field H) first exhibits a similar shape to those of fields C–G, and then starts to drop with time. Considering that the currents at lower fields in the previous X01 sample with RuO_2 anode always show a continuous increase without getting saturated (fields A–D in Figure 6.3), we decided to extend the duration of the leakage current measurement at field B in the present case in order to keep better track of the course of resistance degradation. As the resistance degradation is completed during the application of field B, the current does no more increase with time for higher fields in Figure 6.9, much earlier than the situation in Figure 6.3.

Figure 6.10(a) plots the core-level emissions of In 3d, Sn 3d, Pb 4f, Zr 3d, and O 1s at five important steps throughout the experiment, which are: (i) step RT1: at room temperature without applying any bias (light blue); (ii) step HT: after 30 minutes being at 250°C without bias (dark blue); (iii) step B9: the 9th XPS acquisition at field B (0.02 kV/mm) (light red); (iv) step H: the only one XPS acquisition at field H (0.1 kV/mm) (black); (v) step RT2: after cooling down to room temperature and removing the applied field (green). All Pb $4f_{7/2}$ emissions measured at 250°C with more detailed steps are provided in Figure 6.10(b). Figure 6.10(c) displays the evolution of the binding energies of the Sn 3d, In 3d, Zr 3d,

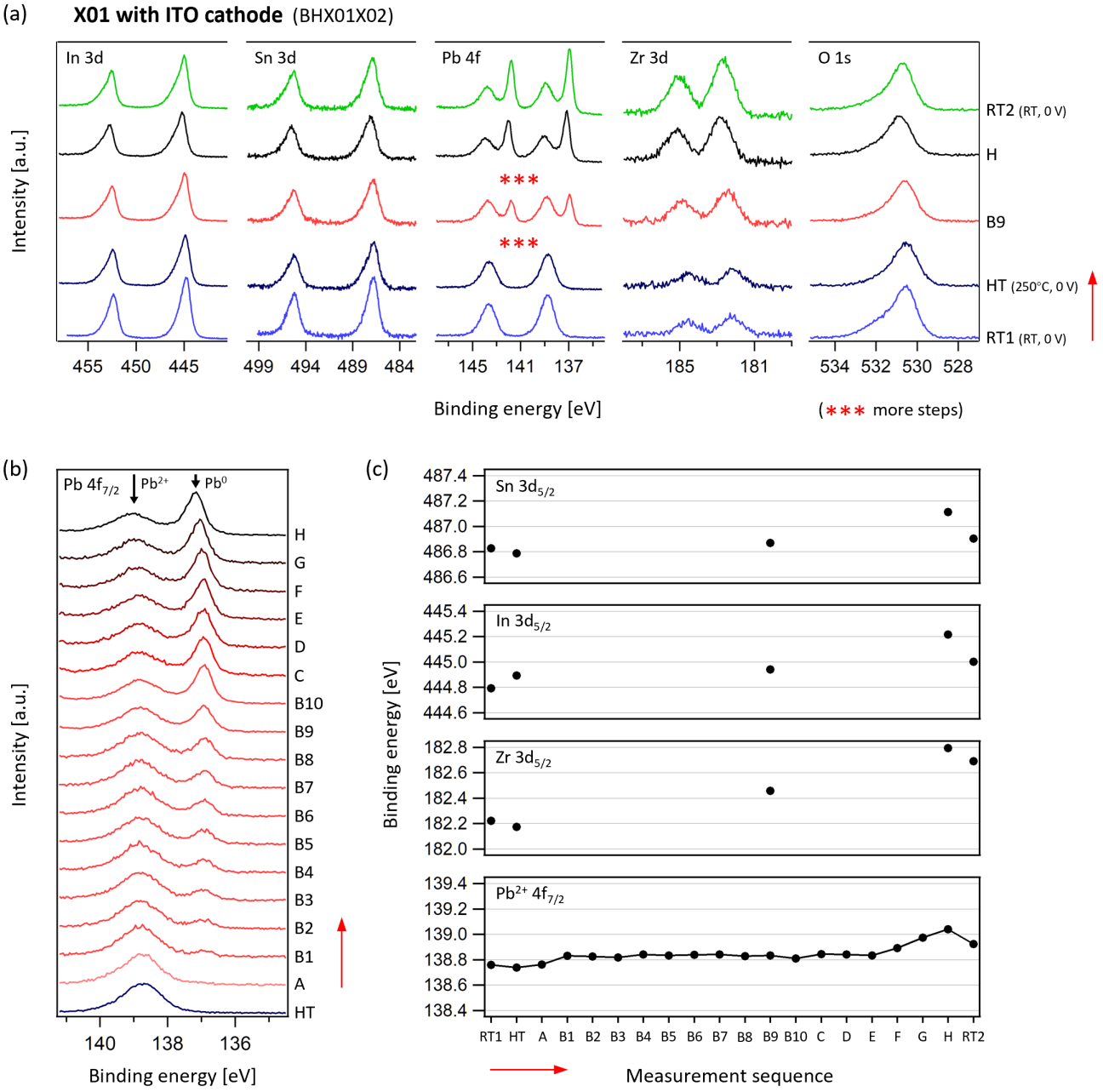

Figure 6.10.: XP spectra recorded at the interface between X01 and ITO cathode during the application of stepwise increasing electric fields (sample No. BHX01X02). (a) In 3d, Sn 3d, Pb 4f, Zr 3d, and O 1s core level spectra in several key steps. (b) Pb $4f_{7/2}$ spectra in detailed measurement sequence at 250°C. (c) Binding energies of Sn $3d_{5/2}$, In $3d_{5/2}$, Zr $3d_{5/2}$, and Pb^{2+} $4f_{7/2}$ extracted from all relevant spectra in (a) and (b). The red arrows indicate the sequence of measurements.

and Pb^{2+} 4f core levels extracted from the spectra in Figure 6.10(a, b) throughout the whole measuring sequence. The most remarkable feature within this experiment is the appearance of the metallic Pb^0 peak at about 136.9 eV in the Pb 4f emission. In contrast to the cases utilizing RuO_2 as anode, where the metallic Pb^0 can already be observed at the anodic interface after a period of vacuum-annealing without applying any electric field, no Pb^0 can be found at step HT and the appearance of the Pb^0 is therefore regarded as a consequence of the combination of high temperature and electric field. The intensity of the Pb^0 peak grows significantly at field B, where a clear process of resistance degradation is observed (see Figure 6.9). Here it seems that the appearance of metallic Pb at the electrode interface may have a relation with the origin of resistance degradation. However, such a direct link is not expected. The next case in this section will show a situation in which the Pb^0 peak occurs when the leakage current of the sample is even decreasing. Back to the present case in Figures 6.9 and 6.10, at the steps with higher applied fields after field B, the Pb^0 peak continues to increase. It should also be noted that the "acceleration" of the growth of the Pb^0 signal at steps B8→B10 is just a technical issue related to the very long measuring duration for step B9. Details of this technical consideration have already been mentioned in Section 3.4.5. Apart from the shape of the spectrum, the binding energy of the Pb^{2+} 4f emission also gives important information. At step B1, where the Pb^0 signal starts to grow, a slight but recognizable increase of the binding energy of the Pb^{2+} component can be observed, which indicates a rising Fermi level at the interface. With the change in the Pb 4f emission of the bulk dielectric, some evolutions can also be found in the core-level emissions belonging to the ITO cathode. First, the binding energies of the In 3d and Sn 3d exhibit approximately parallel shifts compared to that of the Pb^{2+} 4f when electric fields are applied to the sample at 250°C (see steps HT, B9, and H). Second, both the In 3d and the Sn 3d emissions develop an asymmetry on the high-binding-energy side because of the elevated temperature and the electric fields, which evidently indicates an increase of the charge carrier concentration in the ITO electrode [265]. These two points together reveal a change in the SBH at such cathodic interface, which is related to the rise of the Fermi level of the ITO layer. In addition, no metallic In or Sn can be seen throughout the experiment, showing that the ITO electrode remains intact during the operation of the solid electrolyte cell. Furthermore, severe upward shifts in the binding energies of all the core levels are observed at higher electric fields (steps F–H), which could be attributed to the unavoidable voltage drop across the thin-film ITO electrode when the leakage current through the sample becomes too high, analogous to the situation of case 2 in Section 6.1.1. Another important point of this experiment is that all binding energies of the Zr 3d core level measured at 250°C manifest an obviously unparallel evolution compared to the Pb^{2+} 4f. This is very likely related to the formation of $(Zr,Sn,Ti)O_2$ when such a strong reduction (on the Pb-site) of the sample takes place. In short, the observation at the cathodic interface between the ITO electrode and the PZST X01 ceramic sample in this experiment could be assigned to a process dominated by a chemical reduction, which is accompanied by a chemical shift in the XP spectra (change of the relative positions of Pb^{2+} 4f and Zr 3d).

Case 2. PLZST C09 with ITO cathode at 250°C

Composition C09 (2% La doped, 9% Ti on the B-site), one of the standard PLZST materials in this work that exhibits AFE characteristic at room temperature, was investigated with the present in situ XPS method for a comparison to the PZST X01 case. Due to the donor dopant, these two compositions are expected to possess different $[V_O^{\cdot\cdot}]$ that may lead to dissimilar transport properties and interfacial behaviors. The PLZST C09 sample used here was a 0.256 mm thick ceramic pellet, coated with a 4 nm thin ITO top electrode (deposition at 350°C) and a thick Pt bottom electrode. According to the circuit shown in Figure 3.12, positive voltages were applied to the Pt side, so the ITO was used as cathode. Figure 6.11 shows both the acquired currents and the calculated conductivities when stepwise rising

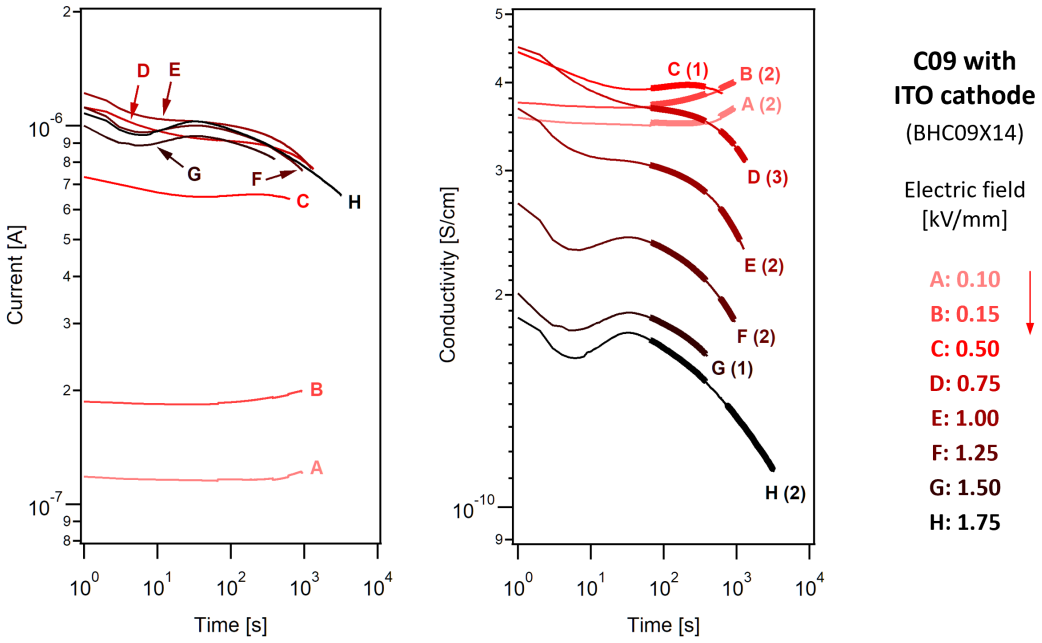

Figure 6.11.: Measured currents and calculated conductivities at 250°C and at stepwise increasing applied electric fields for an C09 sample with ITO cathode (sample No. BHC09X14).

electric fields were applied at 250°C. The temperature used here was also higher than the T_C of the material (see Figure 4.8). Figure 6.12 plots the XPS data measured at the cathodic interface between the ITO and the PLZST C09 bulk ceramic throughout the whole experimental procedure following the descriptions in Section 3.4.5.

Different from the case of undoped PZST X01 (case 1 of Section 6.2.1), where the electrical conductivity increases with the applied field (see Figure 6.9), the conductivity of the La-doped C09 sample remains nearly constant for lower fields (fields A–C) and shows a decreasing tendency at higher fields (fields D–H), as displayed in Figure 6.11. Such decrease of conductivity for higher fields has been mentioned in Sections 5.1.1 and 5.2.1 and Appendix B.2, which is not considered to be important for the present discussion. Additionally, the conductivities of the La-doped sample obtained here are about three orders of magnitude lower than those of the undoped sample given in Figure 6.9, which is in good agreement with the literature in terms of the effect of donor dopant in Pb-based perovskite materials [45, 129]. It should also be noted that the electric fields applied in this case are much higher than those for the undoped PZST X01 sample.

Figure 6.12(a) plots the core-level emissions of In 3d, Sn 3d, Pb 4f, Zr 3d, and O 1s at four important steps throughout the experiment, which are: (i) step RT1: at room temperature without applying any bias (light blue); (ii) step HT: after 30 minutes being at 250°C without bias (dark blue); (iii) step H2: the 2nd XPS acquisition at field H (1.75 kV/mm) (black); (iv) step RT2: after cooling down to room temperature and removing the applied field (green). All Pb $4f_{7/2}$ emissions measured at 250°C with more detailed steps are plotted together in Figure 6.12(b). Figure 6.12(c) shows the change of the binding energies of the Sn 3d, In 3d, Zr 3d, and Pb^{2+} 4f core levels extracted from the spectra in Figure 6.12(a, b) throughout the whole measuring sequence. Similar to the case of undoped PZST X01, the appearance of a metallic Pb^0 peak at a binding energy of about 136.95 eV can also be observed in

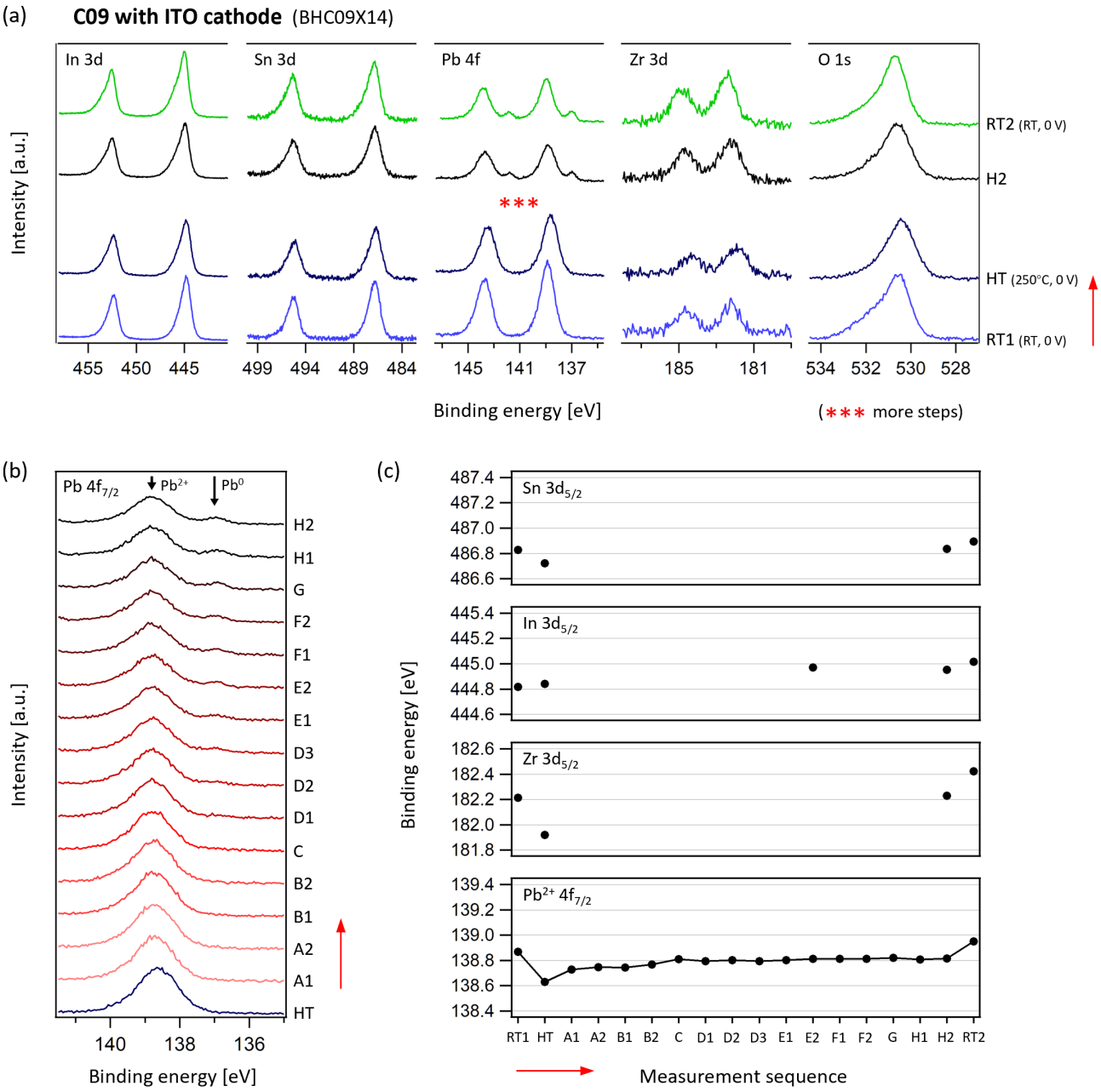

Figure 6.12.: XP spectra recorded at the interface between C09 and ITO cathode during the application of stepwise increasing electric fields (sample No. BHC09X14). (a) In 3d, Sn 3d, Pb 4f, Zr 3d, and O 1s core level spectra in several key steps. (b) Pb $4f_{7/2}$ spectra in detailed measurement sequence at 250°C. (c) Binding energies of Sn $3d_{5/2}$, In $3d_{5/2}$, Zr $3d_{5/2}$, and Pb^{2+} $4f_{7/2}$ extracted from all relevant spectra in (a) and (b). The red arrows indicate the sequence of measurements.

this experiment starting at field D. The growth of this Pb^0 emission is much less pronounced than the situation of the undoped PZST sample. This difference is very probably related to the very low $[V_O^{\cdot\cdot}]$ in the donor-doped composition. Also, the growth of the metallic Pb^0 starts during the leakage curves corresponding to field D, where the electrical conductivity already shows an obvious decrease with time. This phenomenon confirms that the appearance and development of the reduced Pb species have no direct correlation with the resistance degradation of a dielectric material. Concerning the binding energies of relevant core-level emissions, a similar tendency can be found in the La-doped sample compared to the undoped case. It is clear that the appearance of the Pb^0 emission is accompanied by a slight increase of the binding energy of the Pb^{2+} component (see step C $\rightarrow$ step D2), which represents a rising Fermi level at the interface under cathodic polarization. After this small increase, the binding energy of the Pb^{2+} emission does not show further modification until the last measuring step carried out at 250°C, which indicates a pinning effect of the Fermi energy. Also, it is very interesting that for both the PZST and PLZST samples the Pb^0 appears when the binding energy of the Pb^{2+} component reaches 138.8±0.05 eV. More discussions about this value will be given in Section 6.2.4. Although the core levels of the other elements have been acquired at only a few steps throughout the whole experiment, it is still sufficiently clear to see a shift of the binding energy of In 3d that is approximately parallel to the shift of the Pb^{2+} (comparing steps HT, E2, and H2). Besides, a recognizable development of the asymmetry can be identified on the high-binding-energy side of the In 3d and Sn 3d emissions, similar to the case of undoped PZST sample. Combining all these observations, it can be concluded that the PLZST C09 sample also experiences a reduction in the vicinity of the interface with ITO cathode because of the rising Fermi energy of the ITO layer during the operation of the solid electrolyte cell, similar to the case of the undoped PZST X01 sample.

Moreover, from a technical point of view, no parallel shift can be found in the binding energies of all core levels at higher fields (even at 1.75 kV/mm). This makes it possible to identify the binding energies more accurately and conveniently, i.e., without the charging shift on the spectra induced by the extra voltage drop across the ITO thin film. Apparently, such advantage is a consequence of the low leakage currents through the very insulating sample in this case.

Case 3. PIC 151 with ITO cathode at 300°C

Metallic Pb combined with a Fermi level pinning have been observed in both the undoped PZST and La-doped PLZST ceramics by using ITO as cathode material under reducing conditions. However, the Pb^0 component does not always appear. To demonstrate this, another example utilizing the commercial modified PZT ceramic PIC 151 is given with some descriptions. The sample was a 0.23 mm thick ceramic pellet, coated with a 4 nm thin ITO top electrode (deposition at 350°C) and a thick Pt bottom electrode. Based on the circuit in Figure 3.12, positive voltages were applied to the Pt side, so the ITO was used as cathode. Figure 6.13 shows both the acquired currents and the calculated conductivities when stepwise increasing electric fields were applied at 300°C, which is higher than its T_C (250°C). Figure 6.14 plots the XPS data measured at the cathodic interface between the ITO and the PIC 151 bulk ceramic throughout the experimental procedure as described in Section 3.4.5.

As shown in Figure 6.13, the electrical conductivity has the tendency to increase with the applied field. At field D (1.0 kV/mm), a clear resistance degradation can be observed. At higher fields (fields E–F), the leakage currents first increase and reach their maximum values and then start to drop. The decreasing parts for both field E and field F exhibit considerable noise, which might be related to the instability of either the ITO thin film electrode or the PZT ceramic when very high electric fields are applied.

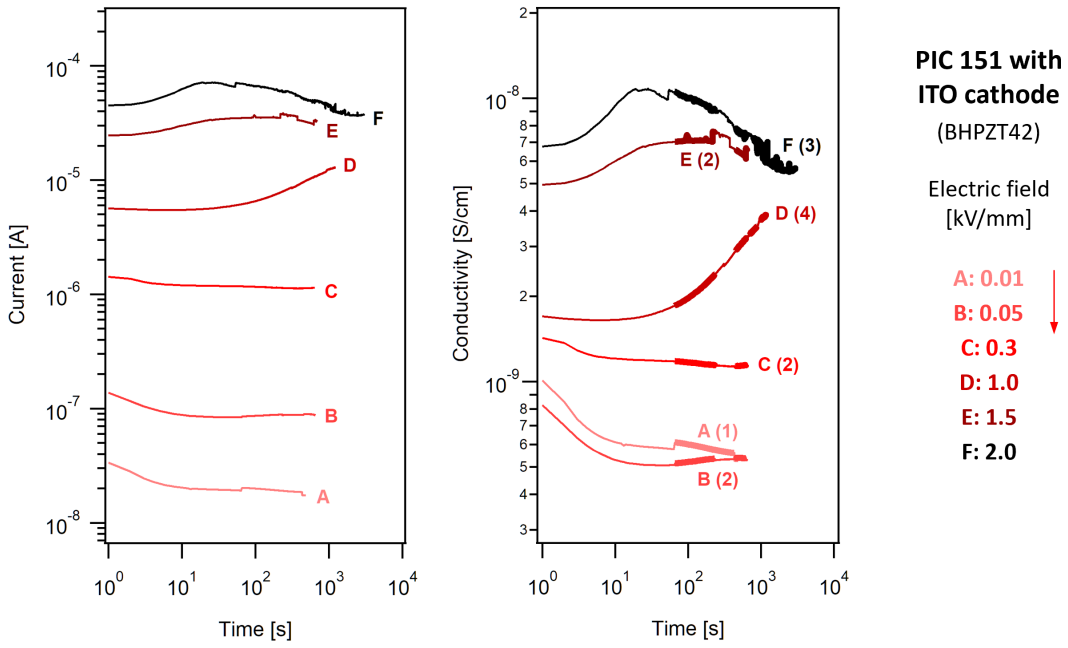

Figure 6.13.: Measured currents and calculated conductivities at 300°C and at stepwise increasing applied electric fields for a PIC 151 sample with ITO cathode (sample No. BHPZT42).

Figure 6.14(a) plots the core-level emissions of In 3d, Sn 3d, Pb 4f, Zr 3d, and O 1s at four important steps throughout the experiment, which are: (i) step RT1: at room temperature without applying any bias (light blue); (ii) step HT: after 30 minutes being at 300°C without bias (dark blue); (iii) step F3: the 3rd XPS acquisition at field F (2.0 kV/mm) (black); (iv) step RT2: after cooling down to room temperature and removing the applied field (green). All Pb $4f_{7/2}$ emissions measured at 300°C with more detailed steps are plotted in Figure 6.14(b). Figure 6.14(c) displays the evolution of the binding energies of the Sn 3d, In 3d, Zr 3d, and Pb^{2+} 4f core-level emissions extracted from the spectra in Figure 6.14(a, b) throughout the measurement sequence. The binding energy of the Pb^{2+} component exhibits a minor and slow increase with the applied electric field. At the same time, an asymmetry of the In 3d and Sn 3d emissions develops when the electrochemical cell is operating under dc bias. Comparing steps HT and F3, parallel shifts can be observed in the binding energies of In 3d and Pb^{2+} 4f core levels, which indicates a slight rising Fermi level at the cathodic interface, same as the previous cases. However, no metallic Pb can be found until the end of this experiment, which is different from the feature of cases 1 and 2 of this section. In addition to the absence of Pb^0, the binding energy of the Pb^{2+} component in this case does not exceed the value of 138.8 eV, unlike the situation when metallic Pb appeared during the electrochemical polarization of the PZST X01 and the PLZST C09 samples.

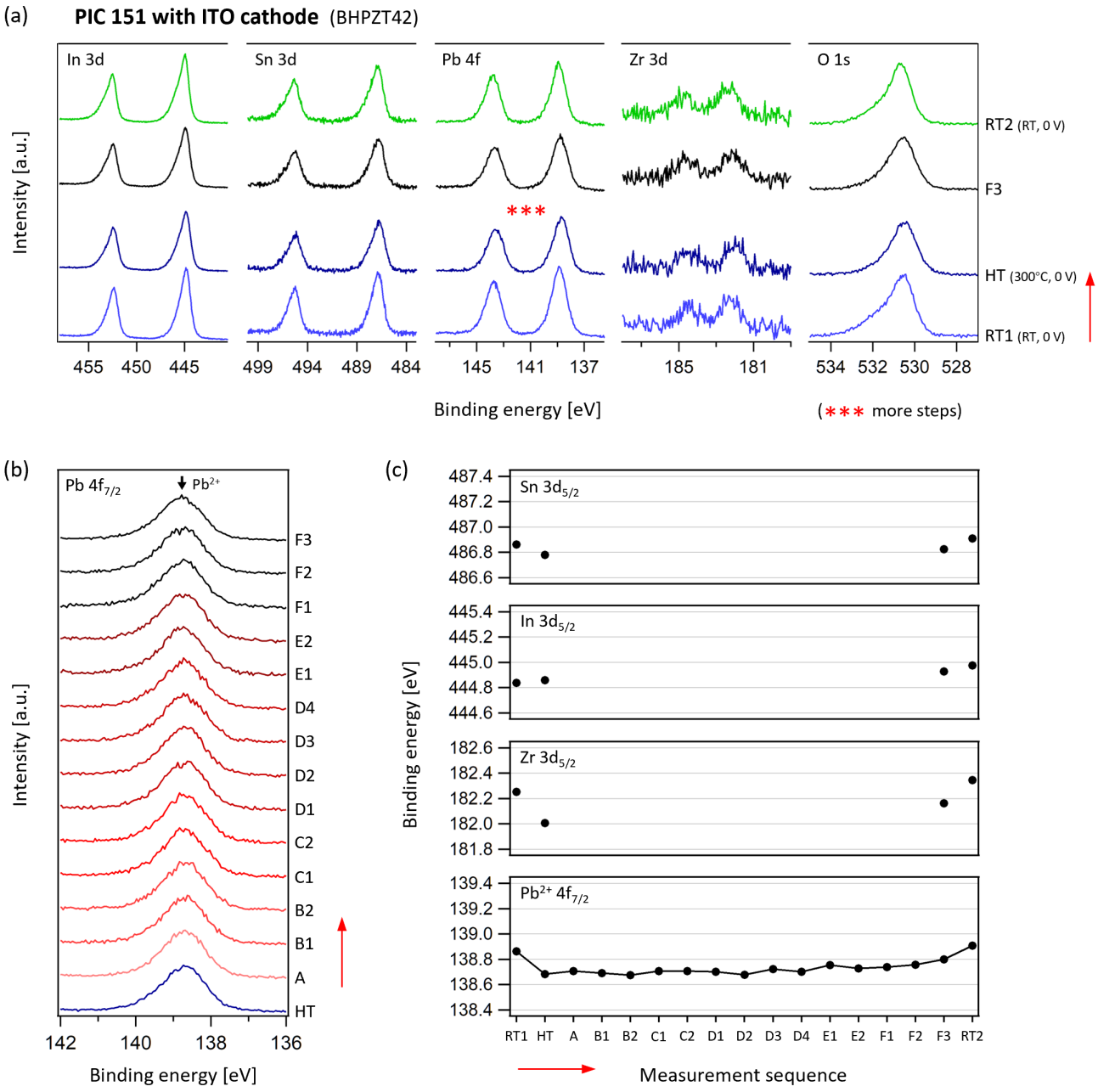

Figure 6.14.: XP spectra recorded at the interface between PIC 151 and ITO cathode during the application of stepwise increasing electric fields (sample No. BHPZT42). (a) In 3d, Sn 3d, Pb 4f, Zr 3d, and O 1s core level spectra in several key steps. (b) Pb $4f_{7/2}$ spectra in detailed measurement sequence at 300°C. (c) Binding energies of Sn $3d_{5/2}$, In $3d_{5/2}$, Zr $3d_{5/2}$, and Pb^{2+} $4f_{7/2}$ extracted from all relevant spectra in (a) and (b). The red arrows indicate the sequence of measurements.

6.2.2. Comparison of different Pb-containing dielectric materials

Besides the three cases described in Section 6.2.1, more experiments using ITO cathode were carried out with the similar strategy. Their detailed experimental steps and results are given in Appendix C.1, as listed in Table 6.1. This part will select important information from three more cases and make comparisons among six different Pb-containing dielectric materials.

Change in the binding energy and asymmetry of the spectra

It has been known from Section 6.2.1 that the reduction of the ITO cathode is always accompanied by a rise of binding energy and a development of asymmetry in the In 3d core-level emission. Figure 6.15 makes comparisons based on six different materials. Here steps RT1, HT, and RT2 always denote the measurements at room temperature with no bias (light blue), at high temperature before applying fields (dark blue), and after cooling down to room temperature and removing the bias (green), respectively. One should be careful about the fact that the operating temperatures and the sequence of applied fields of these samples are different, which depend on the materials' basic dielectric characteristics and the

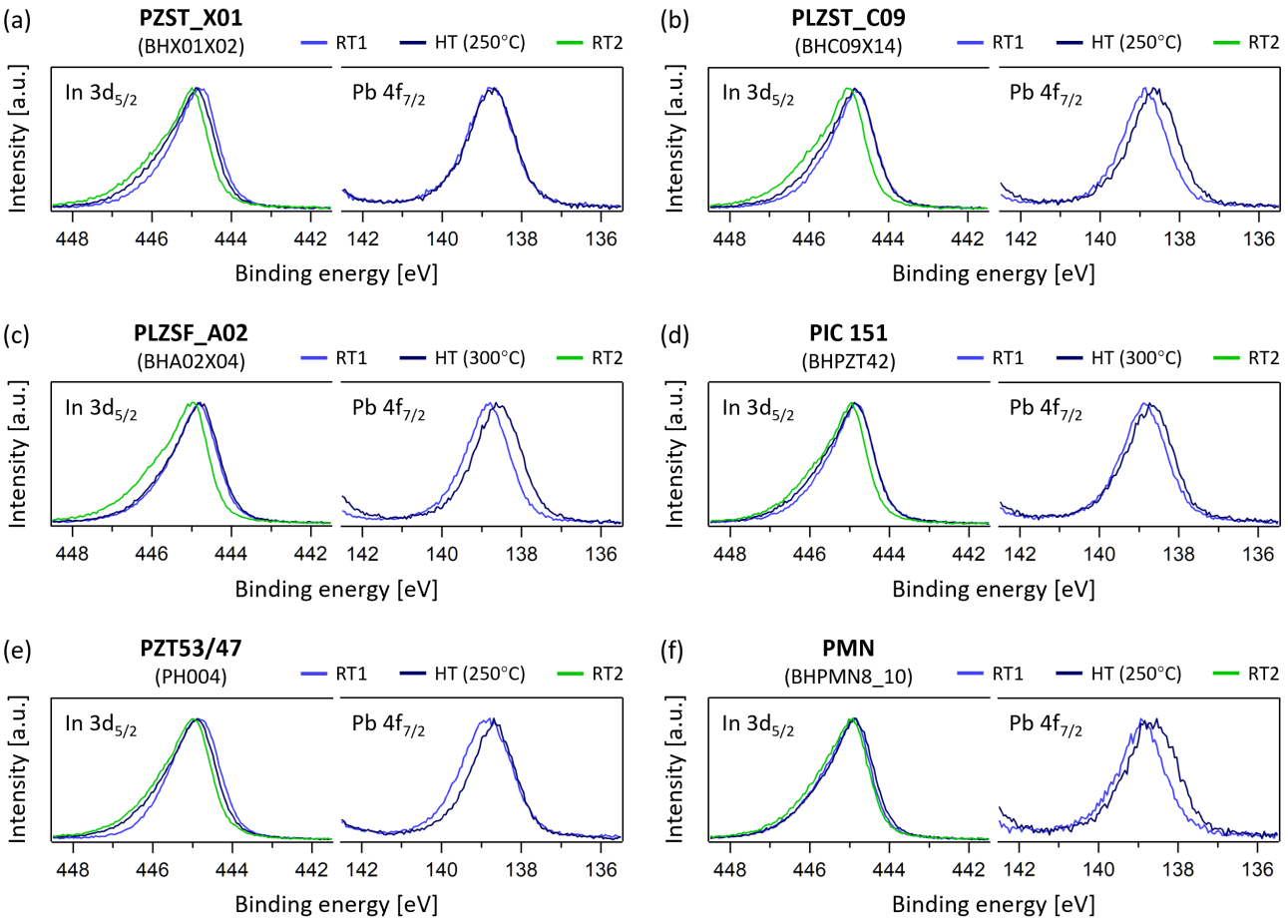

Figure 6.15.: Change in the In $3d_{5/2}$ and Pb $4f_{7/2}$ core-level spectra at selected measuring steps of different Pb-containing samples using ITO cathodes.

actual responses during their respective experimental processes. All XP spectra given here have been normalized for convenient comparisons.

Three aspects of comparisons are involved in Figure 6.15:

(1) The as-deposited interface (comparing step RT1 of all cases): The In 3d emissions of the PZST X01, PLZST C09, PLZSF A02, and PIC 151 samples are basically very similar in terms of both binding energy and peak shape. By contrast, the In 3d peak of the PZT53/47 sample is broader near its maximum and less asymmetric on its high-binding-energy side, implying a lower electric conductivity of the ITO thin film deposited on this substrate material. The obvious broadening near its maximum is very likely caused by the charging effect of insufficiently conductive sample for XPS measurement. Regarding the PMN sample, the In 3d emission has basically the same shape as those in Figure 6.15(a–d), while its binding energy is slightly higher than the others'.

(2) The effect of vacuum-annealing (comparing steps RT1 and HT in each case): After a period of heating in the high vacuum, a development of asymmetry on the high-binding-energy side of the In 3d peak can be observed in the PZST X01, PLZST C09, PIC 151, and PZT53/47 samples, evidently indicating a reduction of the ITO. However, such growth of asymmetry in the In 3d peaks cannot be clearly seen in the PLZSF A02 and PMN samples. Moreover, the Pb 4f emissions in most cases show a broadening of the peak and a lowering of the binding energy after being heated at elevated temperatures, except for the cases of PZST X01 and PZT53/47. The decrease of binding energy in the Pb 4f emissions relative to the binding energy change of the In 3d may be attributed to the deviated energy band alignment at high temperatures compared to the room-temperature situation, which could be most probably explained by the shrinking band gap of ITO with increasing temperature. The coincidence of the two Pb 4f peaks before and after heating of the PZST X01 sample might be related to the very slightly shift of the In 3d peak to the higher binding energy due to annealing. As for the PZT53/47 sample, the Pb 4f emission becomes narrower instead of being broader like the other cases, which is most probably because the ITO turns more conductive during the heating so that the charging effect of XPS could be reduced.

(3) The difference induced by the complete operation of the electrochemical cell (comparing steps RT1 and RT2 in each case): Because of the appearance of metallic Pb in some of these samples, which is not relevant to the current discussion and will be described later in more detail, the Pb 4f emissions after cooling-down are not involved in Figure 6.15. Focusing on the In 3d emissions, it can be found that the asymmetry in spectrum of PZST X01, PLZST C09, PLZSF A02, and PIC 151 increases to varying degrees based on step HT. Meanwhile, the In 3d spectra always exhibit a shift toward higher binding energy if one compares the two room-temperature steps. This can be regarded as the evidence that the ITO cathode has experienced a reduction during the operation of such a solid electrolyte cell. In addition, no obvious further growth of the asymmetry of the In 3d peak can be identified after cooling down in the PZT53/47 and PMN samples. It is assumed for the PZT53/47 that the ITO reduction has already reached a saturation till step HT. By contrast, very little reduction in the ITO can be seen throughout the whole experiment of the PMN sample.

In summary, these measurements provide evidences that the substrate materials can influence the conductivity of the as-deposited ITO electrode and its subsequent evolution during the vacuum-annealing and during the application of electric fields. Such dependence is likely related to different concentrations of $V_O^{\cdot\cdot}$ in the substrates.

Reduction on the Pb-site

The purpose of the in situ XPS studies presented here is to identify the upper limit of the Fermi level and the origin of such upper limit. The origin may be related to an electrochemical reduction that can be observed at the dielectric/cathode interface when the whole capacitor structure is operated as a solid electrolyte cell. For PZT-related materials, the reduction may most likely occur on the Pb- or the Ti-site. Hence, the appearance of the metallic Pb shows great significance for us. However, such reduction on the Pb-site can not be always observed in the Pb-containing dielectric materials involved in this work. Figure 6.16 summarizes the important experimental processes of six different Pb-containing samples, which have been electrochemically polarized with ITO cathodes. For each sample, a color intensity map is utilized to depict the development of the Pb 4f spectrum. Besides, the binding energies of In $3d_{5/2}$, Pb^{2+} $4f_{7/2}$, and Zr $3d_{5/2}$ core levels are plotted versus the measurement sequence. All data points of the Zr $3d_{5/2}$ in the five samples containing Zr have been offset by -43.4 eV so that they can appear near the Pb^{2+} $4f_{7/2}$ for convenient comparisons. Moreover, the intensity ratio of the two Pb components $I(Pb^0)/I(Pb^{2+})$, which has been calculated based on the fitting of every Pb 4f spectrum, is also displayed versus the measurement sequence. Additionally, the measuring conditions at all steps, i.e. the applied electric fields and temperature, are provided in this summary as well. It should be noted that the two room-temperature steps (at the head and the tail of each measurement sequence) are only included in the binding energy plots (rows 2 and 3) and NOT included in the other figures (rows 1, 4, and 5).

The observations in these six cases can be summarized in terms of the following aspects:

(1) The metallic Pb appears only in four samples out of the six. It is clear that PZST X01 and PLZSF A02 exhibit more severe reduction than PLZST C09 and PZT53/47. By contrast, no Pb^0 signal can be observed in PIC 151 and PMN until the end of their measurement sequences.
(2) The Pb^0 component always starts to grow when the binding energy of the Pb^{2+} $4f_{7/2}$ emission reaches a specific value, which is about 138.8 eV for the X01, A02, and C09 samples and a bit lower than 138.8 eV for the PZT53/47. Such correlations are indicated in Figure 6.16 by black dashed lines and blue arrows in the binding energy and the Pb-ratio plots. Regarding the two samples without the Pb^0, the binding energies of their Pb^{2+} $4f_{7/2}$ emissions have not exceeded 138.8 eV until their last high-temperature measuring steps. A more direct comparison is given in Figure 6.17, where the intensity ratio of the two Pb-components is plotted versus the binding energy of the Pb^{2+} for all the samples undergoing reduction. By ignoring the last few data points of the X01 and the PZT53/47 samples, whose deviations are apparently caused by the charging problem (unexpected voltage drop through the ITO layer), a clear saturation or pinning effect of the binding energy can be identified at ca. 138.8 eV (slightly lower for PZT53/47) when the Pb^0 emerges. In this work, such specific binding energy is considered to identify the limits of the Fermi level of the dielectric material. Detailed quantification of the Fermi level limit based on this value will be given in Section 6.2.4.
(3) No direct correlation can be found between the appearance of Pb^0 and the applied electric field according to Figure 6.16.
(4) The binding energies of the In 3d and Pb^{2+} 4f core levels acquired at the elevated temperature exhibit approximately parallel evolution for all these samples, which characterizes a continuous change of the SBH when the electrochemical cell is operating, as shown in the 2nd and 3rd rows of Figure 6.16. (Estimated tendency is used for In 3d emissions if limited data points are available.) By contrast, the evolutions of the Pb^{2+} 4f and Zr 3d are sometimes not parallel. The X01 sample shows the largest deviation between the Pb^{2+} 4f and Zr 3d, implying that this sample has experienced a severe chemical reduction accompanied by formation of a $(Zr,Sn,Ti)O_2$ phase.

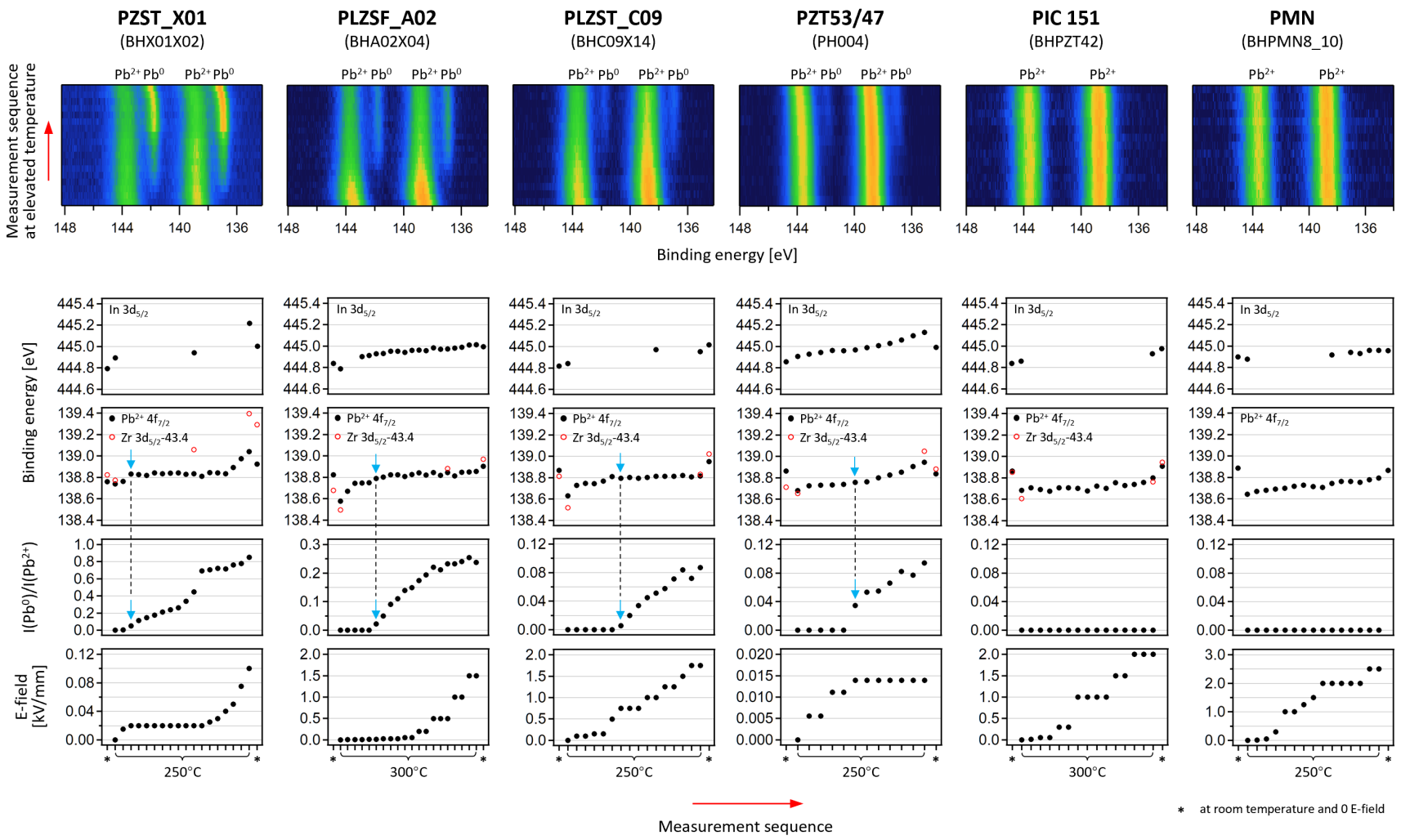

Figure 6.16.: Summary of the experimental processes of six relevant Pb-containing samples. Row 1: color intensity map depicting the development of the Pb 4f emission; row 2 and row 3: evolution of the binding energies of the In $3d_{5/2}$, Pb^{2+} $4f_{7/2}$, and Zr $3d_{5/2}$ core levels; row 4: intensity ratio of the metallic to the oxidic Pb components $I(Pb^0)/I(Pb^{2+})$ extracted from the Pb 4f emissions; row 5: corresponding measuring conditions. All data points are plotted versus the sequence of measurements.

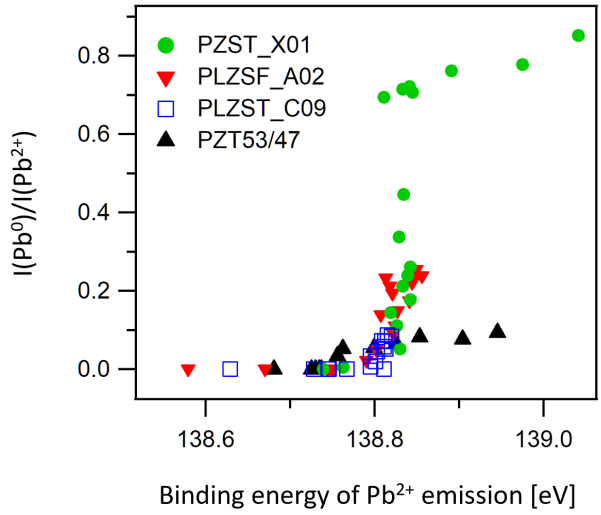

Figure 6.17.: Intensity ratio of the metallic to the oxidic Pb components versus the binding energy of Pb^{2+} $4f_{7/2}$ emission.

Now it is necessary to discuss the following question: why does the reduction take place only in some of the samples?

Considering that the basis of this method is the oxygen migration within the whole structure of the solid electrolyte cell, it is reasonable to speculate that the reducing process depends on the concentration of mobile $V_O^{\cdot\cdot}$ in the dielectric bulk material. The C09 sample, as a donor-doped composition based on X01, is expected to possess an effectively suppressed $[V_O^{\cdot\cdot}]$, which weakens the reduction at the cathodic interface. Similar to C09, the PZT53/47 sample also exhibits very little reduced Pb. However, as a nominally undoped PZT, the existence of certain amount of $V_O^{\cdot\cdot}$ has to be expected, which could be verified by the severe resistance degradation as shown in Figure C.5. Thus, the reason for the minor reduction of this sample should not be the $V_O^{\cdot\cdot}$ deficiency. It can be noticed that the highest electric field applied to the PZT53/47 sample is much lower than those in the other cases. Because of the excessive charging problem induced by the leakage current, the high-temperature experiment of PZT53/47 has been stopped before sufficiently high fields can be applied. This might explain its relatively low degree of the reduction on the Pb-site. Moreover, no reduction can be found in the PMN sample. This could also be related to the $V_O^{\cdot\cdot}$ in terms of its distribution and migration within the material. It has been reported in the literature that the PMN is composed of two kinds of regions from the viewpoint of microstructure: the islands with $1:1$ ordering of the B-site cations, which contain certain amounts of $V_O^{\cdot\cdot}$, and the continuous matrix phase (like a "sea") with Nb-rich composition which forms V''_{Pb} [266, 267]. In such case, the migration of $V_O^{\cdot\cdot}$ is restricted to some discrete regions, which could limit the long-distance transport of oxygen species across the solid electrolyte cell and thereby make the reduction at the cathodic interface more difficult to happen.

Another reason why no reduced Pb can be observed in some of the samples could be that the reduction actually takes place on another trap candidate, for example on the B-site host ions (Ti in PZT, Nb in PMN) or on the doping ions (Ni or Sb in PIC 151). Figure 6.18 shows the schematic band diagrams of three possibilities in the PZT materials. Figure 6.18(a, b) compares the situations of pure PZ (or Zr-rich PZT) and pure PT (or Ti-rich PZT). According to the theoretical description given in Section 2.4.2, the reduction is expected to first occur on the Pb-site in the Zr-rich PZT because the CBM is determined by

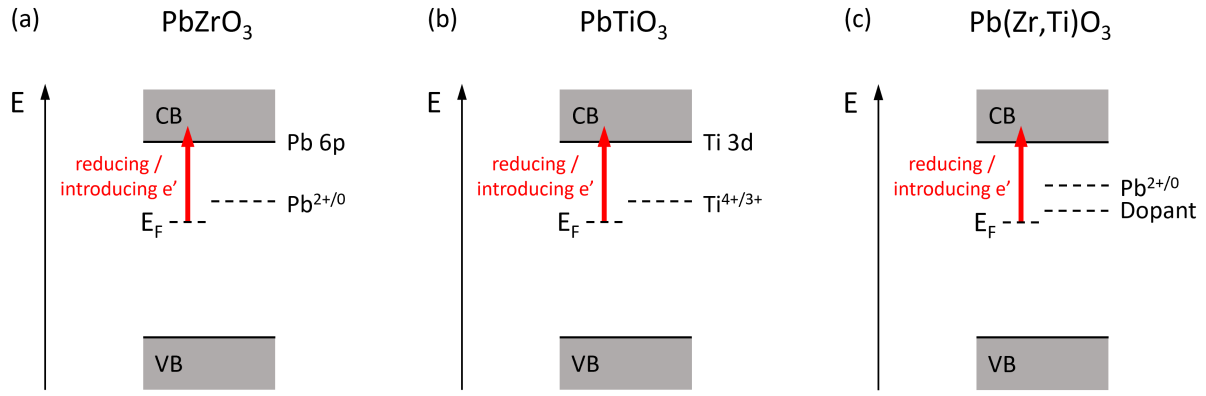

Figure 6.18.: Schematic band diagrams corresponding to three possible electron traps in the $Pb(Zr,Ti)O_3$ systems during a reducing process: (a) reduction on the Pb-site in the pure $PbZrO_3$ or Zr-rich PZT; (b) reduction on the Ti-site in the pure $PbTiO_3$ or Ti-rich PZT; (c) reduction on the doping ions.

the Pb 6p orbital. By contrast, in the Ti-rich PZT one would expect the reduction happening on the Ti-site due to the CBM dominated by Ti 3d. For the X01, C09, and A02 samples, which actually all belong to the Zr-rich type, a clear transition of $Pb^{2+/0}$ can be identified, in good agreement with the hypothesis of this work. The observation of Pb^0 in the undoped PZT53/47 sample, which has approximately an MPB composition (but also on the Zr-rich side), could still be reasonable. Regarding the Ti-site, the Ti 2p emission is not involved in any of the presented XPS experiments due to their very low intensity in the XP spectra and the strong overlap of the In $3d_{3/2}$ peak of the ITO electrode with the most intense Ti emission Ti $2p_{3/2}$. Therefore, the situation on the Ti-site for all these samples remains unclear for the moment. Possible solutions could be either using samples with higher Ti content to increase the emission intensity or selecting another cathode material instead of ITO. As for the PIC 151 sample ($Zr : Ti \approx 0.489 : 0.511$, slightly Ti-rich), the absence of reduction on the Pb-site might be explained by the higher Ti content, which even more prefers a reduction of Ti instead of Pb as compared to the PZT53/47 sample. However, the PIC 151 is not a pure PZT but contains 8% of $Pb(Ni_{1/3}Sb_{2/3})O_3$, where Ni^{2+} is an acceptor and Sb^{5+} is a donor. It is possible that raising the Fermi energy might lead to a reduction of $Sb^{5+} \rightarrow Sb^{3+}$, which would prevent the Fermi level from reaching the reduction potential of Pb. Figure 6.18(c) schematically shows such a situation where the doping ions act as the trap centers and will be reduced prior to the host ions. Furthermore, in the undoped PMN, the reduction may occur first on the Nb-site ($Nb^{5+} \rightarrow Nb^{4+}$) because the bottom of its conduction band might be made of Nb 4d [268]. This is similar to the case of Ti-rich PZT in Figure 6.18(b) and might be able to explain the absence of metallic Pb in the PMN sample.

6.2.3. Chemical reduction versus electrochemical reduction

Ideally, the approach presented in this chapter is based on tuning the Fermi level of the top electrode, which should control the Fermi level of the substrate dielectric material at the interfacial region. Free electrons are supposed to enter the dielectric layer close to the electrode interface, which can be therefore regarded as an electrochemical reduction. In practice, however, one can imagine that the piling-up of a great number of $V_O^{\cdot\cdot}$ on the dielectric side of the cathodic interface may simply result in a strong

chemical reduction of the dielectric material. Taking the PZST as example, such chemical reduction can be written as

$$\mathrm{Pb(Zr,Sn,Ti)O_3} + \mathrm{V_O} \longrightarrow \mathrm{(Zr,Sn,Ti)O_2} + \mathrm{Pb}. \tag{6.1}$$

Here, it is unavoidable to discuss the question how to distinguish and treat the chemical and electrochemical reductions in our experiments.

In theory, a chemical reduction of an oxide refers to a reaction where oxygen is removed until the stability limit is reached. (When the oxygen chemical potential, which is calculated from the oxygen partial pressure, becomes larger than the formation enthalpy of the oxide, the reduction stops and the oxide phase is stable.) This can be achieved by changing the chemical boundary condition [269]. By contrast, during an electrochemical reduction, raising the Fermi energy causes occupation of trap levels, which can lower the oxidation state of the substance. It might be accompanied by the formation of a new reduced phase and the release of oxygen, and it may also be just the occupation of the trap levels. This process can be realized by changing the electrostatic boundary condition.

Figure 6.19(a) gives a flow chart summarizing three crucial experimental steps, which are supposed to realize electrochemical reduction on different levels with the help of ITO top layer. Making use of the low work function of ITO, the deposition of ITO layer itself already provides the first chance to reduce the dielectric electrochemically (Level 1). One example can be found in Ref. [236] where the ITO deposition successfully induced Fe^{2+} from the α-Fe_2O_3 substrate. In this work, no reduction can be observed in the Pb-containing samples just after the ITO deposition. Additionally, using an oxide top layer such as ITO can effectively avoid the chemical reduction on the substrate material caused during the sputtering of metal top layer [217, 218]. If ITO sputtering is not sufficient for realizing the reduction, a vacuum-annealing can be carried out on the as-deposited ITO in order to release some oxygen from

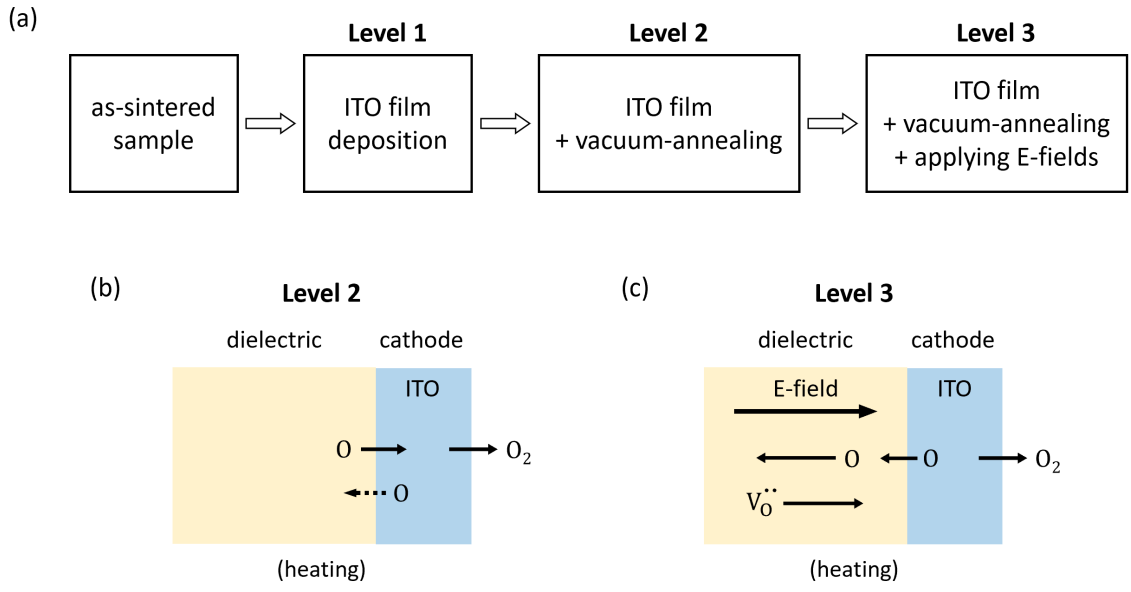

Figure 6.19.: Three experimental steps related to the electrochemical reduction at the interface between a dielectric and an ITO top layer. (a) The flow chart; (b, c) schematic models to depict the evolution of an interface between the thin-film ITO cathode and the dielectric bulk material on levels 2 and 3 in the flow chart, respectively.

the film into the vacuum, which is expected to shift the Fermi level of ITO a little more upward (Level 2) [230–232]. As for this step, extra processes that might bring about chemical reduction should be taken into consideration. As illustrated in Figure 6.19(b), the oxygen diffusion between the dielectric and the ITO may occur in two directions, depending on the $[V_O^{\cdot\cdot}]$ of the dielectric substrate, the vacuum level (oxygen partial pressure), and the annealing temperature and duration. Relevant comparisons about this level based on the materials used in this work have been mentioned in Section 6.2.2. Still, no reduction can be seen in the Pb-containing dielectrics upon heating in vacuum. Lastly, we come up with Level 3 in which more oxygen migration processes are involved via applying external electric fields on the electrochemical cell as shown in Figure 6.19(c). In this case, more attention should be paid to the interfacial region on the dielectric side, where the piling-up of $V_O^{\cdot\cdot}$ induced by the applied field could be compensated to a certain extent by the oxygen migrating from the ITO side. When the accumulated $V_O^{\cdot\cdot}$ are excessively more than the compensating oxygen ions which the ITO layer can effectively provide, a chemical reduction may dominate the interfacial process. The X01 sample, whose reduction on the Pb-site is accompanied by a significantly non-parallel evolution of the binding energies of Pb^{2+} 4f and Zr 3d, could be very likely assigned to such a chemical reduction. In contrast, the electrochemical reduction will possess the dominance over the chemical one if the piling-up effect of $V_O^{\cdot\cdot}$ is tiny enough to match the oxygen migration from the ITO side. Due to the expected very low $[V_O^{\cdot\cdot}]$, the C09 sample might provide a good example for the electrochemical reduction.

6.2.4. Quantification of the upper limit of the Fermi level

As described in Section 6.2.2, the three PLZST-related samples X01, A02, and C09 exhibit a specific binding energy (138.8±0.05 eV) of the Pb^{2+} $4f_{7/2}$ emission where the Pb^0 component starts to occur. This value corresponds to a reduction potential (E_{red}) of $Pb^{2+/0}$, which is considered to be the upper limit of the Fermi level of these dielectric materials. Figure 6.20 is the energy band alignment at the interface between PLZST and ITO, in which a quantitative determination of the Fermi level limit within the band gap of the PLZST is given. In order to calculate the specific Fermi level position (green dashed line) relative to the VBM, we still need the difference between the oxidic Pb 4f core level and the VBM, which can normally be measured by XPS on the bare surface of a material. Based on a large set of

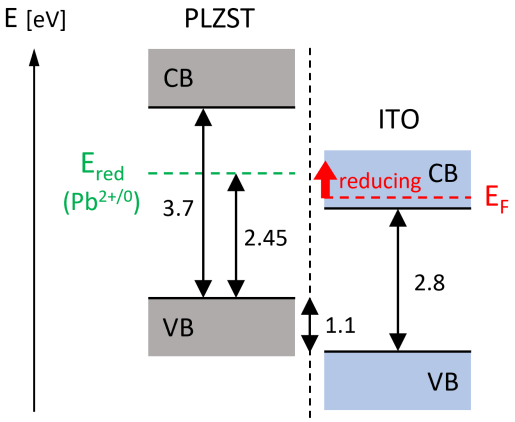

Figure 6.20.: Energy band alignment between PLZST and ITO with the upper limit of the Fermi level (the reduction potential E_{red}) of PLZST derived from the specific binding energy of the Pb^{2+} emission where metallic Pb occurs.

room-temperature XPS data acquired on bulk ceramic and thin film PZT samples, which belong to early studies in the group, we know $E_{\mathrm{VB}} - E_{\mathrm{Pb4f}} = 136.5 \pm 0.2$ eV. Since the band gap varies with temperature, the binding energy acquired at elevated temperature can not be directly used to calculate the room-temperature band diagram. It can be seen that the binding energy of 138.8 eV at 250°C corresponds to the room-temperature value of about 138.95 eV (taking the spectra measured after the cooling-down and the removal of the field). Therefore, the position of the reduction potential relative to the VBM of PLZST should be $E_{\mathrm{red}} - E_{\mathrm{VB}} = 2.45 \pm 0.2$ eV. By taking a band gap of about 3.7 eV [152], it can be known that the upper limit of the Fermi level E_{red} stays about 1.25 eV below the CBM. Besides, the band alignment between PLZST and ITO is derived from the difference of binding energy between the Pb 4f and In 3d emissions, which is consistent with the situation of the PZT/ITO interface [228].

With the band alignment given in Figure 6.20, the process of such a reduction becomes easy to describe. At the beginning, the Fermi energy at the interface (controlled by ITO) stays below the transition level of $Pb^{2+/0}$. When the cathodic polarization is applied to the ITO at elevated temperature, the Fermi level of ITO will increase because the ITO layer is gradually reduced. Once the Fermi energy reaches the position of $Pb^{2+/0}$, the reduction occurs on the Pb-site of the PLZST.

6.2.5. Technical issues about the usage of top electrode

For this novel experimental method based on operating solid oxide electrolyte cells, there are some technical requirements related to the top electrode:

(1) The thickness of the top electrode should be small enough so that the photoelectrons from the ceramic substrate can be detected;
(2) The thin film electrode should be sufficiently electrically conductive;
(3) The deposition of the electrode material should not lead to a chemical reduction at the interface;
(4) The electrode material needs to have a tunable Fermi level when the solid electrolyte cell is operating, and the accessible range of the Fermi level should match the positions of relevant transition energy levels to be identified within the band gap of the dielectric material;
(5) The electrode material should be stable under the operating conditions of the cell.

A 4-nm-thin ITO cathode basically fulfills all these conditions, except for the 2nd point for some occasions. Figure 6.21 demonstrates such consideration. Normally, an ITO film with a thickness of several nanometers is sufficiently conductive for accurate determination of the binding energy by XPS. However, the leakage current through the capacitor/electrochemical cell (i_{leak}) will be superimposed on the XPS emission current (i_{emission}) when the electric field is applied between the two electrodes. It can be noticed in Figure 6.21(a) that between the illuminated position and the ground (reference of the spectrometer) there are two current components, i_{emission} and part of i_{leak}. (The latter term is not exactly equal to i_{leak} and depends on the geometry of the actual connection of the sample.) If i_{leak} is too high, the excessive total current flowing from the illuminated point to the ground through the ITO thin film (also with a resistance) will result in a non-negligible voltage drop across the ITO layer, which further brings about an upward shift of the acquired binding energies of all core-level emissions when ITO is used as cathode, as schematically shown in Figure 6.21(b). Under the circumstances, the specific Fermi energy at which the reduced species starts to grow will also deviate upward. This would cause a too-high calculated position for the trap level within the band gap.

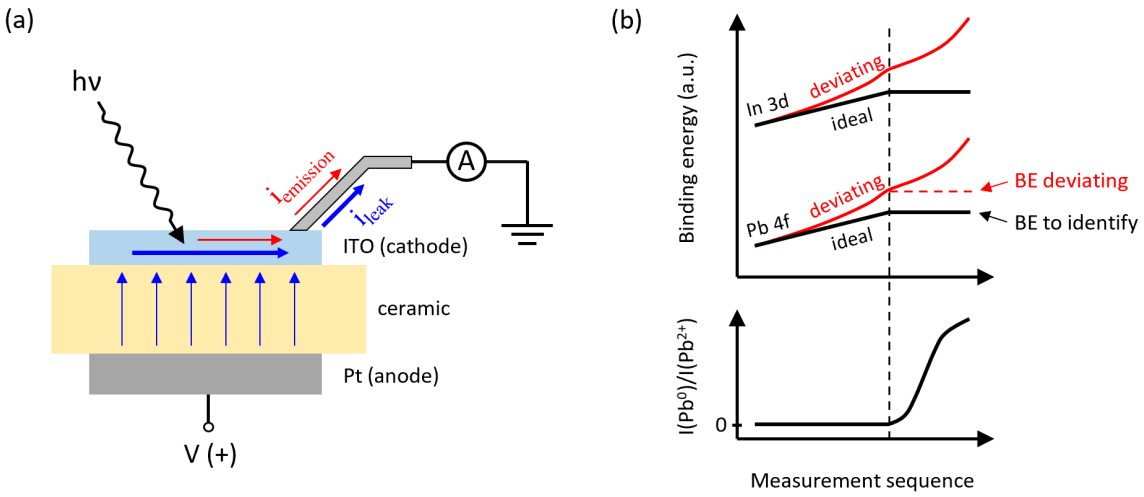

Figure 6.21.: (a) Schematic of the relation between emission and leakage currents during the in situ XPS experiment on a solid electrolyte cell. (b) Probably deviating binding energy determination induced by the superimposition of different current components.

6.3. Summary

A new in situ XPS approach has been developed to study the trap levels and the Fermi level limits of the dielectric materials within their band gaps. The experimental strategy is to operate a solid electrochemical cell at elevated temperature, where a capacitor structure is utilized and the dielectric is regarded as the electrolyte. Similar to a process of resistance degradation, the mobile oxygen species or oxygen vacancies within the dielectric can be driven by the external electric field, so that the anode and cathode interfaces will experience an oxidation and a reduction, respectively. By using the oxide electrodes whose Fermi levels are sensitive to the change of oxygen content, electrochemical oxidation and reduction induced by the shift of the Fermi level are expected in the dielectric (near the interfacial regions). The oxidation and reduction potentials, which correspond to a hole trap and an electron trap, respectively, can be used to characterize the Fermi level limits. Throughout the whole process, the oxidation and reduction at the interfaces, and the potentials where the reactions take place, can be recorded by XPS when thin top electrodes are utilized.

In Section 6.1, RuO_2 with a high work function has been used as anode, so that a relatively low starting point of the Fermi level could be obtained at the anodic interface. This is expected to be convenient for observing the electrochemical oxidation. However, the attempts were not successful. For most of the samples, the vacuum-annealing in the XPS chamber can already reduce the room-temperature deposited RuO_2 and even the dielectric substrate. Such a severe reaction can be assigned to a chemical reduction, which makes the subsequent electrochemical oxidation experiment and the determination of the oxidation potential meaningless. Therefore, a more appropriate anode material is still needed in the future for exploring the lower limit of the Fermi level.

In Section 6.2, the electrode material ITO with a low work function has been used as cathode, so that a relative high starting point of the Fermi level at the interface is expected. In contrast to the RuO_2 anode, ITO seems to be a very suitable cathode material for identifying the upper limit of the Fermi energy. Several experiments have been shown in Sections 6.2.1, 6.2.2, and in Appendix C.1. The reduction on

the Pb-site can be observed for some of these studied materials, for example the three PLZST-related compositions X01, C09, and A02, and the undoped PZT53/47. More importantly, such reduction is always accompanied by an increasing binding energy and a growing asymmetry of the In 3d emission, which clearly indicate a rise of the Fermi energy of the ITO cathode. Besides, the occurrence of the reduction on the Pb-site exhibits a composition dependence. Regarding this problem, Section 6.2.2 has provided some discussion about other possible candidates that might be electrochemically reduced in the relevant material systems.

Based on the experiments with ITO cathodes, more description and discussion have been given in Sections 6.2.3–6.2.5. It has been noticed that complex oxygen migration between the top electrode and the dielectric substrate may occur during the operation of the electrochemical cell, which also depends on the number of $V_O^{\cdot\cdot}$ in the dielectric. As soon as the piling-up of $V_O^{\cdot\cdot}$ within the interfacial region of the dielectric reaches a critical condition, a chemical reduction may happen, instead of the expected electrochemical reduction. Section 6.2.3 has provided some discussion on this issue. Moreover, it has been found that the occurrence of the metallic Pb always corresponds to a specific binding energy of the Pb^{2+} $4f_{7/2}$ emission (138.8$\pm$0.05 eV) for the PLZST-related compositions X01, C09, and A02. According to this value, a quantification of the Fermi level limit of the PLZST materials has been shown in Section 6.2.4. The estimated upper limit of the Fermi level ($E_{\text{red}} - E_{\text{VB}} = 2.45 \pm 0.2$ eV) exhibits a sufficiently large distance to the CBM (>1.0 eV), which might be able to interpret the highly insulating nature of such materials (also see the discussion in Section 8.2 in more detail). Furthermore, Section 6.2.5 has summarized and explained some technical issues of this novel XPS experiment with respect to the usage of the top electrode.

7. In Situ X-Ray Photoelectron Spectroscopy at Interfaces with Ferroelectric Polarization

This chapter describes detailed measurement steps and corresponding results according to the in situ XPS method introduced in Section 3.4.6. First, relevant experiments on both FE- and AFE-based samples have been performed at room temperature in Section 7.1. Two types of materials, RuO_2 and ITO, are used as the top electrode for XPS study. A clear difference can be found between the FE and the AFE compositions in terms of the configuration of the bound and free charges at the electrode/dielectric interfaces. In order to verify such observation, in Section 7.2 a specific PLZST sample that exhibits FE feature at room temperature but AFE feature at elevated temperature has been selected for a temperature-dependent XPS measurement. Subsequently, in Section 7.3 the roles of electrode materials and the difference between the FE and AFE cases will be discussed, and several interface models will be suggested correspondingly. For convenience, Table 7.1 lists all samples described in this chapter.

Table 7.1.: Pb-containing ceramic samples used for the in situ XPS experiments at the electrode/dielectric interfaces with ferroelectric polarization.

Sample No.	Bulk material	Top electrode	Room temperature	Elevated temperature
BHPZT13	PIC 151	RuO_2	Section 7.1.1	Section 7.2
BHC11X10	C11	RuO_2	Section 7.1.1	Section 7.2
BHC10X03	C10	RuO_2	Section 7.1.1	/
BHC09X09	C09	RuO_2	Section 7.1.1	/
BHPZT30	PIC 151	ITO	Section 7.1.2	/
BHC11X07	C11	ITO	Section 7.1.2	/
BHC09X05	C09	ITO	Section 7.1.2	/

7.1. Interfaces with ferroelectric polarization at room temperature

7.1.1. Using RuO_2 as top electrode

The method was first tested at room temperature on the commercial modified PZT composition PIC 151 according to the strategy and procedure described in Section 3.4.6. Figure 7.1 displays the results of such an experiment. The sample was a 0.151 mm thick ceramic pellet with a 5 nm thin RuO_2 top

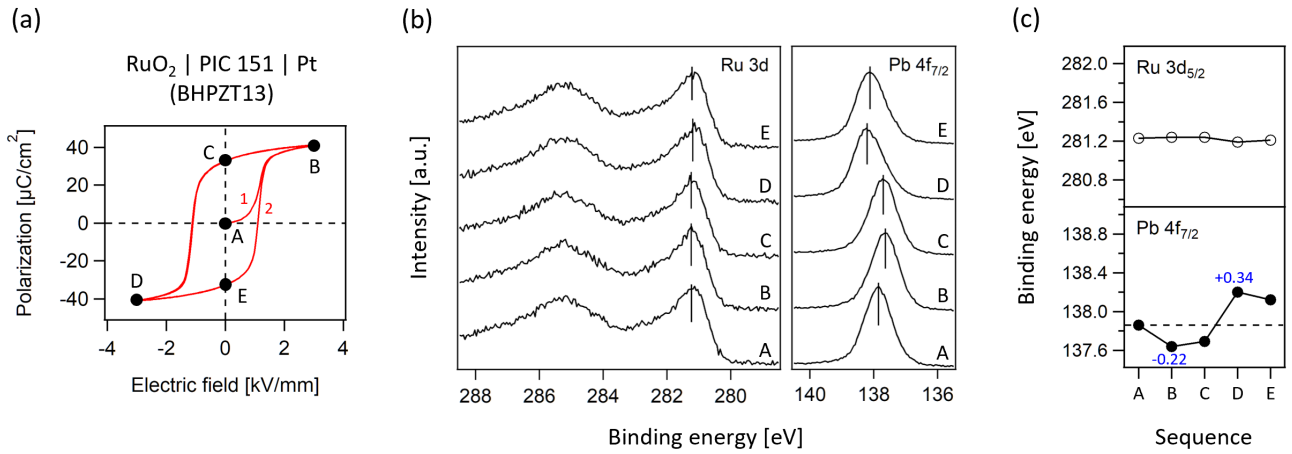

Figure 7.1.: XPS experiment on a PIC 151 sample with RuO_2 top electrode under ferroelectric polarization at room temperature (sample No. BHPZT13). (a) *P*–*E* loops acquired in the XPS chamber and the applied electric fields for different XPS measuring steps (fields A→B→C→D→E, positive field means the RuO_2 top electrode as anode). (b) Ru 3d and Pb $4f_{7/2}$ core level spectra recorded in different steps of applied field. (c) Binding energies of Ru $3d_{5/2}$ and Pb $4f_{7/2}$ extracted from all relevant spectra in (b).

electrode and a thick Pt bottom electrode. An additional Pt layer was applied on the top of RuO_2 for electrical reinforcement, following the schematic in Figure 3.9(a). Figure 7.1(a) depicts the P–E loop of this sample measured in the P–E mode (see Figure 3.15(a)) at 1 Hz inside the XPS chamber. The P–E measurement was performed twice (labeled as "1" and "2") so that the original state of the sample can be seen and a well "developed" polarization state can be ensured. The loops obtained here with specific sample geometry and inside the vacuum chamber are consistent with those measured in air as usual. The XPS measurements were done in the dc mode (see Figure 3.15(b)). Prior to the first P–E loop, relevant XP spectra were obtained without electric field (field A). After the two P–E loops, the XP spectra were measured under a series of fields in the following sequence: $+3 \rightarrow 0 \rightarrow -3 \rightarrow 0$ kV/mm (fields B→C→D→E). Here the positive electric field means the situation where the top electrode was used as anode. In addition, fields A, C, and E are all 0 kV/mm, but they correspond to different polarization states along the FE hysteresis loop. Hence, they are named differently. The Ru 3d and Pb 4f core level spectra measured in these five steps are plotted together in Figure 7.1(b), and their binding energies are given in Figure 7.1(c). It can be seen that the Ru 3d emission basically does not show distinguishable variation with the change of the polarization compared to its original state at field A. Regarding the spectra of Pb 4f, an anodic polarization on the RuO_2 top electrode (field B) leads to a shift of 0.22 eV to the lower binding energy side. When the positive field is removed (at field C), the Pb 4f emission shifts a bit back but the original position has not been reached. This is in line with the hypothesis that the extent of the observed XP spectrum shift should be correlated with the magnitude of FE polarization in the vicinity of the electrode interface (see Figure 3.14). As for the negative polarization state (field D) and the subsequent zero field state (field E), the Pb 4f emissions exhibit shifts to the side of higher binding energy but the absolute magnitudes of such shifts are a bit larger than those of fields B and C, respectively. Besides, there are two more points of details that should be mentioned. The first is about the shape of the shifted spectra of Pb 4f. It can be noticed that some asymmetry occurs when the sample is in a polarized state (most obviously the Pb 4f spectrum at field D). Later in the present section,

more comparisons with spectra recorded from other samples will be provided regarding this point. The second detail is the slight shift/fluctuation appearing in the Ru 3d binding energy, as shown in Figure 7.1(c). This might be attributed either to the effect of using a semiconducting thin film electrode or simply to the uncertainty of the XPS measurement. When the top electrode is a semiconductor instead of a metal, the finite screening effect may take place within the electrode due to its low charge carrier concentration [21, 193]. In this case, an electric potential drop relative to the reference could be produced already on the electrode side, which would further yield a shift in the XP spectrum of the electrode material. Considering that the sputtered RuO_2 is normally metallic and such extra shift in the electrode should have the same sign as that in the dielectric, the very weak fluctuation found in the binding energy of Ru $3d_{5/2}$ may not be related to the screening issue of the electrode. To summarize the case of Figure 7.1, we succeeded in characterizing the FE polarization existing under the top electrode interface by observing the XP spectrum shifts of the bulk element Pb, which is in good agreement with the hypothesis illustrated in Figure 3.14 and with the results of the early in situ XPS studies on BTO single crystals performed in DAISY-MAT [245, 246].

Analogous experiments were subsequently carried out on three C-series PLZST samples so as to investigate the difference between the electrode/FE and the electrode/AFE interfaces in terms of the screening behavior. Figure 7.2 displays the results of three sets of experiments. The C11, C10, and C09 ceramic samples were 0.125, 0.154, and 0.130 mm thick, respectively. Each of them had a 5 nm thin RuO_2 top electrode and a thick Pt bottom electrode. The Pt reinforcement layer was utilized on the top of RuO_2. Figure 7.2(a, d, g) gives the P–E loops of these samples measured at 0.5 Hz in the XPS chamber, which are generally in accordance with the ones obtained in air (see Figure 4.4). Two P–E loops (labeled with "1" and "2") are included for each sample. The black dots with letters denote the steps of electric field where XPS measurements were performed. For the C11 sample, its first P–E loop, which remains at very low polarization until nearly 2 kV/mm in Quadrant I, is strongly different from the second, implying an AFE-like initial state before any poling treatment. Once the P–E measurement has been operated, the sample starts to manifest a FE-like hysteresis feature. Its sequence of applied electric field in the dc mode for XPS measurements is: $0\rightarrow+2.5\rightarrow0\rightarrow-2.5\rightarrow0$ kV/mm (fields A→B→C→D→E). With the decrease of Ti content on the B-site, the C-series PLZST compositions become AFE. Composition C09 is already a typical AFE showing double hysteresis loop at room temperature, while composition C10 is something between C09 and C11. For the C10 sample, its first P–E loop exhibits a small slope until the field reaches 3.5 kV/mm, also indicating an AFE-like initial state. In contrast to C11, the C10 sample has much lower remanent polarization when the field returns to zero. It should be noted that the P–E loops given here were all acquired at 0.5 Hz. However, the XPS measurements were done under dc fields (regarded as infinitely small frequency), with which a further drop of the remanent polarization of the C10 sample to a sufficiently low level is believed to happen within few seconds after the removal of the external field. This has been mentioned in Section 4.1.1 in connection to Figure 4.4(b). Therefore, we expect in Figure 7.2(d) that the field step right following field B can be regarded as a zero-remanent-polarization state very close to the one of field A. To simplify, the two field steps with remanent polarization for the C10 sample are also named field A and the sequence of field for XPS measurements becomes: $0\rightarrow+4\rightarrow0\rightarrow-4\rightarrow0$ kV/mm (fields A→B→A→C→A). With respect to the C09 sample that is surely AFE, a similar field sequence is used: $0\rightarrow+6\rightarrow0\rightarrow-6\rightarrow0$ kV/mm (fields A→B→A→C→A). All relevant core level emissions of Ru 3d and Pb 4f are displayed in Figure 7.2(b, e, h) and their binding energies correspondingly in Figure 7.2(c, f, i). Obviously, the variation in the Ru 3d spectrum under the influence of FE polarization can be neglected in all three cases. By contrast, the evolutions of Pb 4f emissions exhibit different tendencies. For the C11 sample, the Pb 4f emission undergoes almost the same changes as those observed in the PIC 151 sample although their first P–E

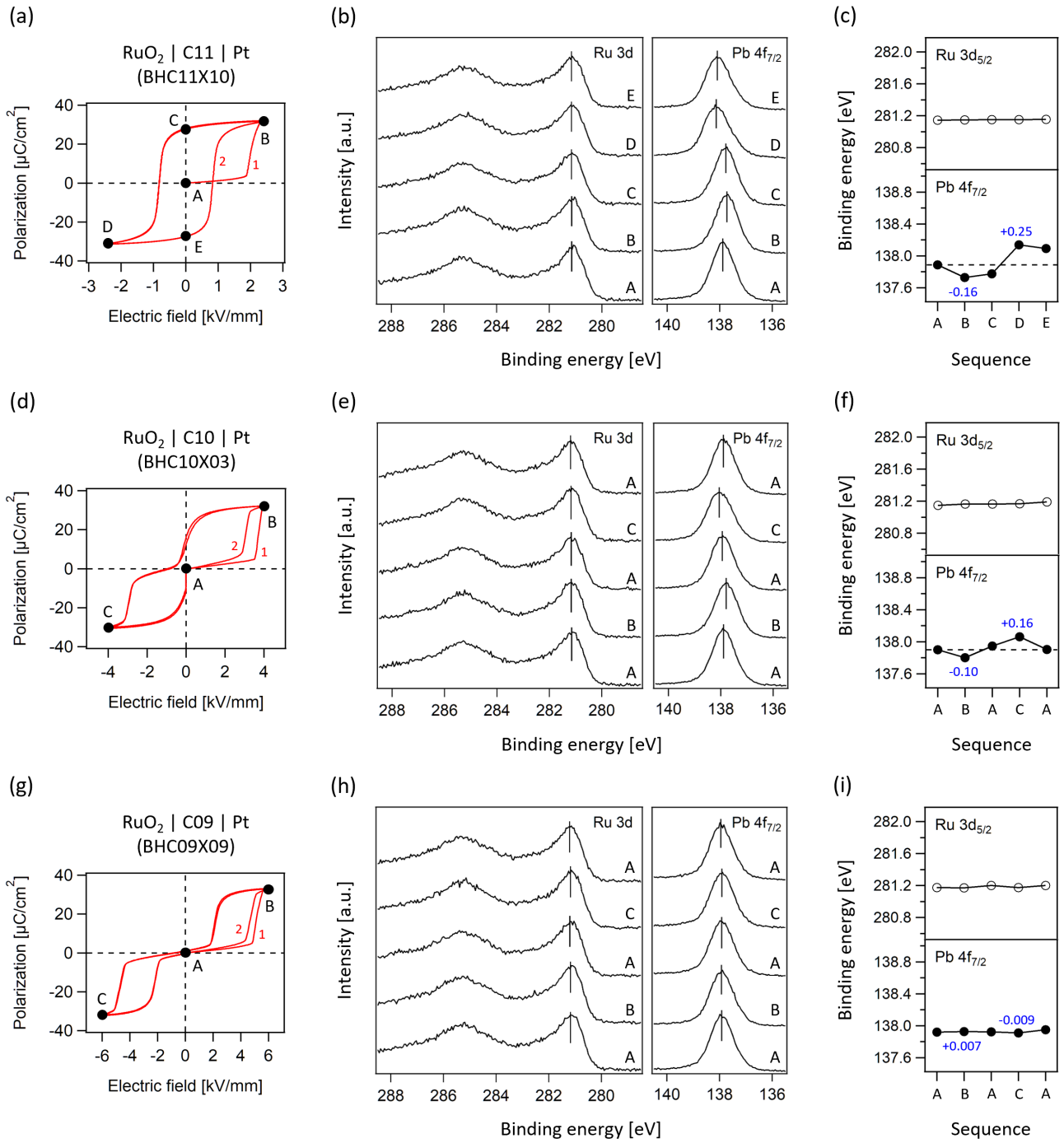

Figure 7.2.: XPS experiment on (a–c) a C11, (d–f) a C10, and (g–i) a C09 sample under ferroelectric polarization at room temperature (sample No. BHC11X10, BHC10X03, BHC09X09, respectively). All of them have RuO_2 top electrodes. (a, d, g) *P–E* loops acquired in the XPS chamber and the applied electric fields for different XPS measuring steps. (C11: fields A→B→C→D→E; C10: fields A→B→A→C→A; C09: fields A→B→A→C→A. Positive field means the RuO_2 top electrode as anode). (b, e, h) Ru 3d and Pb $4f_{7/2}$ core level spectra recorded in different steps of applied field. (c, f, i) Binding energies of Ru $3d_{5/2}$ and Pb $4f_{7/2}$ extracted from all relevant spectra in (b, e, h), respectively.

loops look very different. The Pb 4f spectrum shifts toward lower binding energies at fields B and C, and toward higher binding energies at fields D and E. The latter two have a bit larger absolute magnitudes than the former two, showing asymmetric offsets depending on the polarity which have also been noticed for PIC 151. For the C11 sample the largest difference between the negative and positive offsets of the binding energy is about 0.41 eV from field B to field D, which is less than the value in the PIC 151 case (ca. 0.56 eV). Besides, an obvious asymmetry of the Pb $4f_{7/2}$ emission on the right side of the maximum can be found again at field D where the RuO_2/dielectric interface is under a cathodic polarization, similar to the case of PIC 151. As for the C10 sample, with the vanishing of remanent polarization the Pb 4f spectrum shifts at the two steps with zero field also disappear, in good agreement with the hypothesis that the observed XP spectrum shift is related to the magnitude of FE polarization at the interface. However, the shifts at both fields B and C exhibit obviously less extent compared to the fields B and D in the C11 sample although these two samples have very close polarization values at their respective maximum applied fields. For the C10 sample the largest offset difference of the Pb 4f binding energy is only ca. 0.26 eV from field B to field C, much smaller than those of the PIC 151 and the C11 samples. Totally inconsistent with the other cases, the C09 sample exhibits no recognizable shift in the Pb 4f spectrum, even when the polarization is switched at fields B and C (from an AFE state to a FE state). At the electrode interface, the field-induced FE state should still be able to form a charge configuration as shown in the 2nd and 4th rows of Figure 2.20 and thereby give rise to certain offsets on the XP spectra of the bulk elements. However, this is apparently not the case. In other words, we could speculate that the field-induced FE polarization in an AFE material might not reach the electrode interface, which could be a fundamental difference between the electrode/FE and the electrode/AFE interfaces.

In order to show more details of the variation in the shape of the Pb 4f emission during the polarization switching process, Figure 7.3 plots the normalized Pb $4f_{7/2}$ peaks of all relevant samples according to

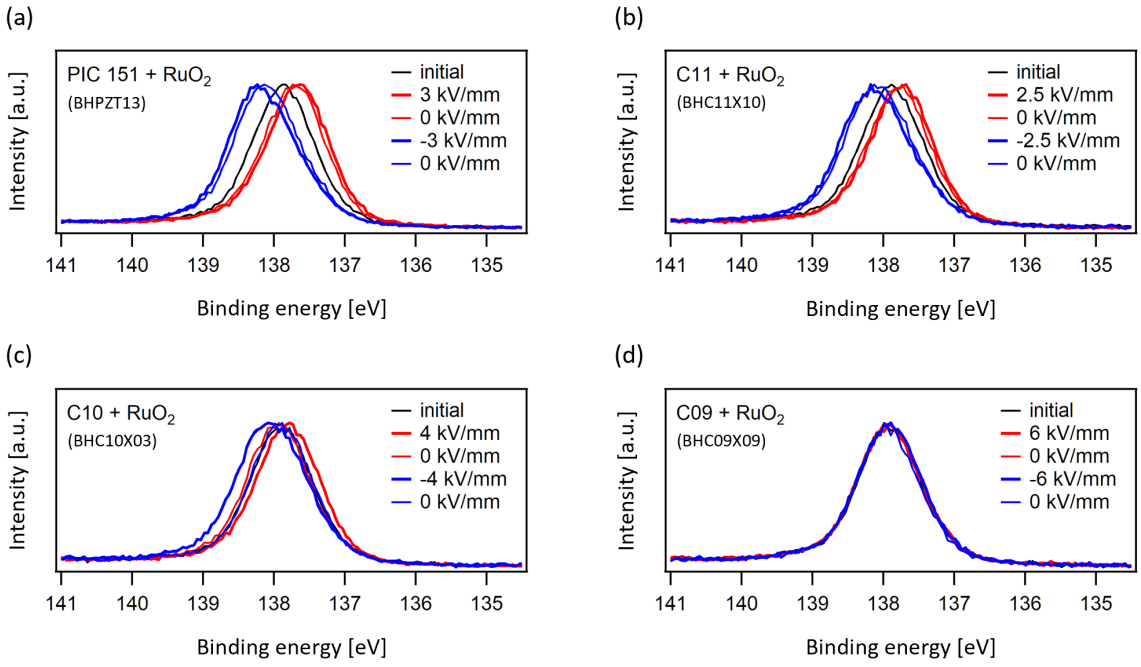

Figure 7.3.: Comparison of normalized Pb $4f_{7/2}$ emissions of all relevant samples with RuO_2 top electrode throughout their respective steps of applied electric field.

their respective steps of applying fields. Comparing the initial states before poling (black curves), all the samples show very similar spectra in terms of the shape and the binding energy. Apparently, the PIC 151 sample undergoes the largest shifts in the Pb 4f emission, as shown in Figure 7.3(a). Besides, the shape of its peak varies differently depending on the polarity. With a cathodic polarization (blue curves), the peak exhibits more asymmetry on the right side, so that it looks obviously broader than the initial state. By contrast, an anodic polarization (red curves) only yields a very minor asymmetry on the left side which is almost unrecognizable, and no broadening of the peak can be observed. Combined with the fact that the peak shifts more under the cathodic polarization, one may speculate that the FE polarization state where $\vec{P}$ points toward the electrode (positive bound charges in the dielectric bulk compensated by negative free charges in the electrode layer) would be more accessible and stable, rather than the other way around. This would indicate that the electrode layer can carry more negative free charges (e.g. electrons) than positive ones to complete the screening. The broadening of the peak is probably caused by an inhomogeneous FE polarization at the electrode as the samples used here are all polycrystals in which the orientations of various domains cannot be perfectly aligned. Since an irregular distribution of the possible domain orientations is always expected, the acquired XP spectra will reflect the different polarization states at the interface. Thus, it is not reasonable to make a spectrum fitting for such measurements. In the following parts, we will only quantify the peak maxima and discuss the peak shape if it is necessary. In Figure 7.3(b–d) by comparing all the three C-series PLZST samples, the clear tendency can be seen that the shifts of the Pb 4f emission gradually vanish when the sample starts to become AFE. The way how the peak shape in the C11 sample varies with the polarization state is very similar to that in the PIC 151 sample. In both the C11 and C10 cases, the previously mentioned phenomenon that the cathodic polarization supports a more polarized state at the electrode interface can be observed as well. As for the C09 sample, the peak shapes of all steps are almost identical and unchanged compared to its initial situation.

7.1.2. Using Sn-doped In_2O_3 as top electrode

ITO is the second top electrode material used for this in situ XPS experimental method. Different from RuO_2, which is usually regarded as a metal with high work function, ITO is an n-type semiconductor. By comparing these two electrode materials, we expect to see the effect of the work function and the charge carrier concentration of electrode materials on the interface screening behavior.

The first attempt was again made on the commercial modified PZT composition PIC 151 at room temperature, displayed in Figure 7.4. The sample was a 0.125 mm thick ceramic pellet with a 3 nm thin ITO top electrode (deposited at 350°C) and a thick Pt bottom electrode. Different from the previous cases, the geometry of this sample followed the style given in Figure 3.9(b) where no additional Pt reinforcement layer was used on the top of ITO. This is because fatal cracks had been formed during the P–E loop measurements on three earlier PIC 151 samples with ITO top electrodes that had extra Pt layers. Figure C.11 in Appendix C.2 is a photograph of one of such failed samples. The crack that passed through two corners of the square-shape hole on the Pt layer was reproducible and might be attributed to inhomogeneous strain response (piezoelectric effect in terms of the responding speed, the magnitude of strain, etc.) in different areas over the ceramic pellet. More explicitly, the large difference in the field-induced strain might yield stress concentration at the corners if the electrode area with extra Pt layer could respond faster than the area only covered by 3 nm thin ITO. In order to avoid the occurrence of such cracks, we used a pure ITO layer as the top electrode for this particular sample. Figure 7.4(a) shows the P–E loops measured in the P–E mode at 1 Hz inside the XPS chamber, which look

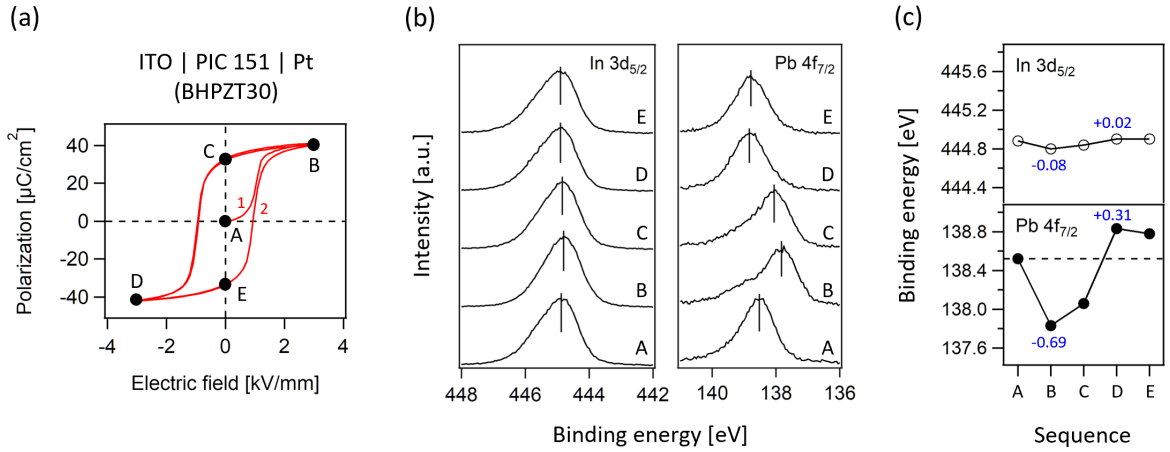

Figure 7.4.: XPS experiment on a PIC 151 sample with ITO top electrode (deposited at 350°C) under ferroelectric polarization at room temperature (sample No. BHPZT30). (a) *P–E* loops acquired in the XPS chamber and the applied electric fields for different XPS measuring steps (fields A→B→C→D→E, positive field means the ITO top electrode as anode). (b) In $3d_{5/2}$ and Pb $4f_{7/2}$ core level spectra recorded in different steps of applied field. (c) Binding energies of In $3d_{5/2}$ and Pb $4f_{7/2}$ extracted from all relevant spectra in (b).

similar to those of the previous PIC 151 sample with RuO_2 top electrode (see Figure 7.1(a)). The XPS measurements were carried out under the electric fields in the following sequence: 0→+3→0→−3→0 kV/mm (fields A→B→C→D→E). Here the positive electric field means that the top ITO electrode was used as anode. Figure 7.4(b) displays all relevant core level emissions of In 3d and Pb 4f and Figure 7.4(c) gives their corresponding binding energies. One of the largest discrepancies compared to the case using RuO_2 top electrode is that not only the Pb 4f emission from the bulk dielectric but also the In 3d from the electrode layer is shifting when the polarization state is switching. Nevertheless, the shifts of the In 3d peaks are much less than those of the Pb 4f. The directions of such shifts of the Pb 4f and In 3d emissions are the same within each step of the applied electric field. This phenomenon is consistent with the previously mentioned theory (in Section 7.1.1) that the separation of the bound and free charges at the electrode interface may take place (partially) on the electrode side when the electrode is a semiconductor. As an n-type semiconductor, ITO might have a non-negligible spatial distribution of its compensating charge carriers along its finite thickness (3 nm), which is generally in accordance with the expectation. Another important discrepancy is about the magnitude of the emission shift of the Pb 4f core level. The shifts caused by cathodic polarization in the PIC 151 samples with ITO and RuO_2 top electrodes are basically the same, whereas the shift due to anodic polarization in the PIC 151|ITO sample is obviously larger than that of the PIC 151|RuO_2 sample (in Figures 7.1(c) and 7.4(c) comparing the two "field B" for $+P_{max}$ or the two "field C" for $+P_r$, respectively). As a result, here in the PIC 151|ITO sample the largest difference between the negative and positive offsets of the Pb $4f_{7/2}$ binding energy comes up to 1.0 eV. According to the understanding of Equation 2.42, one could suppose that such a large variation of the SBHs might be attributed to either a larger magnitude of the FE polarization in the vicinity of the electrode interface or a larger effective screening length across the interface. Both of these two possibilities could be related to the usage of ITO electrode. More discussion will be given in Section 7.3.1.

Since the charge carrier concentration in ITO is believed to play certain roles in screening the bound

charges within the framework of the screening model, extra experiments were carried out on PIC 151. The normalized In $3d_{5/2}$ and Pb $4f_{7/2}$ emissions of the two relevant PIC 151 samples with ITO top electrodes throughout their respective measuring procedures are plotted together in Figure 7.5. Figure

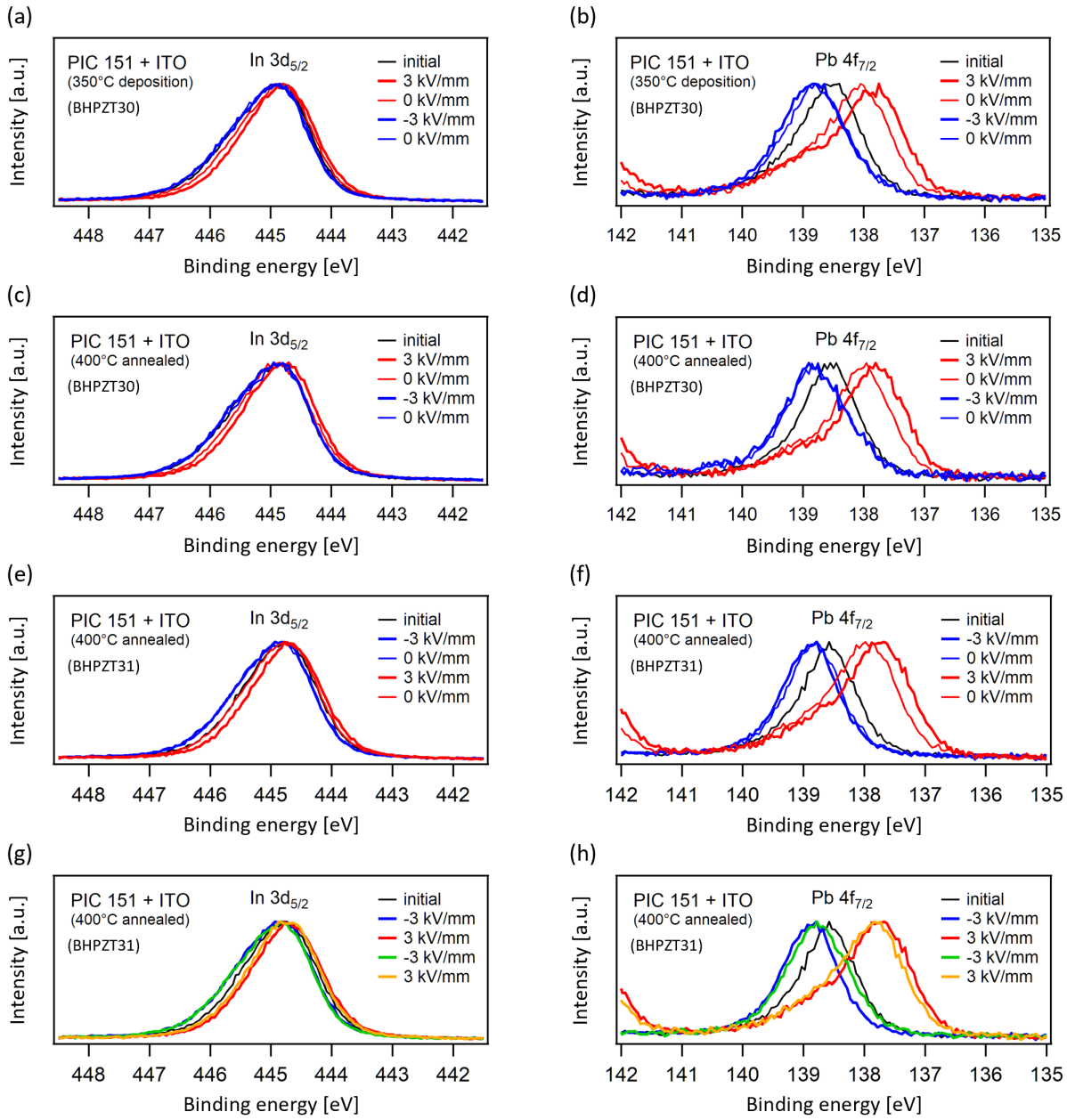

Figure 7.5.: Comparison of normalized In $3d_{5/2}$ and Pb $4f_{7/2}$ emissions of two PIC 151 samples both with ITO top electrode throughout their respective steps of applied electric field. Sample No. BHPZT30: (a, b) ITO deposited at 350°C; (c, d) after post-annealing at 400°C. Sample No. BHPZT31: (e, f) ITO firstly deposited at 350°C and subsequently annealed at 400°C, XPS measured in the reverse sequence of field (fields A→D→E→B→C if schematically taking the *P*–*E* loops in Figure 7.4(a)); (g, h) comparison of two successive rounds with the same reverse sequence.

7.5(a, b) displays again the spectra of sample No. BHPZT30 already given in Figure 7.4(b). After this measurement, the sample was sent back to the deposition chamber for a post-annealing at 400°C in Ar (the same gas as the one used for ITO deposition), by which the ITO layer might be able to carry more charges due to a probable rise of the Fermi energy. Then the same procedure was performed and the XPS data are displayed in Figure 7.5(c, d). It can be seen that the post-annealing does not result in any obvious change in the spectra. Very likely, the ITO films prepared at 350°C and 400°C may have nearly no influence on the Fermi level and the charge carrier concentration. Apart from the deposition condition of ITO, it is doubted that the sequence of applying electric field might also yield some irreversible variation on the ITO electrode. In other words, measuring XPS in the sequence of $+P_{\text{max}} \rightarrow +P_{\text{r}} \rightarrow -P_{\text{max}} \rightarrow -P_{\text{r}}$ might bring about different result from the measurement with a sequence of $-P_{\text{max}} \rightarrow -P_{\text{r}} \rightarrow +P_{\text{max}} \rightarrow +P_{\text{r}}$. Therefore, another PIC 151 sample with ITO top electrode (sample No. BHPZT31) was prepared basically according to the same procedure as the previous one's. The 3 nm ITO was deposited in Ar at 350°C, directly followed by a post-annealing at 400°C. Thick Pt was used as the bottom electrode and no extra Pt layer was coated on the top of ITO. For the XPS measurement, the sequence of applied electric field is: $0 \rightarrow -3 \rightarrow 0 \rightarrow +3 \rightarrow 0$ kV/mm, which is the reverse version of the previous PIC 151|ITO sample. No P–E loop was recorded here because measuring the loop can already introduce an anodic polarization state prior to a cathodic one when the loop measurement starts from Quadrant I. For this sample, we directly started measuring XPS in the dc mode. The field sequence of $0 \rightarrow -3 \rightarrow 0 \rightarrow +3 \rightarrow 0$ kV/mm was run twice. The spectra obtained in the first cycle are plotted in Figure 7.5(e, f) and the spectra corresponding to all the maximum polarization states throughout the two cycles are plotted in Figure 7.5(g, h) in their real sequence.

Interestingly, a difference can be noticed by comparing the spectra measured at -3 kV/mm (thick blue curves) in Figure 7.5(d, f). The Pb $4f_{7/2}$ emission is roughly symmetric and relatively narrow when the cathodic polarization state goes prior to the anodic one (see Figure 7.5(f)). By contrast, the Pb 4f peak looks asymmetric on the right side and thereby becomes clearly broader if the cathodic polarization state is reached after the anodic one (see Figure 7.5(d)). This phenomenon can be verified in Figure 7.5(h) where the green spectrum (at -3 kV/mm) that was measured later than the red one (at $+3$ kV/mm) also exhibits the same asymmetry and broadening effect as that has been shown in Figure 7.5(d). All these observations imply that something must have happened once the ITO was used as anode and the consequence cannot be easily removed by applying a reverse electric field. One possibility which may lead to the asymmetry and broadening of the Pb 4f emission on the right-hand side could be the occurrence of some partially pinned or non-switchable FE domains that prefer to stay in the direction pointing from the ITO toward the Pt side. Similar asymmetry has been also found in the Pb 4f spectra of the PIC 151 sample with RuO_2 top electrode (see the blue curves in Figure 7.3(a)). Hence, it is unclear whether and how this effect is related to the top electrode materials. Besides the broad appearance under the cathodic polarization condition, the special shape of the Pb 4f peaks acquired when ITO was used as anode is also characteristic. On the higher-binding-energy side of the main Pb 4f emission, there is always a shoulder-like signal which seems to be left behind when the main peak is shifting to the right side under an anodic polarization. This phenomenon can be clearly noticed in all the thick red spectra in Figure 7.5(b, d, f, h). The reproducible shoulder might be assigned again to some kind of non-switchable FE domains in the vicinity of the electrode interface like what has been discussed above, or to something else. More investigations are needed to find an interpretation for this phenomenon.

Concerning the peak shape of the In 3d emission, furthermore, one can discover in Figure 7.5(a, c, e, g) that all the peaks measured under anodic polarization (the thick red ones) are slightly narrower and less asymmetric than those measured with cathodic polarization (the thick blue ones). This indicates a

variation in the charge carrier concentration within the ITO layer during the switching process of FE polarization. When the ITO is used as anode, the needed free charges on the electrode side that can compensate for the negative bound charges should be positive, meaning that a certain number of free electrons in the ITO will be spatially pushed away from the interface. As a result, the charge carrier concentration of the n-type ITO would be reduced within the detecting depth of XPS, leading to a shift to lower binding energy and to a less asymmetric shape on the higher-binding-energy side of the In 3d spectrum. When the ITO is used as cathode, the opposite effect would be expected.

With the experience obtained from the PIC 151 samples, similar experiments were subsequently performed on two C-series PLZST samples so that the difference between the ITO/FE and the ITO/AFE interfaces can be studied. Figure 7.6 shows the results of these experiments. The C11 and C09 ceramic samples were 0.127 and 0.137 mm thick, respectively. Each of them had a 4 nm thin ITO top electrode

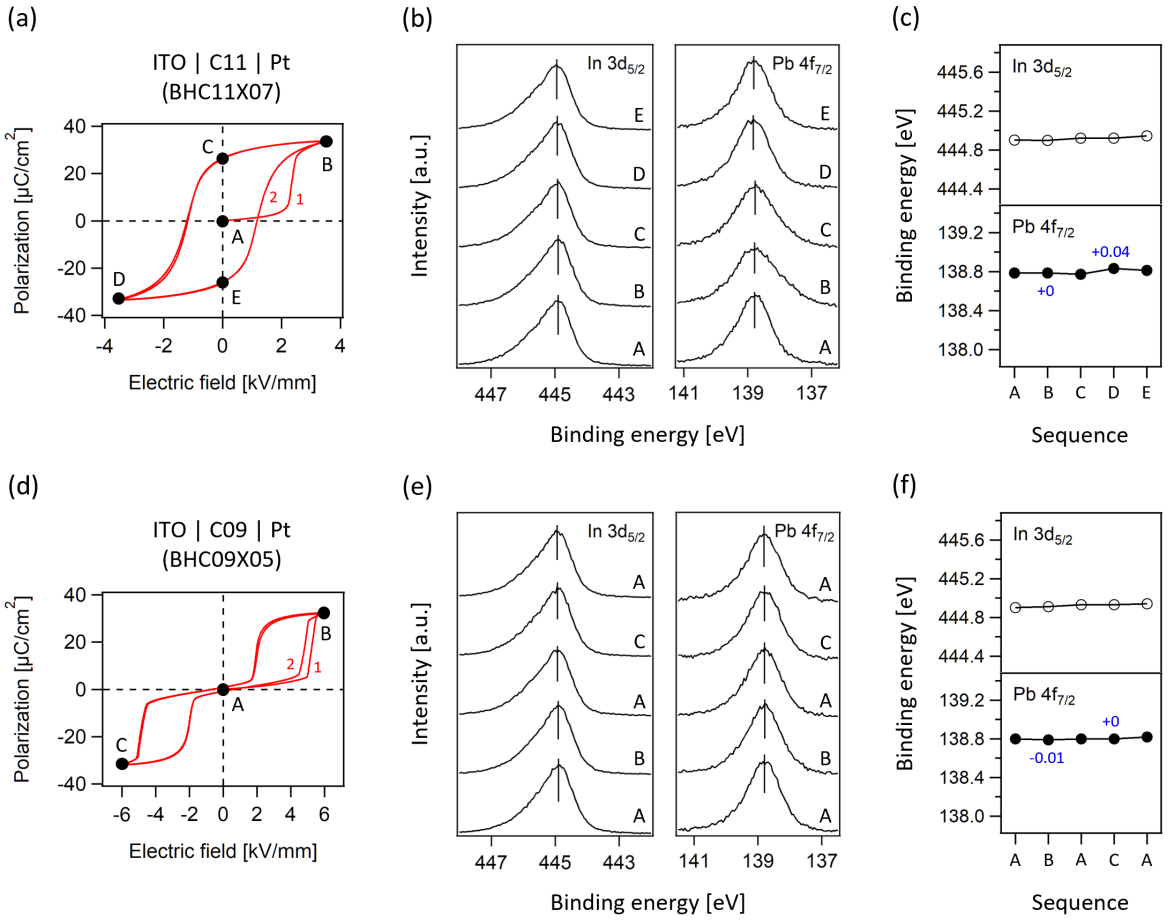

Figure 7.6.: XPS experiment on (a–c) a C11 and (d–f) a C09 sample under ferroelectric polarization at room temperature (sample No. BHC11X07 and BHC09X05, respectively). Both of them have ITO top electrodes. (a, d) *P*–*E* loops acquired in the XPS chamber and the applied electric fields for different XPS measuring steps. (C11: fields A→B→C→D→E; C09: fields A→B→A→C→A. Positive field means the ITO top electrode as anode). (b, e) In $3d_{5/2}$ and Pb $4f_{7/2}$ core level spectra recorded in different steps of applied field. (c, f) Binding energies of In $3d_{5/2}$ and Pb $4f_{7/2}$ extracted from all relevant spectra in (b, e), respectively.

(deposited at 400°C) and a thick Pt bottom electrode. Different from the PIC 151 cases, for these two PLZST samples extra Pt layers were used on the top of ITO for electrical reinforcement and no crack issue was noticed. Figure 7.6(a, d) displays the P–E loops measured at 0.5 Hz in the XPS chamber. Two successive loops are included for each sample. Compared with the previous C11 sample with a RuO_2 top electrode in Figure 7.2(a), this C11 sample possesses an obviously more slanted shape due to the usage of ITO electrode, indicating a "harder" FE feature. By contrast, the C09 sample with ITO electrode shows almost the same P–E loops as the previous one with RuO_2 electrode in Figure 7.2(g). For the C11 sample with FE hysteresis feature, the sequence of applied field for the XPS measurement is: 0→+3.5→0→−3.5→0 kV/mm (fields A→B→C→D→E). For the C09 sample safely showing AFE behavior, the measuring sequence is: 0→+6→0→−6→0 kV/mm (fields A→B→A→C→A). The corresponding In 3d and Pb 4f core level spectra for these two cases are displayed in Figures 7.6(b, e), and the extracted binding energies are given in Figure 7.6(c, f). It can be easily seen that the In 3d emissions of both samples experience almost no recognizable variation throughout the measurements, unlike the PIC 151 cases shown in Figure 7.5. Thus, no more discussion will be given here with respect to the In 3d peaks. One of the most noteworthy phenomena in this part is the evolution of the Pb 4f emission of the C11 sample. One might be very easily misled when only looking at the change in the binding energy of the Pb $4f_{7/2}$ peak in Figure 7.6(c), which only gives a total difference of $\lesssim$0.06 eV between the downward and upward offsets. However, this is not the complete picture. It can be noticed in Figure 7.6(b) that there is a significant change in the shape of the Pb 4f emission on the lower-binding-energy side at fields B and C. Certain part of the signal seems to shift toward the expected direction under an anodic polarization although the main emission (the maximum of the spectrum) tends to remain at its initial binding energy. In contrast to the anodic polarization state, a cathodic polarization can not bring about the similar variation on the other side of the spectrum. All these observations reveal the possibility that there might be only a limited number of domains (probably either FE or AFE ones) in this material behaving freely like normal switchable FE domains. Nevertheless, it is still undeniable that the switching process of the polarization in this PLZST sample can be observed via our in situ XPS method. Regarding the C09 sample, again, no recognizable variation can be seen at all in the Pb 4f peaks, same as what has been found in the case with a RuO_2 top electrode (see Figure 7.2(g–i)). Therefore, the suspected absence of the FE polarization at the interface between the electrode and the field-induced FE phase within an AFE capacitor appears to be a fundamental difference. For better comparisons, Figure 7.7 plots the normalized Pb $4f_{7/2}$ emissions of all relevant measuring steps of the two samples mentioned above. The partially shifted emission can be well seen in the C11 sample when the ITO layer is used as anode, and all Pb 4f spectra of the C09 sample coincide almost perfectly.

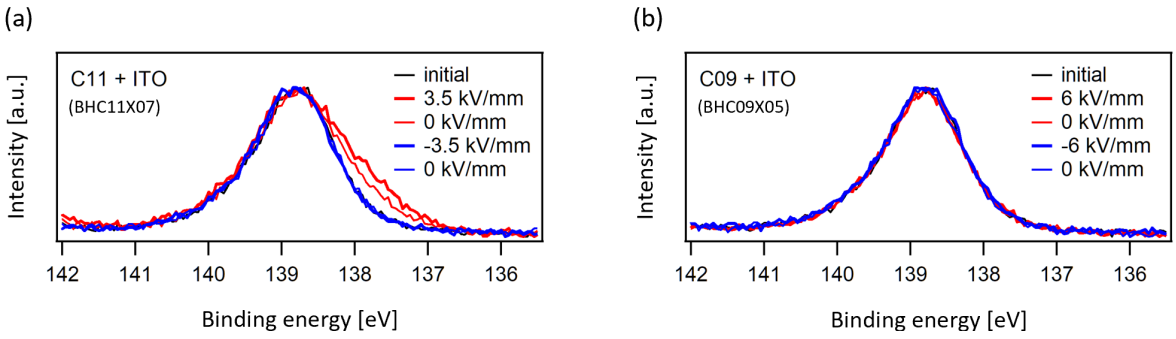

Figure 7.7.: Comparison of normalized Pb $4f_{7/2}$ emissions of both PLZST samples with ITO top electrode throughout their respective steps of applied electric field.

7.2. Interfaces with ferroelectric polarization at elevated temperatures

In Sections 7.1.1 and 7.1.2, there is an important discovery that the formation of FE polarization at the electrode interface in an AFE sample can not be detected via our in situ XPS method. For a FE sample, the XP spectra of the dielectric material under the top electrode will shift with the switching of its polarization state. By contrast, in an AFE sample no variation has ever been observed in the XP spectra on the dielectric side even though the AFE-to-FE transition field is exceeded and the sample stays already in a FE state. The absence of the spectrum shift may have the following two possible origins according to Equation 2.42:

(1) The effective screening length λ_{eff} might be sufficiently small or almost zero so that the induced change in the SBHs could be less than the error of XPS measurements and therefore become undetectable. However, this situation is unlikely for an interface between a ceramic substrate and a sputtered thin film electrode even if the ceramic surface has been polished to a certain degree.
(2) The field-induced FE polarization in an AFE capacitor might not reach the electrode interface, so that the AFE under a certain depth from the electrode interface (at least the part within the detecting depth of XPS) would always stay in the original AFE state.

Prior to a more detailed discussion on the electrostatic situation at the electrode/AFE interfaces, some additional experiments are needed to verify the observation itself. Here we make use of the temperature-induced phase transition of the PLZST composition C11. As shown in Figure 4.5, composition C11 undergoes a phase transition within a certain temperature range between 60°C and 120°C (around 80°C). The material exhibits a FE/AFE hysteresis behavior under/above the transition temperature, respectively. Therefore, our strategy is that the in situ XPS experiment can be carried out first at room temperature and subsequently at an elevated temperature where the sample shows double hysteresis loops. By comparing the spectrum shifts in two different cases but exactly at the same detected position on the same sample, we may be able to verify whether the discrepant potential drop happening at the electrode interface is really dependent on the type of the hysteresis behavior of the material under test.

The C11 sample, which has a 5 nm RuO_2 top electrode and has been used in Section 7.1.1 (sample No. BHC11X10), is selected for this part. After the measurement shown in Figure 7.2(a–c), the sample has not been annealed at any high temperature, so it is still expected to remain in a polarized state. Figure 7.8 displays all important results of this set of temperature-dependent studies. The experiment was first carried out at room temperature (RT1) and then at 100°C. After that, another room-temperature step (RT2) was done in order to provide a better verification for the effect of interest. Figure 7.8(a) gives the P–E loops measured at 0.5 Hz at the three temperature steps. The vertical black arrow on the right-hand side denotes the sequence of the measurements. It can be seen that the C11 sample, which shows a FE hysteresis behavior at room temperature, exhibits a very standard double hysteresis loop at 100°C. When the sample is cooled down to room temperature, it again shows the similar FE-like hysteresis behavior compared to what has been displayed in Figure 7.2(a). It should be noted that the initial P–E loop at RT1 is not included in Figure 7.8(a) and the XPS measurement starts with the positive electric field (field 1B) for RT1. All relevant Ru 3d and Pb 4f core level spectra and corresponding binding energies are displayed in Figure 7.8(b, c). The sequence of the applied electric field is labeled in Figure 7.8(a, b). The highest electric fields used at each temperature step are always $\pm$3.5 kV/mm, higher than those applied in Figure 7.2(a), which would ensure more saturated states of FE polarization. Moreover, the dashed line in Figure 7.8(c), as a reference level, represents the initial binding energy of Pb 4f for the unpoled sample in the previous experiment given in Figure 7.2(a–c). As can be seen in Figure 7.8(b, c), the Ru 3d emission undergoes a shift toward lower binding energies once the sample

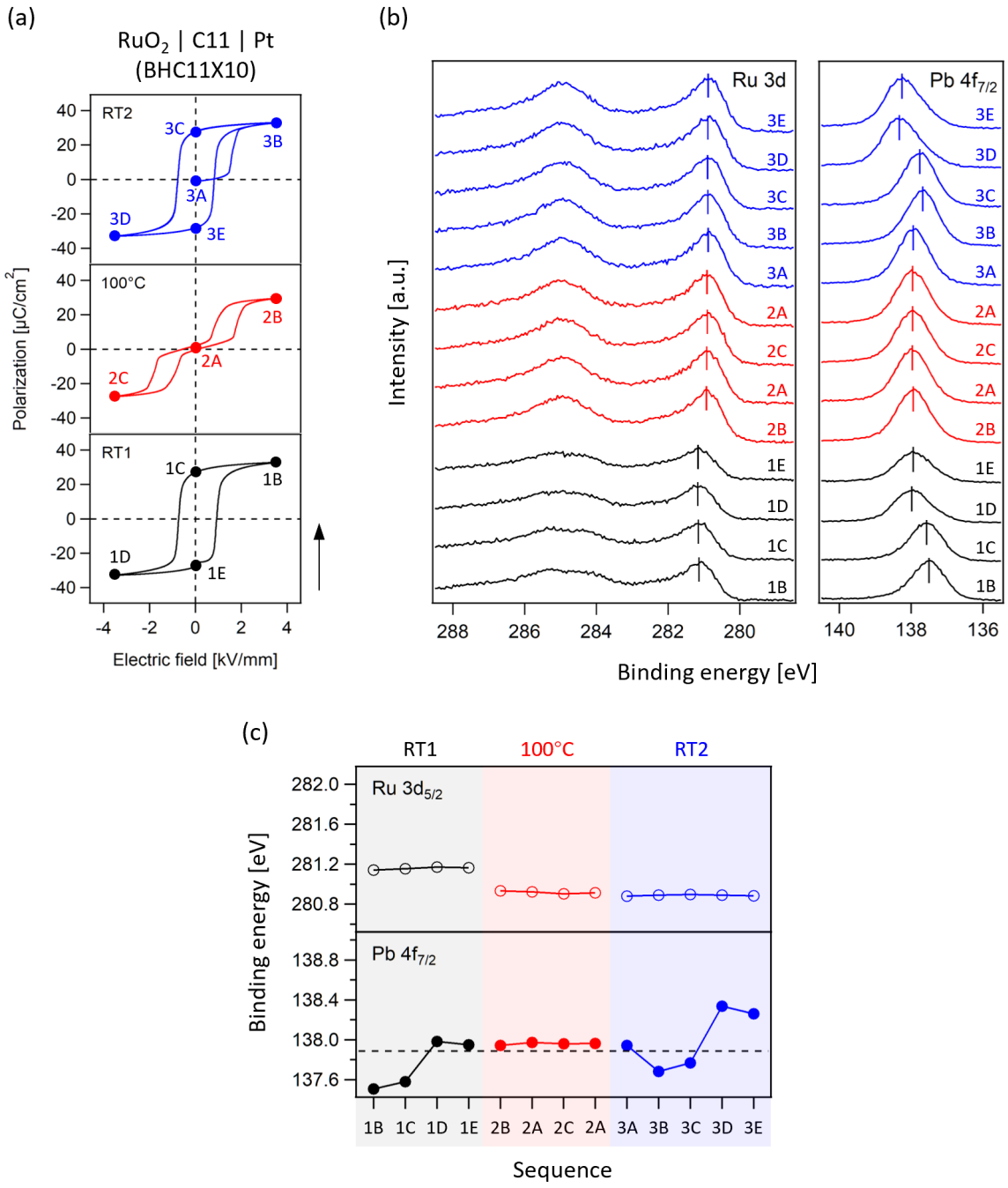

Figure 7.8.: XPS experiment on a C11 sample with RuO_2 top electrode (sample No. BHC11X10) under ferroelectric polarization at three temperature steps: RT1→100°C→RT2. (a) *P*–*E* loops acquired in the XPS chamber and the applied electric fields for different XPS measuring steps. (At RT1: fields 1B→1C→1D→1E; at 100°C: fields 2B→2A→2C→2A; at RT2: fields 3A→3B→3C→3D→3E. Positive field means the RuO_2 top electrode as anode). (b) Ru 3d and Pb $4f_{7/2}$ core level spectra recorded in different steps of applied field. (c) Binding energies of Ru $3d_{5/2}$ and Pb $4f_{7/2}$ extracted from all relevant spectra in (b).

is heated up to 100°C, and no backward shift can be found at RT2. This can be attributed to a slight reduction of RuO_2 due to the annealing in the vacuum chamber, similar to the situation as shown in Figure 6.5(a). Besides, a crystallization could be another possible origin of the shifted Ru 3d emission as the RuO_2 film sputtered at room temperature is expected to be amorphous. Nevertheless, such a change of the RuO_2 electrode is not important in this experiment because the RuO_2 layer has not lost its electrical conductivity and can still act as a good top electrode according to the acquired P–E loops at 100°C and RT2. As for the Pb 4f emission belonging to the dielectric bulk, a clear tendency can be observed that the spectrum shift takes place at the two room-temperature steps but not at 100°C where the material possesses a double loop. It can also be noticed that the largest difference between the negative and positive offsets of the Pb 4f binding energy increases after the heating process at 100°C (from ca. 0.48 eV at RT1 to ca. 0.65 eV at RT2). Based on the results presented here, it could be verified that the electric-field-induced FE polarization of an AFE-based capacitor may not yield a potential step at the electrode interface because of the imperfect screening effect, different from the case of a FE-based capacitor.

In addition to the C11 sample, a similar temperature-dependent experiment was carried out on a PIC 151 sample, which is expected to show FE hysteresis loops at both room temperature and 100°C. An observation of the spectrum shift on the Pb 4f emission at 100°C can be regarded as a good reference and a proof of the validity of the elevated-temperature measurements on the C11 sample. The PIC 151 sample involved here is the one with a RuO_2 top electrode, which has been used in Section 7.1.1 (sample No. BHPZT13). Figure 7.9 displays the results of this experiment. As shown in Figure 7.9(a), the sample exhibits a normal FE-type P–E loop at 100°C, with a reduced coercive field and also a slightly lowered polarization compared to those of the subsequently obtained room-temperature loop. All field steps with zero applied field are omitted here, and the field sequence for the XPS measurement

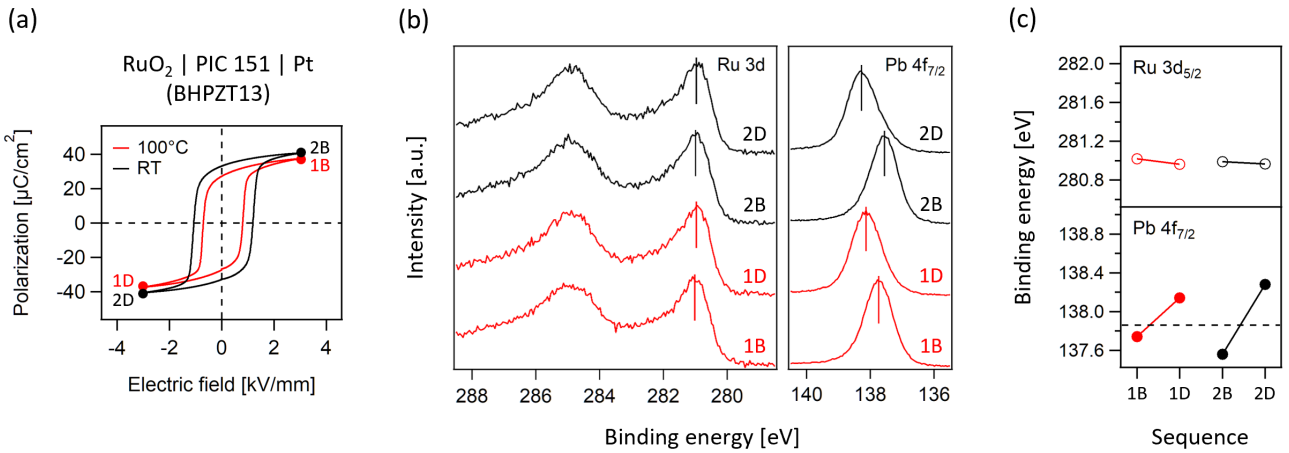

Figure 7.9.: XPS experiment on a PIC 151 sample with RuO_2 top electrode (sample No. BHPZT13) under ferroelectric polarization at two temperature steps: 100°C→RT. (a) P–E loops acquired in the XPS chamber and the applied electric fields for different XPS measuring steps. (At 100°C: fields 1B→1D; at RT: fields 2B→2D. Positive field means the RuO_2 top electrode as anode). (b) Ru 3d and Pb $4f_{7/2}$ core level spectra recorded in different steps of applied field. (c) Binding energies of Ru $3d_{5/2}$ and Pb $4f_{7/2}$ extracted from all relevant spectra in (b).

is: first fields 1B→1D at 100°C, then fields 2B→2D after cooling-down to room temperature. It can be seen in Figure 7.9(b, c) that the shift of Pb 4f emission clearly takes place with the switching of the FE polarization at both temperatures. Therefore, the technical validity can be confirmed for such in situ XPS experiment at an elevated temperature like 100°C.

7.3. Two issues concerning the observed screening behaviors

7.3.1. Comparison of different electrode materials

Based on the results described in Sections 7.1.1 and 7.1.2, a comparison about the effects of using RuO_2 or ITO as top electrode can be performed. Figure 7.10 summarizes the most crucial information of the previous room-temperature experiments. The P–E loops in the left column schematically present the type of the dielectric material. The detailed scales of the loops can be found in Sections 7.1.1 and 7.1.2, so they are omitted here. On the right side of the summary figure, the evolution of Pb $4f_{7/2}$ emission from the dielectric layer in each sample is displayed with the change of its polarization state. The values of polarization are simply read from the P–E loops according to the applied electric fields. It should be noted that the P–E loop measurement can be regarded as an ac approach, while the XPS is done on the samples under dc bias. Hence, the polarization values given here could slightly deviate from the values acquired with a dc method. For each sample, the XP spectra are always plotted from the bottom up. Four samples with RuO_2 top electrode and three samples with ITO top electrode are involved here for the comparison. Moreover, the initial Pb $4f_{7/2}$ peak (the unpoled state) of each sample is included (always the first spectrum from the bottom) and its binding energy is also highlighted by a light color strip, blue for the samples with RuO_2 and red for the ones with ITO.

In general, the PIC 151 samples, possessing an explicitly FE composition, always show the most obvious shifts in the Pb 4f spectrum no matter which electrode material is used. This implies that the observation of a large spectrum shift of the dielectric layer may be related to both the magnitude and the stability of the FE polarization state. Besides, as mentioned above, the AFE composition C09 exhibits no spectrum variation at all even though the bulk has been switched to the field-induced FE state. Also, this behavior cannot be changed by using different top electrode materials. More discussions on this issue will be given in Section 7.3.2. Here we mainly focus on the effects of the work function of the electrodes. When comparing the cases with RuO_2 and ITO top electrodes, we notice the following two phenomena:

(1) The initial binding energies of Pb 4f emission in the unpoled samples show a distinct dependence on the work function of the top electrode material. In the four cases with high-work-function RuO_2 electrode, the starting point of the Pb 4f binding energy is always around 137.9 eV. By contrast, the initial Pb 4f binding energy in the three ITO cases is located between 138.5–138.8 eV. Except the PIC 151|ITO sample which shows a significantly lower value (still 138.52 eV), the two PLZST|ITO samples both have the Pb 4f binding energy ca. 0.9 eV higher than the value of the RuO_2 cases. Such a difference in the induced binding energy at the electrode interface, which actually characterize the SBHs, is expected as the two electrode materials have a ca. 1.1 eV difference in their work functions (RuO_2: ∼5.6 eV [226]; ITO: ∼4.5 eV [227]).

(2) The changes of the Pb 4f emissions in terms of both the binding energy and the shape are not symmetric when the top electrode is used as anode or cathode. Such asymmetric behavior can actually be observed in all the samples showing spectrum shifts of their bulk elements. As can be seen clearly in the cases of PIC 151|RuO_2 and C11|RuO_2, the peak shift towards higher binding

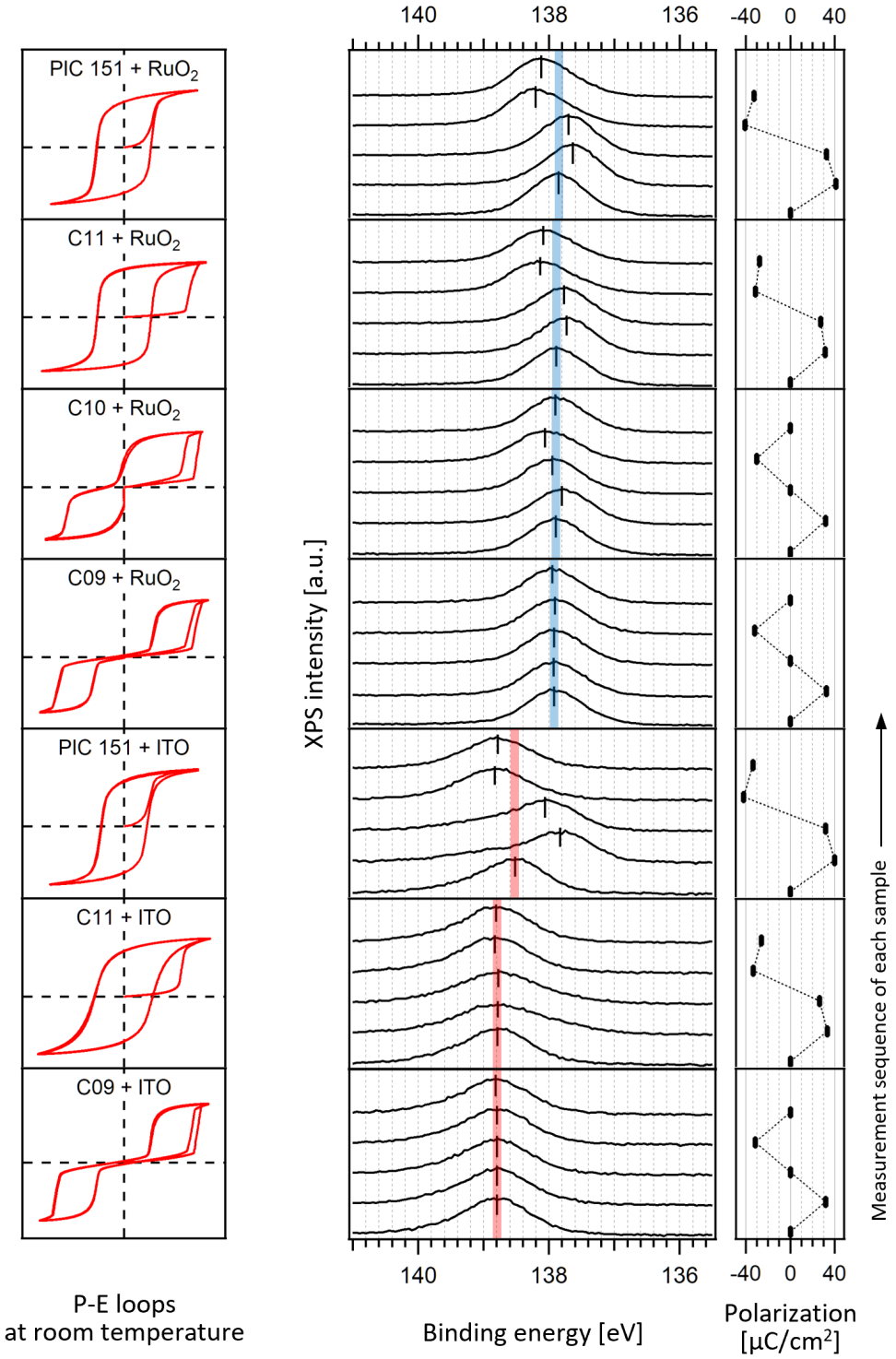

Figure 7.10.: Summary of the evolution of Pb $4f_{7/2}$ emissions in various samples throughout their respective measuring sequences. Four samples with RuO_2 top electrodes and three samples with ITO top electrodes are included. The polarization values corresponding to the applied electric fields (simply extracted from the *P*–*E* loops) are attached on the right-hand side of the Pb $4f_{7/2}$ emissions measured at different steps. The *P*–*E* loops schematically given here are just for showing the material types.

energy is more pronounced than that towards the other side. By contrast, the PIC 151|ITO sample displays an opposite tendency with larger shifts to lower binding energy. Besides, regarding the C11|ITO case, one can observe only a partial shift to the right-hand side under an anodic polarization but nothing under a cathodic polarization, which also indicates a clear asymmetry.

One may speculate that the two points above would be connected to each other. Here one possible interpretation with respect to charge injection by tunneling from the electrode is given schematically in Figure 7.11. For the case with a high work function electrode, the initial situation at the electrode interface is presented by a simplified band diagram as shown in Figure 7.11(a), where the Fermi level is located closer to the valence band. Figure 7.11(b, c) depicts the modification of the band diagram

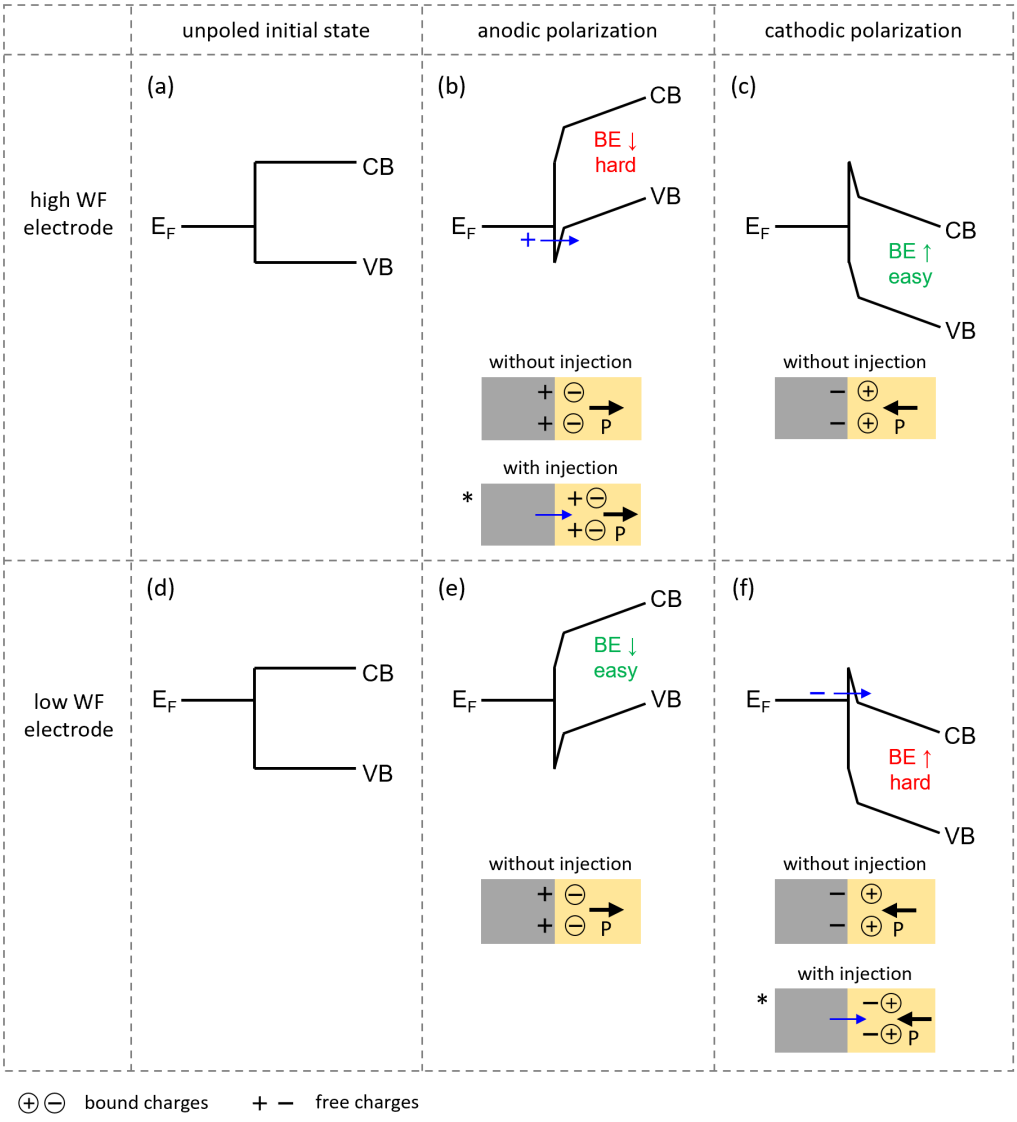

Figure 7.11.: Charge injection model suggested to explain the asymmetric screening behaviors in the ferroelectric samples when the top electrode has a (a–c) high or (d–f) low work function. Schematic band diagrams at the top electrode interfaces (a, d) in the unpoled initial states; (b, e) under anodic polarization; (c, f) under cathodic polarization.

when the electrode is used as anode/cathode, respectively. Under an anodic polarization, the measured binding energy of the dielectric is expected to decrease because of the existence of an effective screening length which leads to a potential step in the vicinity of the electrode. (We still call such distortion of the bands a kind of band bending.) Once the screening length is sufficiently small and the band bending tends to approach a comparable magnitude to $q\phi_p$ during the anodic poling process, a tunneling of holes (or positive free charges) may become possible, as indicated by the blue arrow in Figure 7.11(b). In the circumstances, some free charges could enter the dielectric bulk and compensate the bound charges at a certain distance from the electrode interface. Moreover, the dielectric layer behind the injected free charges may encounter a reduced electric field, so that FE domain switching within this narrow layer would likely not continue to take place (see the situation marked with "$*$"). As a result, the FE polarization and its screening charges that remain in the detecting depth of our XPS approach will be reduced and therefore the observed spectrum shift of Pb 4f emission would be a bit "hard/difficult" (see the PIC 151|RuO_2 and the C11|RuO_2 cases in Figure 7.10). Compared to the case with anodic polarization, the tunneling at a cathodic interface may be more difficult because the $q\phi_n$ is expected to be larger if the Fermi level stays at a low position, as illustrated in Figure 7.11(c). Analogous considerations can be applied to the sample with a low work function top electrode, where the tunneling would be easier to happen under a cathodic polarization condition and therefore the rise in the binding energy of Pb 4f emission is expected to become more difficult (see Figure 7.11(f)).

7.3.2. Difference between the ferroelectric and the antiferroelectric materials at electrode interfaces

The original purpose of this chapter is to investigate the FE-polarization-dependent SBHs in both FE- and AFE-based capacitors. Previous XPS studies on FE BTO single crystals have been already realized in DAISY-MAT, in which the spectrum shifts were observed in Ba 3d core level when the FE polarization state is switching [245, 246]. In this work, PZT-based materials are studied, and similar phenomena can be successfully found in the FE or FE-like compositions. In AFE samples, however, no spectrum shift of the Pb 4f core level can be seen at the electrode interface with a field-induced FE phase. In other words, there is no polarization-dependence of SBHs in an AFE-based capacitor structure. This observation is unexpected in an electrostatic point of view, and it has been verified by several experiments with different comparing strategies (see Sections 7.1 and 7.2). Considering that this observation may reveal some fundamental discrepancies between the electrode/FE and electrode/AFE interfaces, we should make more discussions here.

As has been mentioned in Sections 7.1 and 7.2, one possible scenario for the electrode/AFE could be that the field-induced FE phase does not reach the electrode interface when the AFE-to-FE transition happens. Figure 7.12(a) schematically illustrates such scenario, in which the applied electric field points to the left-hand side and a narrow layer within the original AFE bulk right under each electrode remains an AFE phase when most of the bulk has been already transformed into a FE phase by the sufficiently high external field. In this case, the bound charges are situated in a certain depth of the dielectric. If we assume that the free charges that can compensate the bound ones all stay on the electrode layer, the screening length should be greater than several nanometers (beyond the detecting depth of the XPS technique). However, this picture seems to be electrostatically not reasonable. Figure 7.12(a) also gives a schematic electric potential profile across the capacitor structure for the scenario described above, where the existence of the screening length brings about a steep increase of the potential in the vicinity of the electrode layer. Figure 7.12(b, c) performs a more detailed and intuitive estimation

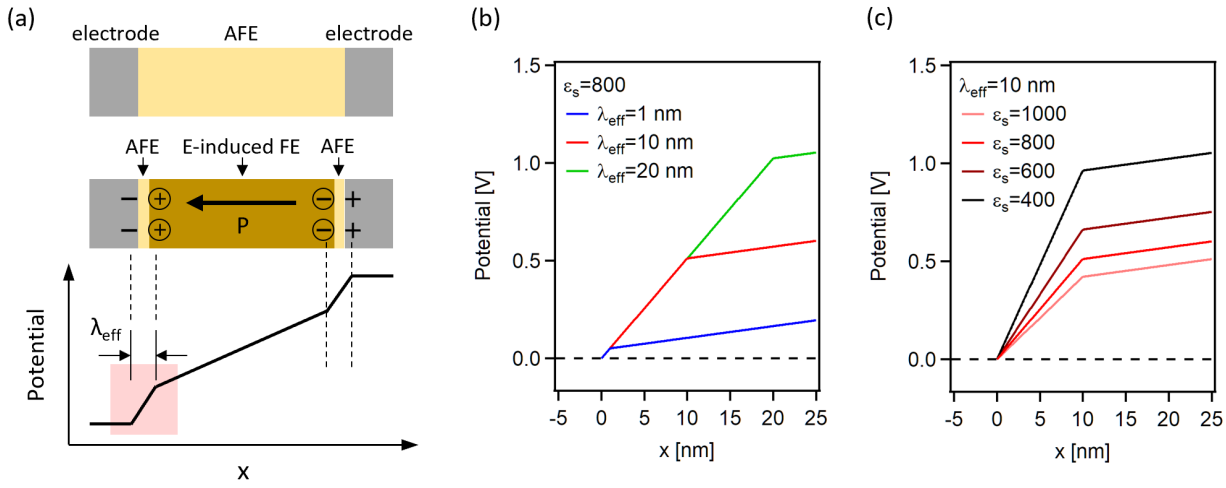

Figure 7.12.: Estimation of the electric potential profile in the vicinity of electrode/antiferroelectric interface based on the assumption that the electric-field-induced ferroelectric phase can not reach the electrode interface and in the meantime all the free compensating charges are located in the electrode layer.

for the potential profile within the red shaded area in Figure 7.12(a). Here we adopt the simplest physical model in which the existence and influence of grain boundaries or domain walls/boundaries are neglected. The electric field inside the screening layer can be approximately calculated by adding the applied field and $P/\varepsilon_0\varepsilon_s$ together. Here ε_s denotes the relative permittivity of the layer that remains in the AFE state. It should be noted that the total field is constant within the screening range, which results in a linear rise of the electric potential starting from the cathode interface. In Figure 7.12(b, c), we suppose a 0.13 mm thick dielectric so that applying dc 780 V (the left electrode as cathode) is expected to generate an overall electric field of roughly 6 kV/mm in the bulk if the screening length is many orders of magnitude smaller than the total thickness of the dielectric. A fixed P value of 32 μC/cm^2 is used for these comparisons. Taking $\varepsilon_s = 800$, which is roughly extracted from the maximum permittivity value at the forward AFE-to-FE transition point of composition C09 at 25°C in Figure 4.9, here Figure 7.12(b) compares three examples of the potential profile near the cathode interface depending on different effective screening lengths. It can be seen that the electric field within the range of screening length, which is dominated by the term of $P/\varepsilon_0\varepsilon_s$ (∼45 kV/mm), is indeed very high. In this case, a 10 nm screening length can already induce a ∼0.5 V potential rise. Moreover, Figure 7.12(c) performs the dependence of the potential profile on the relative permittivity values within the screening layer having a fixed thickness of 10 nm. It is noticeable that strongly reduced ε_s down to 400 can considerably promote the potential step up to almost 1.0 V at 10 nm and enhance the electric field up to ∼90 kV/mm within the screening layer at the same time. Based on these intuitive estimations, we should think of the following problems. On the one hand, an electric field like 45 kV/mm is one order of magnitude higher than the AFE-to-FE phase transition field (e.g. ∼4.5 kV/mm for the PLZST composition C09). If a dielectric layer with a thickness of at least several or tens of nanometers encounters such an extreme field, very probably a breakdown or an instability of the material would be expected. On the other hand, the XPS approach must be able to detect such a noticeable potential shift (e.g. the 0.5–1.0 V at a depth of 5–10 nm under the top electrode) if there is really a considerable and rigid spatial separation of the bound and free charges. However, no such effect has been observed experimentally. Therefore, it could be speculated that the charge compensation at the electrode/AFE interface should not take place in the

way as supposed in Figure 7.12.

In order to solve the problem of having extremely high electric field at the electrode interface due to the large screening length, two additional models that take charge injection into account are proposed here. The concept of charge injection has already been utilized in Section 7.3.1 during the discussion on the origin of asymmetric screening behaviors in the FE samples depending on different electrode materials. Since it is believed that the AFE compositions are basically close to the FE ones in terms of the band structure (e.g. comparing compositions C09 and C11), similar interface-related behaviors including charge injection should also be possible for AFE-based samples. Figure 7.13 schematically illustrates two models in which the capacitor basically undergoes three stages when the applied electric field is stepwise increasing: the initial unpoled state (panels (a–c)); the state under a moderate field that does not exceed the AFE-to-FE transition point (panels (d–f)); and the state under a sufficiently high field where the AFE-to-FE transition takes place (model 1 in panels (g–i), model 2 in panels (j–l)). The two models share the situations of Stages 1 and 2. Here the electrode on the left-hand side is always used as cathode. The left column gives the electric potential profiles between the two electrodes for each stage (using the inverse values $-V(x)$ for convenience). The middle column plots the corresponding band diagrams around the cathodic interface that basically follow the tendency of their potential profiles. Moreover, the right column schematically depicts the distributions of the phases (AFE or FE) and of the bound and free charges in the interfacial region of the cathode.

The first possible discrepancy in the AFE compared to the FE can be seen at the second stage (see Figure 7.13(d–f)). When the applied field is still not high enough to transform the AFE phase into FE, there is no effective FE polarization emerging in the vicinity of the electrode interface, namely, almost no charge compensation is needed at the electrode interface. At this stage, no steep potential variation due to the screening effect is expected, and thereby the energy bands only exhibit a normal tilt that is simply caused by the applied field. Under the circumstances, a tunneling through the Schottky barrier seems very unlikely because the barrier is just too wide. In contrast to the situation presented here, for the FE samples the magnitude of polarization is not limited by any phase transition. Thus, the FE samples can usually perform considerably higher polar states at their electrode interfaces once they have been sufficiently poled, no matter what electric fields they are currently encountering. In such a case, it should be easier for the FE samples to establish screening-induced potential steps at their electrode interfaces. As for the AFE samples, the status with a negligible requirement of screening will remain until the applied field approaches the AFE-to-FE transition point. Panels (g–i) and (j–l) in Figure 7.13 describe the two possible scenarios when the AFE-to-FE phase transition is triggered. The main difference between the two models is the sequence of the phase transition and the charge injection. For model 1, it is assumed that the AFE-to-FE transition takes place first (step I), leading to a considerable potential step and a consequent band bending in the cathodic region, same as the situation without thinking of injection shown in Figure 7.11(f). In this case, a charge injection would be expected, as illustrated in Figure 7.13(h). The injected free charges will then change the electrostatic environment around the cathode. It is speculated here that the narrow dielectric layer right behind the injected free electrons might encounter a considerably lower electric field, which could no longer maintain the field-induced FE structure. Subsequently, the narrow dielectric region behind the injected free charges might turn back into an AFE state very quickly (see step II in panel (i). In contrast to model 1, model 2 displayed in panels (j–l) deals with an opposite sequence where the charge injection happens prior to the AFE-to-FE phase transition. Here it is assumed that the injection would become possible when the energy bands are sufficiently tilted by the external electric field (see panel (k)). Once the free charges enter the AFE, it would be more difficult for the AFE-to-FE phase transition to take place within the narrow dielectric region near the cathodic interface because of the local variation of the electrostatic

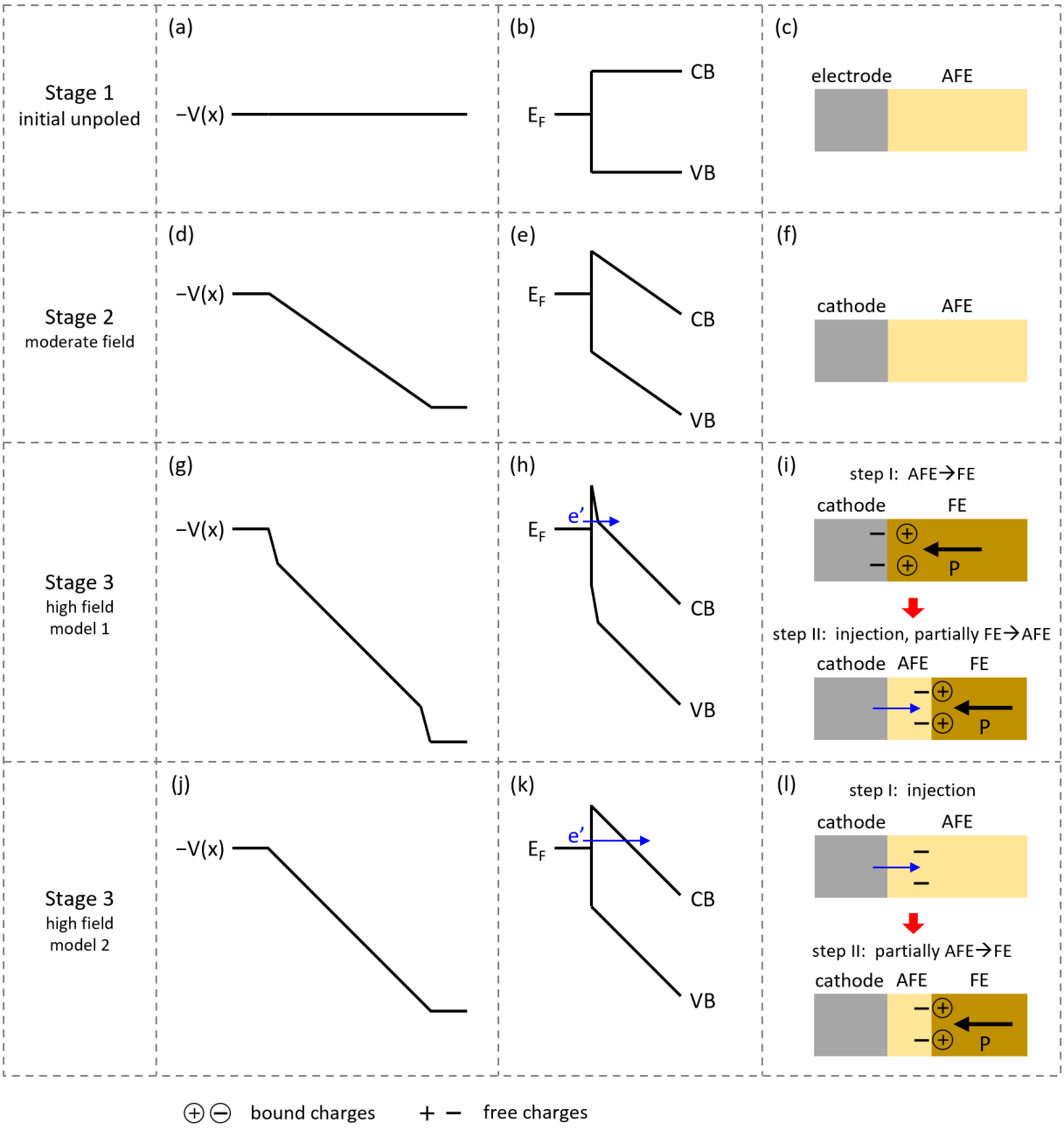

Figure 7.13.: Charge injection models suggested to describe the electrode/antiferroelectric interface during the electric-field-induced antiferroelectric-to-ferroelectric phase transition.

condition. As a result, an AFE layer might remain unswitched, as illustrated by step II in panel (l). For both models given here, the charge compensation would happen at a certain depth from the cathodic interface, which is beyond the detecting range of our XPS method so that no spectrum shift can be measured.

The charge injection model proposed above implies the probable existence of a special surface layer of the AFE, which behaves differently compared to the bulk material. Actually, the concept of thin surface

layer has been widely investigated in FEs, especially in FE thin films. One of the most concerned issues about such surface layers (sometimes also called "passive layer" or "nonswitchable FE layer" [16]) is how they could influence domain switching ability and modify the hysteresis behavior [15, 16, 200, 270–274]. Regarding the surface layers in AFE materials, besides the similar issues of those for FEs, one should also pay extra attention to the stability competition between the AFE and the FE states that belong to the same material. This would decide whether or how easy the AFE-to-FE phase transition can take place under certain conditions. The speculated models in this work with respect to the charge injection effect at electrode interfaces is principally deduced from the experimental observations in the surface-sensitive XPS studies combined with some basic electrostatic considerations. Indeed, the process of the AFE-to-FE phase transition is not only electrical but also mechanical. The establishment of the FE polarization in the AFEs is inevitably accompanied by a change of strain, which has been described in Section 2.2.2. When the material surface sees a specifically restricted/defined mechanical boundary condition, it can be easily imagined that the surface layer may go through a variation significantly different from that of the bulk. In the literature, some reports can be found for FE-related materials about the existence of such special surface phases with different lattice structures [275, 276]. Although it is sometimes difficult to clearly distinguish whether the mechanical condition is the reason or the consequence of the structural preference, the compensation between the bound and the free charges is always needed because the electrostatic conditions of the system must be fulfilled anyway.

One of the interesting consequences of the observation in this experimental chapter is that the backward FE-to-AFE phase transition might take place without a step of nucleation. It is usually believed that the phase transitions in AFE materials (both the forward AFE-to-FE and the backward FE-to-AFE ones) consist of two steps: nucleation and domain expansion [277]. According to normal understanding, the nucleation usually begins somewhere at the electrode interfaces. However, based on our observation the "non-FE" layer (very likely still AFE) could already act as the region where the nucleation step has finished. On the one hand, this could probably help to explain why the field-induced FE phase in an AFE material is actually not stable once the external field is removed. On the other hand, the already existing nuclei for the backward FE-to-AFE transition may also change the spatial distribution of the bound and screening charges around the electrode interface, so that the fatigue theory which has been established on the non-equilibrium transient state of such charge distribution [277, 278] might encounter some difficulties.

Furthermore, there are still some issues concerning the tunneling process, or more broadly, the charge injection mechanisms through the electrode interfaces with FE-related materials. Many studies can be found related to this topic [15, 16, 200, 272, 273, 277–280]. Although most of them utilized the similar strategy where some charges injected from the electrode were placed intentionally at a certain depth of the FE thin film (or at the interface between the special surface layer and the rest of FE film) in order to compensate the bound charges, the destination of these free charges after the injection is usually not very clear. For the electronic charges like electrons or holes, staying at or transferring along the conduction band or the valence band of a wide-gap material like PZT seems unlikely. In the circumstances, trapping and de-trapping are the most commonly used concepts to describe the relevant processes. Here comes again the question what traps the materials can provide. Some more discussions will be given in Chapter 8.

7.4. Summary

The in situ XPS approach based on the electrode screening theory has been upgraded and applied to both FE and AFE compositions. By detecting the extra electrostatic potential step emerging at an electrode/FE interface, which is caused by the spatial separation of the bound charges in the dielectric and the free compensating charges from the conductive electrode, XPS can be used to characterize the FE phase through the thin top electrode layer. Information like the magnitude of polarization, the extent of dipole alignment, and the depth where charge compensation takes place can be extracted from such in situ XPS measurements.

In Section 7.1, different Pb-based FE and AFE materials, including the commercial PZT PIC 151 and three C-series PLZST compositions C09, C10, and C11, have been studied at room temperature. Two types of top electrode materials with different work functions, RuO_2 and ITO, were compared during these experiments. The main observations of this part can be summarized basically into the following two aspects:

(1) The detected screening behaviors of electrode/FE interfaces show clear dependence on the polarity and on the electrode material. For the samples that exhibit stable FE hysteresis loops (PIC 151, PLZST C11), it has been observed that the Pb 4f emission shifts with the polarization state inside the bulk material, which is in good agreement with the expectation. However, these Pb 4f spectra always show asymmetric variations (position and shape) in different cases. It seems that the interface with RuO_2 prefers cathodic polarization, while the interface with ITO prefers the anodic one. Such phenomena might be attributed to the work function of the top electrode.

(2) The electrode/FE and the electrode/AFE interfaces have probably a fundamental discrepancy. Different from the FE samples which always show spectrum shifts depending on the polarization, the room-temperature AFE composition C09 never exhibits any XP spectrum shift in the Pb 4f emission even when it has already been poled into a FE state. From the viewpoint of electrostatics, it could be speculated that in this AFE material the charge compensation for the field-induced FE phase may take place at a certain depth of the dielectric, which is beyond the detection range of the XPS technique. This is totally different from the observations based on the FE samples. Regarding such a speculation, the PLZST C11 sample was studied by the in situ XPS at both room temperature (with a FE loop) and 100°C (with an AFE loop), as described in Section 7.2. By detecting the polarization-induced spectrum shift of Pb 4f emission at room temperature but no shift at 100°C exactly at the same point on the sample, the speculation has been verified experimentally that the field-induced FE state of an AFE material is different from the switchable FE state of a FE composition.

Corresponding to the above points, several models have been proposed in Section 7.3, which take the charge injection through the electrode interfaces into account. The model suggested in Section 7.3.1 correlates the charge injection with the work function of the electrode, which might be able to describe the asymmetric screening phenomena. The models given in Section 7.3.2 deal with the probable sequence between the charge injection and the AFE-to-FE phase transition, which may explain why the charge compensation in AFE materials would take place far away from the electrode interfaces.

8. Discussion

It is known that the dominant charges and charged point defects in the Pb-based FE and AFE materials could be e', $h^{\cdot}$, $V_O^{\cdot\cdot}$, V_{Pb}'', etc. Based on the results described in Chapters 4–7, this chapter will give some short discussion about their states, behaviors, or possible contributions to the structures and properties of such materials. First, Section 8.1 will summarize important observations in this work corresponding to different types of charges. After that, Section 8.2 will discuss the possible roles of the trapped electrons and holes in three different scenarios: the electrical conductivity, the domain structure, and the electrode interface screening.

8.1. Summary of the observations related to different charge carriers

Electronic charge carriers (electrons and holes)

For the material systems having complex charge compensation relations (like PZT), usually the electronic charge carriers (e' and $h^{\cdot}$) should be taken into account during the discussion on the defect chemistry. Particularly, they are considered to play more significant roles at high temperatures, where the intrinsic excitation between the valence band and conduction band becomes easier.

In Chapter 5, we have carried out dc conductivity measurements at elevated temperatures up to 400°C. It seems that most of the Pb-based samples studied in this work, which are differently doped, exhibit nearly parallel Arrhenius relations within the temperature range of 300°C–400°C and thereby similar activation energies of around 1.4 eV can be extracted. This observation suggests that we may first estimate the intrinsic contribution of e' and $h^{\cdot}$ at such high temperatures. With band gap E_g, the intrinsic carrier density n_i can be calculated by

$$n_i = \sqrt{N_C N_V}\exp(-\frac{E_g}{2kT}), \tag{8.1}$$

where N_C and N_V are the effective density of states in the conduction and valence bands, respectively [11]. We can adopt the band gap of 3.7 eV for these materials [152], which has been used in the energy band diagram in Section 6.2.4. Just for making an estimation at 400°C, we could approximately take $N_C = N_V \approx 1 \times 10^{20}$ cm^{-3} [281–283], which will lead to $n_i \approx 1.4 \times 10^6$ cm^{-3}. If we assume that e' and $h^{\cdot}$ have the same mobility μ, the conductivity that is contributed by the band-to-band excitation can be calculated according to

$$\sigma = 2q\mu n_i, \tag{8.2}$$

where q is the elementary charge. In order to get a conductivity of about 10^{-8} S/cm (taken from the C-series compositions, see Figure 5.12), the mobility of the electronic charge carriers should have

$\mu \approx 2.2 \times 10^4$ cm^2/V·s. Such a high mobility value is not reasonable for a polycrystalline ceramic material at 400°C [281].

One possible solution to this problem is to think that a large number of e' and/or $h^{\cdot}$ are trapped in such material systems. In the literature of PZT-related materials, the most widely accepted traps are the Ti^{4+} ions for electrons [145, 146, 148, 149, 153] and the Pb^{2+} ions for holes [14, 143, 145–148, 153]. Different from these two trap centers, in Chapter 6 of this work we have applied a new in situ XPS method and found that the Pb^{2+} may also act as an electron trap according to the following electrochemical reaction:

$$Pb_{Pb}^{\times} + 2e' \rightleftharpoons Pb_{Pb}''; \tag{8.3}$$

which can alternatively be written as

$$Pb^{2+} + 2e^- \rightleftharpoons Pb^0. \tag{8.4}$$

This reaction has not been observed in all Pb-based samples studied in the present work, which implies a probable composition dependence of this trap. The constituent states of the CBM of these perovskite materials are considered to play important roles in such reduction processes. Apart from the electron trap of $Pb^{2+/0}$, we should also consider the single-electron trap $Pb^{2+/+}$, which corresponds to the reaction:

$$Pb^{2+} + e^- \rightleftharpoons Pb^+. \tag{8.5}$$

Although Pb^+ is not a common oxidation state of Pb [284], it might still be reasonable to include such single-electron trap in the bulk conduction mechanism for the studied materials. This is because the surface- or interface-based experiments may provide information different from the bulk material.

Moreover, in the XPS experiments in Chapter 7, we have detected an asymmetric screening behavior at the electrode/FE interface when the electrode is used as anode or cathode. In order to explain this observation, a charge injection model has been suggested, in which the charge injection could take place at both the anode and the cathode interfaces. In other words, both holes and electrons could inject from the electrodes into the dielectric. However, one question should be discussed: where will these charges go after the injection? It is not expected that they would stay in the valence or conduction band, contributing to the electrical conductivity. This is because of the highly insulating characteristic of these materials, even under very high external electric fields (see Section 5.1). Thus, it seems that these injected charges would likely be trapped inside the dielectric material at some depth from the electrode interfaces. In this case, traps for both electrons and holes are needed.

Another place where trapped electronic charge carriers might play a role is the domain wall/boundary of these FE/AFE materials. In Section 5.1.2, a small but non-negligible discrepancy of the conductivity between the unswitched AFE phase and the field-induced FE phase of the same sample that exhibits AFE behavior (double hysteresis loop) has been detected by static dc conductivity test. One of the possible interpretations of this observation could be that some charged domain walls in the field-induced FE phase might bring about an increase of the conductivity. A recent unpublished study with conductive atomic force microscopy (C-AFM), which was performed on several C-series samples by Prof. Dr. Hana Uršič Nemevšek at Jožef Stefan Institute (Ljubljana, Slovenia), could not detect any conductive domain wall. Instead, some conductive grain boundaries have been observed. This may be reasonable because a reduction of Pb^{2+} to Pb^0 might not be easy inside the grains due to the big size of the Pb^0 atom. Therefore, it may be speculated that the reduction of Pb^{2+} would be only possible at electrode interfaces and grain boundaries, where more space for relaxation of atomic positions is available. Further studies are needed to verify such assumption. Nevertheless, the charge compensation related to the domain structures in these FE and AFE materials is still worth considering.

Oxygen vacancies

In perovskite oxides, such as BTO, STO, and PZT, the existence of a large number of $V_O^{\cdot\cdot}$ will lead to resistance degradation [134, 137, 139–143]. In this work, degradation with significant increase of leakage current has been found in compositions X01 (nominally undoped PZST), A02 (2% La and 2% Fe co-doped PLZSF), PIC 151 (Ni and Sb co-doped commercial PZT), and PZT53/47 (undoped PZT near MPB). For the other compositions, very slight increase of leakage current can be sometimes observed as well depending on the conditions of temperature and applied field. Relevant data can be found in Sections 5.1.1, 6.1.1, 6.2.1 and Appendices B.2, C.1. All these data reveal the existence of $V_O^{\cdot\cdot}$ in the studied materials, especially in the ones with a lower/without "net-donor" concentration. This is consistent with the expectation.

Besides, by operating solid electrolyte cells at elevated temperatures in the XPS chamber, we have (electro)chemically reduced the interfaces of several Pb-based samples with ITO cathodes in Chapter 6. The observation of the (electro)chemical reduction needs the migration of oxygen species across the dielectric under an external field, which also indicates the existence of $V_O^{\cdot\cdot}$ in such materials. It should be noticed that even composition C09, which is doped with 2% of donor, still has a certain number of $V_O^{\cdot\cdot}$ although its concentration should be effectively suppressed by the donor.

Lead vacancies

It is known that the existence of a certain number of V_{Pb}'' is usually not avoidable in Pb-based ceramic materials because of the high volatility of PbO during high-temperature sintering [45, 126–129]. Particularly, in donor-doped PZT, for example the PLZST-related compositions used in this work, more V_{Pb}'' are expected to be generated during the sintering in order to compensate the donor dopants ionically, which can be described by Equation 2.30 [13, 45]. Concerning the mobility of V_{Pb}'' and their possible contribution to the electrical conductivity, the present work cannot provide a clear understanding or conclusion. Nevertheless, it would still be helpful to involve them in the conduction mechanism of these materials, especially at higher temperatures. The decreasing tendency of the conductivity at higher temperatures and under higher electric fields, which has been observed for most of the donor-doped samples in this work (see Sections 5.1.1, 5.2 and Appendices B.2, C.1), might be related to the re-distribution of the V_{Pb}'' when they become mobile to some extent. Combined with the migration of $V_O^{\cdot\cdot}$, one could probably give an explanation for the non-equilibrium conduction behaviors described in Appendix B.2. Further studies on the V_{Pb}'' are still needed.

8.2. Possible scenarios involving trapped electrons and holes

After summarizing the evidence of the trapped electrons and holes existing in the Pb-based FE and AFE materials studied in this work, the current section will briefly discuss three relevant scenarios where the trapped electronic charge carriers may play important roles.

Electrical conductivity

The first scenario is about the electrical conductivity of these Pb-based ceramic materials, which is closely related to the experiments shown in Chapters 5 and 6. Figure 8.1 gives a schematic energy band diagram of a dielectric with a band gap of E_g. The upper and lower limits of the Fermi level are

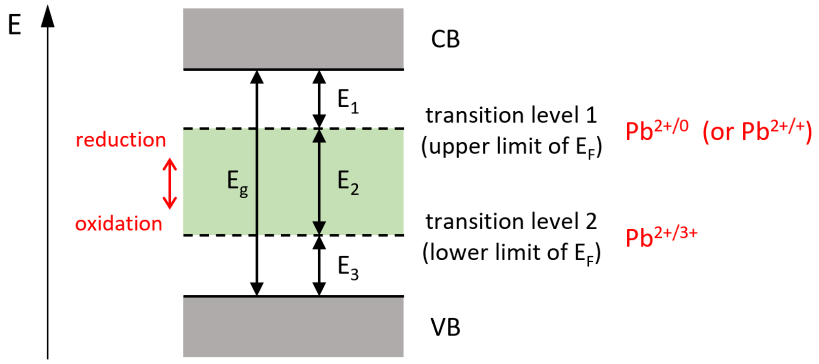

Figure 8.1.: Schematic energy band diagram of a dielectric material, where the upper and lower limits of the Fermi level are included.

drawn within the band gap. It is assumed that the limits are identified by the two transition levels, which correspond to the electrochemical reduction and oxidation potentials detected by the in situ XPS approach described in Chapter 6. The green shaded part between the two limits denotes the accessible range of the Fermi level. In this work, the upper limit of the Fermi level in the PLZST materials is considered to be a transition level (an electron trap) of $Pb^{2+/0}$ based on the XPS results. Alternatively, it might be $Pb^{2+/+}$ from the viewpoint of the bulk transport, as mentioned in Section 8.1. For the lower limit of the Fermi level, no experimental observation is available in this work because RuO_2 does not seem to be an appropriate anode material for such measurements. As the $Pb^{2+/3+}$ (hole trap) has been reported in the literature [145–147, 153], here we assume that it determines the lower limit of the Fermi level.

Regarding such a band diagram, there are two aspects that are worth some more description or discussion:

(1) The highly insulating nature of the PLZST materials: One of the necessary conditions for a good electrical insulator is that the concentrations of mobile free charge carriers in the conduction and valence bands should be as low as possible. This requires sufficiently large distances from the Fermi level to the CBM and to the VBM, respectively. The following equations are used to describe the free carrier concentrations that depend on the Fermi level position within the band gap [11]:

$$n = N_{\mathrm{C}} \exp(-\frac{E_{\mathrm{CB}} - E_{\mathrm{F}}}{kT}), \tag{8.6}$$

$$p = N_{\mathrm{V}} \exp(-\frac{E_{\mathrm{F}} - E_{\mathrm{VB}}}{kT}), \tag{8.7}$$

where E_{CB} and E_{VB} are the energies at the CBM and VBM, respectively. According to the quantification for PLZST given in Section 6.2.4, the distance between the CBM and the upper limit of the Fermi level (labeled as E_1 in Figure 8.1) is about 1.25 eV, which is large enough to ensure a high resistivity of the material. What must be noted here is that the experimental determination of the Fermi level positions (e.g. the upper and lower limits) is based on XPS, which is normally regarded as a surface-sensitive technique. However, the high resistivity of a ceramic is undoubtedly a bulk property. In this case, one may argue against the validity of using surface phenomena to predict bulk behaviors. On the one hand, the obvious (electro)chemical reduction on the Pb-site is restricted to the ITO/dielectric interface, but such a heavy reduction is not expected inside the deep

bulk of the samples, where the Fermi level is expected to be strongly confined below the reduction potential. On the other hand, some other studies, for example on Fe_2O_3, have shown that the specific transition level detected by XPS at the interface with ITO [236] is in sufficiently good agreement with the bulk value obtained by *ab initio* calculations [285]. Therefore, surface-based approaches could be utilized to identify bulk properties in some cases. More theoretical and experimental verification should be done in the further studies regarding this issue.

(2) The meaning of the activation energies obtained in the conductivity measurements: It has been known in Section 8.1 that adopting a simple band-to-band excitation can not describe the magnitude of the conductivity of PLZST-related samples and therefore trapped e' and $h^{\cdot}$ should be involved in the conduction mechanism. In this case, the mobility of the trapped carriers will also become strongly temperature-dependent, exhibiting an extra activation energy which should be added to that of the carrier concentration during a calculation of conductivity. Therefore, the activation energy about 1.4 eV measured on most of the samples (donor-doped, 75% Zr on the B-site) at 300°C–400°C in Section 5.2.2 may not simply correspond to energy level differences (or excitation processes) E_1, E_2, or E_3 in Figure 8.1. Considering that the C-series PLZST samples are 2% La-doped, which should be able to sufficiently suppress the sintering-induced p-type conduction of the PZT-related compositions and bring about an intrinsically low conductivity, without more experiments it is difficult to identify which electronic charge carrier (e' or $h^{\cdot}$) dominates the system. Nevertheless, we could still find a clear discrepancy in the electronic charge transport when comparing the PZT materials with different Zr/Ti ratios. The Zr-rich PLZST compositions studied in this work (75% on the B-site) exhibit activation energies around 1.4 eV, which are much higher than the value of 1.1 eV given in Ref. [148] for donor-doped but more Ti-rich PZT films (Zr/Ti=52:48). Since the 1.1 eV has been associated with electron trapping on the Ti-site ($Ti^{4+/3+}$) [148], it is reasonable to assign the 1.4 eV obtained in this work to some other transport mechanism. In brief, more systematic studies are still needed for a better analysis of the conduction mechanism of these Pb-based ceramics.

Domain structure

The second scenario is about the domain structure of the FE or AFE materials, where compensating charges may exist at the interfaces of domains. In Section 5.1.2, an increase of the conductivity, which is accompanied by the field-induced AFE-to-FE phase transition, has been detected in the AFE material. This phenomenon might be related to the domain configurations of such material, especially in its field-induced FE phase.

As mentioned in Section 2.5.1, Sluka *et al.* suggested a model for charged domain walls in FEs, in which the energy bands are bent parallelly because of the electrostatic field between a pair of charged domain walls [18]. According to this model, the sources of the free compensating e' and $h^{\cdot}$ are the places where the Fermi level reaches the CBM and the VBM, respectively. However, it is also known that the variation of Fermi level usually has limitations [150]. In other words, the Fermi level cannot shift freely across the whole band gap, and such limitation depends on the type of material. In Ref. [18] Sluka *et al.* proposed their model based on BTO, but BTO should exhibit a clear lower limit of Fermi level ($E_F - E_{VB} \approx 2.0$ eV) as reported in Ref. [150]. Thus, extracting free $h^{\cdot}$ from the valence band for compensating the charged domain walls seems to be unlikely for BTO. Another possible problem of this model is that the domain wall may be too thick (>100 nm [18]) if the relatively low density of states of the CBM or VBM is adopted.

A modified model is provided here. The comparison of these two models is illustrated in Figure 8.2.

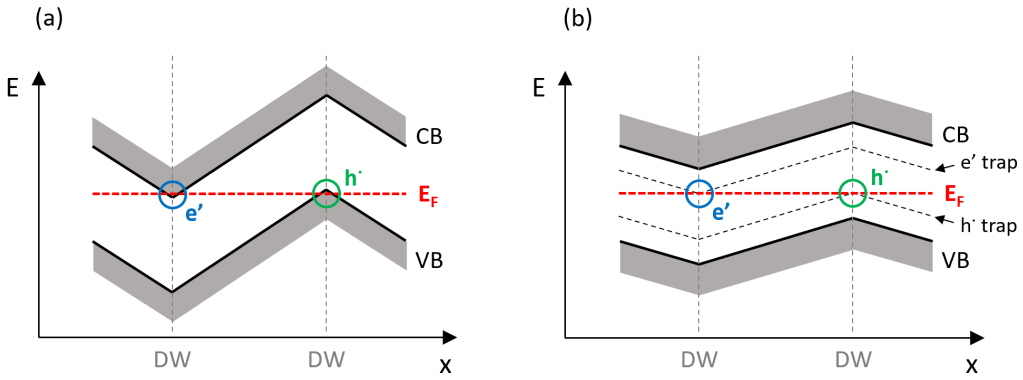

Figure 8.2.: Comparison of two band bending models at a pair of charged domain walls in a FE material. (a) The model following Sluka *et al.* [18] where the electrons and holes generated from the conduction and valence bands act as the compensating charges; (b) the modified model where the trap levels within the band gap provide the needed compensating charges.

Instead of regarding the conduction and valence bands as the sources of e′ and h˙, one might be able to extract free charges from some trap levels within the band gap. In Figure 8.2(b), an electron trap and a hole trap are schematically added, which are also bent following the conduction and valence bands. At the places where the Fermi level touches the two trap levels, a certain concentration of free charges would be available for compensating the bound charges on the domain walls. Apart from fixing the problem of the Fermi level limits, this modified model may also give rise to a more realistic resistance for the charged domain wall because of the lower mobility of the trapped charges. Moreover, the higher density of states of the trap levels compared to the CBM and VBM may also lead to a more reasonable thickness of the charged domain wall.

Screening at electrode interfaces

The third scenario is about the screening behavior at the electrode/dielectric interfaces, based on the charge injection models suggested in Section 7.3 for both FE and AFE materials.

All the injection models given in Section 7.3 can be classified into two situations, as depicted in Figure 8.3. The first one assumes that the bound charges belonging to the FE polarization are located very close to the electrode interface and thereby an obvious potential step is formed between the bound and the free charges. The FE model in Section 7.3.1 and the AFE model 1 in Section 7.3.2 belong to this situation. As for the second situation, which deals with the AFE model 2 (only the moment before the AFE-to-FE switching) in Section 7.3.2, no severe potential step is included because the charge injection is assumed to take place prior to the appearance of any field-induced FE phase. In Figure 8.3, we describe only the cathodic interface and the electron injection from the cathode into the dielectric.

One of the remaining questions in Section 7.3 is about the destination of the injected free charges. As mentioned before, these free charge would very unlikely stay in the conduction or valence band, otherwise the samples will become leaky under high electric fields. This is undesirable for the FE and AFE materials. Here it is assumed that the injected charges can be trapped on the trap levels within the band gap, which should be parallel to the conduction and valence bands. In the case of Figure 8.3(a), the e′ may first be injected to the conduction band, and then trapped on a lower-energy position. By contrast, in Figure 8.3(b) the e′ is assumed to be directly injected to the trap level without reaching the

conduction band. Such a shortcut could also fix the problem of the second AFE model that the barrier width for injecting charges to the bands is too large. Furthermore, the different options for trap levels might result in asymmetric screening behavior that depends also on the material (e.g. PLZST C11 vs. PIC 151, see Figure 7.10). In short, the existence of trap states for both e′ and h˙ can rationalize the charge injection models at the electrode/FE or electrode/AFE interfaces.

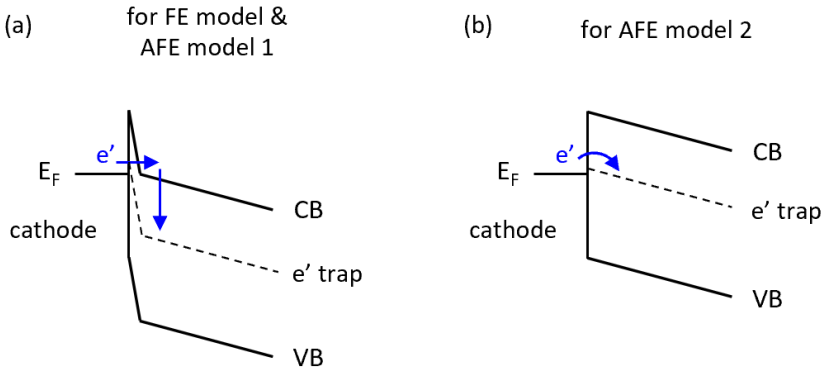

Figure 8.3.: Schematic of the charge injection models at the electrode/(anti)ferroelectric interfaces where trap levels are involved.

9. Conclusion and Outlook

In this work, Pb-based FE and AFE ceramics have been studied in terms of the compensation and transport behaviors of various charges within the bulk and at different interfaces. Novel in situ XPS approaches combined with systematic electrical measurements have provided fundamental insights into specific dielectric properties of such materials from the viewpoint of electronic structures.

Based on the well-known perovskite AFE material system PLZST, three series of compositions (C-, X-, and A-series) were chosen, with which the effects of the Ti/Sn ratio, the La doping (donor), and the La/Fe co-doping (net-donor) can be studied, respectively. These ceramic samples were prepared with the traditional solid-state reaction method at Tongji University (Shanghai, China) by the author of this work. After the synthesis, several types of basic characterizations were carried out at TU Darmstadt, including hysteresis loops, dielectric permittivities, crystalline structures by XRD, and microstructures by SEM. The information about the materials obtained in these measurements is the important basis for the organization of the subsequent conductivity and XPS experiments.

High resistivity is usually thought to be a necessary condition for the FE and AFE materials. This is especially true for AFEs because triggering the AFE-to-FE phase transition needs high electric fields. In Pb-based perovskite oxides, common charges and charged point defects could be e', $h^{\cdot}$, $V_O^{\cdot\cdot}$, V_{Pb}'', etc., whose concentrations and mobilities determine the charge transport properties. In order to describe the transport behaviors of the ceramics sintered for this work, static and dynamic dc conductivity measurements have been performed on most of the relevant compositions. The static method provides an overview of the electric-field- and temperature-dependent conductivity of each sample. Resistance degradation, which is characterized by an increase of conductivity at elevated temperatures, has been observed evidently in the compositions without La doping or with zero “net-doping”, indicating the existence of a large concentration of $V_O^{\cdot\cdot}$ in these materials. Also, the existence of V_{Pb}'' is speculated for the donor-doped samples, which exhibit a decreasing tendency of the conductivity at higher temperature and under higher electric fields. Moreover, by using the static method, a clear increase of the conductivity can be noticed in the field-induced FE phase compared to the unswitched AFE phase of the same sample that exhibits AFE double hysteresis loop. This extra conducting contribution in the FE state might be related to charged domain walls where electronic charge carriers (e' or $h^{\cdot}$) are needed for an effective compensation. In brief, some evidences for different types of charge carriers have been found in these materials during the static dc conductivity studies. In contrast to the static method, the dynamic experiments with ramping of temperature can only give limited information because of the non-equilibrium variation of the sample observed at high temperatures. Nevertheless, a direct comparison of the magnitude of the conductivity has been performed based on the dynamic measurements for all the three series, where the tendency that donor or “net-donor” doping decreases the conductivity can be clearly seen. In addition, it has been noticed that most of the donor-doped samples used in this work display basically parallel Arrhenius relations and similar activation energies around 1.4 eV can thereby be extracted between 300°C and 400°C. This indicates a similarity in the transport mechanism of these

compositions. Indeed, the conductivities measured in this part are too low compared to the possible contribution from an intrinsic band-to-band excitation. It is then reasonable to speculate that a large number of e' and/or $h^{\cdot}$ are trapped in these materials rather than being free charges moving in the valence and conduction bands.

In order to explore the possible electron and/or hole traps, which may contribute to the charge transport properties of the dielectric and at the same time determine the Fermi level limits within the band gap, a novel in situ XPS method has been developed. In such experiments, the sandwich capacitor structure is used as a solid electrochemical cell, where the ceramic is regarded as the electrolyte. When the cell is operated at elevated temperature, the migration of $V_O^{\cdot\cdot}/O^{2-}$ towards the cathode/anode may gradually reduce/oxidize the cathodic/anodic interface. By using oxide electrodes whose Fermi levels are sensitive to the oxygen content, a slight rise/drop of the Fermi level of the oxide cathode/anode will be expected, so that the Fermi level of the dielectric would also shift upward/downward at the electrode interfaces, probably leading to an electrochemical reduction/oxidation. According to such hypothesis, the reduction/oxidation potential, corresponding to an electron trap/a hole trap, respectively, can be regarded as the upper/lower limit of the Fermi level range within which the dielectric can remain stable. In this work, 3–5 nm thin top electrodes are used, through which the XPS can be utilized to monitor the whole evolution at the anodic/cathodic interfaces. The most important observation of this part is the appearance of metallic Pb emissions on some of the samples when low work function ITO is used as cathode, indicating an electron trap $Pb^{2+/0}$ in these materials. The position of this trap, which can be regarded as the upper limit of the Fermi energy, is about 2.45 eV above the VBM (or about 1.25 eV below the CBM) for the PLZST samples. The observation that the Pb^{2+} ions act as electron traps is different from the widely accepted understanding in the literature on PZT where the electrons should be trapped on the Ti-sites and the Pb-sites more likely trap holes. However, the results presented here may still be reasonable. As the reduced Pb has not been observed for every sample, which implies a composition dependence of the electron trap level, it could be assumed that the sites where the (electro)chemical reduction first takes place might be influenced by the dopants or by the electronic structure at the bottom of the conduction band. Different from the experiments with ITO cathode, using high work function RuO_2 anode was not successful in identifying the lower limit of the Fermi level because the room-temperature sputtered RuO_2 has not been stable during the vacuum-annealing. In several attempts with RuO_2 anode, strong chemical reduction has been found already after heating-up in the XPS chamber before the application of electric fields, which makes the determination of the oxidation potential impossible. Hence, an appropriate anode material is still needed for this purpose.

Apart from the previously mentioned charge compensation within the bulk material that determines the bulk transport properties, the compensation can also take place at the electrode/dielectric interfaces between the bound and the free charges. The study on such compensation is necessary because it is directly and fundamentally linked to the measurement of polarization. Based on the electrode screening theory, another in situ XPS technique has been upgraded and applied to both FE and AFE compositions in this work. Again, the sandwich capacitor structure is utilized here. The top electrodes are always 3–5 nm thin RuO_2 or ITO layers, through which the XPS can measure the variations at the electrode interfaces when external fields are applied for switching the FE states in the ceramic pellets. By observing the XP spectrum shift of the dielectric relative to that of the electrode, which is caused by the extra electric potential step emerging at the interface due to a spatial separation of the bound charges and free compensating charges, the FE phase existing under the top electrode can be characterized in terms of the magnitude of polarization, the extent of dipole alignment, the depth of charge compensation, etc. For the samples exhibiting FE hysteresis loops, clear shifts of the Pb 4f peak can be observed as expected, corresponding to different polarization states along their P–E loops. One interesting phenomenon

is that these Pb 4f spectra display asymmetric shifts when the top electrode is in anodic or cathodic polarity, and such asymmetry depends clearly on the top electrode material. In order to explain this observation, charge injection at the electrode interfaces has been taken into account, where the work function of the electrode material may play crucial roles. Besides the comparison among different FE compositions, another important discovery in this part is about the discrepancy between the samples exhibiting FE loops and AFE loops. For the AFE compositions, no spectrum shift of the Pb 4f emission can be detected even when the field is continuously applied and the sample is sufficiently poled into a FE state. This might indicate a fundamental difference between a field-induced FE state of an AFE material and a switchable FE state of a FE composition. For this issue, two charge injection models have been suggested, where the injection across the electrode interface is assumed to happen either prior to or later than the macroscopic AFE-to-FE phase transition. As a result, for both models, the charge compensation of the bound and free ones would again take place at a certain depth inside the dielectric away from the electrode. This could bring specific significance for understanding AFE materials as the narrow dielectric region between the location of the injected free charges and the electrode interface may be kept in an AFE state, which could act as a nucleation of the backward FE-to-AFE phase transition once the external field is removed. Furthermore, the charge injection models presented in this part could also be associated with the above-mentioned electron/hole trap levels in such materials. Considering that the injected free charges should unlikely stay in the conduction or valence band of the FEs and AFEs, involving the trap states for both e' and $h^{\cdot}$ might help to rationalize these charge injection models.

It is undeniable that these Pb-based FE and AFE ceramic materials show great complexity in terms of charge compensation mechanism in the bulk and at various interfaces. The results presented in this work are not sufficient for providing a clear picture of the existence and behaviors of all relevant charges. Further investigations are still necessary. Some probable topics or suggestions for future work are provided here:

(1) A comprehensive conductivity investigation on such highly resistive materials is needed. The dynamic dc method is not recommended because it is not easy to identify or recognize the complicated non-equilibrium variation resulting from the dc bias at high temperature. In order to determine the type of conduction (n- or p-type), the relaxation tests with varying atmosphere are needed.
(2) A wider range of compositions should be involved in the comparison of conduction behavior. For example, within the PZT system the Zr-rich, Ti-rich, and MPB compositions are worth a systematic comparison. Especially for the compositions near MPB, the rapid structural phase transition caused by the change of Ti content might lead to an abrupt change of the dominant trap state and thereby an obvious change of the bulk transport property. Moreover, a comparison between donor- and acceptor-doped materials is also needed because most of the compositions in this work are donor-doped.
(3) Corresponding to the conductivity measurements, a wider range of compositions should also be compared by the XPS approach (the one with solid electrochemical cells) in order to verify the hypothesis that the states at the bottom of the conduction band may determine the most preferred sites for an electrochemical reduction.
(4) The electrode screening models involving charge injection through the interface should still be described quantitatively for both FE and AFE materials.

In conclusion, this work has explored different charge carriers in the Pb-based FE and AFE ceramics. Evidences for e', $h^{\cdot}$, $V_O^{\cdot\cdot}$, and V_{Pb}'' have been found in relevant compositions. The electronic charge carriers (e' and $h^{\cdot}$) are very likely trapped to cause the high resistivities of these materials. Different

from the hole trap $Pb^{2+/3+}$ and electron trap $Ti^{4+/3+}$ reported in the literature, this work has identified another electron trap $Pb^{2+/0}$ on some of the studied samples by in situ XPS measurement. This trap level is considered to reflect the upper limit of the Fermi level of the PLZST materials. Moreover, during the in situ XPS studies on the charge compensating behaviors at the electrode/FE or electrode/AFE interfaces, it has been found that introducing the concepts of charge injection and trap levels of e' and/or $h^{\cdot}$ may not only rationalize the screening models but also shed light on the nature of the AFE behavior.

Bibliography

1. Goodenough, J. B. Energy storage materials: A perspective. *Energy Storage Materials* **1,** 158–161 (2015).
2. Hao, X. A review on the dielectric materials for high energy-storage application. *Journal of Advanced Dielectrics* **03,** 1330001 (2013).
3. Liu, Z. *et al.* Antiferroelectrics for energy storage applications: a review. *Advanced Materials Technologies* **3,** 1800111 (2018).
4. Zhang, H. *et al.* A review on the development of lead-free ferroelectric energy-storage ceramics and multilayer capacitors. *Journal of Materials Chemistry C* **8,** 16648–16667 (2020).
5. Chauhan, A., Patel, S., Vaish, R. & Bowen, C. R. Anti-ferroelectric ceramics for high energy density capacitors. *Materials* **8,** 8009–8031 (2015).
6. Randall, C. A., Fan, Z., Reaney, I., Chen, L.-Q. & Trolier-McKinstry, S. Antiferroelectrics: History, fundamentals, crystal chemistry, crystal structures, size effects, and applications. *Journal of the American Ceramic Society* **104,** 3775–3810 (2021).
7. Griffiths, D. J. *Introduction to Electrodynamics* (Prentice-Hall, Inc., New Jersey, 1999).
8. Lines, M. E. & Glass, A. M. *Principles and Applications of Ferroelectrics and Related Materials* (Oxford University Press, Oxford, 2001).
9. Kittel, C. Theory of antiferroelectric crystals. *Physical Review* **82,** 729–732 (1951).
10. Shirane, G., Sawaguchi, E. & Takagi, Y. Dielectric properties of lead zirconate. *Physical Review* **84,** 476–481 (1951).
11. Sze, S. M. & Ng, K. K. *Physics of Semiconductor Devices* (John Wiley & Sons, Hoboken, New Jersey, 2006).
12. Kao, K. C. *Dielectric Phenomena in Solids* (Elsevier Academic Press, San Diego & London, 2004).
13. Moulson, A. J. & Herbert, J. M. *Electroceramics: Materials, Properties, Applications* (John Wiley & Sons, Chichester, 2003).
14. Slouka, C. *et al.* The effect of acceptor and donor doping on oxygen vacancy concentrations in lead zirconate titanate (PZT). *Materials* **9,** 945 (2016).
15. Grossmann, M. *et al.* The interface screening model as origin of imprint in $PbZr_xTi_{1-x}O_3$ thin films. I. Dopant, illumination, and bias dependence. *Journal of Applied Physics* **92,** 2680–2687 (2002).
16. Tagantsev, A. K. & Gerra, G. Interface-induced phenomena in polarization response of ferroelectric thin films. *Journal of Applied Physics* **100,** 051607 (2006).
17. Gureev, M. Y., Tagantsev, A. K. & Setter, N. Head-to-head and tail-to-tail 180° domain walls in an isolated ferroelectric. *Physical Review B* **83,** 184104 (2011).

18. Sluka, T., Tagantsev, A. K., Damjanovic, D., Gureev, M. & Setter, N. Enhanced electromechanical response of ferroelectrics due to charged domain walls. *Nature Communications* **3,** 748 (2012).
19. Bednyakov, P. S., Sturman, B. I., Sluka, T., Tagantsev, A. K. & Yudin, P. V. Physics and applications of charged domain walls. *npj Computational Materials* **4,** 65 (2018).
20. Mehta, R. R., Silverman, B. D. & Jacobs, J. T. Depolarization fields in thin ferroelectric films. *Journal of Applied Physics* **44,** 3379–3385 (1973).
21. Wurfel, P. & Batra, I. P. Depolarization-field-induced instability in thin ferroelectric films—Experiment and theory. *Physical Review B* **8,** 5126–5133 (1973).
22. Gerra, G., Tagantsev, A. K., Setter, N. & Parlinski, K. Ionic polarizability of conductive metal oxides and critical thickness for ferroelectricity in $BaTiO_3$. *Physical Review Letters* **96,** 107603 (2006).
23. Berlincourt, D. Transducers using forced transitions between ferroelectric and antiferroelectric states. *IEEE Transactions on Sonics and Ultrasonics* **13,** 116–124 (1966).
24. Uchino, K. *Ferroelectric Devices* (CRC press, Boca Raton, 2018).
25. Whatmore, R. W., You, Y.-M., Xiong, R.-G. & Eom, C.-B. 100 years of ferroelectricity—A celebration. *APL Materials* **9,** 070401 (2021).
26. Valasek, J. Piezo-electric and allied phenomena in Rochelle salt. *Physical Review* **17,** 475–481 (1921).
27. Känzig, W. History of ferroelectricity 1938–1955. *Ferroelectrics* **74,** 285–291 (1987).
28. Pan, M.-J. & Randall, C. A. A brief introduction to ceramic capacitors. *IEEE Electrical Insulation Magazine* **26,** 44–50 (2010).
29. Megaw, H. D. Crystal structure of barium titanate. *Nature* **155,** 484–485 (1945).
30. Von Hippel, A., Breckenridge, R. G., Chesley, F. G. & Tisza, L. High dielectric constant ceramics. *Industrial and Engineering Chemistry* **38,** 1097–1109 (1946).
31. Roberts, S. Dielectric and piezoelectric properties of barium titanate. *Physical Review* **71,** 890–895 (1947).
32. Matthias, B. & von Hippel, A. Domain structure and dielectric response of barium titanate single crystals. *Physical Review* **73,** 1378–1384 (1948).
33. Merz, W. J. The electric and optical behavior of $BaTiO_3$ single-domain crystals. *Physical Review* **76,** 1221–1225 (1949).
34. Merz, W. J. Domain formation and domain wall motions in ferroelectric $BaTiO_3$ single crystals. *Physical Review* **95,** 690–698 (1954).
35. Von Hippel, A. Ferroelectricity, domain structure, and phase transitions of barium titanate. *Reviews of Modern Physics* **22,** 221–237 (1950).
36. Shirane, G. & Takeda, A. Phase transitions in solid solutions of $PbZrO_3$ and $PbTiO_3$ (I) Small concentrations of $PbTiO_3$. *Journal of the Physical Society of Japan* **7,** 5–11 (1952).
37. Shirane, G., Suzuki, K. & Takeda, A. Phase transitions in solid solutions of $PbZrO_3$ and $PbTiO_3$ (II) X-ray study. *Journal of the Physical Society of Japan* **7,** 12–18 (1952).
38. Shirane, G. & Suzuki, K. Crystal structure of Pb(Zr-Ti)O_3. *Journal of the Physical Society of Japan* **7,** 333 (1952).
39. Sawaguchi, E. Ferroelectricity versus antiferroelectricity in the solid solutions of $PbZrO_3$ and $PbTiO_3$. *Journal of the Physical Society of Japan* **8,** 615–629 (1953).

40. Jaffe, B., Roth, R. S. & Marzullo, S. Piezoelectric properties of lead zirconate-lead titanate solid-solution ceramics. *Journal of Applied Physics* **25,** 809–810 (1954).

41. Jaffe, B., Roth, R. S. & Marzullo, S. Properties of piezoelectric ceramics in the solid-solution series lead titanate–lead zirconate–lead oxide: tin oxide and lead titanate–lead hafnate. *Journal of Research of the National Bureau of Standards* **55,** 239–254 (1955).

42. Jaffe, H. Piezoelectric ceramics. *Journal of the American Ceramic Society* **41,** 494–498 (1958).

43. Ishiwara, H., Okuyama, M. & Arimoto, Y. *Ferroelectric Random Access Memories: Fundamentals and Applications* (Springer, Berlin & Heidelberg, 2004).

44. Whatmore, R. W. Pyroelectric devices and materials. *Reports on Progress in Physics* **49,** 1335–1386 (1986).

45. Jaffe, B., Cook, W. R. & Jaffe, H. *Piezoelectric Ceramics* (Academic Press, London & New York, 1971).

46. Goldschmidt, V. M. Die Gesetze der Krystallochemie. *Naturwissenschaften* **14,** 477–485 (1926).

47. Roth, R. S. Classification of perovskite and other ABO_3-type compounds. *Journal of Research of the National Bureau of Standards* **58,** 75–88 (1957).

48. Shannon, R. D. Revised effective ionic radii and systematic studies of interatomic distances in halides and chalcogenides. *Acta Crystallographica Section A* **32,** 751–767 (1976).

49. Jaffe, B. Antiferroelectric ceramics with field-enforced transitions: A new nonlinear circuit element. *Proceedings of the IRE* **49,** 1264–1267 (1961).

50. Burn, I. & Smyth, D. M. Energy storage in ceramic dielectrics. *Journal of Materials Science* **7,** 339–343 (1972).

51. Park, S.-E., Pan, M.-J., Markowski, K., Yoshikawa, S. & Cross, L. E. Electric field induced phase transition of antiferroelectric lead lanthanum zirconate titanate stannate ceramics. *Journal of Applied Physics* **82,** 1798–1803 (1997).

52. Liu, H. *et al.* Electric-field-induced structure and domain texture evolution in $PbZrO_3$-based antiferroelectric by in-situ high-energy synchrotron X-ray diffraction. *Acta Materialia* **184,** 41–49 (2020).

53. Roberts, S. Dielectric properties of lead zirconate and barium-lead zirconate. *Journal of the American Ceramic Society* **33,** 63–66 (1950).

54. Sawaguchi, E., Shirane, G. & Takagi, Y. Phase transition in lead zirconate. *Journal of the Physical Society of Japan* **6,** 333–339 (1951).

55. Sawaguchi, E., Maniwa, H. & Hoshino, S. Antiferroelectric structure of lead zirconate. *Physical Review* **83,** 1078 (1951).

56. Megaw, H. D. Crystal structure of double oxides of the perovskite type. *Proceedings of the Physical Society* **58,** 133–152 (1946).

57. Roberts, S. Piezoelectric effect in lead zirconate. *Physical Review* **83,** 1078 (1951).

58. Scott, B. A. & Burns, G. Crystal growth and observation of the ferroelectric phase of $PbZrO_3$. *Journal of the American Ceramic Society* **55,** 331–333 (1972).

59. Fesenko, O. E. & Smotrakov, V. G. Optic and dielectric study of lead zirconate crystals. *Ferroelectrics* **12,** 211–213 (1976).

60. Dai, X., Li, J.-F. & Viehland, D. Weak ferroelectricity in antiferroelectric lead zirconate. *Physical Review B* **51,** 2651–2655 (1995).

61. Jona, F., Shirane, G., Mazzi, F. & Pepinsky, R. X-ray and neutron diffraction study of antiferroelectric lead zirconate, $PbZrO_3$. *Physical Review* **105,** 849–856 (1957).

62. Fujishita, H., Shiozaki, Y., Achiwa, N. & Sawaguchi, E. Crystal structure determination of antiferroelectric $PbZrO_3$ –application of profile analysis method to powder method of X-ray and neutron diffraction–. *Journal of the Physical Society of Japan* **51,** 3583–3591 (1982).

63. Teslic, S. & Egami, T. Atomic structure of $PbZrO_3$ determined by pulsed neutron diffraction. *Acta Crystallographica Section B* **54,** 750–765 (1998).

64. Corker, D. L., Glazer, A. M., Dec, J., Roleder, K. & Whatmore, R. W. A re-investigation of the crystal structure of the perovskite $PbZrO_3$ by X-ray and neutron diffraction. *Acta Crystallographica Section B* **53,** 135–142 (1997).

65. Glazer, A. M., Roleder, K. & Dec, J. Structure and disorder in single-crystal lead zirconate, $PbZrO_3$. *Acta Crystallographica Section B* **49,** 846–852 (1993).

66. Liu, H. & Dkhil, B. A brief review on the model antiferroelectric $PbZrO_3$ perovskite-like material. *Zeitschrift für Kristallographie - Crystalline Materials* **226,** 163–170 (2011).

67. Rabe, K. M. *Antiferroelectricity in Oxides: A Reexamination* in *Functional Metal Oxides: New Science and Novel Applications* 221–244 (Wiley-VCH, Weinheim, 2013).

68. Tagantsev, A. K. *et al.* The origin of antiferroelectricity in $PbZrO_3$. *Nature Communications* **4,** 2229 (2013).

69. Cochran, W. Crystal stability and the theory of ferroelectricity. *Physical Review Letters* **3,** 412–414 (1959).

70. Cochran, W. Crystal stability and the theory of ferroelectricity. *Advances in Physics* **9,** 387–423 (1960).

71. Scott, J. F. Soft-mode spectroscopy: Experimental studies of structural phase transitions. *Reviews of Modern Physics* **46,** 83–128 (1974).

72. Kamba, S. Soft-mode spectroscopy of ferroelectrics and multiferroics: A review. *APL Materials* **9,** 020704 (2021).

73. Cochran, W. & Zia, A. Structure and dynamics of perovskite-type crystals. *physica status solidi (b)* **25,** 273–283 (1968).

74. Fujishita, H. & Hoshino, S. A study of structural phase transitions in antiferroelectric $PbZrO_3$ by neutron diffraction. *Journal of the Physical Society of Japan* **53,** 226–234 (1984).

75. Fujishita, H., Ishikawa, Y., Tanaka, S., Ogawaguchi, A. & Katano, S. Crystal structure and order parameters in the phase transition of antiferroelectric $PbZrO_3$. *Journal of the Physical Society of Japan* **72,** 1426–1435 (2003).

76. Blinc, R. & Žekš, B. *Soft Modes in Ferroelectrics and Antiferroelectrics* (North-Holland Publishing Company, Amsterdam & Oxford, 1974).

77. Blinc, R. The soft mode concept and the history of ferroelectricity. *Ferroelectrics* **74,** 301–303 (1987).

78. Íñiguez, J., Stengel, M., Prosandeev, S. & Bellaiche, L. First-principles study of the multimode antiferroelectric transition in $PbZrO_3$. *Physical Review B* **90,** 220103 (2014).

79. Sawaguchi, E. & Kittaka, T. Antiferroelectricity and ferroelectricity in lead zirconate. *Journal of the Physical Society of Japan* **7,** 336–337 (1952).

80. Shirane, G. Ferroelectricity and antiferroelectricity in ceramic $PbZrO_3$ containing Ba or Sr. *Physical Review* **86,** 219–227 (1952).

81. Shirane, G. & Hoshino, S. X-ray study of phase transitions in $PbZrO_3$ containing Ba or Sr. *Acta Crystallographica* **7,** 203–210 (1954).

82. Haertling, G. H. PLZT electrooptic materials and applications—A review. *Ferroelectrics* **75,** 25–55 (1987).

83. Haertling, G. H. & Land, C. E. Hot-pressed $(Pb,La)(Zr,Ti)O_3$ ferroelectric ceramics for electrooptic applications. *Journal of the American Ceramic Society* **54,** 1–11 (1971).

84. O'Bryan Jr., H. M. Phase relations in $(Pb,La)Zr_{0.65}Ti_{0.35}O_3$. *Journal of the American Ceramic Society* **56,** 385–388 (1973).

85. Carl, K. & Geisen, K. Dielectric and optical properties of a quasi-ferroelectric PLZT ceramic. *Proceedings of the IEEE* **61,** 967–974 (1973).

86. Dai, X. & Viehland, D. Tetragonal-structured PLZT relaxor ferroelectrics. *Ferroelectrics* **158,** 375–379 (1994).

87. Dai, X., Xu, Z. & Viehland, D. The spontaneous relaxor to normal ferroelectric transformation in La-modified lead zirconate titanate. *Philosophical Magazine B* **70,** 33–48 (1994).

88. Haertling, G. H. Ferroelectric ceramics: History and technology. *Journal of the American Ceramic Society* **82,** 797–818 (1999).

89. Berlincourt, D., Jaffe, H., Krueger, H. H. A. & Jaffe, B. Release of electric energy in $PbNb(Zr,Ti,Sn)O_3$ by temperature- and by pressure-enforced phase transitions. *Applied Physics Letters* **3,** 90–92 (1963).

90. Berlincourt, D., Krueger, H. H. A. & Jaffe, B. Stability of phases in modified lead zirconate with variation in pressure, electric field, temperature and composition. *Journal of Physics and Chemistry of Solids* **25,** 659–674 (1964).

91. Chen, S., Wang, X., Yang, T. & Wang, J. Composition-dependent dielectric properties and energy storage performance of $(Pb,La)(Zr,Sn,Ti)O_3$ antiferroelectric ceramics. *Journal of Electroceramics* **32,** 307–310 (2014).

92. Wang, H., Liu, Y., Yang, T. & Zhang, S. Ultrahigh energy-storage density in antiferroelectric ceramics with field-induced multiphase transitions. *Advanced Functional Materials* **29,** 1807321 (2019).

93. Zhao, P. *et al.* Superior energy storage density and giant negative electrocaloric effects in $(Pb_{0.98}La_{0.02})(Zr,Sn)O_3$ antiferroelectric ceramics. *Scripta Materialia* **200,** 113920 (2021).

94. Yang, T. Q. & Yao, X. Effect of compositional variations on field-induced phase transition of $(Pb,La)(Zr,Sn,Ti)O_3$ antiferroelectric ceramics. *Ferroelectrics* **355,** 71–76 (2007).

95. Zheng, Q., Yang, T., Wei, K., Wang, J. & Yao, X. Effect of Sn:Ti variations on electric field induced AFE–FE phase transition in PLZST antiferroelectric ceramics. *Ceramics International* **38,** S9–S12 (2012).

96. Zhuo, F. *et al.* Structural phase transition, depolarization and enhanced pyroelectric properties of $(Pb_{1-1.5x}La_x)(Zr_{0.66}Sn_{0.23}Ti_{0.11})O_3$ solid solution. *Journal of Materials Chemistry C* **4,** 7110–7118 (2016).

97. Park, S.-E., Markowski, K., Yoshikawa, S. & Cross, L. E. Effect on electrical properties of barium and strontium additions in the lead lanthanum zirconate stannate titanate system. *Journal of the American Ceramic Society* **80,** 407–412 (1997).

98. Pan, M.-J. *et al.* Electric field induced phase transition in lead lanthanum stannate zirconate titanate (PLSnZT) antiferroelectrics: tailoring properties through compositional modification. *Ferroelectrics* **215,** 153–167 (1998).

99. Tanaka, M., Saito, R. & Tsuzuki, K. Electron microscopic studies on domain structure of $PbZrO_3$. *Japanese Journal of Applied Physics* **21,** 291–298 (1982).

100. Pokharel, B. P. & Pandey, D. Dielectric studies of phase transitions in $(Pb_{1-x}Ba_x)ZrO_3$. *Journal of Applied Physics* **88,** 5364–5373 (2000).

101. Bharadwaja, S. S. N. & Krupanidhi, S. B. Study of La-modified antiferroelectric $PbZrO_3$ thin films. *Thin Solid Films* **423,** 88–96 (2003).

102. Dai, X. & Viehland, D. Effects of lanthanum modification on the antiferroelectric-ferroelectric stability of high zirconium-content lead zirconate titanate. *Journal of Applied Physics* **76,** 3701–3709 (1994).

103. Xu, Z., Dai, X., Li, J.-F. & Viehland, D. Coexistence of incommensurate antiferroelectric and relaxorlike ferroelectric orderings in high Zr-content La-modified lead zirconate titanate ceramics. *Applied Physics Letters* **68,** 1628–1630 (1996).

104. Breval, E. *et al.* PLZT phases near lead zirconate: 2. Determination by capacitance and polarization. *Journal of the American Ceramic Society* **89,** 3681–3688 (2006).

105. Ciuchi, I. V. *et al.* Field-induced antiferroelectric to ferroelectric transitions in $(Pb_{1-x}La_x)(Zr_{0.90}Ti_{0.10})_{1-x/4}O_3$ investigated by in situ X-ray diffraction. *Journal of the European Ceramic Society* **37,** 4631–4636 (2017).

106. Pan, W. Y., Dam, C. Q., Zhang, Q. M. & Cross, L. E. Large displacement transducers based on electric field forced phase transitions in the tetragonal $(Pb_{0.97}La_{0.02})(Ti,Zr,Sn)O_3$ family of ceramics. *Journal of Applied Physics* **66,** 6014–6023 (1989).

107. Speck, J. S., De Graef, M., Wilkinson, A. P., Cheetham, A. K. & Clarke, D. R. Hierarchical domain structures and in situ domain migration in the antiferroelectric ceramic PLSnZT. *Journal of Applied Physics* **73,** 7261–7267 (1993).

108. Cai, Y. *et al.* TEM study of superstructure in a perovskite lead lanthanum zirconate stannate titanate ceramic. *Acta Materialia* **51,** 6429–6436 (2003).

109. Gao, J. *et al.* Electric field induced phase transition and domain structure evolution in $(Pb,La)(Zr,Sn,Ti)O_3$ single crystal. *Applied Physics Letters* **107,** 072909 (2015).

110. Lu, T. *et al.* Electric-field-induced AFE-FE transitions and associated strain/preferred orientation in antiferroelectric PLZST. *Scientific Reports* **6,** 23659 (2016).

111. Zhuo, F. *et al.* Giant shape memory and domain memory effects in antiferroelectric single crystals. *Materials Horizons* **6,** 1699–1706 (2019).

112. Fu, Z. *et al.* Unveiling the ferrielectric nature of $PbZrO_3$-based antiferroelectric materials. *Nature Communications* **11,** 3809 (2020).

113. He, H. & Tan, X. Electric-field-induced transformation of incommensurate modulations in antiferroelectric $Pb_{0.99}Nb_{0.02}[(Zr_{1-x}Sn_x)_{1-y}Ti_y]_{0.98}O_3$. *Physical Review B* **72,** 024102 (2005).

114. Lu, T. *et al.* Critical role of the coupling between the octahedral rotation and A-site ionic displacements in $PbZrO_3$-based antiferroelectric materials investigated by in situ neutron diffraction. *Physical Review B* **96,** 214108 (2017).

115. Ma, T. *et al.* Uncompensated polarization in incommensurate modulations of perovskite antiferroelectrics. *Physical Review Letters* **123,** 217602 (2019).

116. Liu, H. *et al.* An intriguing intermediate state as a bridge between antiferroelectric and ferroelectric perovskites. *Materials Horizons* **7,** 1912–1918 (2020).

117. Chen, X. *et al.* Charge-discharge properties of lead zirconate stannate titanate ceramics. *Journal of Applied Physics* **106,** 034105 (2009).

118. Zhang, G. *et al.* High-energy storage performance of $(Pb_{0.87}Ba_{0.1}La_{0.02})(Zr_{0.68}Sn_{0.24}Ti_{0.08})O_3$ antiferroelectric ceramics fabricated by the hot-press sintering method. *Journal of the American Ceramic Society* **98,** 1175–1181 (2015).

119. Zhang, Q. *et al.* High recoverable energy density over a wide temperature range in Sr modified $(Pb,La)(Zr,Sn,Ti)O_3$ antiferroelectric ceramics with an orthorhombic phase. *Applied Physics Letters* **109,** 262901 (2016).

120. Bharadwaja, S. S. N., Saha, S., Bhattacharyya, S. & Krupanidhi, S. B. Dielectric properties of La-modified antiferroelectric $PbZrO_3$ thin films. *Materials Science and Engineering: B* **88,** 22–25 (2002).

121. Atkin, R. B. & Fulrath, R. M. Point defects and sintering of lead zirconate-titanate. *Journal of the American Ceramic Society* **54,** 265–270 (1971).

122. Härdtl, K. H. & Hennings, D. Distribution of A-site and B-site vacancies in $(Pb,La)(Ti,Zr)O_3$ ceramics. *Journal of the American Ceramic Society* **55,** 230–231 (1972).

123. Chan, N.-H., Sharma, R. K. & Smyth, D. M. Nonstoichiometry in undoped $BaTiO_3$. *Journal of the American Ceramic Society* **64,** 556–562 (1981).

124. Chan, N.-H., Sharma, R. K. & Smyth, D. M. Nonstoichiometry in acceptor-doped $BaTiO_3$. *Journal of the American Ceramic Society* **65,** 167–170 (1982).

125. Chan, N.-H. & Smyth, D. M. Defect chemistry of donor-doped $BaTiO_3$. *Journal of the American Ceramic Society* **67,** 285–288 (1984).

126. Lupascu, D. C. *Fatigue in Ferroelectric Ceramics and Related Issues* (Springer, Berlin & Heidelberg, 2004).

127. Donnelly, N. J. & Randall, C. A. Pb loss in $Pb(Zr,Ti)O_3$ ceramics observed by in situ ionic conductivity measurements. *Journal of Applied Physics* **109,** 104107 (2011).

128. Gerson, R. & Jaffe, H. Electrical conductivity in lead titanate zirconate ceramics. *Journal of Physics and Chemistry of Solids* **24,** 979–984 (1963).

129. Wu, L., Wu, T.-S., Wei, C.-C. & Liu, H.-C. The DC resistivity of modified PZT ceramics. *Journal of Physics C: Solid State Physics* **16,** 2823–2832 (1983).

130. Morozov, M. I. & Damjanovic, D. Charge migration in $Pb(Zr,Ti)O_3$ ceramics and its relation to ageing, hardening, and softening. *Journal of Applied Physics* **107,** 034106 (2010).

131. Kulcsar, F. Electromechanical properties of lead titanate zirconate ceramics modified with certain three-or five-valent additions. *Journal of the American Ceramic Society* **42,** 343–349 (1959).

132. Takahashi, M. Electrical resistivity of lead zirconate titanate ceramics containing impurities. *Japanese Journal of Applied Physics* **10,** 643–651 (1971).

133. Chan, N.-H. & Smyth, D. M. Defect chemistry of $BaTiO_3$. *Journal of The Electrochemical Society* **123,** 1584 (1976).

134. Waser, R., Baiatu, T. & Härdtl, K.-H. dc electrical degradation of perovskite-type titanates: I, Ceramics. *Journal of the American Ceramic Society* **73,** 1645–1653 (1990).

135. Raymond, M. V., Chen, J. & Smyth, D. M. Degradation of ferroelectric thin films: A defect chemistry approach. *Integrated Ferroelectrics* **5,** 73–78 (1994).

136. Donnelly, N. J. & Randall, C. A. Mixed conduction and chemical diffusion in a $Pb(Zr_{0.53},Ti_{0.47})O_3$ buried capacitor structure. *Applied Physics Letters* **96,** 052906 (2010).

137. Völkl, E., Hillebrand, P. & Fleig, J. Resistance variation in donor-doped PZT stacks with Cu inner electrodes under high field stress. *Journal of Electroceramics* **27,** 66–77 (2011).

138. Frömling, T., Hutter, H. & Fleig, J. Oxide ion transport in donor-doped $Pb(Zr_xTi_{1-x})O_3$: Near-surface diffusion properties. *Journal of the American Ceramic Society* **95,** 1692–1700 (2012).

139. Schulze, W. A., Cross, L. E. & Buessem, W. R. Degradation of $BaTiO_3$ ceramic under high ac electric field. *Journal of the American Ceramic Society* **63,** 83–87 (1980).

140. Waser, R., Baiatu, T. & Härdtl, K.-H. dc electrical degradation of perovskite-type titanates: II, Single crystals. *Journal of the American Ceramic Society* **73,** 1654–1662 (1990).

141. Baiatu, T., Waser, R. & Härdtl, K.-H. dc electrical degradation of perovskite-type titanates: III, A model of the mechanism. *Journal of the American Ceramic Society* **73,** 1663–1673 (1990).

142. Andrejs, L. & Fleig, J. Resistance degradation in donor-doped PZT ceramic stacks with Ag/Pd electrodes: I. Phenomenology of processes. *Journal of the European Ceramic Society* **33,** 779–794 (2013).

143. Akkopru-Akgun, B. *et al.* The influence of Mn doping on the leakage current mechanisms and resistance degradation behavior in lead zirconate titanate films. *Acta Materialia* **208,** 116680 (2021).

144. Bieger, T., Maier, J. & Waser, R. An optical in-situ method to study redox-kinetics in $SrTiO_3$. *Berichte der Bunsengesellschaft für physikalische Chemie* **97,** 1098–1104 (1993).

145. Robertson, J., Warren, W. L., Tuttle, B. A., Dimos, D. & Smyth, D. M. Shallow Pb^{3+} hole traps in lead zirconate titanate ferroelectrics. *Applied Physics Letters* **63,** 1519–1521 (1993).

146. Robertson, J., Warren, W. L. & Tuttle, B. A. Band states and shallow hole traps in $Pb(Zr,Ti)O_3$ ferroelectrics. *Journal of Applied Physics* **77,** 3975–3980 (1995).

147. Baude, P. F., Ye, C. & Polla, D. L. Deep level transient spectroscopy characterization of ferroelectric $Pb(Zr,Ti)O_3$ thin films. *Applied Physics Letters* **64,** 2670–2672 (1994).

148. Akkopru-Akgun, B. *et al.* Leakage current characteristics and DC resistance degradation mechanisms in Nb doped PZT films. *Journal of Applied Physics* **129,** 174102 (2021).

149. Ghorbani, E., Villa, L., Erhart, P., Klein, A. & Albe, K. Self-consistent calculations of charge self-trapping energies: A comparative study of polaron formation and migration in $PbTiO_3$. *Physical Review Materials* **6,** 074410 (2022).

150. Schafranek, R., Li, S., Chen, F., Wu, W. & Klein, A. $PbTiO_3/SrTiO_3$ interface: Energy band alignment and its relation to the limits of Fermi level variation. *Physical Review B* **84,** 045317 (2011).

151. Cardona, M. Optical properties and band structure of $SrTiO_3$ and $BaTiO_3$. *Physical Review* **140,** A651–A655 (1965).

152. Lee, H. *et al.* Dielectric functions and electronic band structure of lead zirconate titanate thin films. *Journal of Applied Physics* **98,** 094108 (2005).

153. Smyth, D. M. Defect structure in perovskite titanates. *Current Opinion in Solid State and Materials Science* **1,** 692–697 (1996).

154. Goo, E. K. W., Mishra, R. K. & Thomas, G. Electron microscopy study of the ferroelectric domains and domain wall structure in $PbZr_{0.52}Ti_{0.48}O_3$. *Journal of Applied Physics* **52,** 2940–2943 (1981).

155. Lucuţa, P. G., Teodorescu, V. & Vasiliu, F. SEM, SAED, and TEM investigations of domain structure in PZT ceramics at morphotropic phase boundary. *Applied Physics A* **37,** 237–242 (1985).

156. Ricote, J., Whatmore, R. W. & Barber, D. J. Studies of the ferroelectric domain configuration and polarization of rhombohedral PZT ceramics. *Journal of Physics: Condensed Matter* **12,** 323–337 (2000).

157. Woodward, D. I., Knudsen, J. & Reaney, I. M. Review of crystal and domain structures in the $PbZr_xTi_{1-x}O_3$ solid solution. *Physical Review B* **72,** 104110 (2005).

158. Sluka, T., Tagantsev, A. K., Bednyakov, P. & Setter, N. Free-electron gas at charged domain walls in insulating $BaTiO_3$. *Nature Communications* **4,** 1808 (2013).

159. Bednyakov, P. S., Sluka, T., Tagantsev, A. K., Damjanovic, D. & Setter, N. Formation of charged ferroelectric domain walls with controlled periodicity. *Scientific Reports* **5,** 15819 (2015).

160. Fesenko, E. G., Gavrilyatchenko, V. G., Martinenko, M. A., Semenchov, A. F. & Lapin, I. P. Domain structure peculiarities of lead-titanate crystals. *Ferroelectrics* **6,** 61–65 (1973).

161. Fesenko, E. G., Gavrilyatchenko, V. G., Semenchev, A. F. & Yufatova, S. M. Regularities in domain structure formation in multiaxial ferroelectric crystals. *Ferroelectrics* **63,** 289–298 (1985).

162. Randall, C. A., Barber, D. J. & Whatmore, R. W. Ferroelectric domain configurations in a modified-PZT ceramic. *Journal of Materials Science* **22,** 925–931 (1987).

163. Jia, C.-L. *et al.* Atomic-scale study of electric dipoles near charged and uncharged domain walls in ferroelectric films. *Nature Materials* **7,** 57–61 (2008).

164. Guyonnet, J., Gaponenko, I., Gariglio, S. & Paruch, P. Conduction at domain walls in insulating $Pb(Zr_{0.2}Ti_{0.8})O_3$ thin films. *Advanced Materials* **23,** 5377–5382 (2011).

165. Li, L. *et al.* Atomic scale structure changes induced by charged domain walls in ferroelectric materials. *Nano Letters* **13,** 5218–5223 (2013).

166. Rojac, T. *et al.* Domain-wall conduction in ferroelectric $BiFeO_3$ controlled by accumulation of charged defects. *Nature Materials* **16,** 322–327 (2017).

167. Esin, A. A. *et al.* Dielectric relaxation and charged domain walls in $(K,Na)NbO_3$-based ferroelectric ceramics. *Journal of Applied Physics* **121,** 074101 (2017).

168. Tang, Y. L. *et al.* Atomic-scale mapping of dipole frustration at 90° charged domain walls in ferroelectric $PbTiO_3$ films. *Scientific Reports* **4,** 4115 (2014).

169. Vul, B. M., Guro, G. M. & Ivanchik, I. I. Encountering domains in ferroelectrics. *Ferroelectrics* **6,** 29–31 (1973).

170. Zheludev, I. S. *Physics of Crystalline Dielectrics: Volume 1 Crystallography and Spontaneous Polarization* (Plenum Press, New York, 1971).

171. Tan, X., Ma, C., Frederick, J., Beckman, S. & Webber, K. G. The antiferroelectric ↔ ferroelectric phase transition in lead-containing and lead-free perovskite ceramics. *Journal of the American Ceramic Society* **94,** 4091–4107 (2011).

172. Xu, Z. *et al.* Ferroelectric domains and incommensuration in the intermediate phase region of lead zirconate. *Journal of the American Ceramic Society* **78,** 2220–2224 (1995).

173. Chan, W.-H., Xu, Z., Zhang, Y., Hung, T. F. & Chen, H. Microstructural evolution and macroscopic property relationship in antiferroelectric lead lanthanum stannate zirconate titanate ceramics. *Journal of Applied Physics* **94,** 4563–4565 (2003).

174. Asada, T. & Koyama, Y. La-induced conversion between the ferroelectric and antiferroelectric incommensurate phases in $Pb_{1-x}La_x(Zr_{1-y}Ti_y)O_3$. *Physical Review B* **69,** 104108 (2004).

175. Guo, H. & Tan, X. Direct observation of the recovery of an antiferroelectric phase during polarization reversal of an induced ferroelectric phase. *Physical Review B* **91,** 144104 (2015).

176. Fan, Z., Xue, F., Tutuncu, G., Chen, L.-Q. & Tan, X. Interaction dynamics between ferroelectric and antiferroelectric domains in a $PbZrO_3$-based ceramic. *Physical Review Applied* **11,** 064050 (2019).

177. Shen, G. J. & Shen, K. Electron microscope study of domains in $PbZrO_3$. *Journal of Materials Science* **34,** 5153–5156 (1999).

178. Ma, T., Fan, Z., Tan, X. & Zhou, L. Atomically resolved domain boundary structure in lead zirconate-based antiferroelectrics. *Applied Physics Letters* **115,** 122902 (2019).

179. Nord, M., Vullum, P. E., MacLaren, I., Tybell, T. & Holmestad, R. Atomap: a new software tool for the automated analysis of atomic resolution images using two-dimensional Gaussian fitting. *Advanced Structural and Chemical Imaging* **3,** 9 (2017).

180. Tolédano, P. & Guennou, M. Theory of antiferroelectric phase transitions. *Physical Review B* **94,** 014107 (2016).

181. Aramberri, H., Cazorla, C., Stengel, M. & Íñiguez, J. On the possibility that $PbZrO_3$ not be antiferroelectric. *npj Computational Materials* **7,** 196 (2021).

182. Fan, Z. *et al.* TEM investigation of the domain structure in $PbHfO_3$ and $PbZrO_3$ antiferroelectric perovskites. *Journal of Materials Science* **55,** 4953–4961 (2020).

183. Junquera, J. & Ghosez, P. Critical thickness for ferroelectricity in perovskite ultrathin films. *Nature* **422,** 506–509 (2003).

184. Dawber, M., Rabe, K. M. & Scott, J. F. Physics of thin-film ferroelectric oxides. *Reviews of Modern Physics* **77,** 1083–1130 (2005).

185. Stengel, M. & Spaldin, N. A. Origin of the dielectric dead layer in nanoscale capacitors. *Nature* **443,** 679–682 (2006).

186. Black, C. T. & Welser, J. J. Electric-field penetration into metals: consequences for high-dielectric-constant capacitors. *IEEE Transactions on Electron Devices* **46,** 776–780 (1999).

187. Sinnamon, L. J., Bowman, R. M. & Gregg, J. M. Investigation of dead-layer thickness in $SrRuO_3/Ba_{0.5}Sr_{0.5}TiO_3$/Au thin-film capacitors. *Applied Physics Letters* **78,** 1724–1726 (2001).

188. Kohlstedt, H., Pertsev, N. A. & Waser, R. Size effects on polarization in epitaxial ferroelectric films and the concept of ferroelectric tunnel junctions including first results. *MRS Online Proceedings Library* **688,** 651 (2011).

189. Stengel, M., Spaldin, N. A. & Vanderbilt, D. Electric displacement as the fundamental variable in electronic-structure calculations. *Nature Physics* **5,** 304–308 (2009).

190. Baudry, L. & Tournier, J. Lattice model for ferroelectric thin film materials including surface effects: Investigation on the “depolarizing” field properties. *Journal of Applied Physics* **90,** 1442–1454 (2001).

191. Stengel, M., Aguado-Puente, P., Spaldin, N. A. & Junquera, J. Band alignment at metal/ferroelectric interfaces: Insights and artifacts from first principles. *Physical Review B* **83,** 235112 (2011).

192. Batra, I. P. & Silverman, B. D. Thermodynamic stability of thin ferroelectric films. *Solid State Communications* **11,** 291–294 (1972).

193. Batra, I. P., Wurfel, P. & Silverman, B. D. Phase transition, stability, and depolarization field in ferroelectric thin films. *Physical Review B* **8,** 3257–3265 (1973).

194. Kittel, C. & McEuen, P. *Introduction to Solid State Physics* 8th ed. (John Wiley & Sons, Hoboken, New Jersey, 2005).

195. Tilley, D. R. & Zeks, B. TfC23. Phase transitions in ferroelectric films. *Ferroelectrics* **134,** 313–318 (1992).

196. Black, C. T., Farrell, C. & Licata, T. J. Suppression of ferroelectric polarization by an adjustable depolarization field. *Applied Physics Letters* **71,** 2041–2043 (1997).

197. Hadni, A., Thomas, R., Ungar, S. & Gerbaux, X. Drastic modifications of electrical properties of ferroelectric crystal plates with thickness, the case of triglycine sulphate. *Ferroelectrics* **47,** 201–220 (1983).

198. Kretschmer, R. & Binder, K. Surface effects on phase transitions in ferroelectrics and dipolar magnets. *Physical Review B* **20,** 1065–1076 (1979).

199. Binder, K. Surface effects on phase transitions in ferroelectrics and antiferroelectrics. *Ferroelectrics* **35,** 99–104 (1981).

200. Tagantsev, A. K. & Stolichnov, I. A. Injection-controlled size effect on switching of ferroelectric thin films. *Applied Physics Letters* **74,** 1326–1328 (1999).

201. Tagantsev, A. K., Stolichnov, I., Colla, E. L. & Setter, N. Polarization fatigue in ferroelectric films: Basic experimental findings, phenomenological scenarios, and microscopic features. *Journal of Applied Physics* **90,** 1387–1402 (2001).

202. Stengel, M., Vanderbilt, D. & Spaldin, N. A. Enhancement of ferroelectricity at metal–oxide interfaces. *Nature Materials* **8,** 392–397 (2009).

203. Sinnamon, L. J., Saad, M. M., Bowman, R. M. & Gregg, J. M. Exploring grain size as a cause for “dead-layer” effects in thin film capacitors. *Applied Physics Letters* **81,** 703–705 (2002).

204. Saad, M. M. *et al.* Intrinsic dielectric response in ferroelectric nano-capacitors. *Journal of Physics: Condensed Matter* **16,** L451–L456 (2004).

205. Junquera, J. & Ghosez, P. First-principles study of ferroelectric oxide epitaxial thin films and superlattices: role of the mechanical and electrical boundary conditions. *Journal of Computational and Theoretical Nanoscience* **5,** 2071–2088 (2008).

206. Hong, S., Nakhmanson, S. M. & Fong, D. D. Screening mechanisms at polar oxide heterointerfaces. *Reports on Progress in Physics* **79,** 076501 (2016).

207. Stengel, M., Vanderbilt, D. & Spaldin, N. A. First-principles modeling of ferroelectric capacitors via constrained displacement field calculations. *Physical Review B* **80,** 224110 (2009).

208. Markowski, K., Park, S.-E., Yoshikawa, S. & Cross, L. E. Effect of compositional variations in the lead lanthanum zirconate stannate titanate system on electrical properties. *Journal of the American Ceramic Society* **79,** 3297–3304 (1996).

209. Wang, X., Yang, T., Shen, J., Dong, Y. & Liu, Y. Phase transition and dielectric properties of (Pb,La)(Zr,Sn,Ti)O_3 ceramics at morphotropic phase boundary. *Journal of Alloys and Compounds* **673,** 67–72 (2016).

210. Young, S. E., Zhang, J. Y., Hong, W. & Tan, X. Mechanical self-confinement to enhance energy storage density of antiferroelectric capacitors. *Journal of Applied Physics* **113,** 054101 (2013).

211. Schneider, C. A., Rasband, W. S. & Eliceiri, K. W. NIH Image to ImageJ: 25 years of image analysis. *Nature Methods* **9,** 671–675 (2012).

212. *Low Level Measurements Handbook: Precision DC Current, Voltage, and Resistance Measurements* 7th ed. (Keithley).

213. Hüfner, S. *Photoelectron Spectroscopy: Principles and Applications* (Springer, Berlin & Heidelberg, 2003).

214. Klein, A., Mayer, T., Thissen, A. & Jaegermann, W. *Photoelectron Spectroscopy in Materials Science and Physical Chemistry: Analysis of Composition, Chemical Bonding, and Electronic Structure of Surfaces and Interfaces* in *Methods in Physical Chemistry* 477–512 (Wiley-VCH, Weinheim, 2012).

215. Moulder, J. F., Stickle, W. F., Sobol, P. E. & Bomben, K. D. *Handbook of X-ray Photoelectron Spectroscopy: A Reference Book of Standard Spectra for Identification and Interpretation of XPS Data* (eds Chastain, J. & King Jr., R. C.) (Physical Electronics, Inc., Chanhassen, 1995).

216. Klein, A. Interface properties of dielectric oxides. *Journal of the American Ceramic Society* **99,** 369–387 (2016).

217. Chen, F., Schafranek, R., Wu, W. & Klein, A. Formation and modification of Schottky barriers at the PZT/Pt interface. *Journal of Physics D: Applied Physics* **42,** 215302 (2009).

218. Chen, F., Schafranek, R., Wu, W. & Klein, A. Reduction-induced Fermi level pinning at the interfaces between Pb(Zr,Ti)O_3 and Pt, Cu and Ag metal electrodes. *Journal of Physics D: Applied Physics* **44,** 255301 (2011).

219. Lee, J.-g. & Choh, S.-k. M. Deposition and properties of reactively sputtered ruthenium dioxide thin films as an electrode for ferroelectric capacitors. *Japanese Journal of Applied Physics* **33,** 7080 (1994).

220. Koch, N. Organic electronic devices and their functional interfaces. *ChemPhysChem* **8,** 1438–1455 (2007).

221. Rogers, D. B., Shannon, R. D., Sleight, A. W. & Gillson, J. L. Crystal chemistry of metal dioxides with rutile-related structures. *Inorganic Chemistry* **8,** 841–849 (1969).

222. Riga, J. *et al.* Electronic structure of rutile oxides TiO_2, RuO_2 and IrO_2 studied by X-ray photoelectron spectroscopy. *Physica Scripta* **16,** 351 (1977).

223. Ryden, W. D., Lawson, A. W. & Sartain, C. C. Electrical transport properties of IrO_2 and RuO_2. *Physical Review B* **1,** 1494–1500 (1970).

224. Hamberg, I. & Granqvist, C. G. Evaporated Sn-doped In_2O_3 films: Basic optical properties and applications to energy-efficient windows. *Journal of Applied Physics* **60,** R123–R160 (1986).

225. Minami, T. Transparent conducting oxide semiconductors for transparent electrodes. *Semiconductor Science and Technology* **20,** S35 (2005).

226. Hermans, Y. *et al.* Energy-band alignment of $BiVO_4$ from photoelectron spectroscopy of solid-state interfaces. *The Journal of Physical Chemistry C* **122,** 20861–20870 (2018).

227. Klein, A. *et al.* Surface potentials of magnetron sputtered transparent conducting oxides. *Thin Solid Films* **518,** 1197–1203 (2009).

228. Chen, F., Schafranek, R., Li, S., Wu, W. B. & Klein, A. Energy band alignment between $Pb(Zr,Ti)O_3$ and high and low work function conducting oxides—from hole to electron injection. *Journal of Physics D: Applied Physics* **43,** 295301 (2010).

229. Li, S. *et al.* Intrinsic energy band alignment of functional oxides. *physica status solidi (RRL) – Rapid Research Letters* **8,** 571–576 (2014).

230. Klein, A. Transparent conducting oxides: electronic structure–property relationship from photoelectron spectroscopy with in situ sample preparation. *Journal of the American Ceramic Society* **96,** 331–345 (2013).

231. Gassenbauer, Y. *et al.* Surface states, surface potentials, and segregation at surfaces of tin-doped In_2O_3. *Physical Review B* **73,** 245312 (2006).

232. Harvey, S. P., Mason, T. O., Gassenbauer, Y., Schafranek, R. & Klein, A. Surface versus bulk electronic/defect structures of transparent conducting oxides: I. Indium oxide and ITO. *Journal of Physics D: Applied Physics* **39,** 3959–3968 (2006).

233. Frank, G. & Köstlin, H. Electrical properties and defect model of tin-doped indium oxide layers. *Applied Physics A* **27,** 197–206 (1982).

234. Hwang, J.-H., Edwards, D. D., Kammler, D. R. & Mason, T. O. Point defects and electrical properties of Sn-doped In-based transparent conducting oxides. *Solid State Ionics* **129,** 135–144 (2000).

235. Chen, S. & Wang, L.-W. Thermodynamic oxidation and reduction potentials of photocatalytic semiconductors in aqueous solution. *Chemistry of Materials* **24,** 3659–3666 (2012).

236. Lohaus, C., Klein, A. & Jaegermann, W. Limitation of Fermi level shifts by polaron defect states in hematite photoelectrodes. *Nature Communications* **9,** 4309 (2018).

237. Hermans, Y., Murcia-López, S., Klein, A. & Jaegermann, W. $BiVO_4$ surface reduction upon water exposure. *ACS Energy Letters* **4,** 2522–2528 (2019).

238. Bein, N. S. *et al.* Electrochemical reduction of undoped and cobalt-doped $BiFeO_3$ induced by water exposure: Quantitative determination of reduction potentials and defect energy levels using photoelectron spectroscopy. *The Journal of Physical Chemistry Letters* **10,** 7071–7076 (2019).

239. Yang, G. Y. *et al.* Oxygen nonstoichiometry and dielectric evolution of $BaTiO_3$. Part II—insulation resistance degradation under applied dc bias. *Journal of Applied Physics* **96,** 7500–7508 (2004).

240. Opitz, A. K. *et al.* Enhancing electrochemical water-splitting kinetics by polarization-driven formation of near-surface iron(0): an in situ XPS study on perovskite-type electrodes. *Angewandte Chemie International Edition* **54,** 2628–2632 (2015).

241. Giesecke, R., Hertwig, R., Bayer, T. J. M., Randall, C. A. & Klein, A. Modification of the Schottky barrier height at the RuO_2 cathode during resistance degradation of Fe-doped $SrTiO_3$. *Journal of the American Ceramic Society* **100,** 4590–4601 (2017).

242. Nenning, A. *et al.* Ambient pressure XPS study of mixed conducting perovskite-type SOFC cathode and anode materials under well-defined electrochemical polarization. *The Journal of Physical Chemistry C* **120,** 1461–1471 (2016).

243. Opitz, A. K. *et al.* The chemical evolution of the $La_{0.6}Sr_{0.4}CoO_{3-\delta}$ surface under SOFC operating conditions and its implications for electrochemical oxygen exchange activity. *Topics in Catalysis* **61,** 2129–2141 (2018).

244. Lu, Q. *et al.* Electrochemically triggered metal–insulator transition between VO_2 and V_2O_5. *Advanced Functional Materials* **28,** 1803024 (2018).

245. Chen, F. & Klein, A. Polarization dependence of Schottky barrier heights at interfaces of ferroelectrics determined by photoelectron spectroscopy. *Physical Review B* **86,** 094105 (2012).

246. Hubmann, A. H., Li, S., Zhukov, S., von Seggern, H. & Klein, A. Polarisation dependence of Schottky barrier heights at ferroelectric $BaTiO_3$ / RuO_2 interfaces: influence of substrate orientation and quality. *Journal of Physics D: Applied Physics* **49,** 295304 (2016).

247. Rault, J. E. *et al.* Interface electronic structure in a metal/ferroelectric heterostructure under applied bias. *Physical Review B* **87,** 155146 (2013).

248. Kröger, E. *et al.* In situ hard X-ray photoemission spectroscopy of barrier-height control at metal/PMN-PT interfaces. *Physical Review B* **93,** 235415 (2016).

249. Steinmann, J. *Polarisationseinfluss auf die Schottky Barrierenhöhe an der Elektrodengrenzfläche von PMN-PT/ITO und PMN-PT/RuO_2* Bachelor thesis (Technische Universität Darmstadt, 2021).

250. Ding, H. *Domain morphology and atomic structure of antiferroelectric perovskites* PhD thesis (Technische Universität Darmstadt, 2022).

251. Egert, S. *Local structure-property relations in antiferroelectric oxides* PhD thesis (Technische Universität Darmstadt, 2022).

252. Forst, D., Li, J.-F. & Viehland, D. Observation of multiple electrically induced phase transitions and a decoupling of the induced strain and polarization in Sn-modified lead zirconate titanate. *Applied Physics Letters* **71,** 1472–1474 (1997).

253. Brodeur, R. P., wa Gachigi, K., Pruna, P. M. & Shrout, T. R. Ultra-high strain ceramics with multiple field-induced phase transitions. *Journal of the American Ceramic Society* **77,** 3042–3044 (1994).

254. Fesenko, O. E., Kolesova, R. V. & Sindeyev, Y. G. The structural phase transitions in lead zirconate in super-high electric fields. *Ferroelectrics* **20,** 177–178 (1978).

255. Pan, W., Zhang, Q., Bhalla, A. & Cross, L. E. Field-forced antiferroelectric-to-ferroelectric switching in modified lead zirconate titanate stannate ceramics. *Journal of the American Ceramic Society* **72,** 571–578 (1989).

256. Viehland, D., Forst, D. & Li, J.-F. Compositional heterogeneity and the origins of the multicell cubic state in Sn-doped lead zirconate titanate ceramics. *Journal of Applied Physics* **75,** 4137–4143 (1994).

257. Novak, N. *et al.* Interplay of conventional with inverse electrocaloric response in (Pb,Nb)(Zr,Sn,Ti)O_3 antiferroelectric materials. *Physical Review B* **97,** 094113 (2018).

258. Blue, C. T., Hicks, J. C., Park, S.-E., Yoshikawa, S. & Cross, L. E. In situ x-ray diffraction study of the antiferroelectric–ferroelectric phase transition in PLSnZT. *Applied Physics Letters* **68,** 2942–2944 (1996).

259. Liu, P. *et al.* High energy density at high temperature in PLZST antiferroelectric ceramics. *Journal of Materials Chemistry C* **7,** 4587–4594 (2019).

260. Kingon, A. I. & Clark, J. B. Sintering of PZT ceramics: I, Atmosphere control. *Journal of the American Ceramic Society* **66,** 253–256 (1983).

261. Kingon, A. I. & Clark, J. B. Sintering of PZT ceramics: II, Effect of PbO content on densification kinetics. *Journal of the American Ceramic Society* **66,** 256–260 (1983).

262. Hammer, M. & Hoffmann, M. J. Sintering model for mixed-oxide-derived lead zirconate titanate ceramics. *Journal of the American Ceramic Society* **81,** 3277–3284 (1998).

263. Zhou, L., Zimmermann, A., Zeng, Y.-P. & Aldinger, F. Effects of PbO content on the sintering behavior, microstructure, and properties of La-doped PZST antiferroelectric ceramics. *Journal of Materials Science: Materials in Electronics* **15,** 145–151 (2004).

264. Schafranek, R., Schaffner, J. & Klein, A. In situ photoelectron study of the (Ba,Sr)TiO_3/RuO_2 contact formation. *Journal of the European Ceramic Society* **30,** 187–192 (2010).

265. Körber, C. *et al.* Electronic structure of In_2O_3 and Sn-doped In_2O_3 by hard X-ray photoemission spectroscopy. *Physical Review B* **81,** 165207 (2010).

266. Shrout, T. R., Huebner, W., Randall, C. A. & Hilton, A. D. Aging mechanisms in $Pb(Mg_{1/3}Nb_{2/3})O_3$-based relaxor ferroelectrics. *Ferroelectrics* **93,** 361–372 (1989).

267. Smyth, D. M., Harmer, M. P. & Peng, P. Defect chemistry of relaxor ferroelectrics and the implications for dielectric degradation. *Journal of the American Ceramic Society* **72,** 2276–2278 (1989).

268. Yang, K., Wang, C. L. & Li, J. C. Electronic structure of relaxor PMN. *Integrated Ferroelectrics* **78,** 113–117 (2006).

269. Atkins, P., de Paula, J. & Keeler, J. *Physical Chemistry* 12th ed. (Oxford University Press, Oxford, 2022).

270. Larsen, P. K., Dormans, G. J. M., Taylor, D. J. & van Veldhoven, P. J. Ferroelectric properties and fatigue of $PbZr_{0.51}Ti_{0.49}O_3$ thin films of varying thickness: Blocking layer model. *Journal of Applied Physics* **76,** 2405–2413 (1994).

271. Tagantsev, A. K., Landivar, M., Colla, E. & Setter, N. Identification of passive layer in ferroelectric thin films from their switching parameters. *Journal of Applied Physics* **78,** 2623–2630 (1995).

272. Grossmann, M., Lohse, O., Bolten, D., Boettger, U. & Waser, R. The interface screening model as origin of imprint in $PbZr_xTi_{1-x}O_3$ thin films. II. Numerical simulation and verification. *Journal of Applied Physics* **92,** 2688–2696 (2002).

273. Tagantsev, A. K., Stolichnov, I., Setter, N. & Cross, J. S. Nature of nonlinear imprint in ferroelectric films and long-term prediction of polarization loss in ferroelectric memories. *Journal of Applied Physics* **96,** 6616–6623 (2004).

274. Do, M. T. *et al.* Interfacial dielectric layer as an origin of polarization fatigue in ferroelectric capacitors. *Scientific Reports* **10,** 7310 (2020).

275. Lu, T. *et al.* Susceptible ferroelectric/antiferroelectric phase transition near the surface of Nb-doped lead zirconate stannate titanate from surface processing. *ACS Applied Materials & Interfaces* **8,** 14313–14317 (2016).

276. Kong, S., Kumar, N., Checchia, S., Cazorla, C. & Daniels, J. Defect-driven structural distortions at the surface of relaxor ferroelectrics. *Advanced Functional Materials* **29,** 1900344 (2019).

277. Lou, X. J. Why do antiferroelectrics show higher fatigue resistance than ferroelectrics under bipolar electrical cycling? *Applied Physics Letters* **94,** 072901 (2009).

278. Lou, X. J., Zhang, M., Redfern, S. A. T. & Scott, J. F. Fatigue as a local phase decomposition: A switching-induced charge-injection model. *Physical Review B* **75,** 224104 (2007).

279. Cillessen, J. F. M., Prins, M. W. J. & Wolf, R. M. Thickness dependence of the switching voltage in all-oxide ferroelectric thin-film capacitors prepared by pulsed laser deposition. *Journal of Applied Physics* **81,** 2777–2783 (1997).

280. Stolichnov, I., Tagantsev, A. K., Colla, E. L. & Setter, N. Cold-field-emission test of the fatigued state of $Pb(Zr_xTi_{1-x})O_3$ films. *Applied Physics Letters* **73,** 1361–1363 (1998).

281. Denk, I., Münch, W. & Maier, J. Partial conductivities in $SrTiO_3$: Bulk polarization experiments, oxygen concentration cell measurements, and defect-chemical modeling. *Journal of the American Ceramic Society* **78,** 3265–3272 (1995).

282. Moos, R. & Härdtl, K. H. Defect chemistry of donor-doped and undoped strontium titanate ceramics between 1000° and 1400°C. *Journal of the American Ceramic Society* **80,** 2549–2562 (1997).

283. Wang, J.-J. *et al.* Defect chemistry and resistance degradation in Fe-doped $SrTiO_3$ single crystal. *Acta Materialia* **108,** 229–240 (2016).

284. *CRC Handbook of Chemistry and Physics* 95th ed. (ed Haynes, W. M.) (CRC Press, Boca Raton, 2014).

285. Lee, J. & Han, S. Thermodynamics of native point defects in α-Fe_2O_3: an ab initio study. *Physical Chemistry Chemical Physics* **15,** 18906–18914 (2013).

286. Jia, Q. X., Shi, Z. Q., Jiao, K. L., Anderson, W. A. & Collins, F. M. Reactively sputtered RuO_2 thin film resistor with near zero temperature coefficient of resistance. *Thin Solid Films* **196,** 29–34 (1991).

287. Wang, Q., Gladfelter, W. L., Fennell Evans, D., Fan, Y. & Franciosi, A. Reactive-sputter deposition and structure of RuO_2 films on sapphire and strontium titanate. *Journal of Vacuum Science & Technology A* **14,** 747–752 (1996).

288. Dih, J. J. & Fulrath, R. M. Electrical conductivity in lead zirconate-titanate ceramics. *Journal of the American Ceramic Society* **61,** 448–451 (1978).

289. Al-Shareef, H. N. & Dimos, D. Leakage and reliability characteristics of lead zirconate titanate thin-film capacitors. *Journal of the American Ceramic Society* **80,** 3127–3132 (1997).

290. Zhao, S. *et al.* Time dependent dc resistance degradation in lead-based perovskites: $0.7Pb(Mg_{1/3}Nb_{2/3})O_3-0.3PbTiO_3$. *Journal of Applied Physics* **105,** 053705 (2009).

291. Ossmer, H. *et al.* Electrocoloration of donor-doped lead zirconate titanate under DC field stress. *Solid State Ionics* **281,** 49–59 (2015).

292. Guiffard, B., Boucher, E., Eyraud, L., Lebrun, L. & Guyomar, D. Influence of donor co-doping by niobium or fluorine on the conductivity of Mn doped and Mg doped PZT ceramics. *Journal of the European Ceramic Society* **25,** 2487–2490 (2005).

293. Chiang, Y.-M. & Takagi, T. Grain-boundary chemistry of barium titanate and strontium titanate: I, High-temperature equilibrium space charge. *Journal of the American Ceramic Society* **73,** 3278–3285 (1990).

294. Waser, R. & Hagenbeck, R. Grain boundaries in dielectric and mixed-conducting ceramics. *Acta Materialia* **48,** 797–825 (2000).

295. De Souza, R. A. The formation of equilibrium space-charge zones at grain boundaries in the perovskite oxide $SrTiO_3$. *Physical Chemistry Chemical Physics* **11,** 9939–9969 (2009).

Appendices

A. Extended results of basic characterizations of ceramic samples

A.1. Dielectric properties

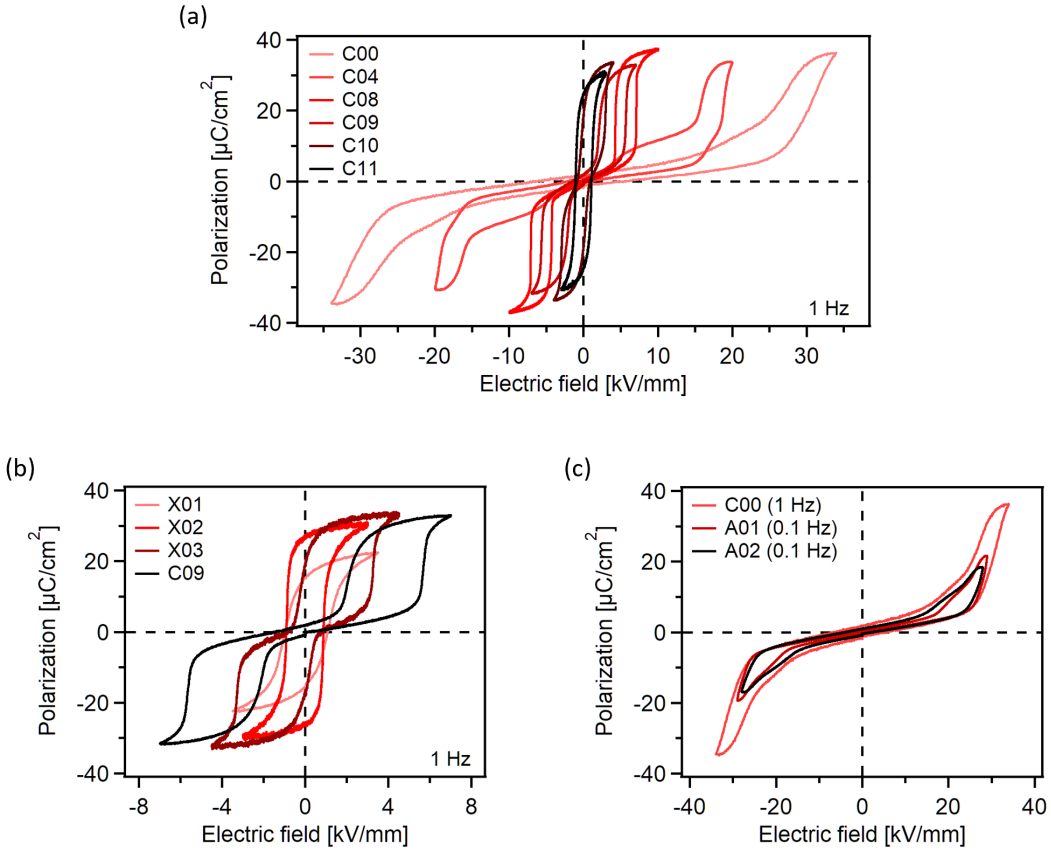

Figure A.1.: Direct comparisons of the polarization versus electric field hysteresis loops of all C-, X-, and A-series compositions at room temperature. Compositions C09 and C00 are appended to the X- and A-series, respectively.

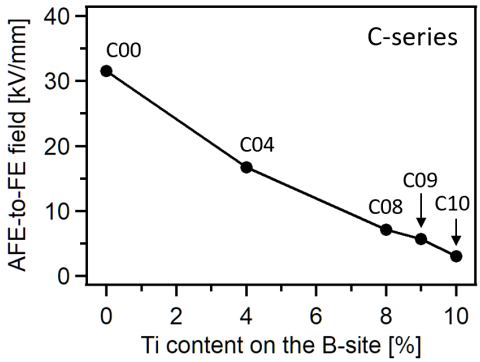

Figure A.2.: Dependence of the forward AFE-to-FE transition field on the *B*-site Ti concentration in C-series. For composition C04, which clearly shows the field-induced multiphase transitions, the AFE-to-FE transition point refers to the field where the largest slope is during its first transition stage. Composition C11 is not included here because its developed loop exhibits a FE hysteresis feature.

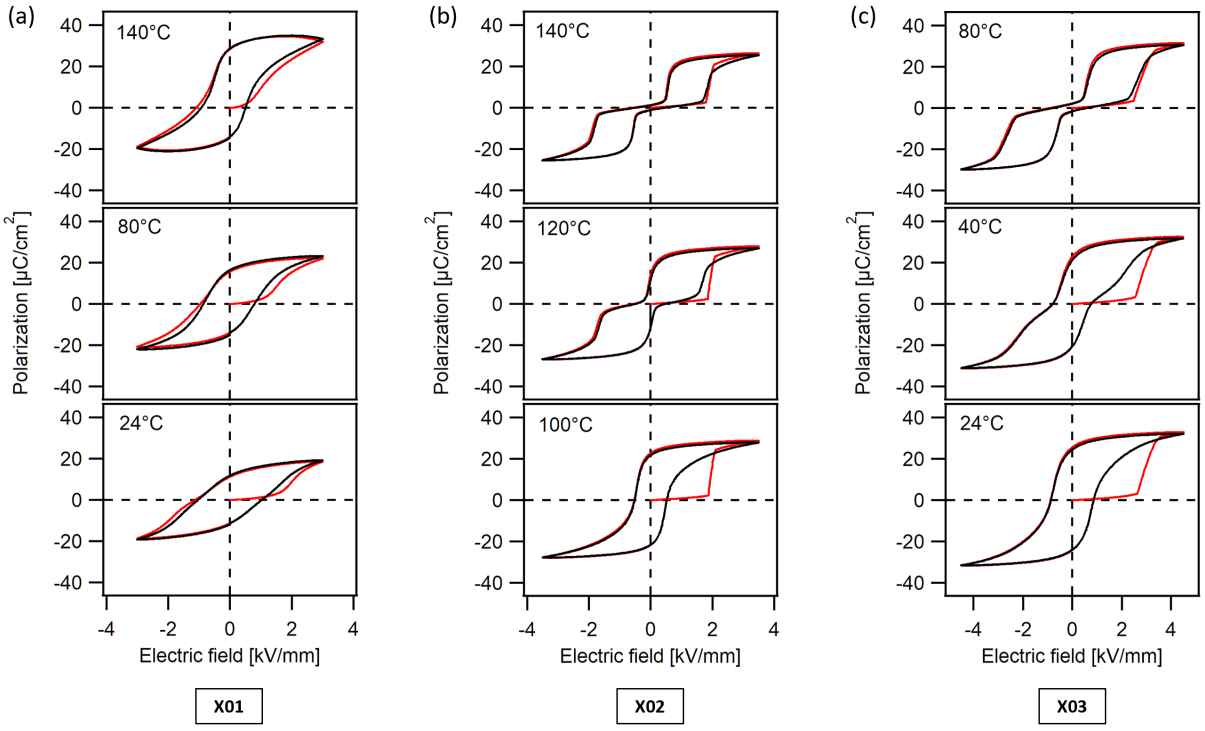

Figure A.3.: Temperature-dependent polarization versus electric field hysteresis loops of compositions X01, X02, and X03. The red and black loops represent the initial and the developed ones, respectively.

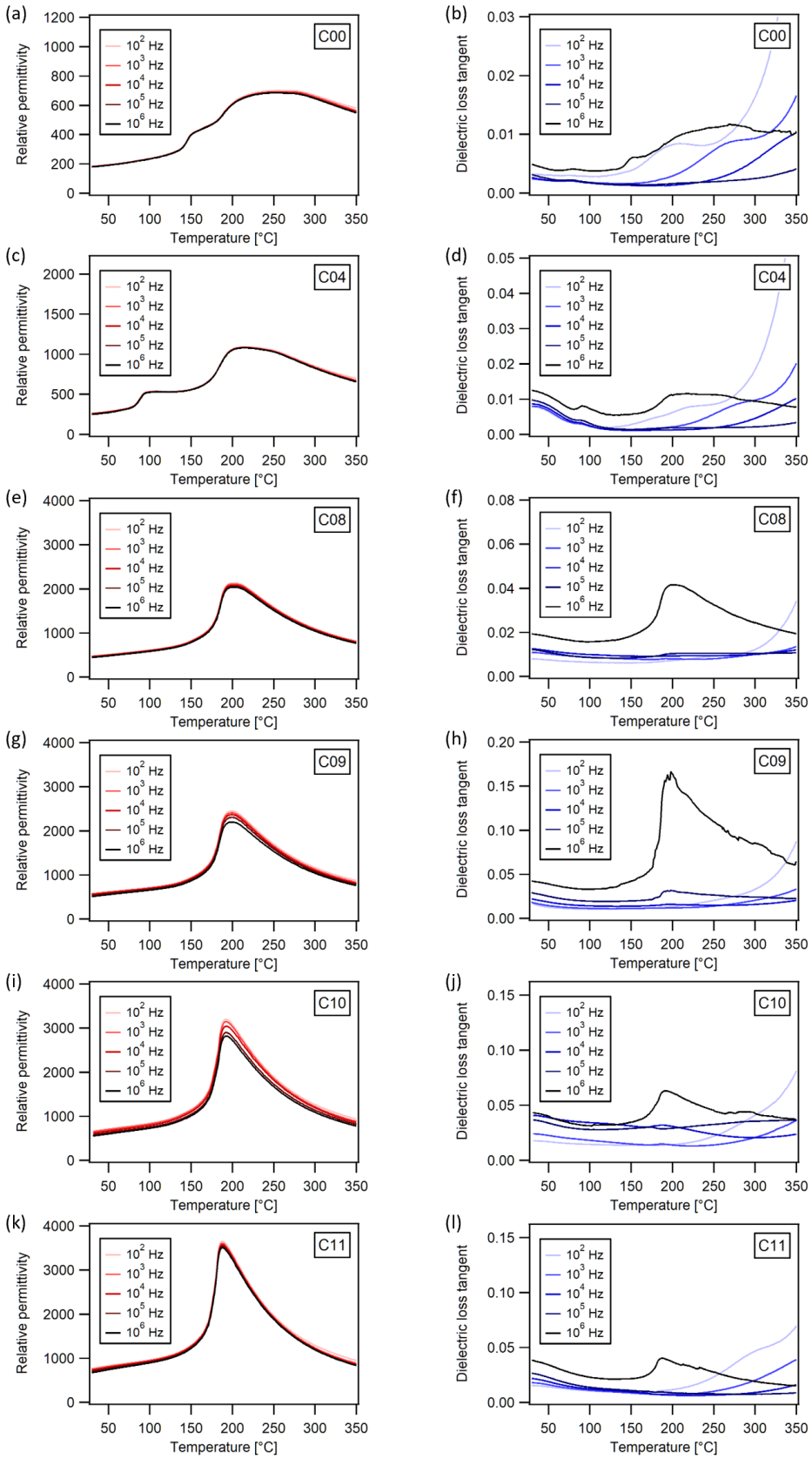

Figure A.4.: Temperature-dependent relative dielectric permittivity and dielectric loss tangent of all C-series compositions measured at different frequencies.

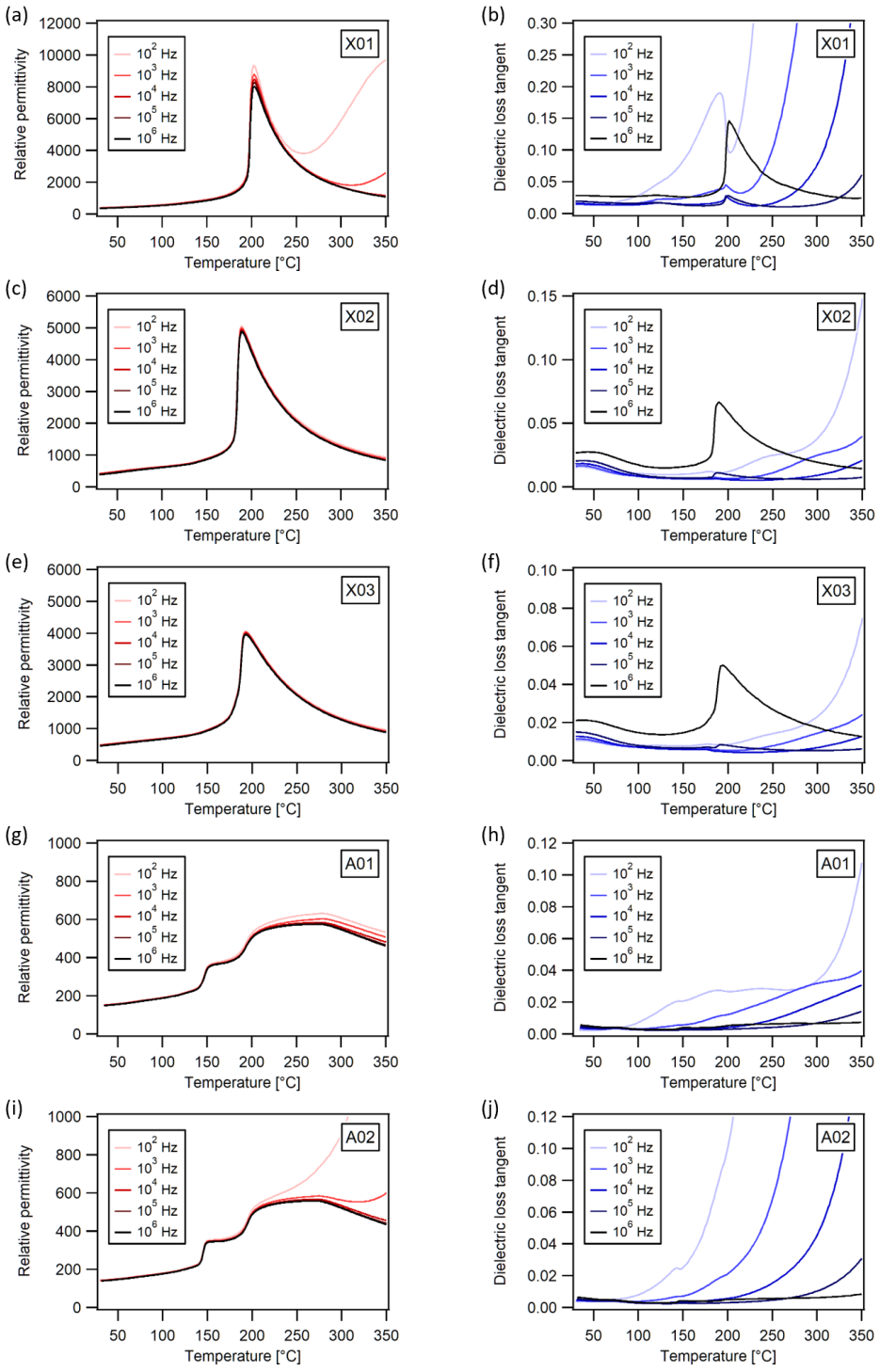

Figure A.5.: Temperature-dependent relative dielectric permittivity and dielectric loss tangent of all X- and A-series compositions measured at different frequencies.

A.2. Crystalline structures

X-ray diffraction patterns measured on poled pellets with electrodes

XRD measurements were carried out on ceramic pellets with RuO_2 top electrodes (ca. 30 nm, deposited at room temperature) and Pt bottom electrodes. With the capacitor structure, one can apply electric fields on these samples and compare their crystalline structures before and after poling. RuO_2 thin films deposited by reactive sputtering at room temperature are believed to be amorphous [286, 287], which can help the determination of the reflections belonging to the substrates. The procedure of the XRD measurements basically follows the description in Section 3.2.3. Compositions C09–C11, which are close to the phase boundary between the A_T and the $F_{R(LT)}$ regions, were selected for these experiments. In particular, at room temperature composition C11 firstly exhibits an AFE-to-FE transition in Quadrant I of its initial P–E loop and subsequently shows a FE behavior in its developed P–E loop (see Figure 4.4(c)). For this composition, a clear change of the crystalline structure corresponding to the irreversible field-induced phase transition is expected to be observed. Figure A.6 displays the {111} and {200} peaks in the XRD patterns of these three samples before and after poling. Here "poling" refers to running P–E loop measurements normally with 1 Hz at room temperature. The highest applied electric fields are $\pm$6 kV/mm, $\pm$4.5 kV/mm, and $\pm$4.0 kV/mm for the C09, C10, and C11 samples, respectively. It can be clearly seen that the C11 sample undergoes a phase transition from a tetragonal structure (split {200}) to a rhombohedral one (split {111}). However, this transition seems to be not complete. The {200} reflection of the C11 sample still exhibits a little splitting after poling.

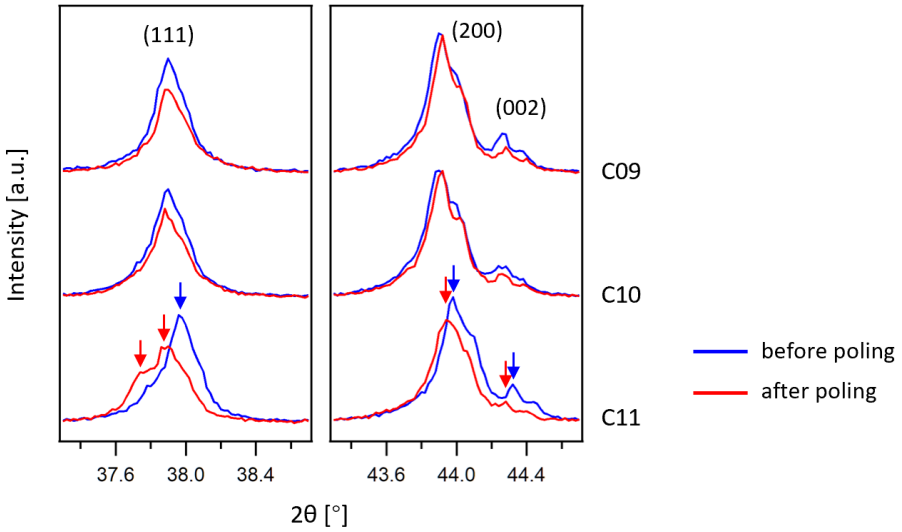

Figure A.6.: Comparison of the X-ray diffraction patterns before and after poling on three ceramic pellets (compositions C09, C10, and C11) with top (RuO_2) and bottom (Pt) electrodes. Pseudo-cubic index of perovskite unit cell is used to indicate the reflections.

X-ray diffraction patterns measured on ceramic pellets vs. on ceramic powders

Powder diffraction was performed on compositions C08–C11, as shown in Figure A.7(a). The sintered ceramic pellets were ground to powders and mixed with silicon powder standard. All patterns were measured at room temperature in Huber Guinier camera (HUBER Diffraktionstechnik GmbH & Co. KG,

Germany) with Cu-$K_{\alpha 1}$ radiation (1.5406 Å) and a step size of 0.005°. The measurements were carried out by Mr. Jean-Christophe Jaud and Mr. Leif Carstensen.

Figure A.7(b) displays the {200} reflections of compositions C08–C11 measured on pellets and powders. It is obvious that for every composition the intensity ratio between the (200) and (002) peaks of the pellet sample is larger than that of the powder, which indicates the existence of texture in the pellets of such materials. In Figure A.7(c), we simply compare the height ratios of the two peaks for all these compositions obtained by two different methods. Apart from the undoubted difference between the data of pellets and powders, it is also interesting to see the composition dependence of the height ratio just for the powder diffraction data. The deviation of the C10 and C11 powders from the ideal value $2:1$ implies some other structural discrepancies of these compositions in their unpoled states compared to the room-temperature AFE compositions C08 and C09. The data given here are just for reference, and further study is still needed.

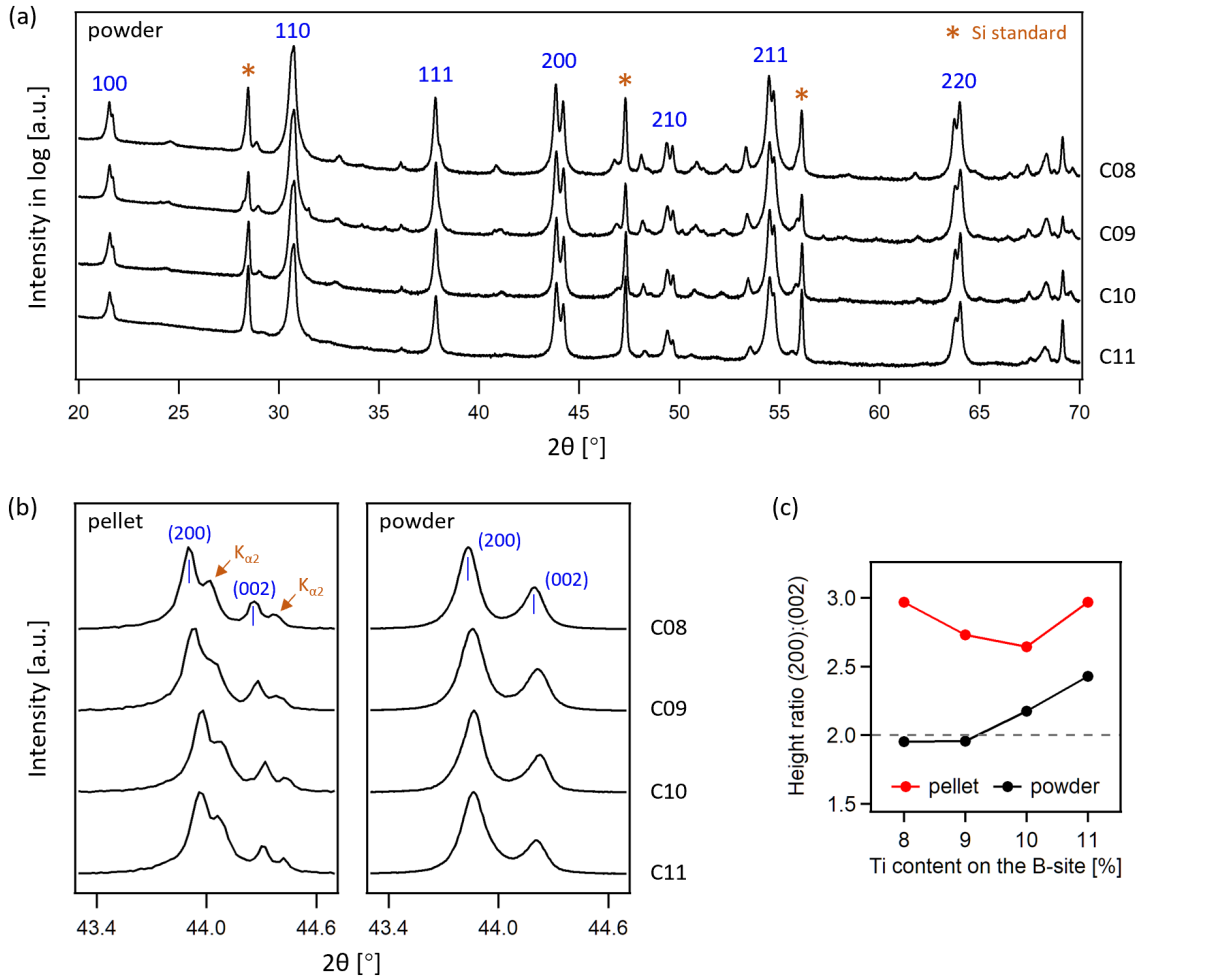

Figure A.7.: (a) X-ray diffraction patterns measured on ceramic powders of compositions C08–C11; (b) comparison of the {200} reflections measured on pellets and powders; (c) dependence of the height ratios between the (200) and (002) peaks on the Ti concentration. Pseudo-cubic index of perovskite unit cell is used to indicate the reflections.

Lattice parameters extracted from X-ray diffraction data

Table A.1.: Lattice constants of the perovskite unit cells of all C-, X-, and A-series samples determined by the indexing program Dicvol.

Composition	Symmetry	a(=b) (Å)	c (Å)	$\alpha(=\beta=\gamma)$ (°)	Cell volume (Å^3)
C00	Tetrag.	4.1369±0.0006	4.1034±0.0007	90.000	70.23
C04	Tetrag.	4.1339±0.0004	4.1005±0.0005	90.000	70.07
C08	Tetrag.	4.1308±0.0005	4.0993±0.0006	90.000	69.95
C09	Tetrag.	4.1283±0.0004	4.0981±0.0004	90.000	69.84
C10	Tetrag.	4.1300±0.0007	4.1010±0.0008	90.000	69.95
C11	Tetrag.	4.1291±0.0008	4.1002±0.0011	90.000	69.91
X01	Rhomb.	4.1298±0.0004	4.1298±0.0004	89.800	70.43
X02	Tetrag.	4.1275±0.0006	4.0961±0.0007	90.000	69.78
X03	Tetrag.	4.1315±0.0005	4.0994±0.0006	90.000	69.97
A01	Tetrag.	4.1339±0.0007	4.1006±0.0008	90.000	70.08
A02	Tetrag.	4.1336±0.0006	4.0995±0.0008	90.000	70.05

The lattice constants of the unit cells are needed to calculate the theoretical densities of the synthesized ceramic materials. Here indexing program Dicvol was applied to identify both the edge lengths (a, b, c) and the angles (α, β, γ) of the perovskite unit cells for all the relevant compositions, as displayed in Table A.1. According to Section 4.3, it is known that all the compositions should be assigned to the A_T or the A_O phase except composition X01 which should have a rhombohedral symmetry and show FE features. The A_T and the A_O have tetragonal perovskite unit cell if their supercell structures are temporarily not considered. Thus, all these compositions were indexed to tetragonal systems. As for the rhombohedral composition X01, program Dicvol regarded it as a hexagonal system when searching for solutions, and Table A.1 gives the converted results from the hexagonal index back to the rhombohedral one. At the same time, the volume of the perovskite unit cell is calculated for each composition by the program. Based on the cell volume and the corresponding chemical formula, the theoretical density of each composition can be calculated. Relevant density values will be given in Section A.4.

A.3. Microstructures

Thermal etching

Thermal etching treatment is commonly needed for the ceramic samples in SEM studies. After being properly polished, the ceramic pellet can be annealed at a high temperature, which is normally several hundred degrees lower than its sintering temperature. Ideally, the grain boundaries can be etched by this means and manifest themselves in a micrograph because they usually have different resistance to the high temperature compared to grains. However, suitable and effective parameters for such a thermal etching treatment vary depending on the materials. For Pb-containing samples, one should take the Pb evaporation into account and carefully control the etching temperature and the atmosphere in the oven. The attempts of doing thermal etching in this work were not really successful. Figure A.8 shows two examples of unsatisfactory SEM images which were taken on composition C09. Both surfaces were etched at 900°C for ca. 10 min surrounded by pure PZ packing powder. Figure A.8(a) belongs to an insufficiently etched state without clear contrast on the grain boundaries, whereas Figure A.8(b) gives a good example of over-etching in which the grain boundaries seem to have severely melted. Such a large discrepancy of the quality of thermal etching between these two cases might be attributed to many factors, including the temperature gradient inside the crucible, the usage history/condition of the packing powder, or the distance between the imaging region and the packing powder. In this work, the main purpose of SEM experiments is to extract the grain size distributions of the sintered ceramic samples. Therefore, not much effort was made to figure out the best etching parameters.

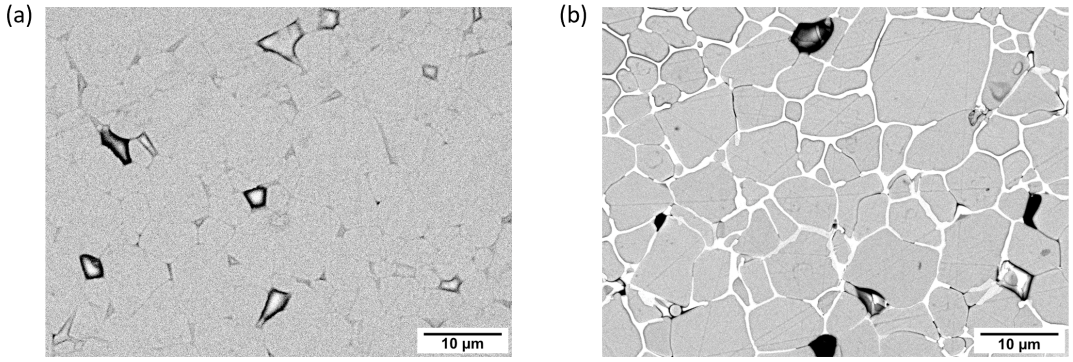

Figure A.8.: Two examples of SEM images taken on composition C09 after thermal etching at 900°C. (a) An insufficiently etched sample; (b) an over-etched sample.

Statistics of grain size by using software ImageJ

Software ImageJ was used to recognize the grains and their dimensions in the SEM images. Figure A.9 shows an example of an etched C09 sample, basically following three steps:

(1) An SEM image showing sufficient contrast between grains and grain boundaries is needed. The contrast can be obtained by thermal etching or by adjusting the accelerating voltage of SEM. Figure A.9(a) gives an example of composition C09 after thermal etching at 900°C.
(2) The grain boundaries can be counterdrawn onto a piece of transparent paper with a black marker. The pores or pull-outs, and the incomplete grains located at the edges of the image should be painted in black (by marker or subsequently by software). Note that the scale bar should be counterdrawn as well. See Figure A.9(b).
(3) Run software ImageJ and all grains can be recognized, as shown in Figure A.9(c). The dimensions of the recognized grains can be exported. For each composition, several images of different regions should be chosen for the grain recognition and analysis in order to have better statistics.

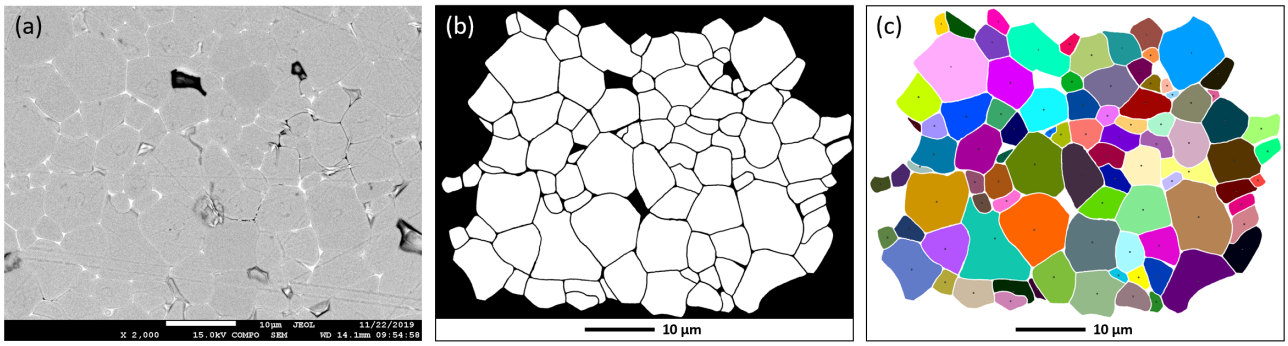

Figure A.9.: Three steps to recognize grains in an SEM image (using an etched C09 sample as example).

A.4. Appearance and densification of as-sintered ceramics

The as-sintered ceramic pellets possess different colors, as shown in the photograph in Figure A.10.

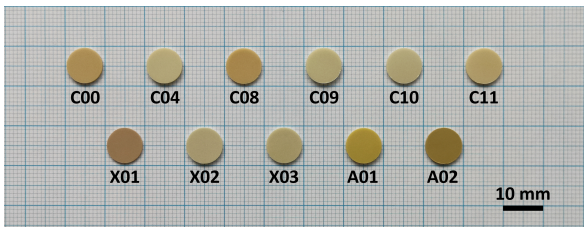

Figure A.10.: Photograph of as-sintered ceramic pellets. The sample surfaces are not ground.

The densities of the synthesized bulk ceramics were measured with Archimedes' method. The measurements were carried out by Dr. Lovro Fulanović. The densities can be calculated by

$$\rho_{\text{abs}} = \frac{m_{\text{air}} \cdot (\rho_{\text{water}} - \rho_{\text{air}})}{0.99983 \cdot (m_{\text{air}} - m_{\text{water}})} + \rho_{\text{air}}, \tag{A.1}$$

in which m_{air} and m_{water} denote the masses of the ceramic pellet measured in air and water, respectively. ρ_{air} and ρ_{water} are the densities of air and water, respectively. Note that these density values are temperature dependent. Here we take $\rho_{\text{air}} = 0.0012$ g/cm^3 and $\rho_{\text{water}} = 0.997608$ g/cm^3 for 22.7°C. With the absolute densities measured here and the theoretical densities obtained based on the XRD data, the relative densities of the sintered ceramics can be calculated, as listed in Table A.2. Besides, the radial shrinkages of the pellets after sintering are also given here. It can be noticed that compositions X02 and A02 have the smallest shrinkages, which is consistent with the fact that they have the lowest relative densities in the list.

Table A.2.: Densification of all C-, X-, and A-series samples.

Composition	Radial shrinkage (%)	Density		
		Absolute (g/cm^3)	Theoretical (g/cm^3)	Relative (%)
C00	10.98	8.035	8.269	97.17
C04	10.83	8.043	8.221	97.84
C08	10.74	7.991	8.168	97.83
C09	10.53	7.901	8.164	96.77
C10	10.98	7.950	8.134	97.73
C11	10.21	7.856	8.122	96.72
X01	10.42	7.691	8.177	94.07
X02	8.78	7.532	8.212	91.72
X03	10.42	7.705	8.169	94.31
A01	10.84	7.945	8.275	96.00
A02	8.61	7.521	8.267	90.97

B. Extended results of electrical conductivity

B.1. Supplementary sample information

Table B.1.: Supplementary details for the samples used in Figure 5.11.

Composition	Method	Thickness [mm]	Voltage [V]	Electric field [kV/mm]
C00	dynamic	0.150	5	0.0333
C00	static	0.141	5	0.0355
C09	dynamic	0.140	5	0.0357
C09	static	0.149	5	0.0336
C11	dynamic	0.146	5	0.0342
C11	static	0.146	5	0.0342
X01	dynamic	0.140	0.1	0.000714
X01	static	0.141	1	0.00709
X02	dynamic	0.132	5	0.0379
X02	static	0.150	5	0.0333
A01	dynamic	0.139	5	0.0360
A01	static	0.144	5	0.0347
A02	dynamic	0.145	0.5	0.00345
A02	static	0.146	1	0.00685

B.2. Resistance-degradation-like behaviors under thermal cycling conditions by dynamic dc conductivity measurement

The following issues have been noticed in Chapter 5:

(1) In the electric-field- and temperature-dependent dc conductivity study in Section 5.1.1, it can be seen that for most of the PLZST-related ceramics used in this work the conductivity drops at $\geqslant$300°C when higher voltages are applied (see Figures 5.1(b), 5.3(a, b), 5.4(b), and 5.5(a, b)).
(2) In the dynamic conductivity measurements in Section 5.2, the situation can be always observed that within a single thermal cycle the cooling-down curve does not coincide with the heating-up curve, especially in the higher-temperature region of the Arrhenius plot, which leads to non-negligible uncertainties in the determination of the activation energies (see Figures 5.9(a) and 5.11). Besides, the heating-up and the cooling-down segments could be neither a strictly straight line nor a broken line made up of several straight parts. Rather, both segments seem to be curved.
(3) Throughout the studies with the dynamic method, it has been found that the conductivity–temperature relation sometimes varies if a second cycle is performed with the same condition as the previous one. In other words, the result of such experiments would depend on the history of the sample.
(4) During both the static and the dynamic measurements, clear electric-field dependence of the conductivity has been observed. This implies the importance of selecting appropriate voltages for such conductivity studies.

All these phenomena indicate a certain slow evolution of such materials under electric fields and at elevated temperatures, very likely related to the migration and redistribution of the charged point defects, just like the resistance degradation [134, 140, 141]. Therefore, it is necessary to investigate this issue in more detail. As the phenomena possess great complexity and it is difficult to reach a clear conclusion at the end, this part is given here only as an appendix.

Experimental details

As shown in Figure B.1, the experimental strategy of this part is to extend the dwelling time at the maximum temperature (always 400°C) and to do more thermal cycles. The ramping rate of temperature is still set as 2.5°C/min, and the dwelling time at 400°C is 60 min in order to monitor more potential changes in the stage of the maximum temperature. For studying the electric-field-dependence of such

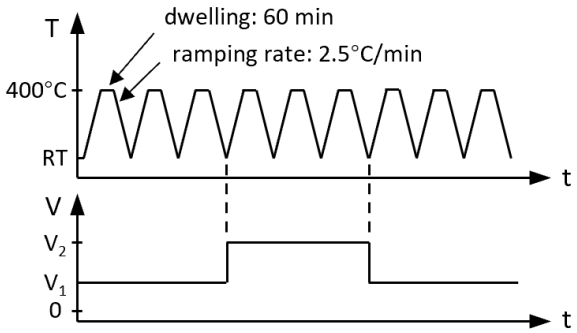

Figure B.1.: Schematic measuring procedures for the dynamic dc method with multiple thermal cycles.

measurements, the applied dc voltage is not constant. In practical experiments, the cycling numbers for different voltage steps can be flexibly decided depending on the real progress of the variations in the Arrhenius relations, and the dc voltage sequence can also be adjusted according to the conductivity of individual sample. Since all the samples involved here have similar thicknesses (0.13–0.15 mm), we usually controlled the voltages rather than electric fields just for convenience. All pellets have always been annealed at temperatures higher than T_C before their first thermal cycles with the lowest voltages.

Detailed results on compositions C09 and X01

Figure B.2 displays a complete process of such conductivity measurement under multiple thermal cycling carried out on a normal C09 sample. Following the style shown in Figure 5.8, the heating-up, cooling-down, and dwelling segments of the Arrhenius relations of all cycles are plotted separately. For this sample, the measuring sequence is: 4 cycles with 0.1 V (in red) → 8 cycles with 5.0 V (in black) → 7 cycles again with 0.1 V (in yellow). In Figure B.2(c), the changes of the conductivity during the dwelling times at 400°C are plotted in such a way that the cycles within the same voltage step can be directly compared by using a relative time axis but the ones belonging to different voltage steps can be clearly separated. Although the dwelling time of each cycle at 400°C is 60 min, only the last 55 min, where the sample temperature becomes sufficiently stable, are plotted here. Within each voltage step, the black arrows in the conductivity–time plots are used to indicate the sequence or tendency how the conductivity at 400°C develops when the temperature condition is doing continuously cycling. At the beginning, when the lower voltage 0.1 V is used, all the lines for both heating-up and cooling-down are slightly curved at the temperatures >200°C. With the increase of cycling number, the conductivity shows minor decrease within the whole temperature range shown here. Once 5.0 V is applied, a stronger decreasing tendency of the conductivity occurs at all temperatures, so that significant downward shifts of the conductivity curves can be observed in all the three plots in Figure B.2. By comparing the 1st cycle with 0.1 V and the 8th cycle with 5.0 V in Figure B.2(c), a remarkable drop of the conductivity at 400°C by about one order of magnitude can be noticed. Particular attention should be paid to the 1st cycle with 5.0 V in Figure B.2(a) where an obvious drop on the slope of the heating-up curve can be found at ca. 300–350°C, which may provide an important evidence for determining the possible

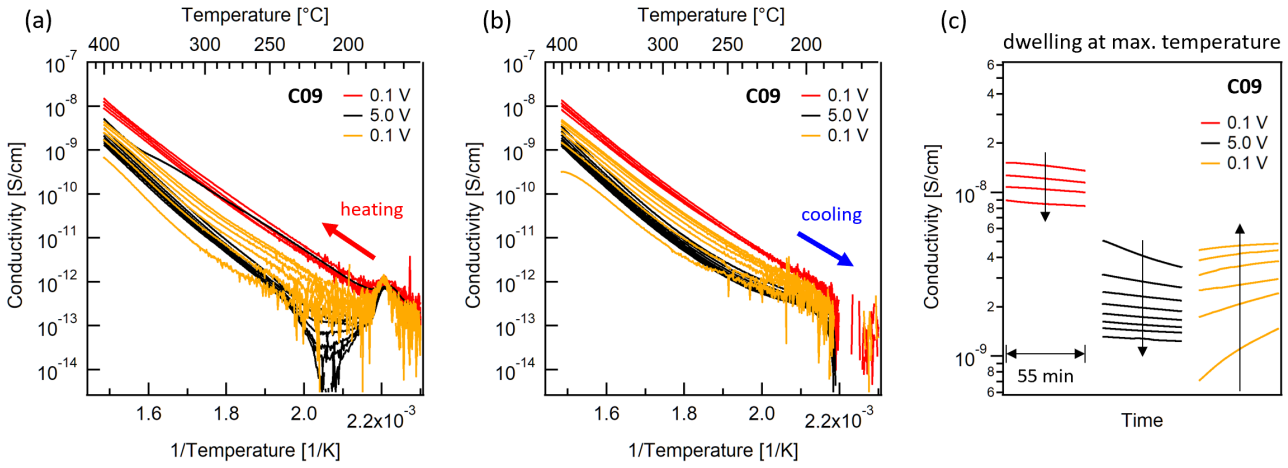

Figure B.2.: Evolution of the Arrhenius relations of a C09 sample during multiple thermal cycling. (a) The heating-up, (b) the cooling-down, and (c) the dwelling segments are separately plotted.

conduction behaviors within such materials. After the 8 cycles with 5.0 V, the voltage is switched back to 0.1 V. It should be noted that the 1st cycle of the second round with 0.1 V is not included in Figure B.2(a, c) because of the discharging-induced negative currents. Within the temperature range displayed here, the conductivity curves start shifting upward back. It reveals that the decrease of conductivity under 5.0 V could be a (partly) reversible process. Moreover, the slopes of the heating-up and the cooling-down curves also exhibit interesting variations. It can be seen that most of the black curves in the two Arrhenius plots always have larger slopes than the red and yellow ones, which indicates larger activation energies caused by higher applied dc bias.

Besides the above-mentioned composition C09, similar studies have been performed on composition X01, as displayed in Figure B.3. The measuring sequence is: 4 cycles with 0.01 V (in light red) $\rightarrow$ 4 cycles with 0.1 V (in medium red) $\rightarrow$ 4 cycles with 0.5 V (in dark red) $\rightarrow$ 8 cycles with 2.5 V (in black) $\rightarrow$ 4 cycles again with 0.1 V (in yellow). Considering that the X01 sample is generally much more conductive than composition C09, the stepwise increasing voltages utilized here are smaller than the previous cases and more voltage steps are included. It can be seen that the situation of composition X01 is strongly different from that of the C09 sample. One of the most obvious differences is the opposite voltage-dependence of the measured conductivity within the whole temperature range. This can be easily noticed for example in Figure B.3(c) where the highest conductivity curve (with 2.5 V, in black) is nearly one order of magnitude higher than the lowest one (with 0.1 V, in medium red). Apart from the magnitude of conductivity, the shapes of the Arrhenius plots are also impressively different from those of composition C09, as shown in Figure B.3(a, b). Firstly, the heating-up and cooling-down curves belonging to the same cycle do not coincide with each other, which can be observed in all the five voltage steps. This will cause difficulty of determining activation energies even at 400°C. Secondly, the 1st heating-up segment of each voltage step usually shows strong difference compared to the subsequent ones. The most evident example takes place when the maximum voltage 2.5 V is applied (see the uppermost black curve in Figure B.3(a)). Thirdly, all the heating-up curves in Figure B.3(a) are generally concave at the temperatures >200°C, which seems to be different from the special temperature range of the C09 sample in Figure B.2(a) where a smaller slope of the conductivity curves can be identified.

Regarding the discrepancy of the conductivity–temperature relation between the C09 and the X01

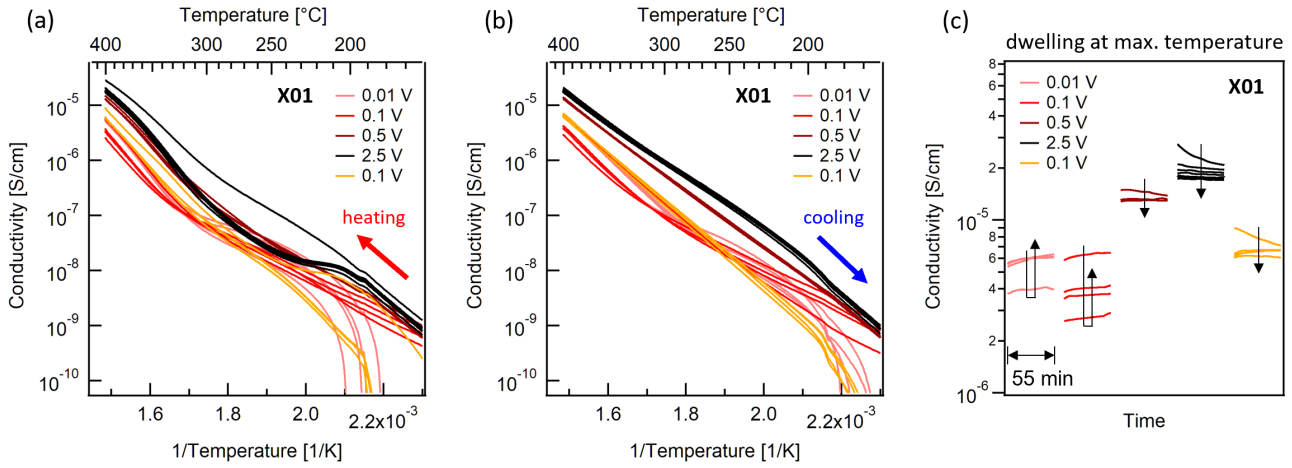

Figure B.3.: Evolution of the Arrhenius relations of an X01 sample during multiple thermal cycling. (a) The heating-up, (b) the cooling-down, and (c) the dwelling segments are separately plotted.

samples during heating-up, only short discussion is given here. It is easy to see that the downward shift of composition C09 takes place at the temperatures $\gtrsim$300°C, whereas for composition X01 the obvious concavity can be already observed from ∼200°C on. In general, V''_{Pb} and $V^{\cdot\cdot}_{O}$ are the two most commonly discussed ionic point defects in PZT material systems. $V^{\cdot\cdot}_{O}$ is usually considered to be sufficiently mobile at temperatures >200°C in perovskite oxides (adopted from STO), whose migration and redistribution within the bulk material are regarded as the origin of the resistance degradation [140, 141, 281, 283]. In the nominally undoped PZST composition X01, a certain concentration of $V^{\cdot\cdot}_{O}$ are expected to exist although the material is generally assigned to a p-type conduction, which stems from the excess V''_{Pb} over $V^{\cdot\cdot}_{O}$ (analogous to the situation of undoped PZT [45]). It is reasonable to speculate that the concavity of the Arrhenius plots of the X01 sample might be caused by the movement of $V^{\cdot\cdot}_{O}$. Different from $V^{\cdot\cdot}_{O}$, the mobility of V''_{Pb} has been rarely mentioned in the literature. Rather, the discussions about V''_{Pb} always focused on the p-type conduction where p is compensated by the V''_{Pb} [288–290]. Nevertheless, it is still difficult to rigorously exclude that V''_{Pb} can become somewhat mobile at elevated temperatures and under electric fields. The migration or conduction of V''_{Pb} has been sometimes reported, for example in Ref. [291] (at 500°C) and Ref. [292] (>300°C). Since the downward conductivity shift of composition C09 takes place at temperatures $\gtrsim$300°C and is electric-field-dependent, it is worth a consideration about the possible role of V''_{Pb} in the conduction behaviors of such materials.

Apart from the possible contributions of the mobile vacancies in the bulk material, we may also take grain-boundary-related effects into consideration because all samples involved in this work are polycrystalline ceramics. It is well known in polycrystalline materials that the grain boundaries could block the migration of various types of defects. When the positively charged $V^{\cdot\cdot}_{O}$ stay in a grain-boundary core, a downward band bending will be formed accompanied by two depletion regions. The whole grain boundary structure can therefore be regarded as an extra barrier for the mobile positive charge carriers (for example $h^{\cdot}$) in the system [293–295]. Analogously, the accumulation of the negatively charged V''_{Pb} in a grain-boundary core could result in a potential barrier for mobile e'. Applying this theory, some behaviors of compositions X01 and C09 could probably be described, particularly in the temperature ranges where their conductivities tend to decrease. However, this is just speculative and more investigations should be done in order to get a clear explanation.

Conductivities of different compositions measured in the dwelling stages at 400°C during the multiple thermal cycling

The dwelling segments at the maximum temperature of the thermal cycles are worth a detailed comparison. These conductivity measurements at 400°C can be regarded as a type of static dc tests that carry the information how the samples gradually approach the equilibrium with the atmosphere under the specific thermal and electrical conditions. As already shown in Figures B.2(c) and B.3(c), the Pb-containing dielectrics involved in this study experience very complex evolution of the conductivities. It can be seen that the conductivities are constantly varying with the increase of cycling number. More importantly, clear electric-field dependence of the conductivities has been noticed. Similar conductivity experiments under multiple thermal cycling conditions have been carried out with different voltage steps for selected compositions of C- and X-series. Based on abundant data, the comparisons of such dwelling segments are performed here. The rest of the measurements (the heating-up and cooling-down segments) on all the relevant samples will be given in Figures B.8–B.13 at the end of the current appendix.

Figure B.4 deals with the C-series, and a PIC 151 sample is appended here as a reference. It should be noted that the conductivity scale of the PIC 151 sample is different from those of the C-series PLZST samples. The comparison should concern the following two aspects:

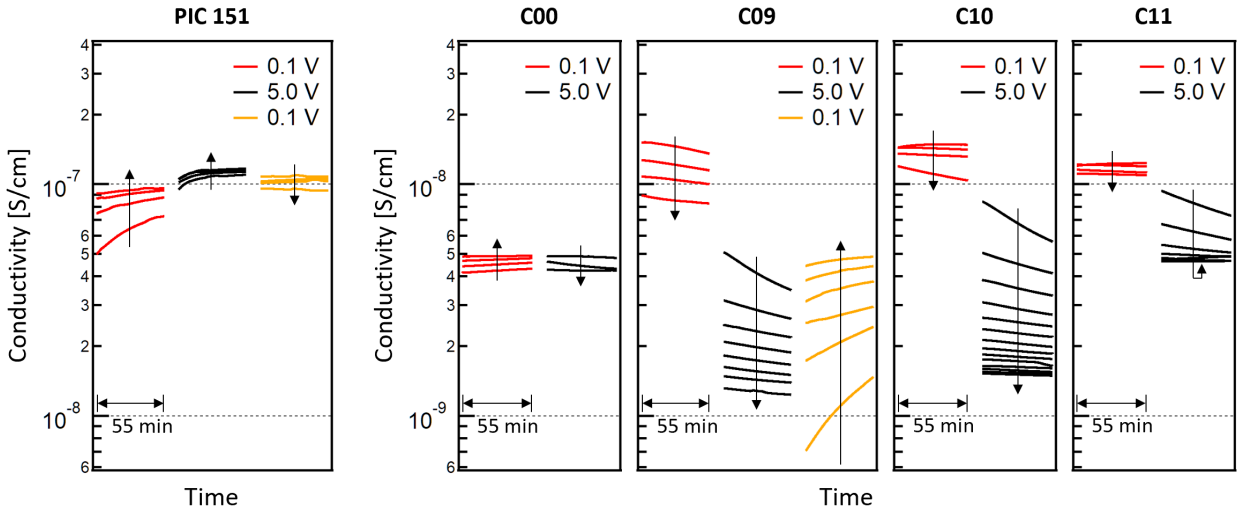

Figure B.4.: Conductivities of selected C-series compositions measured at the dwelling segments at 400°C throughout the multiple thermal cycling. A PIC 151 sample is appended as a reference.

(1) The dependence of conductivity on the applied voltage or field by comparing the general conductivity ranges among different voltage steps. It is easy to see that compositions C09–C11 should belong to one group where the conductivity generally decreases with the increase of applied field. Composition C00 could be basically assigned to the same group as the other three C-series samples, but its conductivity range is only weakly influenced by the voltage. In contrast to the C-series, the conductivity of the PIC 151 sample exhibits a slightly rising tendency with the voltage.

(2) The magnitude and direction of the conductivity variation by comparing the dwelling curves within the same voltage step. It can be observed that the samples of C09–C11 manifest significant downward conductivity variations, especially when the higher voltage (5.0 V) is applied. By contrast, the variation within each voltage step of the C00 and PIC 151 samples is less pronounced. The PIC 151 sample has always upward conductivity variations for the steps of 0.1 V (the 1st one in red) and 5.0 V, while the C00 sample only shows upward variation within the step of 0.1 V. Additionally, it can be noticed that for the samples of PIC 151, C10, and C11 the conductivities measured in their last cycles of 5.0 V seem to reach or approach saturations.

Apparently, the most obvious characteristic of the C-series compositions is the impressive decreasing tendency of the conductivity when the electrical measurement is carried out with higher fields and at sufficiently high temperature, which has already been observed firstly in the data obtained by the static method (the top right corners of Figures 5.1(b) and 5.3(a, b)) and subsequently in the heating-up segments of the Arrhenius plots (Figure B.2(a)). Such feature would be related to the V''_{Pb} and $V^{\cdot\cdot}_{O}$, which are considered to exist widely in these La-doped PZST materials. The fact that composition C00 possesses much milder voltage-dependence might be attributed to either technical issues during high-temperature sintering or the influence of the Ti/Sn ratio. As for the PIC 151 sample in which no decreasing tendency for conductivity has been discovered, its co-doping (Ni^{2+} as acceptor and Sb^{5+} as donor) might play important roles in effectively controlling $[V''_{Pb}]$.

Based on the comparison in Figure B.4, it can be noticed that at a given temperature the measured electrical conductivity would vary non-negligibly with the applied field and with the measuring history of

the sample. Therefore, a comprehensive study like what is being presented here seems to be necessary for the samples whose defect chemistry is not very clear yet. Furthermore, using electric fields as low as possible is recommended in the measurements involving elevated temperatures even for highly resistive materials. Here we can adopt the conductivities acquired at 400°C with 0.1 V (the red curves) in Figure B.4 for a simplified comparison of these C-series samples. It can be concluded that compositions C09–C11 exhibit similar conductivities at 400°C and composition C00 has the lowest.

Figure B.5 displays the comparison among X-series samples. The C09 sample is also added. All these four compositions constitute a complete series having the same B-site ratio but varying La content on the A-site. It should be noted that the conductivity scale of the X01 sample is different from the others because it has the highest conductivities. Obviously, compositions X02 and X03 show similar characteristic compared to C09–C11 in terms of the voltage-dependence of the measured conductivity. The speculated vacancies-related effect already occurs when only 1% La is added to the PZST materials. By contrast, the X01 behaves in a totally different way. Moreover, it is clear that the conductivity (simply adopted from the levels of 0.1 V in medium red) increases with the decrease of La content.

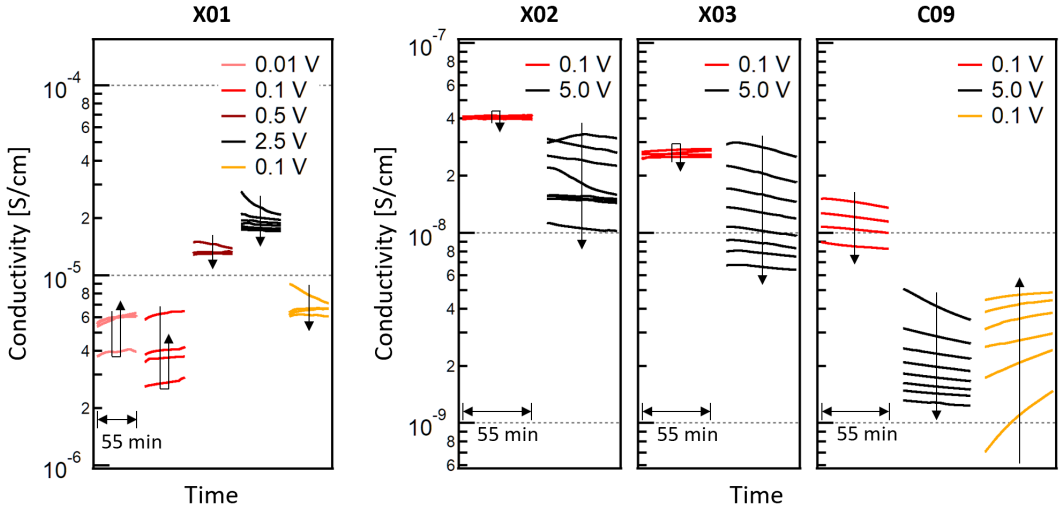

Figure B.5.: Conductivities of X-series compositions measured at the dwelling segments at 400°C throughout the multiple thermal cycling. A C09 sample is appended for comparison.

Determination of activation energies

Based on the multiple thermal cycles of different compositions involved in Figures B.2, B.3, B.8–B.13, we plot the activation energies of these samples throughout their respective experimental steps (versus the cycling numbers) in Figures B.6 and B.7. In order to avoid the impact of the capacitive currents near the T_C, the activation energies only at 300°C and 400°C are included (for composition X01 only at 400°C). The applied voltages throughout the cycling are labeled for each sample. It should be noted that for composition C09 the 1st cycle of the second round of 0.1 V does not appear in these figures due to the negative discharging current.

Figure B.6 compares the selected C-series compositions, and the data of PIC 151 are attached as a reference. It can be seen that the activation energies determined during heating-up and cooling-down are not always consistent. For instance, severe discrepancy can be found in compositions C09–C11 at

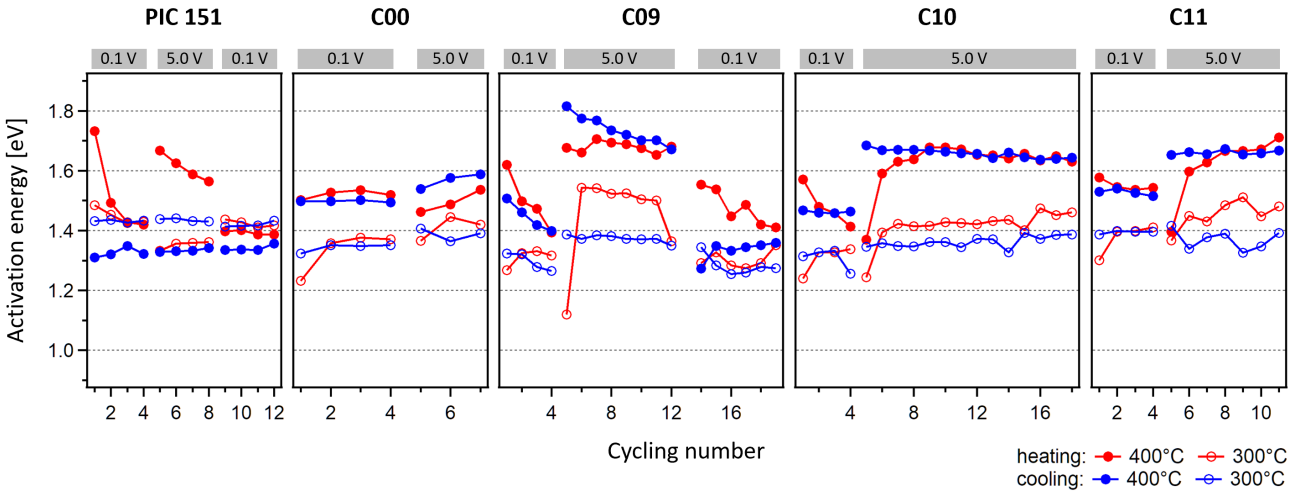

Figure B.6.: Activation energies extracted from the Arrhenius plots of selected C-series compositions throughout the multiple thermal cycling. A PIC 151 sample is appended as a reference.

300°C when 5.0 V is utilized. If such phenomenon is caused just technically by the capacitive signals, one could simply estimate the possible range of the activation energy (taking the range between the two numbers) instead of trying to get a specific value. Another case where the heating-up and the cooling-down data points might show large deviation is the very early cycles within a voltage step, for example the earlier data points measured with 5.0 V in the samples of C09–C11. This indicates a clear instability of the sample, namely a status with inadequate equilibrium with the atmosphere under the thermal and electrical conditions. In the circumstances, one should be cautious about directly using the activation energy values. Nevertheless, there are also occasions where the activation energies extracted from the heating-up and the cooling-down stages exhibit sufficiently small differences, for example at 400°C in the last few cycles of compositions C09–C11 when 5.0 V is applied, and at both 300°C and 400°C during the cycles using lower voltages (the first round of 0.1 V) for most samples. In these cases, the materials are stable and the obtained activation energies are worth further analyzing. In addition to the difference between heating-up and cooling-down, it is also obvious that the activation energies again show some dependences on the applied voltage (field). This is most pronounced for samples C09–C11, in which the activation energies during the cycles with 5.0 V possess a significant upward shift compared to the ones with 0.1 V. This effect occurs in the PLZST compositions accompanied by the specific decreasing tendency of conductivity at temperatures $\gtrsim$300°C during the long-term thermal cycling. Besides, such increase of the activation energy with applied voltage is reversible when the voltage is switched back to the lower level (see the second round of 0.1 V of the C09 sample).

Figure B.7 compares the X-series samples, and the data of composition C09 are again included. In general, the X02 and X03 samples are similar to C09–C11 but show more complexity. It can be seen that the differences between the heating-up and cooling-down stages in compositions X02 and X03 are somehow more obvious than those in compositions C09–C11, which indicates that a bit stronger changes are taking place in these two X-series samples under the same cycling conditions. Particularly, the data points of composition X02 show larger fluctuation than the others, which are correlated with the observation in Figure B.5 that the dwelling curves acquired with 5.0 V experience an unstably downward variation. This reveals that the previously mentioned features, which very probably result from the 2% La-doping, might be attenuated or disturbed gradually by the reduction of the La content.

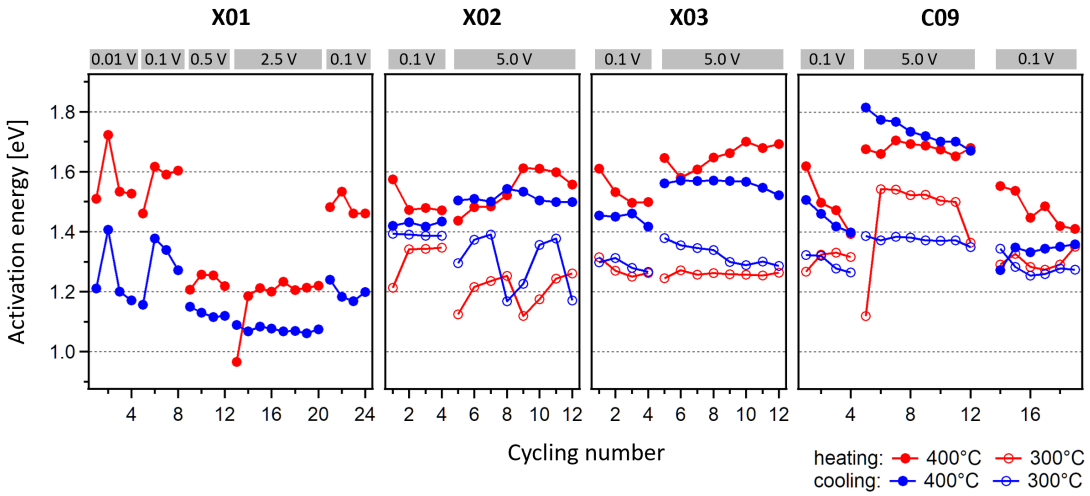

Figure B.7.: Activation energies extracted from the Arrhenius plots of X-series compositions throughout the multiple thermal cycling. A C09 sample is appended for comparison.

One of the factors that should be considered here is the change of $[V''_{Pb}]$ with the doping concentration. As for the X01 sample, the shape of Arrhenius plot varies heavily in the whole temperature range (see Figure B.3), which renders the quantification of activation energy at lower temperatures (e.g. 300°C) meaningless. Thus, only the activation energies at 400°C are given here. Even so, the X01 sample still exhibits evident differences between the heating-up and the cooling-down processes within every voltage step, which indicates that the sample is undergoing a continuous change throughout the cycling experiment. In addition, the X01 sample displays an opposite voltage-dependence of the activation energies compared to all the La-doped compositions, namely, higher applied voltages lead to lower activation energies.

With respect to the values of the activation energies, it can be found in Figure B.6 that for the C-series compositions the activation energy ranges generally between 1.3 eV and 1.7 eV (approximately taking the data points of the last few cycles within each voltage step). At 300°C, the values measured with 5.0 V stay around 1.4 eV, and the ones with 0.1 V are a little bit lower, roughly between 1.3 eV and 1.4 eV. At 400°C, the activation energies are always clearly higher than those at 300°C. The values measured with 5.0 V can even reach or approach 1.7 eV, while the ones with 0.1 V vary around 1.5 eV. As shown in Figure B.7, the ranges of the activation energies of compositions X02 and X03 with lower La content than 2% generally exhibit a downward offset compared to the 2% La composition C09. For composition X01, the lowest activation energies can be found at 400°C in the last few cycles with 2.5 V, where the heating-up branch saturates around 1.2 eV and the cooling-down branch gives a level slightly below 1.1 eV. The change of the determined activation energies due to the reduction of La concentration in the PLZST materials is actually expected because the La-doping can modify the balance of defect chemistry in the bulk materials by introducing extra electronic charges, different from the situation of the C-series compositions where the B-site modification is expected to do nothing about electronic charge carriers.

All the conductivity and activation energy data provided in this appendix can be regarded as an extension for the information presented in Figures 5.11–5.13. It is undeniable that these Pb-containing samples show great complexity in terms of defect chemistry and the dynamic dc method used in this work has limitations for studying their conduction mechanisms.

Evolution of the heating-up and cooling-down segments of the Arrhenius relations during the multiple thermal cycling for selected samples

PIC 151, thickness: 0.146 mm. Measuring sequence: 4 cycles with 0.1 V (in red) → 4 cycles with 5.0 V (in black) → 4 cycles again with 0.1 V (in yellow).

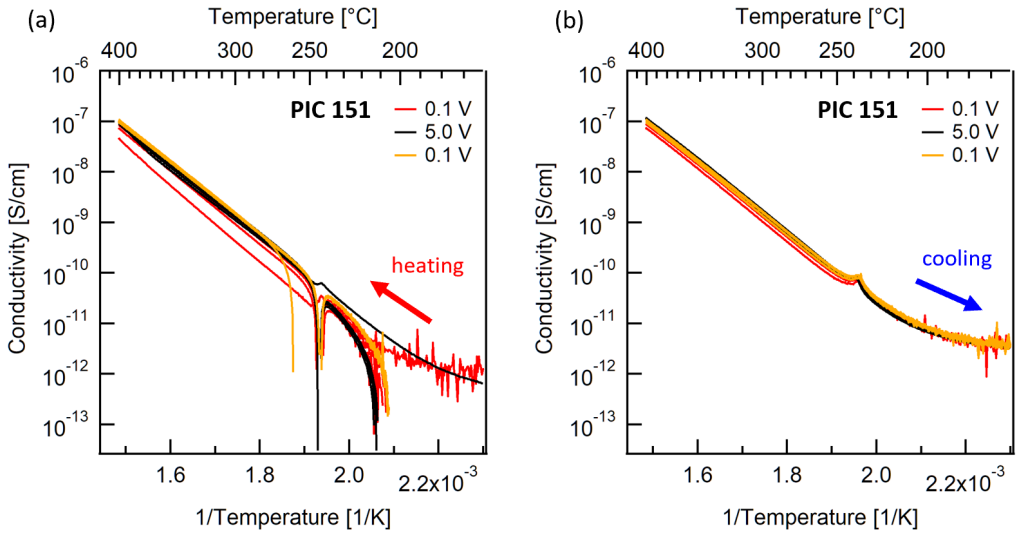

Figure B.8.: Evolution of the Arrhenius relations of a PIC 151 sample during multiple thermal cycling. The separately plotted (a) heating-up and (b) cooling-down segments.

Composition C00, thickness: 0.147 mm. Measuring sequence: 4 cycles with 0.1 V (in red) → 3 cycles with 5.0 V (in black).

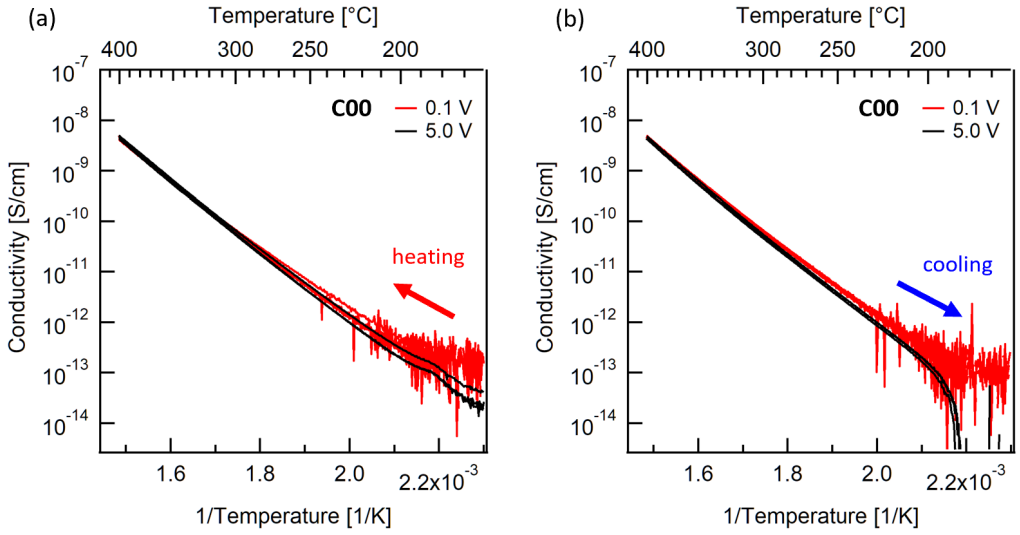

Figure B.9.: Evolution of the Arrhenius relations of composition C00 during multiple thermal cycling. The separately plotted (a) heating-up and (b) cooling-down segments.

Composition C10, thickness: 0.150 mm. Measuring sequence: 4 cycles with 0.1 V (in red) → 14 cycles with 5.0 V (in black).

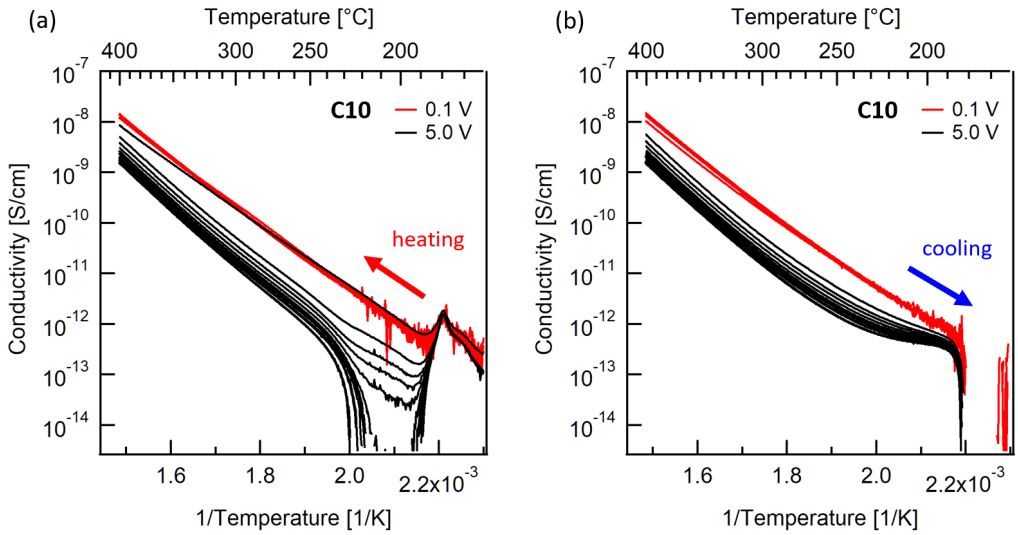

Figure B.10.: Evolution of the Arrhenius relations of composition C10 during multiple thermal cycling. The separately plotted (a) heating-up and (b) cooling-down segments.

Composition C11, thickness: 0.136 mm. Measuring sequence: 4 cycles with 0.1 V (in red) → 7 cycles with 5.0 V (in black).

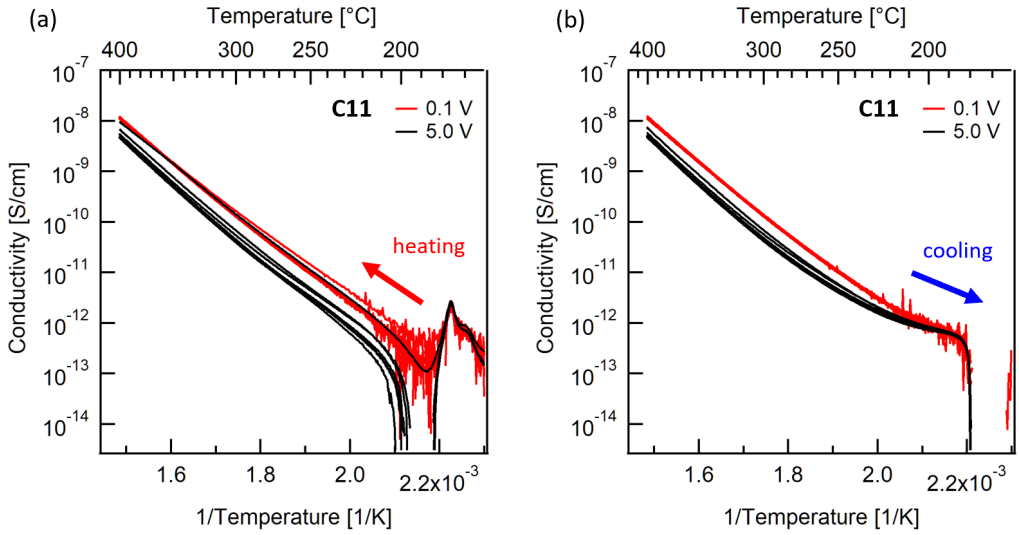

Figure B.11.: Evolution of the Arrhenius relations of composition C11 during multiple thermal cycling. The separately plotted (a) heating-up and (b) cooling-down segments.

Composition X02, thickness: 0.147 mm. Measuring sequence: 4 cycles with 0.1 V (in red) → 8 cycles with 5.0 V (in black).

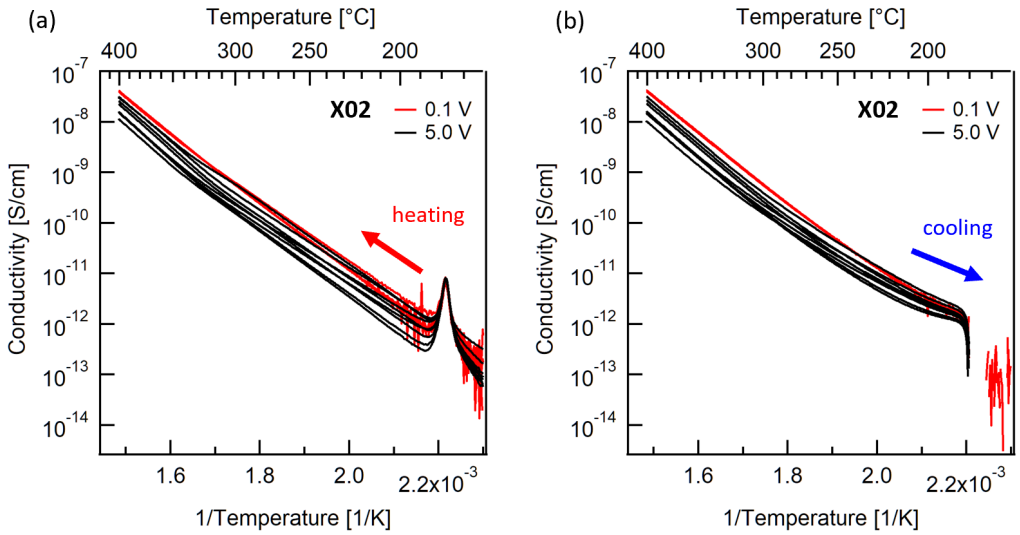

Figure B.12.: Evolution of the Arrhenius relations of composition X02 during multiple thermal cycling. The separately plotted (a) heating-up and (b) cooling-down segments.

Composition X03, thickness: 0.144 mm. Measuring sequence: 4 cycles with 0.1 V (in red) → 8 cycles with 5.0 V (in black).

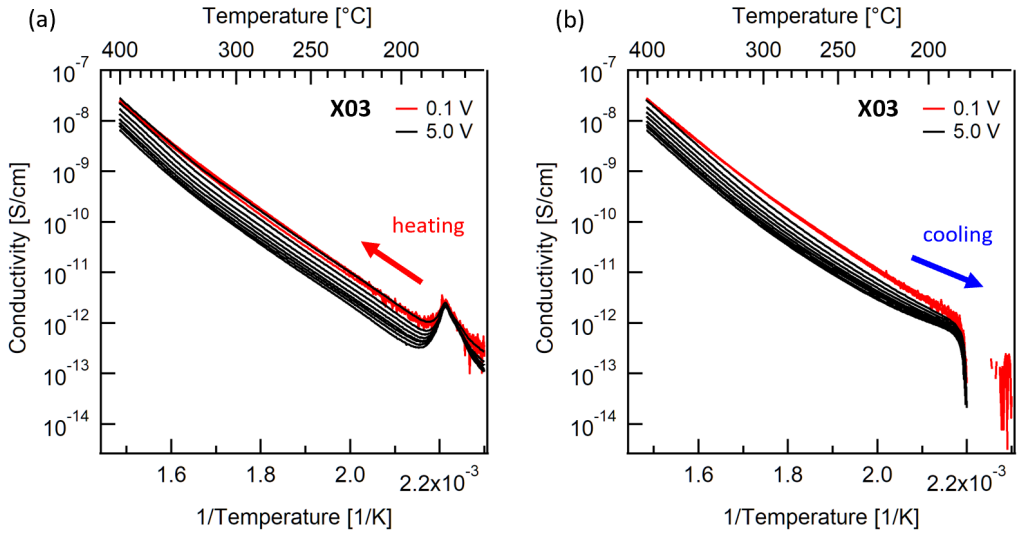

Figure B.13.: Evolution of the Arrhenius relations of composition X03 during multiple thermal cycling. The separately plotted (a) heating-up and (b) cooling-down segments.

C. Extended results of X-ray photoelectron spectroscopy

C.1. In situ X-ray photoelectron spectroscopy at interfaces with electrochemical oxidation and reduction

C.1.1. PLZSF A02 with RuO_2 anode

This PLZSF A02 ceramic sample was 0.20 mm thick, with a 5 nm thin RuO_2 top electrode (used as anode) and a thick Pt bottom electrode. The operating temperature of the solid electrolyte cell was 300°C. Figure C.1 gives the current and conductivity plots corresponding to stepwise increasing electric fields. Figure C.2 shows all XPS data measured at the anodic interface between RuO_2 and A02 ceramic throughout the whole experiment.

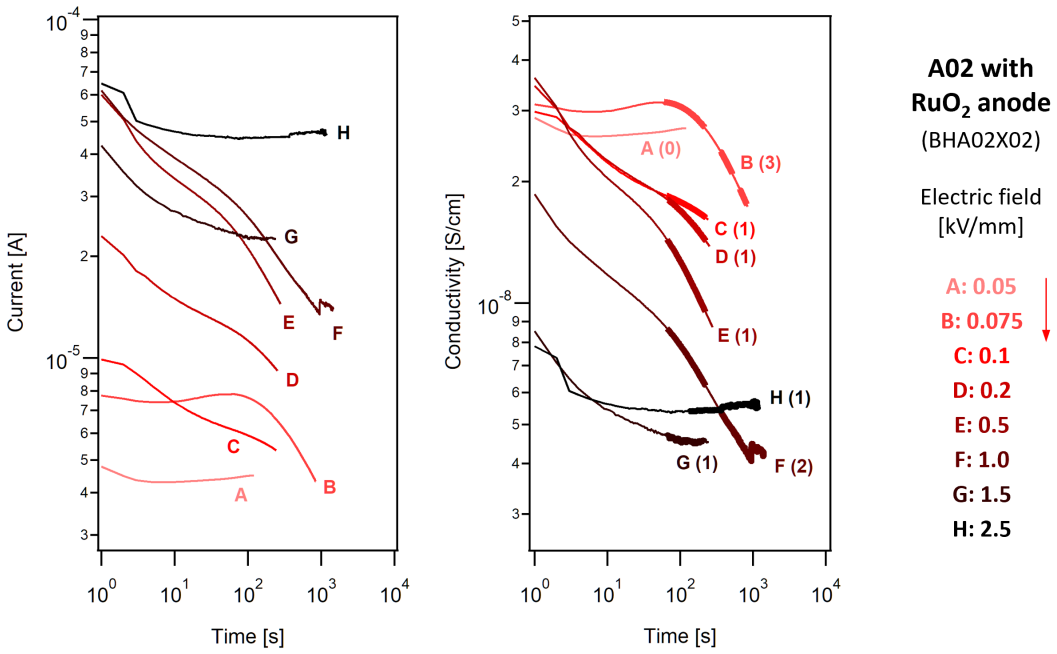

Figure C.1.: Measured currents and calculated conductivities at 300°C and at stepwise increasing applied electric fields for an A02 sample with RuO_2 anode (sample No. BHA02X02).

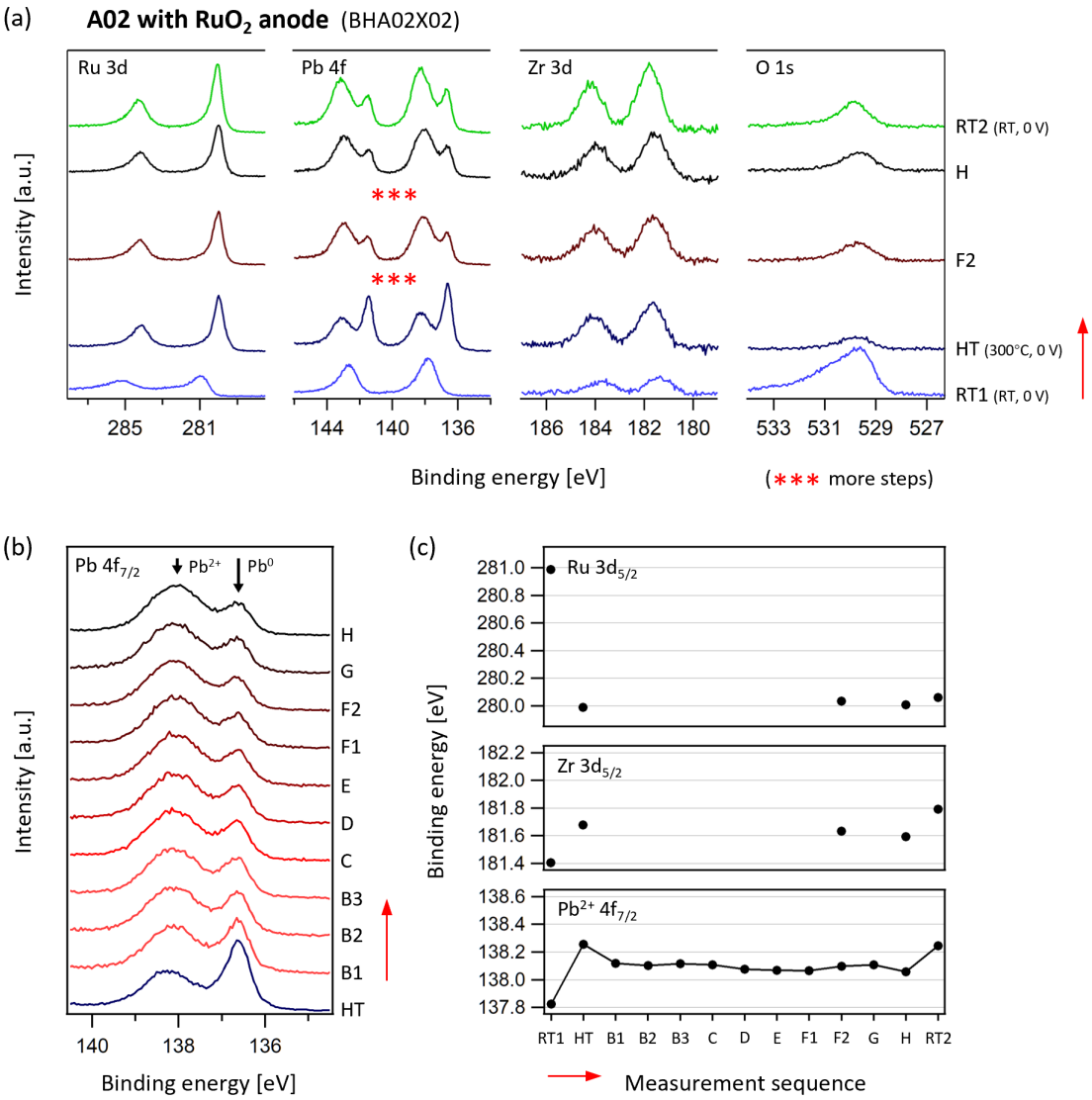

Figure C.2.: XP spectra recorded at the interface between A02 and RuO_2 anode during the application of stepwise increasing electric fields (sample No. BHA02X02). (a) Ru 3d, Pb 4f, Zr 3d, and O 1s core level spectra in several key steps. (b) Pb $4f_{7/2}$ spectra in detailed measurement sequence at 300°C. (c) Binding energies of Ru $3d_{5/2}$, Zr $3d_{5/2}$, and Pb^{2+} $4f_{7/2}$ extracted from all relevant spectra in (a) and (b). The red arrows indicate the sequence of measurements.

C.1.2. PLZSF A02 with ITO cathode

This PLZSF A02 ceramic sample was 0.25 mm thick, with a 4 nm thin ITO top electrode (deposited at 350°C, used as cathode) and a thick Pt bottom electrode. The operating temperature of the solid electrolyte cell was 300°C. Figure C.3 gives the current and conductivity plots corresponding to stepwise increasing electric fields. Figure C.4 shows all XPS data measured at the cathodic interface between ITO and A02 ceramic throughout the whole experiment.

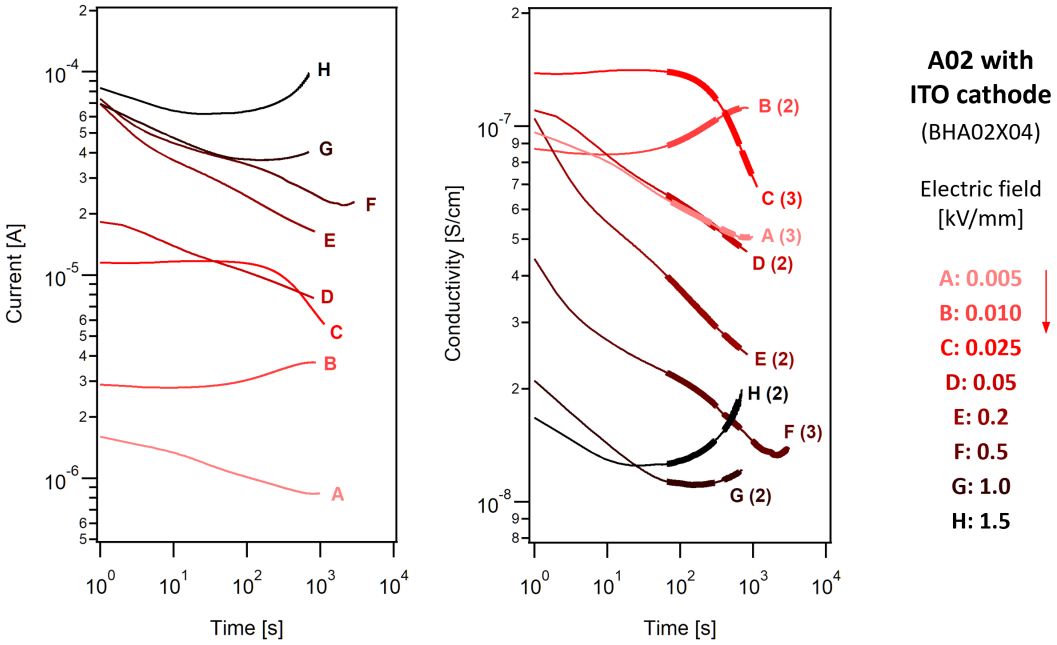

Figure C.3.: Measured currents and calculated conductivities at 300°C and at stepwise increasing applied electric fields for an A02 sample with ITO cathode (sample No. BHA02X04).

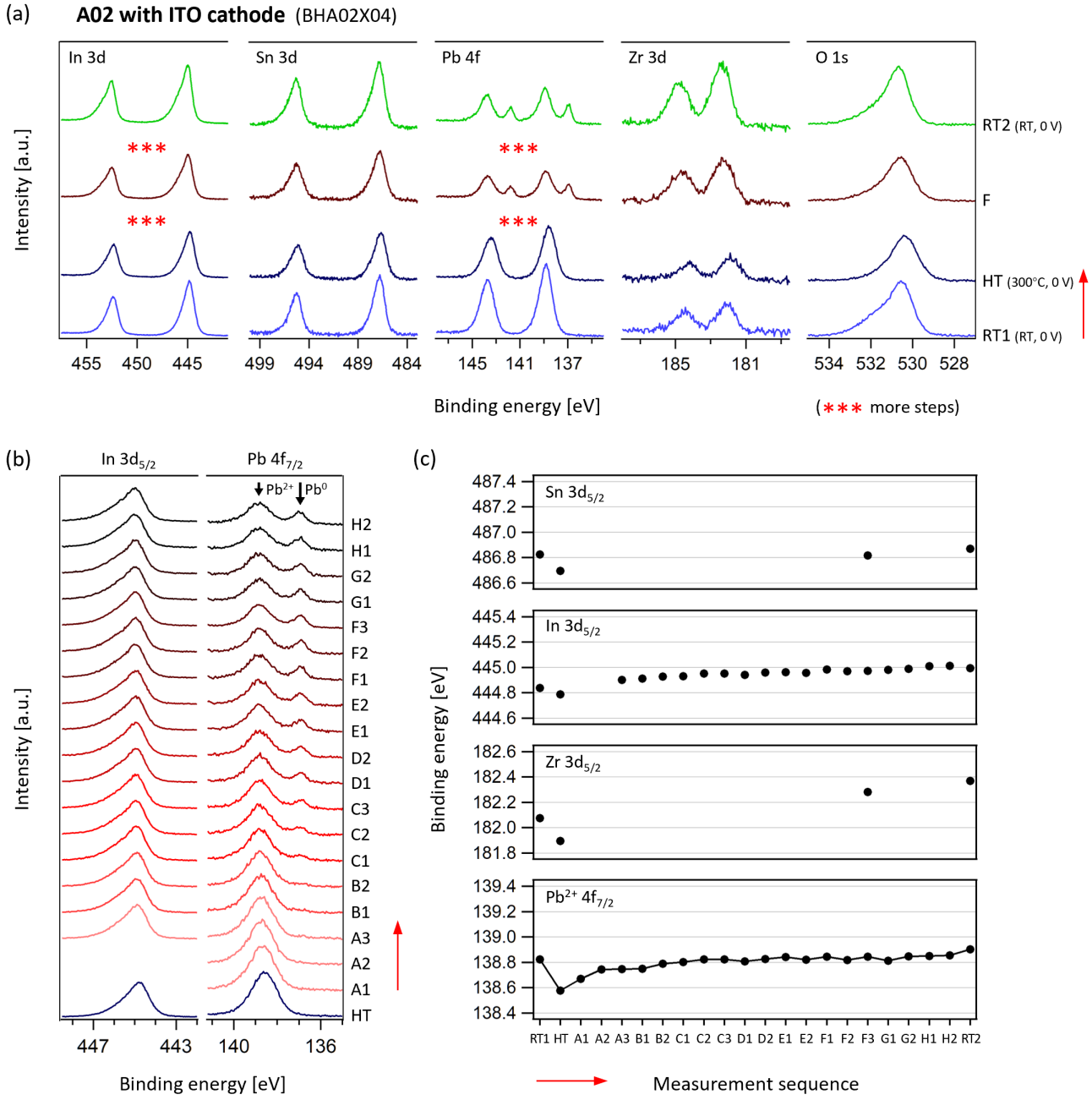

Figure C.4.: XP spectra recorded at the interface between A02 and ITO cathode during the application of stepwise increasing electric fields (sample No. BHA02X04). (a) In 3d, Sn 3d, Pb 4f, Zr 3d, and O 1s core level spectra in several key steps. (b) In $3d_{5/2}$ and Pb $4f_{7/2}$ spectra in detailed measurement sequence at 300°C. (c) Binding energies of Sn $3d_{5/2}$, In $3d_{5/2}$, Zr $3d_{5/2}$, and Pb^{2+} $4f_{7/2}$ extracted from all relevant spectra in (a) and (b). The red arrows indicate the sequence of measurements.

C.1.3. Undoped PZT53/47 with ITO cathode

This undoped PZT53/47 ceramic sample was 0.18 mm thick, with a 4 nm thin ITO top electrode (deposited at 400°C, used as cathode) and a thick Pt bottom electrode. The operating temperature of the solid electrolyte cell was 250°C. Figure C.5 gives the current and conductivity plots corresponding to stepwise increasing electric fields. Figure C.6 shows all XPS data measured at the cathodic interface between ITO and PZT53/47 ceramic throughout the whole experiment. The sample preparation and the subsequent in situ XPS measurements on this sample were finished together with Mr. Pengcheng Hu.

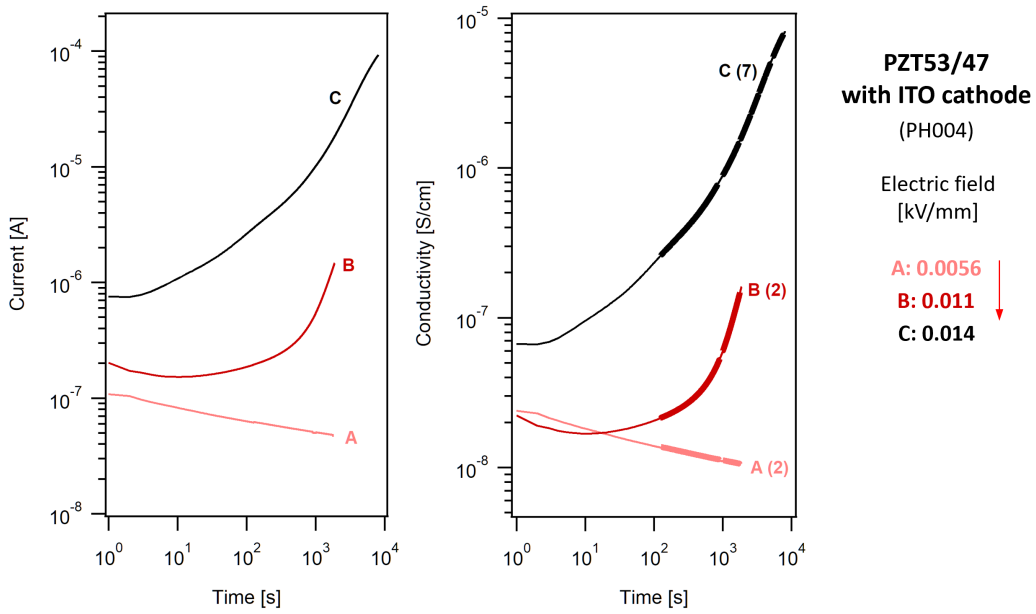

Figure C.5.: Measured currents and calculated conductivities at 250°C and at stepwise increasing applied electric fields for the undoped PZT53/47 sample with ITO cathode (sample No. PH004).

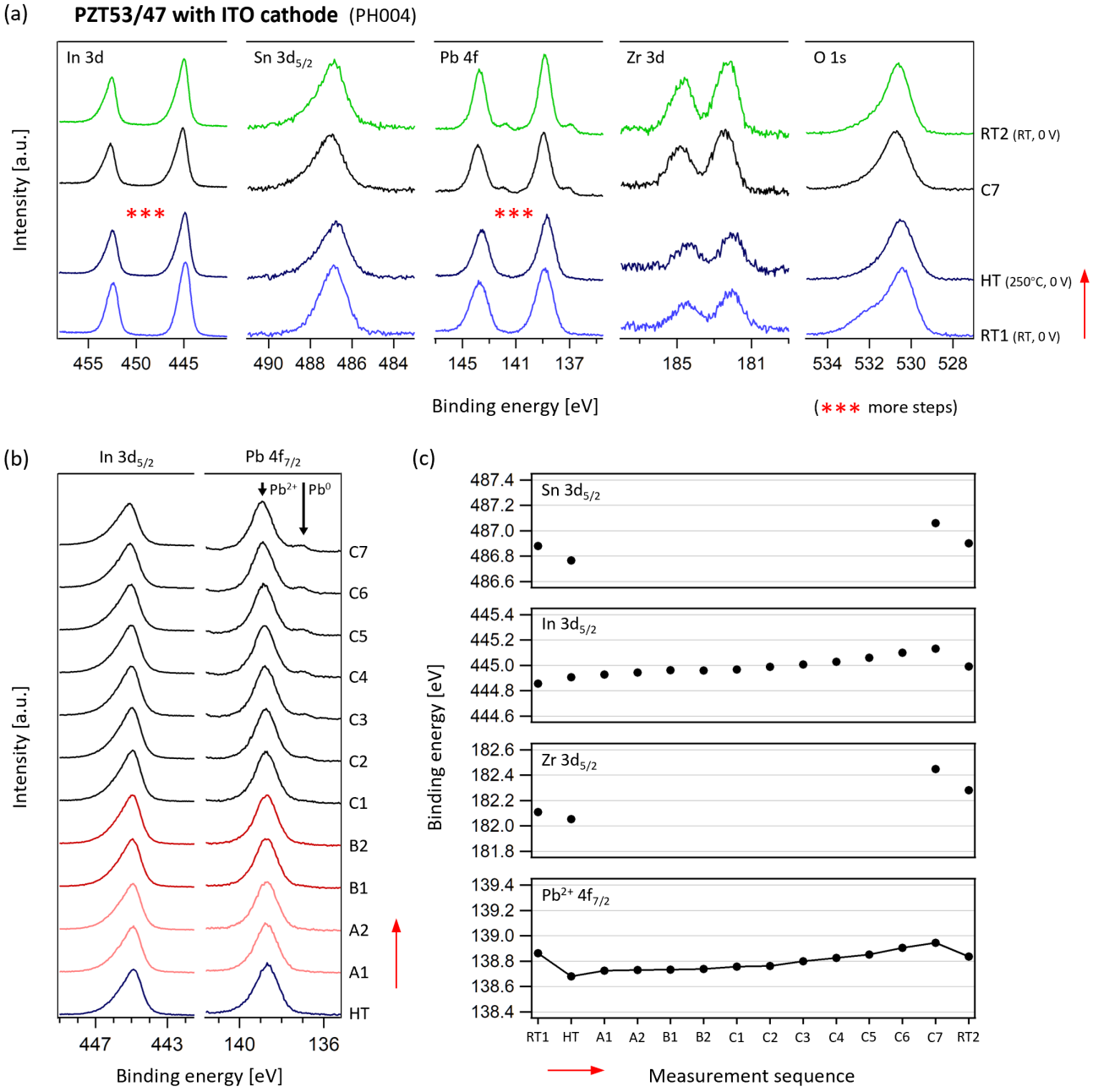

Figure C.6.: XP spectra recorded at the interface between undoped PZT53/47 and ITO cathode during the application of stepwise increasing electric fields (sample No. PH004). (a) In 3d, Sn 3d, Pb 4f, Zr 3d, and O 1s core level spectra in several key steps. (b) In $3d_{5/2}$ and Pb $4f_{7/2}$ spectra in detailed measurement sequence at 250°C. (c) Binding energies of Sn $3d_{5/2}$, In $3d_{5/2}$, Zr $3d_{5/2}$, and Pb^{2+} $4f_{7/2}$ extracted from all relevant spectra in (a) and (b). The red arrows indicate the sequence of measurements.

C.1.4. PIC 151 with ITO cathode at 300°C

This PIC 151 ceramic sample was 0.233 mm thick, with a 4 nm thin ITO top electrode (deposited at 350°C, used as cathode) and a thick Pt bottom electrode. The operating temperature of the solid electrolyte cell was 300°C. Figure C.7 gives the current and conductivity plots corresponding to stepwise increasing electric fields. Figure C.8 shows all XPS data measured at the cathodic interface between ITO and PIC 151 ceramic throughout the whole experiment.

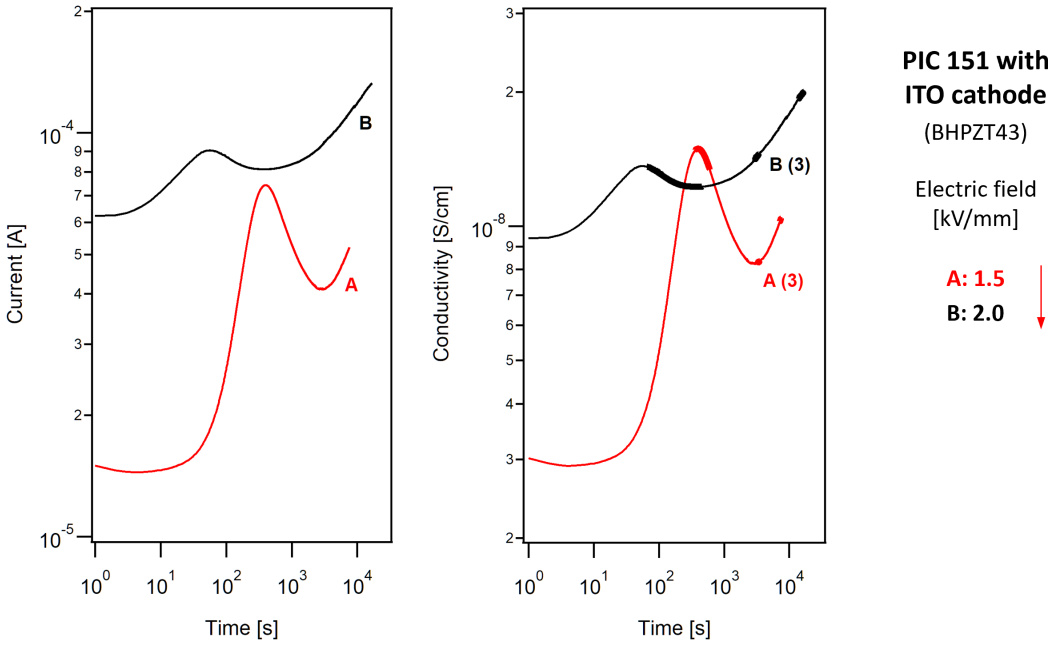

Figure C.7.: Measured currents and calculated conductivities at 300°C and at stepwise increasing applied electric fields for a PIC 151 sample with ITO cathode (sample No. BHPZT43).

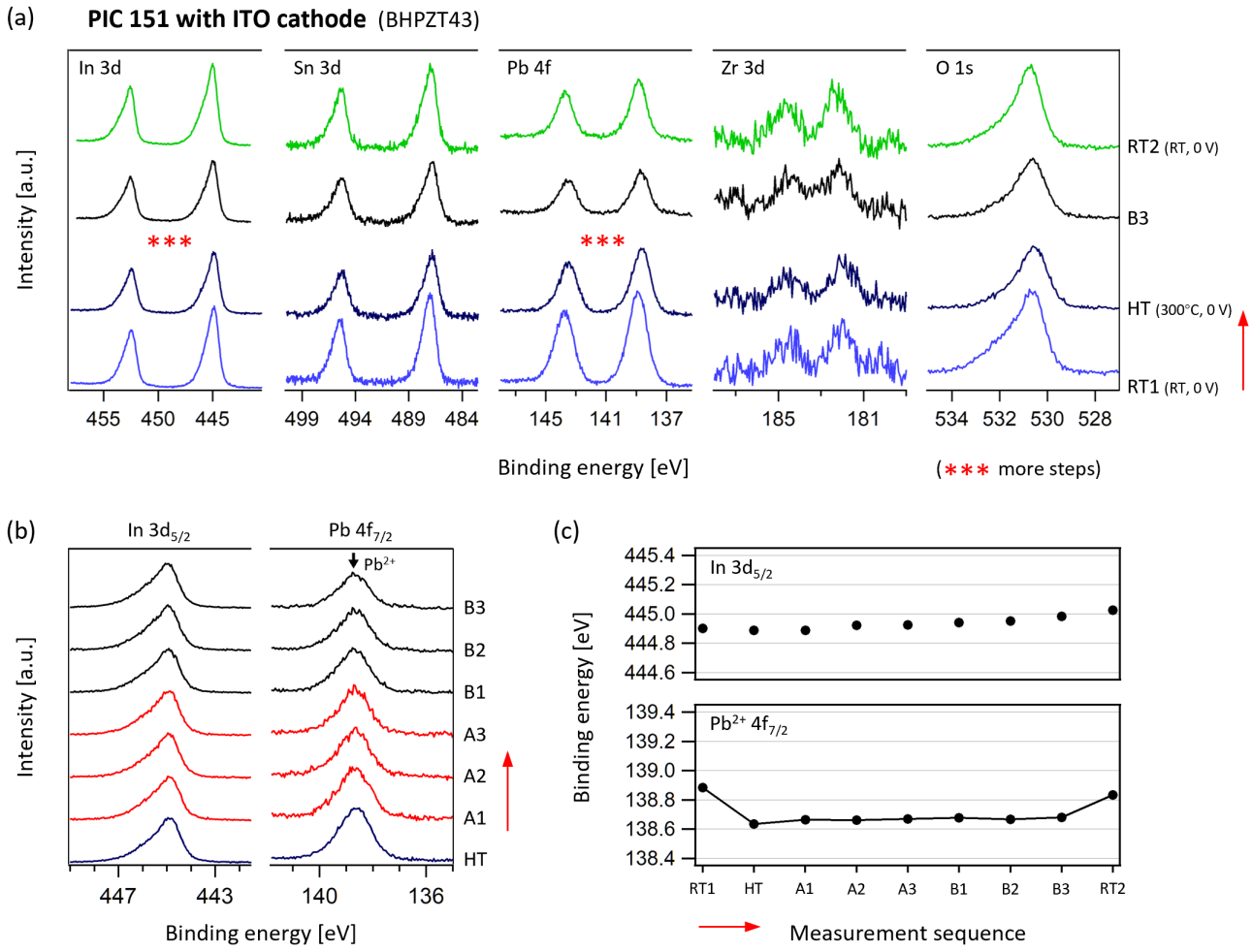

Figure C.8.: XP spectra recorded at the interface between PIC 151 and ITO cathode during the application of stepwise increasing electric fields (sample No. BHPZT43). (a) In 3d, Sn 3d, Pb 4f, Zr 3d, and O 1s core level spectra in several key steps. (b) In $3d_{5/2}$ and Pb $4f_{7/2}$ spectra in detailed measurement sequence at 300°C. (c) Binding energies of In $3d_{5/2}$ and Pb^{2+} $4f_{7/2}$ extracted from all relevant spectra in (a) and (b). The red arrows indicate the sequence of measurements.

C.1.5. PMN with ITO cathode at 250°C

This PMN ceramic sample was 0.175 mm thick, with a 4 nm thin ITO top electrode (deposited at 350°C, used as cathode) and a thick Pt bottom electrode. The operating temperature of the solid electrolyte cell was 250°C. Figure C.9 gives the current and conductivity plots corresponding to stepwise increasing electric fields. Figure C.10 shows all XPS data measured at the cathodic interface between ITO and PMN ceramic throughout the whole experiment.

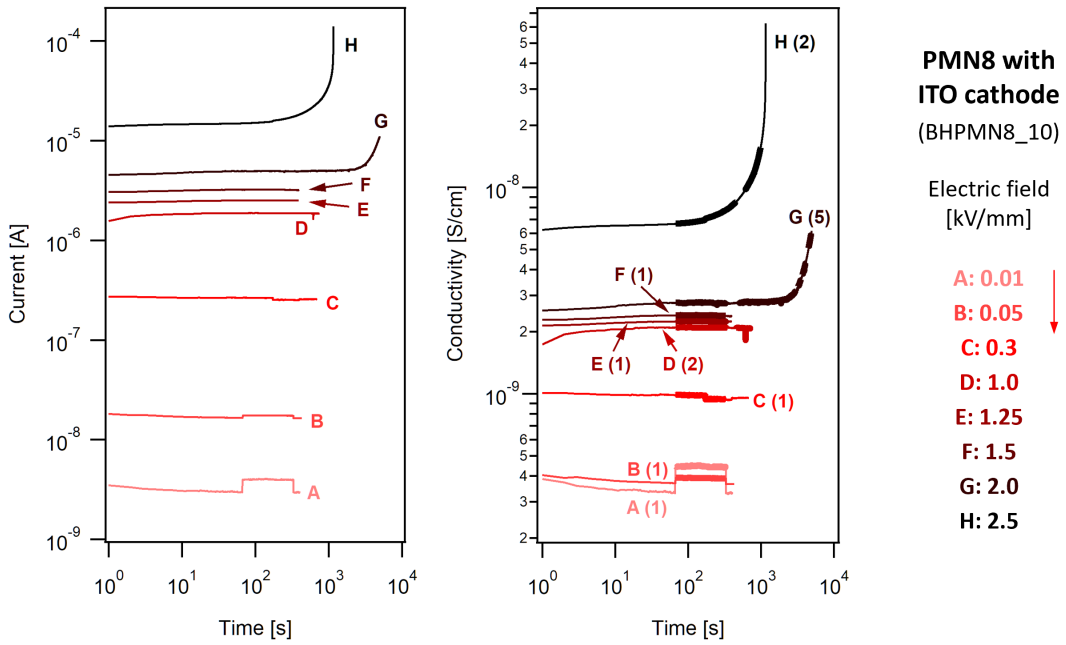

Figure C.9.: Measured currents and calculated conductivities at 250°C and at stepwise increasing applied electric fields for a PMN sample with ITO cathode (sample No. BHPMN8_10).

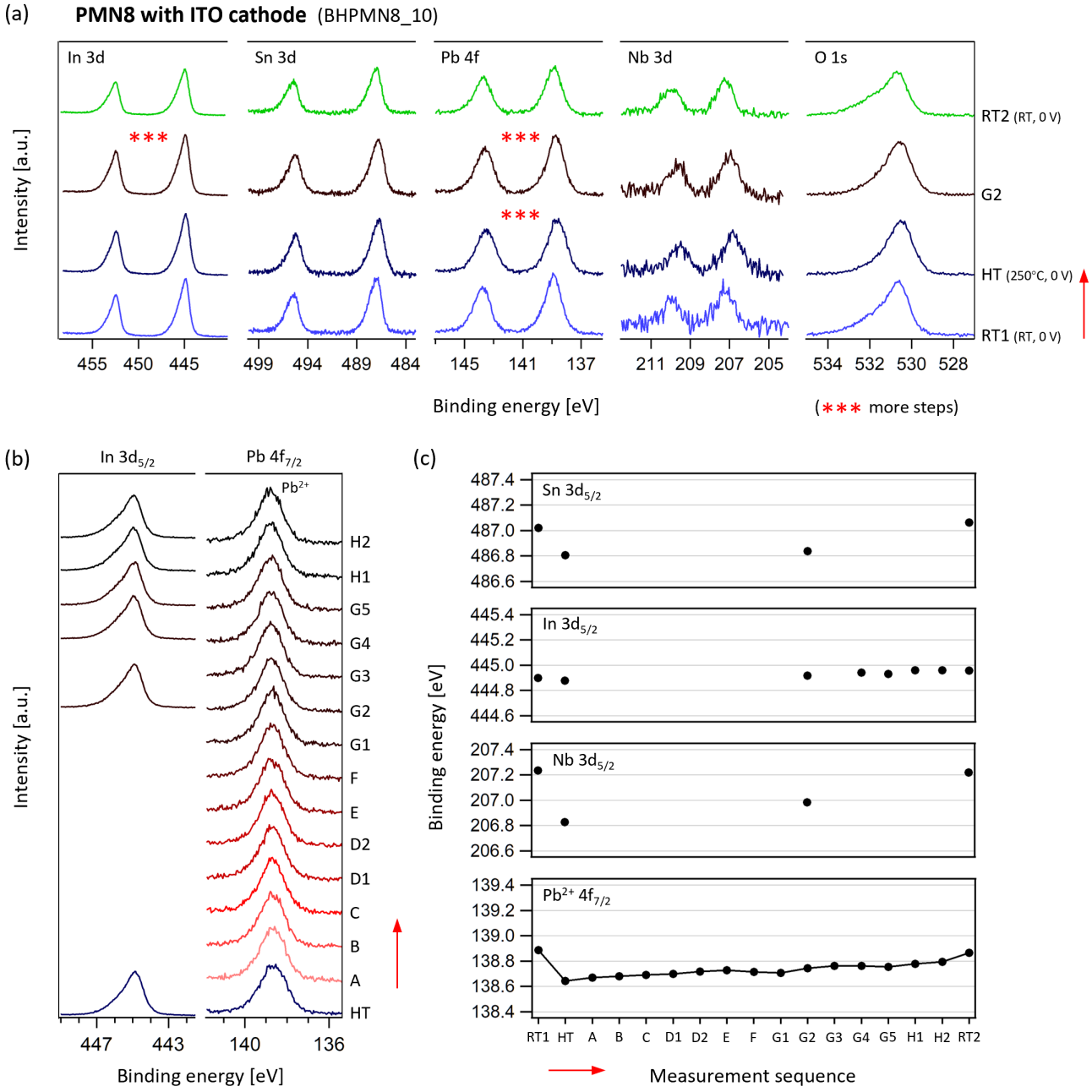

Figure C.10.: XP spectra recorded at the interface between PMN8 and ITO cathode during the application of stepwise increasing electric fields (sample No. BHPMN8_10). (a) In 3d, Sn 3d, Pb 4f, Nb 3d, and O 1s core level spectra in several key steps. (b) In $3d_{5/2}$ and Pb $4f_{7/2}$ spectra in detailed measurement sequence at 250°C. (c) Binding energies of Sn $3d_{5/2}$, In $3d_{5/2}$, Nb $3d_{5/2}$, and Pb^{2+} $4f_{7/2}$ extracted from all relevant spectra in (a) and (b). The red arrows indicate the sequence of measurements.

C.2. In situ X-ray photoelectron spectroscopy at interfaces with ferroelectric polarization

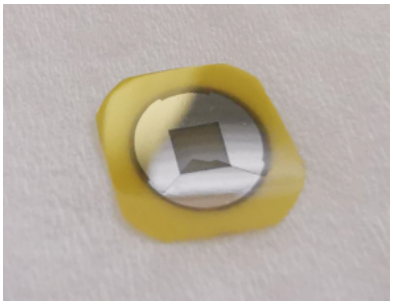

Figure C.11.: Photograph of one of the earlier PIC 151 samples on which cracks occurred during the *P*–*E* loop measurements at 1 Hz. Such samples had 3 nm ITO top electrodes and thick Pt bottom electrodes. Additional Pt layers were coated on the top of ITO for electrical reinforcement.

Curriculum Vitae

Personal information

Name	Huang, Binxiang
Nationality	Chinese

Education

10.2017 – 08.2023	Doctoral student, Technical University of Darmstadt, Germany
03.2015 – 08.2017	Master, Technical University of Darmstadt, Germany
09.2009 – 06.2013	Bachelor, Shanghai Jiaotong University, China

Publications

- **Huang, B.**, Erhart, P., Yang, T. & Klein A. Electrostatic boundary conditions and (electro)chemical interface stability. *Advanced Materials Interfaces* **10**, 2300332 (2023).
- Klein, A., Albe, K., Bein, N., Clemens, O., Creutz, K. A., Erhart, P., Frericks, M., Ghorbani, E., Hofmann, J. P., **Huang, B.**, Kaiser, B., Kolb, U., Koruza, J., Kübel, C., Rödel, J., Rohrer, J., Rheinheimer, W., Schuldt, K. N. S., De Souza, R. A., Streibel, V., Weidenkaff, A., Widenmeyer, M., Xu, B.-X. & Zhang, H. The Fermi energy as common parameter to describe charge compensation mechanisms: A Path to Fermi level engineering of oxide electroceramics. *Journal of Electroceramics* (2023).
- Suzuki, I., Lin, Z., Nogami, T., Kawanishi, S., **Huang, B.**, Klein, A. & Omata, T. High open-circuit voltage in single-crystalline n-type SnS/MoO_3 photovoltaics. *APL Materials* **11**, 031116 (2023).
- Suzuki, I., **Huang, B.**, Kawanishi, S., Omata, T. & Klein, A. Avoiding Fermi level pinning at the SnS interface for high open-circuit voltage. *The Journal of Physical Chemistry C* **126**, 20570–20576 (2022).
- Ren, P., Gehringer, M., **Huang, B.**, Hoang, A.-P., Steiner, S., Klein, A. & Frömling, T. High field electroformation of sodium bismuth titanate and its solid solutions with barium titanate. *Journal of Materials Chemistry C* **9**, 3334–3342 (2021).
- Suzuki, I., **Huang, B.**, Omata, T. & Klein, A. Fermi energy limitation at β-$CuGaO_2$ interfaces induced by electrochemical oxidation/reduction of Cu. *ACS Applied Energy Materials* **3**, 9117–9125 (2020).

Conference contributions

- **Huang, B.** & Klein, A. Polarization dependence of Schottky barrier heights of antiferroelectrics by in-situ photoelectron spectroscopy, poster presentation in Electroceramics XVII (online, 2020).
- **Huang, B.**, Schuldt, K., Bein, N., Suzuki, I. & Klein, A. Energy band alignment and electrical properties of ferroelectrics, poster presentation in Joint ISAF/EMF/ICE/IWPM/PFM Conference (Lausanne, Switzerland, 2019).
- **Huang, B.**, Suzuki, I., Giesecke, R. & Klein, A. The influence of electrode material on the resistance degradation of Fe-doped $SrTiO_3$, poster presentation in Electroceramics XVI (Hasselt, Belgium, 2018).

Acknowledgements

This interesting and challenging doctoral work could not have been completed without the great support and help from many people. I would like to take this opportunity to express my sincere thanks to them.

First and foremost, my deepest gratitude goes to my supervisor Prof. Dr. Andreas Klein, who gave me the opportunity to join the ESM group since my master study and provided the doctoral position for me. I am delighted that I could always have chance to make deep discussions about science with him. I also very much appreciate the freedom which he gave me for the lab work throughout the whole PhD.

I would like to thank Prof. Dr. Tadej Rojac for being the second reviewer of this thesis. I am also very thankful to him for the thoughtful discussions during our collaborations.

I would like to acknowledge the LOEWE project FLAME (Fermi Level Engineering of Antiferroelectric Materials for Energy Storage and Insulation Systems) funded by the State of Hesse. This project is a nice platform where I could really enjoy working with different people about so many interesting scientific and technical topics. Special thanks to Lovro Fulanović, Hui Ding, Sonja Egert, Leif Carstensen for the nice collaborations, discussions, chats, and so on. I am also grateful to our project secretary Jessica Bagnoli who contributed so much to the organization of the whole project. Besides, I would like to extend my sincere thanks to all the other FLAME members and wish everyone a successful future.

I would like to express my gratitude to Prof. Tongqing Yang who strongly supported us with the ceramic samples. I also want to thank the students from Tongji University: Yucheng Liu, Wenna Chao, Yu Han, Yunjing Shi, Xia He, etc. They helped me a lot when I stayed in Shanghai making all these ceramic samples that have been intensively used in this work.

I am deeply grateful to the technicians in the workshop of our department, especially Michael Weber and Jochen Rank. Without their professional and efficient technical support, such a large number of new setups and new sample holders would not have been possible.

Special thanks should go to all the friendly, interesting, and reliable colleagues in the ESM group: Marga Lang, Philipp Wendel, Andreas Hubmann, Getnet Deyu, Raphaël Poulain, Katharina Lohaus, Nicole Bein, Kim Alexander Creutz, Pengcheng Hu, Imke Murschel, etc. I would like to thank everyone for bringing the nice atmosphere to the offices and the labs. Also, I am deeply indebted to the former ESM member Dr. Issei Suzuki who is still making very productive collaboration with us. I am also thankful to receive his kind encouragement regarding both academic research and daily life.

Moreover, thanks should go to Mr. Jean-Christophe Jaud for his professional and careful XRD measurements. I also appreciate the scientific suggestions given by Fangping Zhuo.

Last but not least, I would like to express my love and gratitude to my parents, who strongly supported me in my life during these years despite the long distance between China and Germany.